Hydrodynamic and Transport Phenomena at the Interface between Flow and Aquatic Vegetation: from the Forest to the Blade Scale

by

Jeffrey Tsaros Rominger

S.M., Massachusetts Institute of Technology (2009)
B.S., University of Virginia (2007)

Submitted to the Department of Civil and Environmental Engineering
in Partial Fulfillment of the Requirements for the Degree of

Doctor of Philosophy in the Field of Environmental Fluid Mechanics

at the

MASSACHUSETTS INSTITUTE OF TECHNOLOGY

February 2014

Author .....
Department of Civil and Environmental Engineering
October 3, 2013

Certified by .....
Heidi M. Nepf
MacVicar Faculty Fellow, Professor of Civil and Environmental Engineering
Thesis Supervisor

Accepted by .....
Heidi M. Nepf
Chair, Departmental Committee for Graduate Students

Hydrodynamic and Transport Phenomena at the Interface between Flow and Aquatic Vegetation: from the Forest to the Blade Scale

by

Jeffrey Tsaros Rominger

Submitted to the Department of Civil and Environmental Engineering
on October 3, 2013, in Partial Fulfillment of the
Requirements for the Degree of
Doctor of Philosophy in the Field of Environmental Fluid Mechanics

Abstract

From the canopy scale to the blade scale, interactions between fluid motion and kelp produce a wide array of hydrodynamic and scalar transport phenomena. At the kilometer scale of the kelp forest, coastal currents transport nutrients, microorganisms and spores. But, kelp forests exert a drag force on currents, causing the flow to decelerate and divert as it encounters the canopy, affecting the fate of species transported by the current. We identify a dimensionless flow-blockage parameter, based on canopy width and density, that controls both the length of the flow deceleration region and the total flow in the canopy. We further find that shear layers at the canopy edges can interact across the canopy, providing additional exchange between the canopy and the surrounding water.

At the sub-meter scale, kelp blades are the photosynthetic engines of kelp forests, but are also responsible for the majority of the fluid drag force on the plants and for acquiring nutrients directly from the surrounding water. These blades are highly flexible structures which move in response to the local fluid forcing. Recent studies documenting changes in blade flexural rigidity in response to changes in flow demonstrate a need for understanding the role blade flexural rigidity plays in setting both drag forces, and nutrient flux at the blade surface. We create a model physical system in which we investigate the role of blade rigidity in setting blade forces and rates of scalar exchange in a vortex street. Using a combination of experimental and theoretical investigations, we find that, broadly, forces are higher for more flexible blades, countering the adage that "going with the flow" is beneficial. Below a critical value of the dimensionless blade rigidity, inertial forces from the rapidly deforming blade become significant, increasing the likelihood of blade failure. Nutrient transport is also affected by blade rigidity. As blades deform, they alter the relative fluid motion at the blade surface, affecting nutrient fluxes. We develop a novel experimental method that simulates nutrient uptake to a blade using the transport of a tracer into polyethylene. Through these experiments and modeling, we demonstrate that increased blade flex-

ibility leads to increased scalar transport. Ultimately, blade flexural rigidity affects both mass and momentum flux.

Thesis Supervisor: Heidi M. Nepf
Title: MacVicar Faculty Fellow, Professor of Civil and Environmental Engineering

Acknowledgments

First, I would like to thank my research advisor, Heidi Nepf, for her direction and support throughout my graduate school career. I've had the good fortune to work on a variety of projects while at MIT, all with Heidi's consistent encouragement and guidance. Heidi has further helped me to develop as an instructor, both as a TA for her class, and while mentoring graduate students and undergraduates in the laboratory. She has been an excellent role model both as a scientist and instructor. My interactions with my committee members, Eric Adams, Phil Gschwend and Sally MacIntyre, both individually and together as a group have always helped to clarify difficult questions and offered new insights into my research. Their wide range of expertise has greatly improved this thesis.

I am further indebted to the many outstanding students that I have worked alongside in the Nepf Laboratory over the past six years. Brian White, Anne Lightbody, Yukie Tanino, Kevin Zhang, Mitul Luhar, Lijun Zong, Elizabeth Finn, Aleja Ortiz, John Kondziolka and Erin Connor have assisted with experiments, offered advice, edited papers and have, above all, provided the camaraderie and collaboration that is essential in research. Expertise from the larger environmental fluid mechanics community, and, specifically, from Aaron Chow, Mack Durham, David Gonzalez-Rodriguez, Chris MacMinn and Luis Cueto-Felgueroso has been invaluable. I could not have completed the nutrient flux portion of this thesis without assistance from John MacFarlane and the entire Gschwend Laboratory. I was also fortunate to work with several outstanding undergraduates: Marisa Fryer, Connie Lu, Ivy Huang and Tracey Hayse.

Throughout this process, I've been supported by many friends and family. The Parsons Laboratory is remarkable for its diversity of research interests, but also for its strong sense of community. Every day of my research career in Parsons I've been extremely fortunate to be surrounded by friends. And most importantly, my family and those closest to me have always provided encouragement, helping me grow as a person throughout my career at MIT.

Funding for this work was provided by the Earth Systems Initiative Linden Fellowship, a Schoettler Fellowship, the Martin Family Foundation, an MIT Teaching Assistantship and the National Science Foundation.

Contents

1 Introduction **17**

1.1 Outline 18

2 Flow adjustment and interior flow in a rectangular porous obstruction **21**

2.1 Introduction and Motivation 21

2.2 Problem description and scaling analysis 23

2.2.1 Patch geometry 23

2.2.2 Canopy regions and governing equations 26

2.3 Methods 36

2.4 Results and discussion 41

2.4.1 Flow adjustment regions 41

2.4.2 The shear layer and canopy interior regions 50

2.4.3 Vortex organization and enhancement 52

2.5 Conclusions 57

3 Forces on flexible blades in a vortex street **59**

3.1 Introduction and Motivation 59

3.2 Theory 60

3.3 Methods 64

3.3.1 Experimental Methods 64

3.3.2 Experimental Flowfield 67

3.3.3 Numerical Model 73

3.4 Results 75
3.4.1 Flow Field Comparison 75
3.4.2 Experimental Results 76
3.4.3 Numerical Results 86
3.5 Discussion & Conclusion 88

4 Scalar Transfer at the Surface of a Model Blade 91
4.1 Introduction 91
4.2 History of Nutrient Flux Measurements 93
4.3 Methods 94
4.3.1 Application of the Passive Sampler Technology 94
4.3.2 Laboratory Methods: Full Strips 95
4.3.3 Laboratory Methods: Strip Sections 101
4.4 Flux Models 102
4.5 Model 105
4.5.1 Transfer Velocity 107
4.5.2 Diffusion Coefficient 109
4.6 Results 111
4.6.1 Full Blade Results 111
4.6.2 Blade Section Results 113
4.7 Discussion 120
4.7.1 Flux is set by relative fluid motion 120
4.7.2 Similarity Between Mass and Momentum Flux 125
4.7.3 Predicting Transfer Velocities in the Field 126
4.7.4 Cut blade sections discussion 128
4.7.5 Mass Loss from Blades 129
4.7.6 Experimental method discussion 134

5 Kelp Blade Morphologies: Implications for Drag Force and Nutrient Flux 137
5.1 Blade Morphology and Plasticity 138

5.2 Benefits for Kelp from Morphological Plasticitiy 145
5.2.1 Drag Force Benefits 145
5.2.2 Flapping Flag Instability 147
5.2.3 Nutrient Acquisition 151
5.3 Kelp Blade Differences Across a Kelp Forest 152
5.4 Relative Velocity Measurements and Modeling 153

6 Conclusions **155**

A Patch Experiments Data **159**

B Numerical Solution of Dynamic Flag Equation **191**

C Flume Mixing Test **205**

D Flux Experiments Data **207**

E Measuring THM Concentration **213**
E.1 Overview 213
E.2 Purge and Trap System 213
E.3 Gas Chromatograph 214
E.4 Concentration Calibration 215

F Finite Difference Flux Model **221**

List of Figures

2-1 Plan view of patch 25
2-2 Patch element arrangement 25
2-3 Flow at leading edge 29
2-4 Patch flow regimes 31
2-5 Photograph of patch from above 38
2-6 Photograph of wave gauges 39
2-7 Measured streamwise velocity profiles 42
2-8 Measured kinetic energy 43
2-9 Normalized streamwise velocity profiles 44
2-10 Interior flow regime profiles 47
2-11 Profile of momentum balance terms 49
2-12 Interior adjustment region profiles 49
2-13 Cross-stream velocity and stress profiles 51
2-14 Surface displacement time record 53
2-15 Surface displacement phase lag 54
2-16 Lateral profiles of v_{rms} 55

3-1 Detailed flag position schematic 61
3-2 Unit flag length force balance 63
3-3 Photograph of model blade in flume 66
3-4 Profiles of velocity and vortex strength 68
3-5 Time-averaged velocity field from PIV for $D = 2.5$ cm 69
3-6 Time-averaged velocity field from PIV for $D = 5.0$ cm 70

3-7 Time-averaged vorticity field from PIV for $D = 2.5$ cm 71
3-8 Time-averaged vorticity field from PIV for $D = 5.0$ cm 72
3-9 PIV experimental setup 72
3-10 PIV and theoretical flow field comparison for $D = 2.5$ cm 77
3-11 PIV and theoretical flow field comparison for $D = 5.0$ cm 78
3-12 Experimental instantaneous postures 79
3-13 Experimental and numerical flag oscillation amplitude with scaling . . 82
3-14 Drag force measurements on flag 83
3-15 Flag tip position and acceleration record 84
3-16 Flag peak force measurements 85
3-17 Symmetric and asymmetric response states 87
3-18 Numerical drag predictions 89
3-19 Numerical oscillation amplitude: varying C_D 90

4-1 Foiled flume photo 1 96
4-2 Foiled flume photo 2 97
4-3 Photo of LDPE in flume 98
4-4 LDPE cut sections schematic 102
4-5 LDPE strip schematic 107
4-6 Profile of $w_{rel,rms}$ over strip length 109
4-7 Profile of transfer velocity over strip length 110
4-8 Experimental mass accumulation data 114
4-9 50 μm model and data 115
4-10 250 μm model and data 116
4-11 Cut section model and data for $h = 50$ μm 118
4-12 Cut section model and data for $h = 50$ μm 119

5-1 Schematic of kelp frond and kelp blade geometry 138
5-2 Schematic of blade forces under tension and bending 140
5-3 *Macrocystis* blade photo 142
5-4 Cut-away photo of *Macrocystis* corrugations 143

5-5 Drawing of corrugation section 143
5-6 Effects of kelp morphologies on drag in the vortex street 146
5-7 Flapping flag instability boundary 150

C-1 Flume mixing test 206

List of Tables

2.1 Porous obstruction terminology 36

2.2 Experimental canopy parameters 37

3.1 Experimental flow parameters 68

3.2 Experimental flag parameters 75

3.3 Experimental force, inertia and amplitude data 80

4.1 Experimental time points in mass flux experiments 96

4.2 Model-predicted transfer velocities 110

4.3 Experimental mass accumulation data 112

4.4 Experimental transfer velocities 112

4.5 Experimental mass accumulation data: cut sections 117

4.6 Experimental transfer velocities 117

4.7 Calculated effective velocity scales 121

4.8 Calculated effective diffusive boundary layer thicknesses 123

4.9 Calculated effective renewal timescales 125

4.10 Mass loss model data, $D_{PE} = 1E-10.3$ m^2/s, $h = 50E-6$ m 131

4.11 Mass loss model data, $D_{PE} = 1E-10.3$ m^2/s, $h = 250E-6$ m . . . 132

4.12 Mass loss model data, $D_{PE} = 1E-11.3$ m^2/s, $h = 50E-6$ m 132

4.13 Mass loss model data, $D_{PE} = 1E-11.3$ m^2/s, $h = 250E-6$ m . . . 132

4.14 Mass loss model data, $D_{PE} = 1E-12.3$ m^2/s, $h = 50E-6$ m 133

4.15 Mass loss model data, $D_{PE} = 1E-12.3$ m^2/s, $h = 250E-6$ m . . . 133

5.1 *Macrocystis* blade morphology observations 144

5.2 *Macrocystis* blade dimensionless parameters 145

A.1 Table of $C_D ab = 0.21$ data 160
A.2 Table of $C_D ab = 0.53$ data 163
A.3 Table of $C_D ab = 0.58$ data 165
A.4 Table of $C_D ab = 0.96$ data 167
A.5 Table of $C_D ab = 1.20$ data 170
A.6 Table of $C_D ab = 1.25$ data 173
A.7 Table of $C_D ab = 2.0$ data 175
A.8 Table of $C_D ab = 3.0$ data 178
A.9 Table of $C_D ab = 4.8$ data 183
A.10 Table of $C_D ab = 8.0$ data 185
A.11 $C_D ab = 0.53$ Reynolds Stress data 187
A.12 $C_D ab = 0.53$ lateral transect data 188
A.13 $C_D ab = 0.53$ split lateral transect data 188
A.14 $C_D ab = 2.0$ Reynolds Stress data 189
A.15 $C_D ab = 2.0$ lateral transect data 190
A.16 $C_D ab = 2.0$ split lateral transect data 190

D.1 Flux experiments data, $h = 50$ μm 208
D.2 Flux experiments data, $h = 250$ μm 209
D.3 Flux experiments cut sections data, $h = 50$ μm 210
D.4 Flux experiments cut sections data, $h = 250$ μm 211

E.1 GC calibration data 216
E.2 $CHBr_2Cl$ calibration curves 217

Chapter 1

Introduction

In this thesis, I present a series of studies on hydrodynamic and transport phenomena that occur at the interface between flow and aquatic vegetation. Throughout, I draw motivation from coastal macroalga, or kelp, which are of vital importance ecologically and of great significance economically. Charles Darwin once remarked in awe on the vast number of species which thrive in kelp forests, "if in any country a forest was destroyed, I do not believe nearly so many species of animals would perish as would here, from the destruction of kelp." We now know the number of macro-organisms that rely directly on kelp for food and for shelter to be in the hundreds, albeit less than in tropical rain forests. The number of microorganisms that rely on kelp dwarves this number, however, and we are just beginning to understand these microbial-kelp interactions. Indirectly, kelp provides an essential habitat for breeding, foraging and shelter for flora and fauna of all scales. Moreover, economically, kelp has been essential in both traditional as well as modern cultures as a source of food, fuel and fertilizer.

The studies we present here span several important ecological and dynamical length-scales: the kilometer scale of the kelp forest, the meter scale of kelp blades and the millimeter scale boundary layer at the surface of kelp blades. At the largest scales, ocean currents flow around and through kelp forests, replenishing nutrients, flushing waste products, transporting microscopic organisms and dispersing spores. At the scale of individual blades, the kelp must withstand enormous drag forces created by waves and turbulence, while simultaneously maintaining basic biological functions.

Meanwhile, kelp acquires nutrients and exchanges gases passively via a diffusional process at the millimeter and sub-millimeter scale of the diffusive boundary layer. By studying hydrodynamic and transport phenomena across these scales, we can understand the ways kelp alters the local hydrodynamic environment in the coastal ocean and we can understand the adaptations which allow kelp to thrive in this high-drag, often nutrient-limited environment.

When abstracted, these problems can be framed in a manner applicable not only to aquatic vegetation, but also to a wide range of both fundamental and applied scientific problems. Phenomena at the scale of a kelp forest are analogous not only to flow through natural terrestrial canopies, but to the movement of air in urban environments as well. The dynamics of kelp blades, which are highly-flexible, elongated bodies, can provide insight into the dynamics of other flexible flora and fauna as well as flexible engineered structures. Finally, through studying the exchange of nutrients at the surface of a moving model kelp blade, we can gain insight into the steady diffusion and surface renewal models which are applied to gas, heat and chemical exchange throughout science and industry. Throughout, we attempt to frame these ecologically motivated studies in the broadest possible context in order to derive the most fundamental understanding of the problems.

1.1 Outline

In a kelp forest, kelp individuals grow in close proximity to form a porous obstruction with finite boundaries. Near shore currents bring fresh nutrients, plankton and larvae to kelp ecosystems. These currents are altered by the step change in the drag force at the kelp boundaries and flow through and around these forests in a manner set by the drag and geometry of the forest. In Chapter 2, we examine the flow at the leading edge and interior regions of a finite porous obstruction. we examine both the steady and unsteady flow patterns that form at the porous obstruction and interpret the results in the contexts of both aquatic and terrestrial obstructions.

In Chapter 3, inspired by the dynamics of kelp blades, we examine the problem of

a flexible flag in a vortex street. In the ocean, kelp blades are subjected to unsteady currents, waves and turbulence at a wide spectrum of scales. Rather than attempt to replicate the oftentimes messy fluid environment in the coastal ocean, we select a model flow field, the vortex street, for our experiments. A vortex street presents a simple, unsteady flow field which we can use to perturb our model kelp blades at a specific frequency and wavelength. Dynamically, a thin, flexible flag serves as an appropriate model for a single kelp blade. Through a combination of experiments and analytics, we demonstrate that a flag in a vortex street responds with two fundamental regimes: a symmetric state about the flow centerline, and below a critical value of rigidity, an asymmetric state trapped in half of the vortex street. The forces on the flag are ultimately determined by the response state. In the symmetric state, the force is proportional to the oscillation amplitude. In the asymmetric state, the force increases with the contribution of inertial forces at the flag tip.

In Chapter 4, we further utilize our flag-in-flow model system to examine the rate of scalar flux at a flexible surface with the use of a novel experimental method. We first describe the design of this experimental method in which we measure the rate of diffusion of an organic compound from the surrounding water into our model flexible blades. We then describe the results of these experiments, which demonstrate how scalar flux is affected by blade flexural rigidity. These results provide insight into the mechanism of nutrient acquisition by kelp blades in the coastal ocean.

In Chapter 5, we examine recent morphological observations of kelp blades in the context of blade drag force and nutrient acquisition. Studies have shown that blade morphology adapts to its local flow environment primarily by increasing its flexural rigidity. We demonstrate that increases in flexural rigidity in high-flow environments effectively reduce the drag force on the kelp blades via altering the blades' dynamic response to turbulent flow. These changes in flexural rigidity also effectively decrease nutrient acquisition rates. In high-drag environments, however, blades can already acquire sufficient nutrients from the flow such that the blade drag force is the overriding environmental stimulus.

Finally, in Chapter 6, we summarize the results presented in this thesis. We

discuss how, by treating kelp as a model system, we can gain insight into not only physical phenomena in the coastal ocean, but can gain insight into a much broader set of scientific questions.

Chapter 2

Flow adjustment and interior flow in a rectangular porous obstruction

In this chapter, we describe an experimental study on the flow through a finite porous obstruction. This chapter begins with a scaling analysis for the upstream adjustment region (§2.2.2), the interior adjustment region (§2.2.2), and the canopy interior (§2.2.2). In the methods section (§2.3), we describe our experiments using a model canopy in the middle of the experimental water channel. In §2.4, we compare our experimental results with the theoretical scalings. This chapter has been adapted from Rominger and Nepf (2011) [88].

2.1 Introduction and Motivation

There are many examples of flow encountering fixed, porous obstructions. For generality, we refer to all such obstructions as canopies. Man-made canopies include urban areas with close groupings of buildings, and wind farms. Terrestrial and aquatic vegetation is often organized in canopies. Coastal ocean canopies include coral reefs, seagrasses and kelp forests. Agricultural fields are porous obstructions, organized in regular rows, and aquaculture, such as oyster farms, are dense underwater canopies in estuarine zones.

When the height of these canopies is very small relative to the depth of flow,

and it is only of interest to understand the flow structure outside of the canopy, it is sufficient to treat the canopy as surface roughness. However, when the canopy is emergent or occupies a significant fraction of the flow depth, or when the flow through the canopy has significant physical and/or biological implications, it becomes necessary to describe the flow within it.

Many studies have looked at the effect of porous layers on flow characteristics, such as mean velocity, turbulence level, and scalar and momentum flux. [7] described laminar flow adjacent to a porous layer, and several authors have extended this work to describe turbulent flow adjacent to more general arrays [83, 113]. In urban settings, [10] predicted a steady-state value for the in-canopy velocity based on the element density within the array and the exterior flow speed above the canopy. [83] showed how the presence of a canopy creates an unstable shear layer that generates Kelvin-Helmholtz vortices, which enhance transport between the layer and the adjacent open flow. Other studies have described the parameters that set the length scale of momentum penetration from a free stream into a canopy and the size of the shear layer [105, 113]. The above studies have all focused on fully-developed flow, or the development of flow at the flow-parallel interface of an infinitely long canopy. However, vegetation and man-made structures rarely exist as continuous canopies, but rather are often organized in patches of finite dimensions and, specifically, have a distinct leading edge perpendicular to the direction of mean flow. Where flow encounters the leading edge of a finite-width canopy, a portion of the flow is diverted, and a portion of the flow enters and advects through the length of the canopy. The fraction of flow moving through the canopy can influence the water and air quality within the canopy, as well as the ecosystem function of natural canopies.

In this chapter we consider the leading edge and the interior regions of an emergent, rectangular canopy in uniform, shallow flow. In a region close to the leading edge, the velocity responds to the step change in flow resistance from only bed friction to the addition of canopy drag. This adjustment region has previously been described by a balance between fluid inertia and the streamwise canopy drag force [53, 9, 19, 38]. We show that this balance is applicable in canopies with low flow-blockage in both

terrestrial and aquatic flows. The canopy flow-blockage is a dimensionless parameter that is a function of the canopy solid volume fraction and the canopy width. In this chapter we also describe the different flow behavior for canopies with high flow-blockage, for which the simple balance of fluid inertia and drag does not apply, and we define the expected transition between canopies that exhibit low and high flow-blockage behavior.

The mean streamwise velocity in the interior of a canopy has been well-described for terrestrial canopies with low flow-blockage [9, 10, 28], however it less well understood for canopies with high flow-blockage. We present new scaling arguments for high flow-blockage canopies, and provide experimental data that clearly depict different interior regimes for canopies with low and high flow-blockage. Finally, we investigate the role played by the KH vortices that form at the two flow-parallel interfaces in the transport of momentum and scalars to the canopy interior.

2.2 Problem description and scaling analysis

2.2.1 Patch geometry

We consider a finite rectangular canopy located in a fluid of depth h. The canopy is emergent, i.e. its height is greater than or equal to the water depth, and the canopy is uniform over the depth, such that the system can be approximated as two-dimensional. The canopy length is parallel to the mean flow direction with velocities u and v in the streamwise and transverse directions, respectively. The x-axis is parallel to the mean flow and sits along the centerline of the array. The y-axis is at the leading edge of the canopy and is perpendicular to the mean flow direction (Fig. 2-1). The array is described by its half-width, b. The full width of the canopy perpendicular to the oncoming flow is $B = 2b$. We restrict our analysis to canopies where the overall length is much larger than the canopy width, and where the canopy width is much smaller than the flow domain.

In these experiments the canopy half-width is geometrically similar to the height

of urban, terrestrial or submerged canopies, for which the flow passes over the top of the canopy and $y = 0$ is the impermeable ground. However, there are important differences between terrestrial canopies and the shallow water configuration that we study in this chapter. The upstream velocity profile for canopies in shallow water is uniform (Fig. 2-1), while for terrestrial canopies the upstream flow profile is logarithmic. Furthermore, shallowness inhibits large-scale three-dimensional turbulence, while in deeply submerged aquatic canopies or in terrestrial canopies, this large-scale turbulence can play a role in the transport of momentum and scalars. Submerged canopies have been classified as sparse or dense based on the magnitude of canopy drag relative to the bed shear stress. Dense canopies contribute sufficient drag to transform the velocity profile into a mixing layer form [83]. In the limit of very sparse submerged aquatic canopies or very sparse terrestrial canopies, the velocity profile remains logarithmic and the canopy behaves like bed roughness [29, 9].

In this study, the model canopy elements have a diameter, d, and the mean spacing between the centers of two adjacent elements is s. The solid volume fraction, ϕ, is the volume within the canopy occupied by solid elements, which is the complement of the canopy porosity, $\eta = 1 - \phi$. The frontal area per unit volume of the canopy is $a = nd$, where n is the number of elements per unit planar area. Within the array, the flow is both unsteady in time and spatially heterogeneous at the scale of the individual elements. A double-averaging method is used to remove the temporal and element-scale spatial heterogeneity [40, 84, 75]. The instantaneous equations are first averaged over a period of time longer than the timescale of turbulence or instabilities in the flow. The time-averaged equations are then averaged over an area of size s^2 including only area occupied by the fluid. The spatial average is denoted by the angled brackets and the overbar indicates the time average. The parameter a is valid only for length scales longer than the canopy spacing, s, and therefore in a small region near the leading edge the definition of a breaks down. However, in all of the arrays tested in this study, the element spacing, s, is much smaller than the length scales of the array, and the definition of a is sufficient for our analysis.

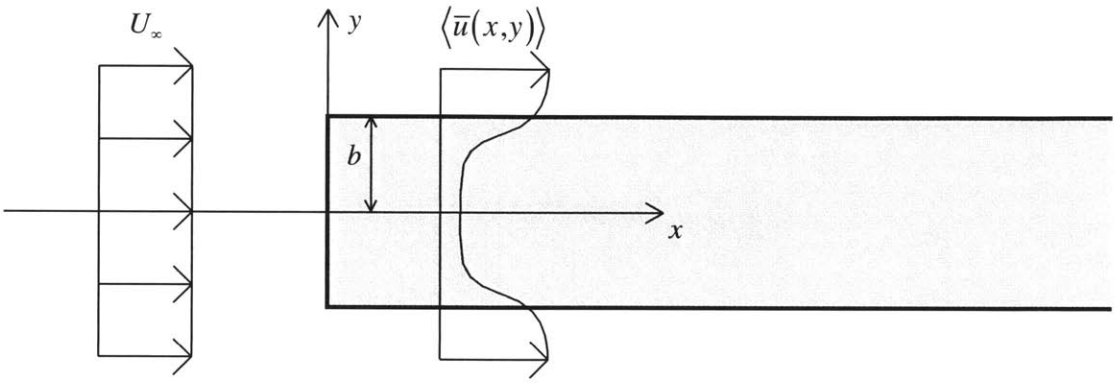

Figure 2-1: Plan view of a rectangular porous obstruction in a uni-directional current with steady and uniform velocity, U_∞, upstream.

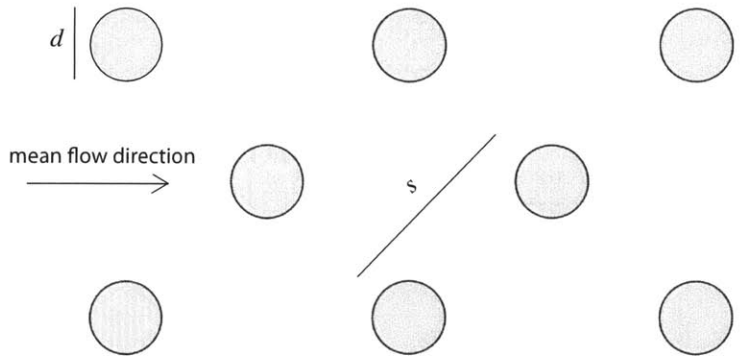

Figure 2-2: Plan view of the array elements, with diameter, d, and spacing, s.

2.2.2 Canopy regions and governing equations

Governing Equations

The shallow water equations for continuity, streamwise momentum, and cross-stream momentum are

$$\frac{\partial h\langle\overline{u}\rangle}{\partial x} + \frac{\partial h\langle\overline{v}\rangle}{\partial y} = 0 \tag{2.1}$$

$$\frac{\partial h\langle\overline{u}\rangle\langle\overline{u}\rangle}{\partial x} + \frac{\partial h\langle\overline{v}\rangle\langle\overline{u}\rangle}{\partial y} = -\frac{1}{\rho}\frac{\partial h\langle\overline{p}\rangle}{\partial x} + \frac{1}{\rho}\left[\frac{\partial h\langle\overline{\tau_{xx}}\rangle}{\partial x} + \frac{\partial h\langle\overline{\tau_{xy}}\rangle}{\partial y}\right] - hF_x \tag{2.2}$$

$$\frac{\partial h\langle\overline{u}\rangle\langle\overline{v}\rangle}{\partial x} + \frac{\partial h\langle\overline{v}\rangle\langle\overline{v}\rangle}{\partial y} = -\frac{1}{\rho}\frac{\partial h\langle\overline{p}\rangle}{\partial y} + \frac{1}{\rho}\left[\frac{\partial h\langle\overline{\tau_{yx}}\rangle}{\partial x} + \frac{\partial h\langle\overline{\tau_{yy}}\rangle}{\partial y}\right] - hF_y \tag{2.3}$$

in which u, v are the fluid velocities in the x, y directions, respectively, h is the flow depth, ρ is the fluid density, p is the fluid pressure and τ is the shear stress. We define F_i as the drag force exerted on the fluid in the direction i.

Outside the canopy:

$$F_x = \frac{1}{2}\frac{C_f}{h}\langle\overline{u}\rangle\left(\langle\overline{u}\rangle^2 + \langle\overline{v}\rangle^2\right)^{1/2} \tag{2.4}$$

$$F_y = \frac{1}{2}\frac{C_f}{h}\langle\overline{v}\rangle\left(\langle\overline{u}\rangle^2 + \langle\overline{v}\rangle^2\right)^{1/2} \tag{2.5}$$

Inside the canopy:

$$F_x = \frac{1}{2}\frac{C_D a}{(1-\phi)}\langle\overline{u}\rangle\left(\langle\overline{u}\rangle^2 + \langle\overline{v}\rangle^2\right)^{1/2} \tag{2.6}$$

$$F_y = \frac{1}{2}\frac{C_D a}{(1-\phi)}\langle\overline{v}\rangle\left(\langle\overline{u}\rangle^2 + \langle\overline{v}\rangle^2\right)^{1/2} \tag{2.7}$$

where C_f is the bed friction coefficient and C_D is the drag coefficient of the array elements. Outside of the canopy, $\phi = 0$. Measurements of Δh around the canopy show the maximum values of $\Delta h/h$ are $O(10^{-3})$ and too small to affect continuity. Therefore, from this point forward, we adopt a rigid lid approximation and assume that $h(x, y) = h = constant$ both outside of and in the interior of the canopy.

Upstream adjustment region

Far upstream, the flow is assumed to be uniform ($u = U_\infty$ and $v = V_\infty = 0$) and unaffected by the canopy. At the canopy leading edge, there is a step change in the flow resistance with the addition of canopy drag. In aquatic vegetation, canopy drag is generally an order of magnitude or more larger than bed friction. Approaching the leading edge, the fluid begins to decelerate in response to the increase in pressure (Fig. 2-4). The pressure gradient causes lateral flow diversion in a region upstream of the canopy termed the *upstream adjustment region* (equivalent to the *impact region* in [9]). Based on measurements, the lateral divergence of turbulent stress in this region is small and negligible compared to the remaining terms in the momentum equation, and so they are dropped from the momentum equations. Within this region the flow is governed by the following equations of continuity and momentum balance:

$$\frac{\partial\langle\overline{u}\rangle}{\partial x} + \frac{\partial\langle\overline{v}\rangle}{\partial y} = 0 \tag{2.8}$$

$$\langle\overline{u}\rangle\frac{\partial\langle\overline{u}\rangle}{\partial x} + \langle\overline{v}\rangle\frac{\partial\langle\overline{u}\rangle}{\partial y} = -\frac{1}{\rho}\frac{\partial\langle\overline{p}\rangle}{\partial x} - \frac{1}{2}\frac{C_f}{h}\langle\overline{u}\rangle\left(\langle\overline{u}\rangle^2 + \langle\overline{v}\rangle^2\right)^{1/2} \tag{2.9}$$

$$\langle\overline{u}\rangle\frac{\partial\langle\overline{v}\rangle}{\partial x} + \langle\overline{v}\rangle\frac{\partial\langle\overline{v}\rangle}{\partial y} = -\frac{1}{\rho}\frac{\partial\langle\overline{p}\rangle}{\partial y} - \frac{1}{2}\frac{C_f}{h}\langle\overline{v}\rangle\left(\langle\overline{u}\rangle^2 + \langle\overline{v}\rangle^2\right)^{1/2} \tag{2.10}$$

Although, this region is upstream of the porous array, we employ a double average notation for consistency with later equations describing the flow within the array.

Unlike flow near a bluff body, flow can move both through and around a porous array, and the element density plays a role in determining how much of the flow goes through versus around. For low flow-blockage canopies, the streamlines show very little upstream diversion, while for high flow-blockage canopies, the streamlines show significant upstream diversion (Fig. 2-3). Within the low flow-blockage canopy, the spreading of dye is due primarily to turbulent diffusion, rather than divergence, based on the observed velocity field. The visualization shown in Fig. 2-3 suggests that high flow-blockage canopies affect upstream flow in a manner similar to bluff bodies, with divergence beginning upstream of the body over a length scale proportional to the canopy width. Therefore, similar to a bluff body, we expect that the pressure increase at the leading edge of high flow-blockage canopies, Δp, scales on ρU_∞^2. In contrast, for low flow-blockage canopies, there is little upstream change in the flow velocity, which implies that the pressure increase at the leading edge is small, and that $\Delta p \to 0$ as the canopy flow-blockage approaches zero. The dependency of Δp on the flow-blockage is verified through experimental observations discussed in §2.4.

To find the upstream adjustment length, L_O, the governing equations, 2.8, 2.9 and 2.10, are scaled using the following characteristic values:

$$x \sim L_O \tag{2.11a}$$

$$y \sim b \tag{2.11b}$$

$$u \sim U_\infty \tag{2.11c}$$

$$v \sim \frac{bU_\infty}{L_O} \text{ (from 2.8)} \tag{2.11d}$$

$$\frac{\partial u}{\partial x} \sim \frac{\Delta u}{L_O} \tag{2.11e}$$

$$\frac{\partial p}{\partial x} \sim \frac{\Delta p}{L_O} \tag{2.11f}$$

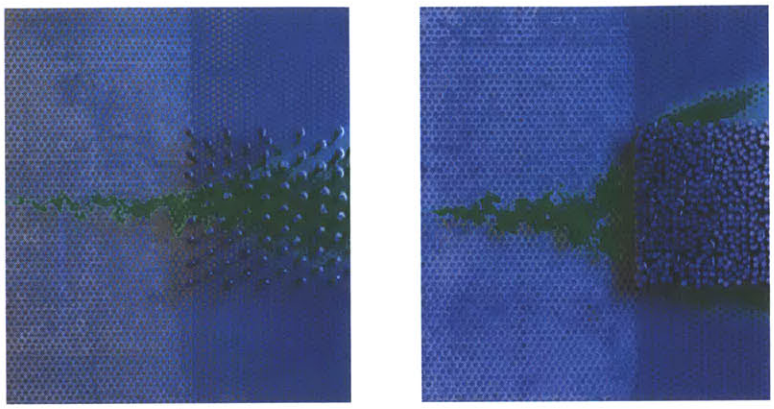

Figure 2-3: Flow at the leading edge of a low flow-blockage canopy (left image) and of a high flow-blockage canopy (right image). For the low flow-blockage canopy, the dye trace released at the centerline shows little divergence upstream of the canopy, while for the high flow-blockage canopy, the dye trace diverges significantly upstream of the canopy. Within the low-flow blockage canopy, the spread of the dye trace is due primarily to diffusion.

The scaled governing equations are then:

$$\rho\frac{U_\infty \Delta u}{L_O} \sim -\frac{\Delta p}{L_O} - \rho\frac{C_f}{2h(1-\phi)}U_\infty^2\left[1+\left(\frac{b}{L_O}\right)^2\right]^{1/2} \tag{2.12}$$

$$\rho\frac{U_\infty \Delta u}{L_O}\frac{b}{L_O} \sim -\frac{\Delta p}{b} - \rho\frac{C_f}{2h(1-\phi)}U_\infty^2\frac{b}{L_O}\left[1+\left(\frac{b}{L_O}\right)^2\right]^{1/2} \tag{2.13}$$

From these scaled equations we can infer that for all canopies, regardless of the magnitude of the velocity and pressure changes, the pressure and inertial terms balance only if

$$L_O \sim b. \tag{2.14}$$

Interior adjustment region

The deceleration that began upstream of the canopy continues within the canopy. However, the retarding force increases due to the addition of canopy drag which is large enough to make bed friction negligible within the canopy. In addition, within

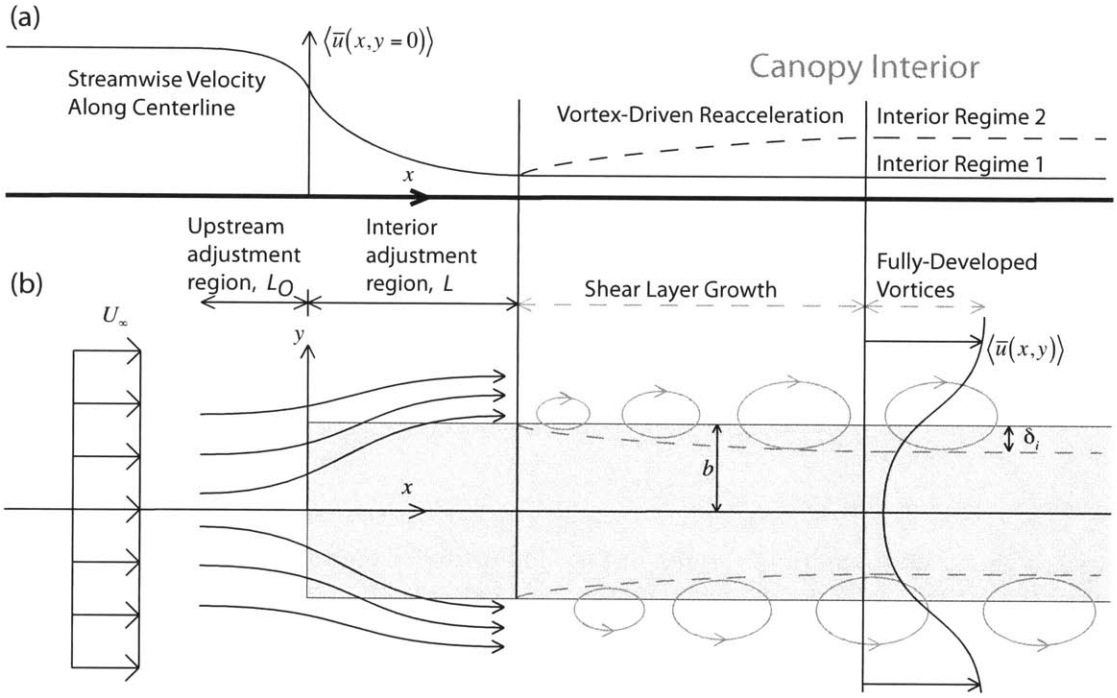

Figure 2-4: (a) The streamwise velocity depicted along the canopy centerline. (b) Plan-view of the flow adjustment at the leading edge of the canopy and the growth of the shear layer and coherent structures along the flow-parallel edges. The flow begins to decelerate upstream of the canopy (*upstream adjustment region*) and continues to decelerate within the canopy (*interior adjustment region*). Following the adjustment regions, the flow can enter two different uniform regimes in the *canopy interior*: (Regime 1) a balance between the pressure gradient and the drag force, or, (Regime 2) a balance between momentum penetration from the canopy edges and the drag force.

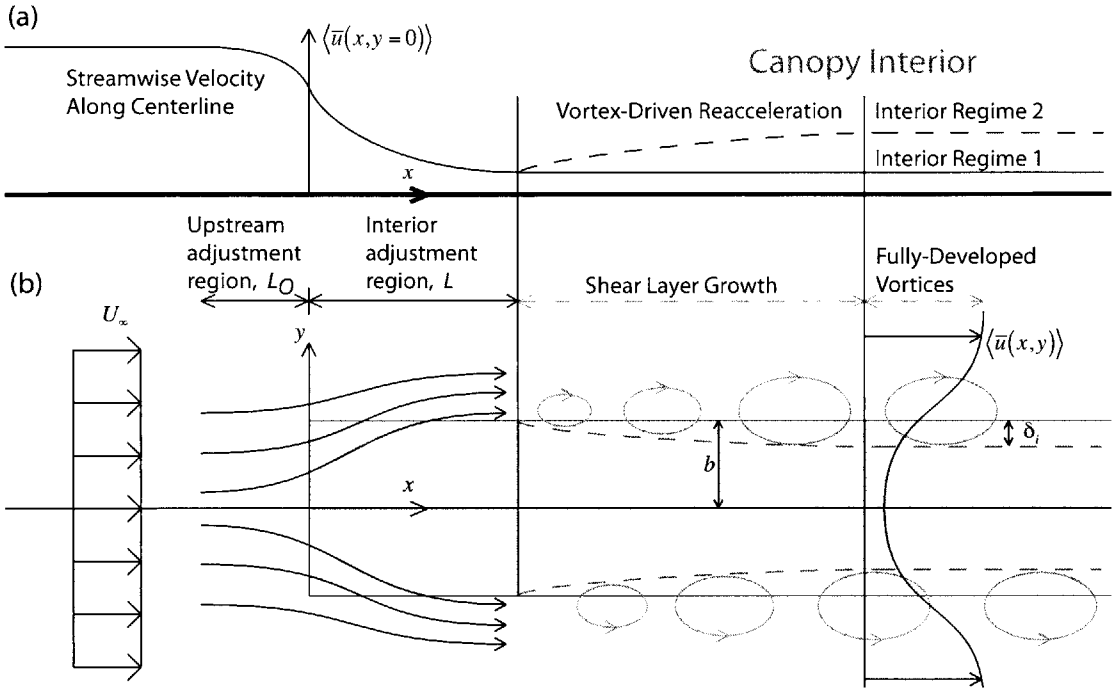

Figure 2-4: (a) The streamwise velocity depicted along the canopy centerline. (b) Plan-view of the flow adjustment at the leading edge of the canopy and the growth of the shear layer and coherent structures along the flow-parallel edges. The flow begins to decelerate upstream of the canopy (*upstream adjustment region*) and continues to decelerate within the canopy (*interior adjustment region*). Following the adjustment regions, the flow can enter two different uniform regimes in the *canopy interior*: (Regime 1) a balance between the pressure gradient and the drag force, or, (Regime 2) a balance between momentum penetration from the canopy edges and the drag force.

The scaled equations are

$$\rho\frac{U_\infty^2}{L} \sim -\frac{\Delta p}{L} - \rho\frac{C_D a}{2(1-\phi)}U_\infty^2\left[1+\left(\frac{b}{L}\right)^2\right]^{1/2} \tag{2.18}$$

$$\rho\frac{U_\infty^2}{L}\frac{b}{L} \sim -\frac{\Delta p}{b} - \rho\frac{C_D a}{2(1-\phi)}U_\infty^2\left[\left(\frac{b}{L}\right)^2+\left(\frac{b}{L}\right)^4\right]^{1/2} \tag{2.19}$$

Dividing by the inertial term in each equation, respectively, the equations simplify to:

$$1 \sim -\frac{\Delta p}{\rho U_\infty^2} - \frac{1}{2(1-\phi)}\left[(C_D aL)^2+(C_D ab)^2\right]^{1/2} \tag{2.20}$$

$$1 \sim -\frac{L^2\Delta p}{b^2\rho U_\infty^2} - \frac{1}{2(1-\phi)}\left[(C_D aL)^2+(C_D ab)^2\right]^{1/2} \tag{2.21}$$

This form of the scaled equations brings out an important non-dimensional parameter, $C_D ab$, which represents the non-dimensional flow-blockage of the array. The parameter $(C_D a)^{-1}$, called the canopy drag length scale, represents the length-scale of flow deceleration associated with canopy drag. The canopy flow-blockage factor is therefore a ratio of two length scales: the canopy width, b, and the canopy drag length scale. When this ratio is large, $C_D ab \gg 1$, canopies will be referred to as high flow-blockage canopies, while those with a value of $C_D ab \ll 1$ will be referred to as low flow-blockage canopies. The transition between these two regimes is expected to occur when $b \approx (C_D a)^{-1}$, or $C_D ab \approx 1$. Measurements described later in the chapter suggest that the threshhold is closer to 2, i.e. $C_D ab \geq 2$ fall in the high flow-blockage regime. We will later show that $C_D ab$ also describes the pressure increase at the leading edge, specifically for high flow-blockage $\Delta p \sim \rho U_\infty^2$, and for low flow-blockage, $\Delta p \to 0$.

Using the dual scaling for the pressure increase at the leading edge (Eq. 2.17), we can now find the length scale of the interior adjustment region. For low flow-blockage

canopies, $C_D ab \ll 1$, and to the first order we assume that $\Delta p = 0$, so that the first and last terms on the right hand side of (Eq. 2.20) and (Eq. 2.21) drop out, indicating $L \sim 2(1-\phi)/C_D a$. However, for these conditions, $\phi \ll 1$, and thus we can simply write,

$$L \sim \frac{2}{C_D a} \tag{2.22}$$

and therefore $L \gg b$. This result is equivalent to that reported by [9].

For high flow-blockage canopies, $C_D ab \gg 1$ and $\Delta p \sim \rho U_\infty^2$. The pressure term must be $\mathcal{O}(1)$ in both equations, which indicates

$$L \sim b \tag{2.23}$$

and therefore $L \gg 2/C_D a$. Taken together, (Eq. 2.22) and (Eq. 2.23) imply that L scales on the maximum of $2(C_D a)^{-1}$ and b, a dependency we can capture with:

$$L \sim \left[\left(\frac{2}{C_D a}\right)^2 + (b)^2\right]^{1/2} \tag{2.24}$$

which allows for a smooth transition between the two limits.

Canopy interior region

Downstream of the flow adjustment region, $x > L$, the flow can enter two different uniform regimes. In the interior region, the streamlines become parallel to the canopy edges, and the velocity within the canopy is less than the adjacent free stream velocity, creating a shear layer at the canopy's flow-parallel edges (Fig. 2-4). When $C_D ab \geq 0.1$, the velocity profile in the shear layer exhibits an inflection point [74] that is unstable and promotes the growth of Kelvin-Helmholtz vortices [17, 25, 47, 37, 113]. Canopies in which $ab < 0.1$ are generally classified as sparse canopies, and those in

which $ab > 0.1$ are called dense canopies [9, 19]. We are interested in canopies that generate an inflection point in the shear layer, and therefore, with respect to this classification, all of the canopies considered in this analysis are dense. Coherent, Kelvin-Helmholtz vortices have been observed in many experimental settings, including the interfaces of both terrestrial and aquatic canopies [83, 102, 92]. These coherent structures penetrate a distance δ_i into the canopy and dominate mass and momentum exchange in this region. The lateral penetration of coherent structures into a canopy is given by $\delta_i \sim (C_D a)^{-1}$ [81, 113, 74]. The influence of the vortices on the canopy interior depends on how this penetration length scale compares with the transverse dimension of the canopy, i.e. the ratio:

$$\frac{\delta_i}{b} \sim \frac{1}{C_D ab} \tag{2.25}$$

which is the inverse of the canopy flow-blockage factor. When this ratio is small, the canopy interior is isolated from the turbulent stress generated at the canopy edges, and we anticipate that the interior streamwise flow is governed by a balance between the pressure gradient and the canopy drag:

$$0 = -\frac{1}{\rho}\frac{\partial \langle \overline{p} \rangle}{\partial x} - \frac{1}{2}\frac{C_D a}{(1-\phi)}\langle \overline{u} \rangle^2 \tag{2.26}$$

where the lateral velocity, $\langle \overline{v} \rangle = 0$. However, when δ_i is equal to or greater than b, turbulent stress penetrates into the canopy interior and is the dominant driving force for the flow, resulting in a different momentum balance in the interior:

$$0 = -\frac{1}{2}\frac{C_D a}{(1-\phi)}\langle \overline{u} \rangle^2 - \frac{\partial}{\partial y}\left(\langle \overline{u'v'} \rangle\right) \tag{2.27}$$

where $-\rho\langle \overline{u'v'} \rangle$ is the Reynolds stress. The following scale analysis indicates that the pressure gradient is negligible in this interior regime. If the vortices penetrate to the center of the canopy, the Reynolds stress term will scale as

$$\frac{\partial}{\partial y}\left(\langle\overline{u'v'}\rangle\right) \sim \frac{U_\infty^2}{b} \tag{2.28}$$

Because the uniform upstream velocity is set by the balance between the pressure gradient and bed drag, we can also write

$$\frac{1}{\rho}\frac{\partial p}{\partial x} = \frac{C_f}{h}U_\infty^2 \tag{2.29}$$

Combining (Eq. 2.28) and (Eq. 2.29), the ratio of the Reynolds stress term to the pressure term is h/bC_f, which is large (> 50) for every experiment in this study, confirming that when the vortices penetrate to the canopy centerline, the Reynolds stress gradient dominates over the pressure gradient and (Eq. 2.27) applies.

[9] also defines submerged canopies as shallow or deep based on the ratio of the canopy height, defined h_e in that work, and the penetration of the shear layer into the canopy. If the two length scales are comparable, the canopy is shallow, and if the canopy height is much greater than the penetration length of the shear layer, the canopy is deep. Using the fact that the penetration of the shear layer into the canopy scales on $(C_Da)^{-1}$, and drawing on the geometric parallel between the canopy height in submerged canopies, h_e, and the canopy width in shallow water canopies, b, it is evident that the definitions shallow and deep are similar to the definitions of low and high flow-blockage. Therefore, the canopy flow-blockage factor, C_Dab, governs both the length scale of the flow adjustment regions (Eq. 2.24), and the influence the turbulent stresses have on the interior velocity, downstream of the adjustment regions. Experiments described below suggest that the transition between high and low flow-blockage occurs near a threshold value of $C_Dab = 2$. To summarize, high flow-blockage canopies, where $C_Dab \geq 2$, have an interior adjustment length proportional to the canopy width, b, and an interior velocity driven by the ambient pressure gradient, while low flow-blockage canopies, $C_Dab < 2$, have an interior adjustment length proportional to the canopy drag length scale, $(C_Da)^{-1}$, and an interior velocity driven

Table 2.1: A summary of the terminology used to categorize porous obstructions in flow.

Dense & Sparse Canopies	Dense $ab > 0.1$	Canopy contributes sufficient drag to transform velocity profile into a mixing layer form, with inflection point at canopy edge.
	Sparse $ab < 0.1$	Perturbed velocity profile does not contain inflection point.
High and Low Flow-blockage	High $C_D ab \geq 2$	$L \sim b$. Interior velocity driven by pressure gradient
	Low $C_D ab < 2$	$L \sim (C_D a)^{-1}$. Interior velocity driven by turbulent stress

by the lateral gradient in the turbulent stress. This scaling, and the transition between low flow-blockage and high flow-blockage canopies will be tested and discussed in §2.4.

2.3 Methods

Experiments were conducted in the Environmental Fluid Mechanics Laboratory at MIT in a 13 m long, 1.2 m wide recirculating flume. In this flume, a 25 hp pump draws water from the tailbox and pumps it upstream to the headbox, where a large baffle helps disperse the flow evenly across the flume width. A weir at the downstream end of the test section sets the flow depth.

Several different model canopies were constructed and tested in this flume. The canopies were placed at mid-channel and 6 m from the flume outlet. The canopies were constructed of maple dowels, 6.4 mm in diameter and 15 cm high, in a flow of depth $h = 14$ cm. The dowels were arranged in rectangular canopies in perforated PVC boards which lined the flume bed. The two parameters of canopy geometry that were varied were the half-width, b, and the density, a. The density was varied between $\phi =$ 2.6% and 40%, or $a = 0.053$ to 0.8 cm^{-1}. The canopy half-width was varied between $b = 4$ cm and $b = 13$ cm. The corresponding range of flow-blockage was $C_D ab = 0.2$

Table 2.2: The parameters of the twelve experimental canopies. The densities were dictated by the board hole spacings. The asterisk (*) indicates a velocity profile measured by L. Zong and reported in [116]. Although the drag coefficient varies with velocity over the length of the array, it was defined as $C_D = 1$ in the following table.

C_Dab	a (cm^{-1})	b (cm)	$\phi(\%)$
0.21	0.053	4	2.6
0.53	0.053	10	2.6
0.58	0.096	6	4.6
0.96	0.096	10	4.6
1.2	0.20	6	10.3
1.25	0.096	13	4.6
2.0	0.20	10	10.3
3.0	0.20	15	10.3
4.8	0.80	6	40
8.0	0.80	10	40
8.0*	0.20	40	10.3

to 8.0, which covers many field canopies. For example, kelp forests have values of $C_Dab \approx 0.5$ to 30, based on parameters reported by [52, 89, 32]. [66] reports values of C_Dab between 1 and 15 for seagrasses in the coastal ocean. [15] constructed model marshgrass canopies of $C_Dab = 0.19$ and 3.1 which are representative of naturally occurring canopies of emergent aquatic vegetation. [29] reports values of $C_Dab = 0.2$ to 1.5 for agricultural canopies, and $C_Dab = 1$ to 5 for terrestrial forests (note that for terrestrial canopies, b is the canopy height). Large urban areas typically have values of C_Dab between 0.1 and 0.3 [41]. In all of these reported ranges of C_Dab, C_D is assumed to be unity. In our experiments, to minimize the influence of the flume walls, the canopy width was never larger than 26 cm, or $\approx$ 20% of the total flume width. The canopy length was not a parameter expected to influence the flow adjustment region, provided that the overall canopy length was much larger than the adjustment length. The flowrate was held constant with a uniform approach velocity of $U_\infty \approx 10$ cm/s for all experiments.

Velocities were measured along the x-axis upstream of the canopy and within the canopy using a 3D Nortek Vectrino Acoustic Doppler Velocimeter (ADV). The sampling volume of the ADV was located at mid-depth in the flow. At each point, the

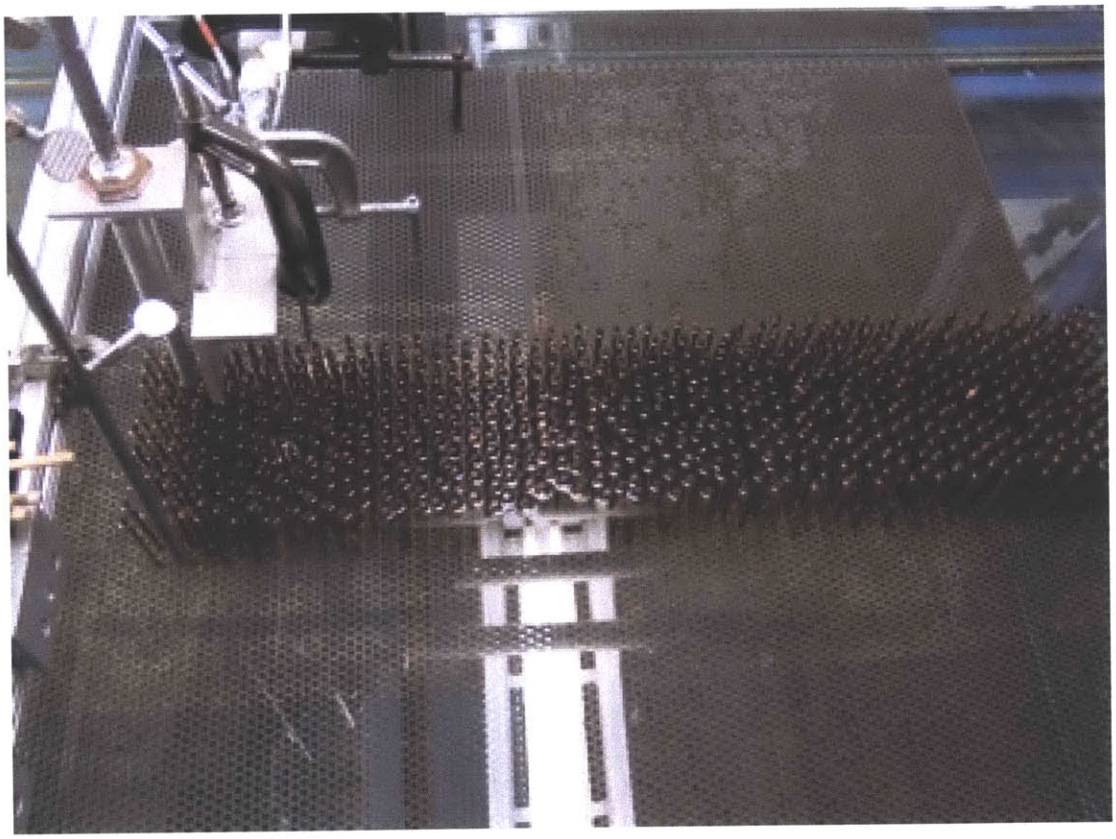

Figure 2-5: A photograph of the $C_D ab = 2.0$ patch from above with the capacitance-based wave gauges visible on the left hand side of the photo.

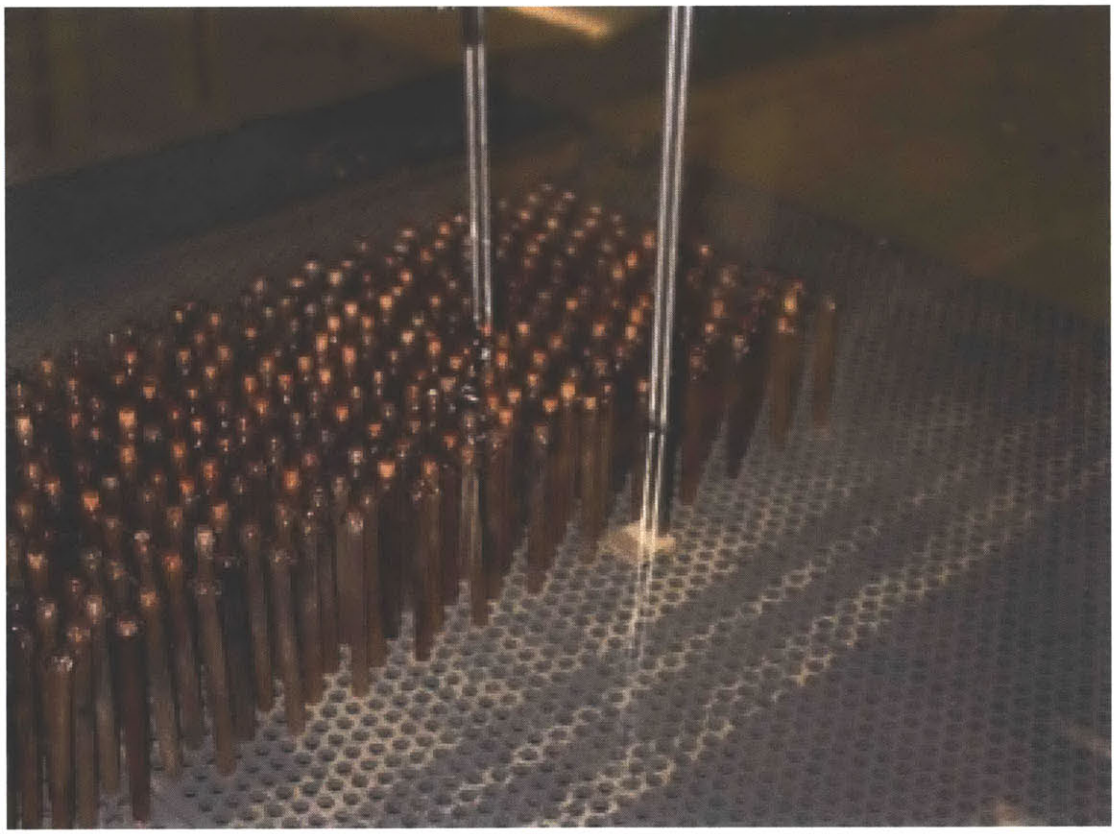

Figure 2-6: A detailed photo of the capacitance-based wave gauges and their placement at the edge and at the centerline of the $C_D ab = 2.0$ patch.

three velocity components (u,v,w) were recorded at 25 hz for 240 seconds. Upstream of the canopy, velocities were measured at 10 cm intervals, starting between x = -150 cm and x = -100 cm. Within the canopy, velocities were measured at intervals proportional to the expected adjustment length of the individual canopy. For example, for a canopy with a longer adjustment length, velocities were measured at intervals of 10 cm or greater. For a canopy with a shorter adjustment length, measurements were taken at intervals of between 3 and 5 cm. Within the canopies, the exact sample spacing was determined by the dowel geometry and spacing.

At all of the sampling points, the ADV was placed in the same orientation relative to the surrounding dowels. Consistency in placement and orientation was critical to minimize the error introduced by spatial heterogeneity in the velocity through the dowel array. The sampling volume was positioned as close as possible to the midpoint between two dowels. The velocity at this position has been shown to be within 20% of the spatially-averaged velocity, $\langle\overline{u}\rangle$, for all of the array densities investigated here (White and Nepf 2003). The error due to velocity variations in time was negligible due to the large number of data points. Within the canopies of density $a \geq 0.2$ cm^{-1}, it was necessary to remove a few individual dowels to fit the head of the ADV probe into the canopy. The ADV sampling volume is 6mm in diameter, 2.5mm in height and is located 7cm below the probe head of the ADV. The instrument is designed to produce minimal local distortion in the sampling volume.

At intervals of 10 cm along the canopy edges, two capacitance-based wave gauges were used to monitor the displacement of the water surface. The displacement was recorded at 25 hz for 240 seconds and was filtered to remove high-frequency noise. The Kelvin-Helmholtz vortices create a small dimple in the water surface, which appears as a small negative displacement. The filtered surface displacement signals are then used to deduce the phase and period of the passing vortices.

Velocity profiles were also measured in the cross-stream direction for select canopies in the fully-developed region of the flow (Fig. 2-4). The measurements were taken at intervals of between 2 and 4 cm starting at the canopy centerlines and continuing into the free stream. To investigate the interaction between vortices on the two

flow-parallel edges, a second set of cross-stream velocity profiles were taken with a thin splitter plate in place at the canopy centerline. This splitter plate prohibited communication between the vortices at the two canopy edges.

2.4 Results and discussion

2.4.1 Flow adjustment regions

The streamwise velocity profiles exhibit a range of behavior both upstream of and within the canopy (Fig. 2-7). We first consider the upstream adjustment region and define the upstream velocity change as $\Delta u = U_\infty - u_{(x=0)}$. The upstream adjustment length, L_O, was defined as the distance over which 90% of this velocity change occurred, i.e. the upstream adjustment region begins at the point where $u = u_{(x=0)} + 0.9\Delta u$. This definition was chosen to remove the biases associated with the magnitude of the velocity drop. The scaling of the governing equations suggests that for both high and low flow-blockage canopies, $L_O \sim b$. The observations support this scaling even though the upstream deceleration is weaker for sparser canopies. Across all of the canopies, $L_O = (4.0 \pm 0.7)b$, with no dependence on $C_D ab$, where the uncertainty is the standard error of the normalized, measured values.

In the canopies with the highest solid volume fractions, a flow reversal is observed within the canopy and near the leading edge (Fig. 2-7). In these canopies, the upstream flow divergence is so strong that the velocity at the two leading-edge corners ($x = 0$, $y = \pm b$) is elevated above the free-stream velocity (see details in Fig. 4 of [116]), such that a low pressure zone is created at these corners. For flow around solid obstructions, a similar local pressure is associated with flow separation. In the porous arrays studied here, this local adverse pressure gradient is sufficient, relative to the low inertia of the flow within the canopy, to cause a flow reversal within the canopy. This phenomenon has also been observed in dense terrestrial canopies [60]. A flow reversal was observed for two high flow-blockage cases, $C_D ab = 4.8$ ($\triangleright$) and 8.0 ($\triangleleft$), which were also the narrowest canopies, $b = 6$ cm and 10 cm, respectively

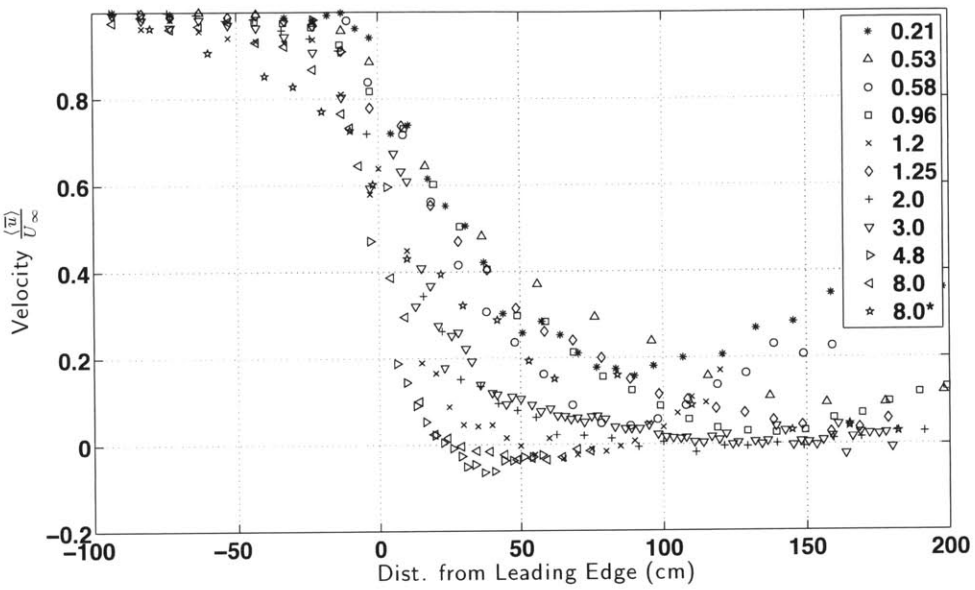

Figure 2-7: The streamwise velocity profiles along the canopy centerline, starting upstream of the canopies and through the length of the adjustment region. The canopies begin at $x = 0$. The streamwise velocity $\langle\overline{u}\rangle$ has been normalized by the upstream velocity U_∞.

(see $\langle\overline{u}\rangle < 0$ at $x \approx 40$ cm in Fig. 2-7). In wider canopies, flow reversals may also be present, but may be found closer to the corners and not at the centerline, where our profiles are made.

We can use the measured velocity profiles to examine the magnitude of the pressure change, Δp, at the leading edge, and to confirm the scaling proposed in §2.2.2. For bluff bodies, the pressure at the stagnation point is proportional to the kinetic energy of the flow upstream, $\frac{1}{2}\rho U_\infty^2$. We anticipate that canopies with high values of $C_D ab$ will approach this limit, but canopies with a value of $C_D ab \to 0$ will experience a negligible elevation of pressure, $\Delta p \to 0$. According to Bernoulli, we can define the scale of the pressure change using the change in kinetic energy between a position far upstream and at the leading edge,

$$\frac{\Delta p}{\rho U_\infty^2} \sim \frac{\rho U_\infty^2 - \rho \langle\overline{u}\rangle_{x=0}^2}{\rho U_\infty^2} \tag{2.30}$$

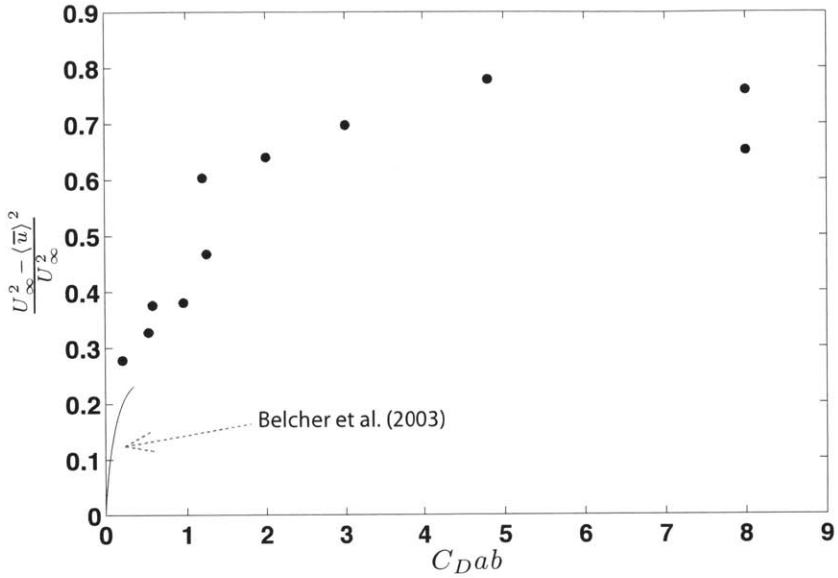

Figure 2-8: The measured kinetic energy change at the leading edge of the canopy for the full range of values of $C_D ab$. The prediction of [9], valid only for canopies with very low flow-blockage, $C_D ab \ll 1$, is plotted with a solid line.

When this value is a constant close to unity, it is reasonable to define the pressure change at the leading edge as $\Delta p \sim \rho U_\infty^2$. This scaling for Δp is valid for $C_D ab > 2$ (Fig. 2-8). For values of $C_D ab < 2$, the data shown in Fig. 2-8 suggests that $\Delta p / \rho U_\infty^2$ increases with $C_D ab$ and that $\Delta p \to 0$ for $C_D ab \to 0$. These results support the assumption of a dual scaling for the pressure as represented in (Eq. 2.17).

Within the canopy, the interior adjustment length is estimated from the data as the point downstream of the leading edge at which the velocity reaches a minimum or constant value. The measured interior adjustment length is the shortest for narrow and dense canopies, and is the longest for wide and sparse canopies (Fig. 2-7). For example, the canopy with $b = 6$ cm and $a = 0.8$ cm^{-1} ($C_D ab = 4.8$, $\triangleright$) has an interior adjustment length of 30 cm, while the canopy with $b = 10$ cm and $a = 0.053$ cm^{-1} ($C_D ab = 0.53$, $\triangle$) has an interior adjustment length of 150 cm. By normalizing the x-coordinates by the length scale of the interior adjustment region, L, as given in (2.24), the streamwise velocity profiles collapse, confirming the scaling argument derived in §2.2.2. (Fig. 2-9). The mean and the standard error of the measured

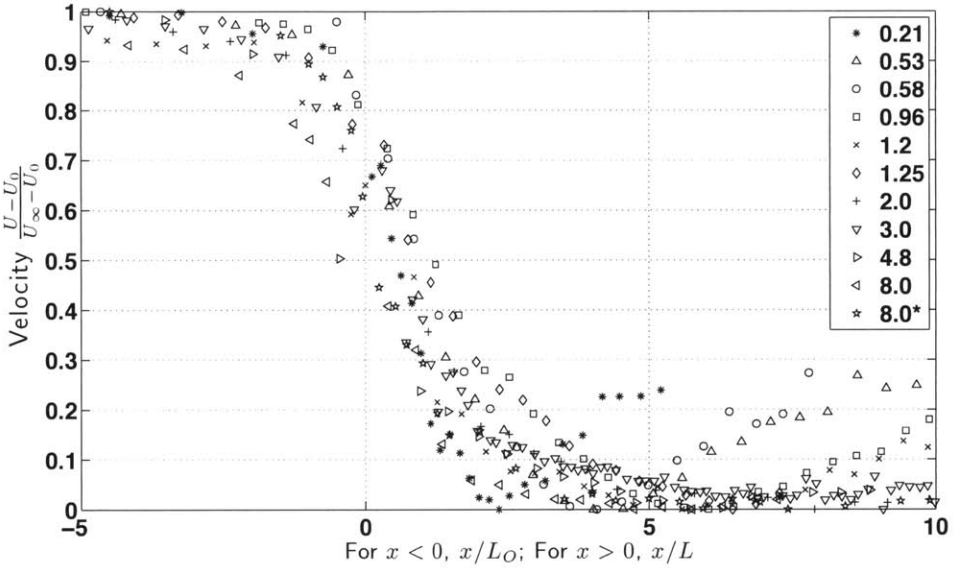

Figure 2-9: The streamwise velocity profiles along the centerline, normalized by the length scale (Eq. 2.24) predicted from scaling the governing equations. Within the canopy, L is given by (Eq. 2.24). Upstream of the canopy, the velocity profiles are normalized by L_O, which is given by (Eq. 2.14). The velocity has been normalized by the difference between the upstream velocity, $U\infty$, and the minimum velocity at the end of the flow adjustment region, U_0.

adjustment lengths provide the scale constant for (Eq. 2.24), specifically

$$L = (5.5 \pm 0.4)\left[\left(\frac{2}{C_D a}\right)^2 + (b)^2\right]^{1/2} \tag{2.31}$$

The drag coefficient, C_D, was set equal to unity for simplicity. For low flow-blockage canopies, for which L reduces to $L \sim (C_D a)^{-1}$, this result is in agreement with the adjustment length scale of [19].

Drawing on the work of [9], we can add a correction term to the scaling that accounts for the small, but non-zero, pressure change at the leading edge of low flow-blockage canopies. For sparse canopies, $ab < 0.1$, [9] found the velocity deficit at the canopy leading edge to be proportional to $C_D ab$. This scaling is shown as a solid line in Fig. 2-8. Utilizing this result, we can define the pressure change $\Delta p/\rho U_\infty^2 \sim (C_D ab)^2$. Thus for low flow-blockage canopies, the interior adjustment length with the small correction term is

$$L \sim \frac{2}{C_D a}\left(1 + (C_D ab)^2\right). \tag{2.32}$$

In Fig. 2-10, the data is separated into two different sets, low flow-blockage and high flow-blockage, and compared against the appropriate scaling, either (Eq. 2.32) or (Eq. 2.23). Based on the scaling (Eq. 2.24) and the data in Fig. 2-8, the transition between low and high flow-blockage is expected to occur at $C_D ab = 2$, and this is the threshold used to separate the cases in Fig. 2-10. This figure shows more clearly how the higher values of $C_D ab$ scale with canopy width, b, and how lower values of $C_D ab$ scale with the canopy drag length scale. Further, note that all of the low flow-blockage canopies exhibit the same flow reacceleration behavior downstream of the adjustment regions. In the low flow-blockage canopies, the refined adjustment length (Eq. 2.32) is found to be

$$L = (3.0 \pm 0.3)\left[\frac{2}{C_D a}\left(1 + (C_D ab)^2\right)\right] \tag{2.33}$$

This scale constant is consistent with the observations reported in [19], who find $L = 3L_c$, with $L_c = 2(1-\phi)/(C_D a)$, where $\phi \ll 1$ for low flow-blockage canopies. In the high flow-blockage canopies, the adjustment length is found to be

$$L = (7.0 \pm 0.4)b \tag{2.34}$$

In the results for both low and high flow-blockage canopies, the uncertainty reported is the standard error of the normalized, measured adjustment lengths.

[8] reports that both the upstream and interior adjustment regions in low flow-blockage canopies scale on $(C_D a)^{-1}$. Our observations do not support this conclusion. While we find that the interior adjustment region of canopies with low flow-blockage scale on $(C_D a)^{-1}$, the measurements and scale analysis indicate that the upstream adjustment region scales on the canopy width, b. In high flow-blockage canopies, our scaling analysis indicates that both the upstream and interior adjustment regions share the same length scale, the canopy width b, and the results support this conclusion. All of the canopies tested in this paper are considered dense ($C_D ab \geq 0.1$) using the terminology of [9] and [19]. Canopies with very low flow-blockage ($C_D ab \leq 0.1$), i.e. sparse canopies, were not tested in this study, and may exhibit different behavior.

The spread that remains in the normalized data (Fig. 2-9) can be attributed to several factors. First, the half-width of a uniform, staggered array is not clear, particularly for sparse arrays, as there is a staggered interface between the free stream and the canopy. Second, there is uncertainty in the drag coefficient, C_D, which is described by empirical formulas as a function of ϕ and velocity, and based on uniform flow conditions. Finally, spatial error in the velocity profiles can also influence the adjustment region. Although point measurements were taken with constant geometric positioning with respect to the surrounding canopy elements, spatial deviations from the mean velocity exist, and finer scale measurements would be unattainable within dense canopies.

For the flow within the canopies to decelerate, fluid must be diverted laterally

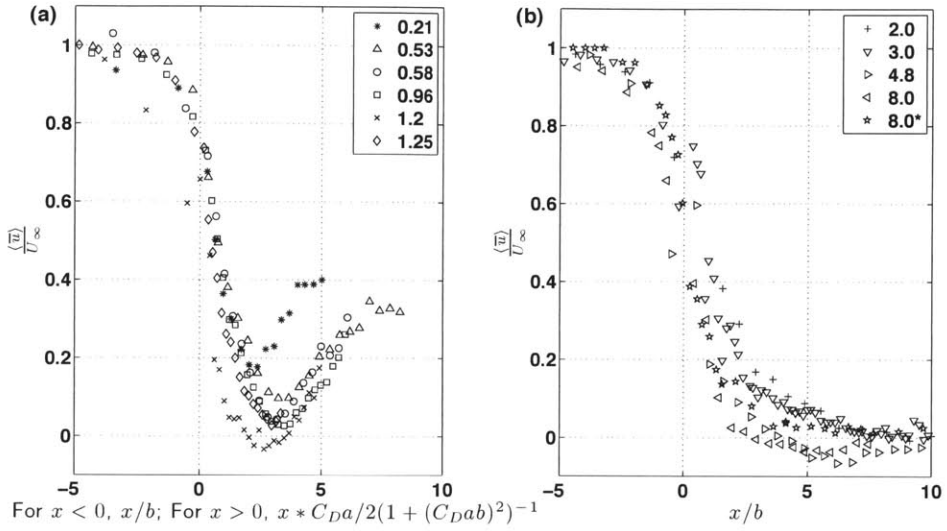

Figure 2-10: The streamwise velocity profiles along the centerline. (a.) Low flow-blockage canopies normalized by (Eq. 2.32) within the canopy and by (Eq. 2.23) upstream of the canopy. The values of $2/C_D a$ range from 10 to 38 cm (table 2.2). (b.) High flow-blockage canopies normalized by (Eq. 2.23). The values of b range from 6 to 40 cm (table 2.2).

across a distance b to the canopy edges. The laterally moving flow also experiences a drag force (the last term in 2.16). For high flow-blockage canopies, $L \sim b$, (Eq. 2.11d) indicates that $v \sim u$, and therefore the flow resistance in the lateral direction is comparable to the streamwise flow resistance and provides an equal control on the flow. That is for high flow-blockage canopies, the streamwise flow can adjust only as rapidly as fluid can laterally evacuate the canopy interior. This is why the canopy width is the controlling length-scale of flow adjustment. In contrast, for canopies with low values of $C_D ab$, $L \gg b$ and $v \ll u$, and the lateral flow resistance is small compared to the streamwise flow resistance. Fluid is able to evacuate the canopy interior with negligible constraint on the lateral flow, and therefore the interior flow adjustment length scale depends on the canopy drag, with very little dependence on the canopy width. For canopies that fall in the transition region between these two distinct regimes, the adjustment length is controlled by a combination of the canopy width and the canopy drag (Eq. 2.31).

It was assumed *a priori* that within the adjustment region there is a negligible

contribution from turbulent stress and that the governing equations for the flow reduced to (Eq. 2.15) and (Eq. 2.16). The experimental measurements confirmed this, showing the Reynolds stress gradient was negligible within the region of streamwise velocity deceleration. For this scaling analysis, the Reynolds stress gradient at the centerline of the canopy is approximated as

$$\frac{\partial \langle \overline{u'v'} \rangle}{\partial y}\Big|_{y=0} \approx \frac{\langle \overline{u'v'} \rangle_{y=b}}{b} \tag{2.35}$$

Note that this estimate is quantitatively accurate when $\delta_i \geq b$, indicating stress can penetrate to the centerline. Otherwise, (Eq. 2.35) overestimates the stress gradient at the centerline. First-order, forward differences were used to approximate the inertial term.

The estimated magnitudes of the inertial, stress and drag terms are shown in Fig. 2-11 for a high and low flow-blockage case. The inertial term (dashed line) of the momentum equation has non-zero values in the interior flow adjustment region ($x < L$), where it is balanced by canopy drag. As assumed, the Reynolds stress term (thin, solid line) is negligible within the interior adjustment region. Downstream of the interior adjustment region, $x > L$, the inertial terms drop to zero. In the low flow-blockage canopy ($C_D ab = 0.53$, Fig. 2-11a), the Reynolds stress and drag terms are in balance. In the high flow-blockage canopy (Fig. 2-11b), $\delta_i < b$, such that (Eq. 2.35) is an overestimate of the turbulent stress gradient at the centerline. Indeed, this estimator is clearly out of balance with the drag term in Fig. 2-11. The relevant force balance is then between the canopy drag and the pressure gradient. These two regimes of interior flow are discussed further in the next section. Measurements of the lateral divergence of the Reynolds stress show that this term is negligible in comparison to the inertial terms upstream of the array as well.

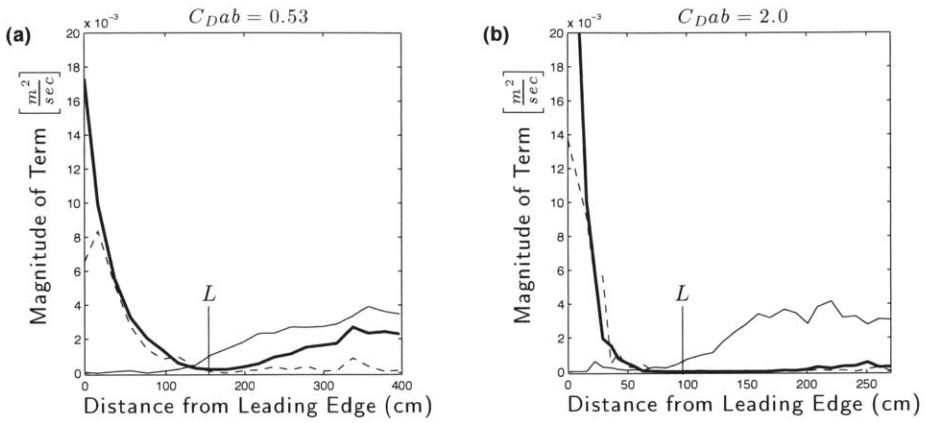

Figure 2-11: Magnitudes of the inertial term (dashed line), the Reynolds stress term (thin solid line) and the canopy drag term (heavy solid line) in the momentum equation. The inertial term shows non-zero values during the adjustment region. For the low flow-blockage canopy, $C_D ab = 0.53$, the Reynolds stress term becomes significant beyond the interior adjustment region and is balanced by the canopy drag term. For the high flow-blockage canopy, $C_D ab = 2.0$, the Reynolds stress does not penetrate to the centerline and the force balance is between the pressure gradient and canopy drag. The adjustment length, L, is denoted on the x-axis.

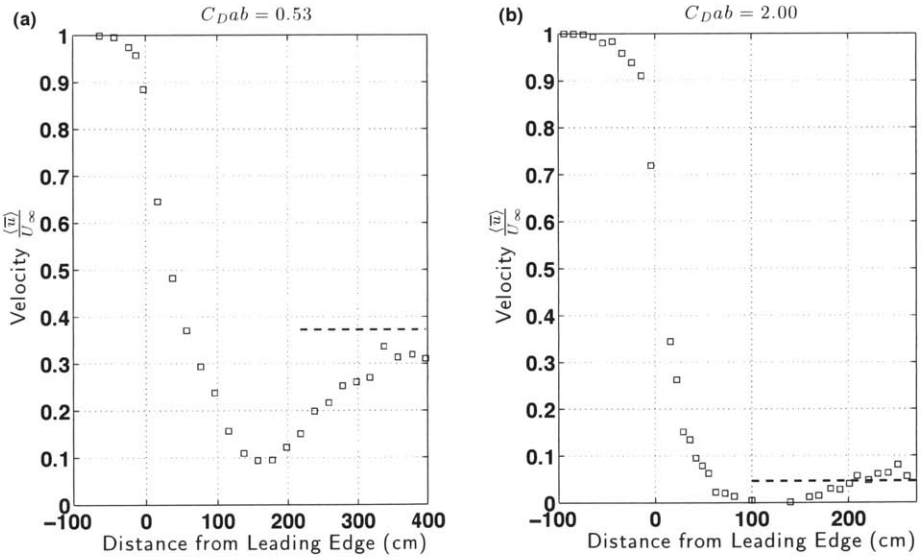

Figure 2-12: The streamwise velocity profiles through the interior adjustment region and the canopy interior. (a) In the low flow-blockage canopy, $C_D ab = 0.53$, reacceleration occurs beyond the initial adjustment region, and the interior velocity is set by a balance of turbulent stress penetration and canopy drag. The prediction (Eq. 2.37) is shown by the dashed line. (b) In the high flow-blockage canopy, $C_D ab = 2.0$, the interior velocity is set by a balance of the pressure gradient and canopy drag. The prediction (Eq. 2.39) is plotted with the dashed line.

2.4.2 The shear layer and canopy interior regions

In Fig. 2-10, the velocity profiles were separated based on their values of $C_D ab$. The canopies with low flow-blockage ($C_D ab < 2$) all show a clear reacceleration after the adjustment region, while this behavior is absent in the high flow-blockage canopy profiles. Two specific streamwise velocity profiles are shown in Fig. 2-12 for a representative high flow-blockage and low flow-blockage canopy. For the low flow-blockage canopy, $C_D ab = 0.53$, the streamwise velocity reaccelerates after the flow adjustment regions and approaches a uniform interior flow velocity which is set by the balance of turbulent stress penetrating to the canopy interior and canopy drag, as suggested by (Eq. 2.27).

Using the estimator of the turbulent stress gradient shown in (Eq. 2.35) and the definition,

$$u_* = \sqrt{-\langle \overline{u'v'} \rangle_{y=b}} \tag{2.36}$$

the interior velocity of low flow-blockage canopies given by (Eq. 2.27) can be written

$$\frac{\langle \overline{u} \rangle}{U_\infty} = \frac{1}{U_\infty} \sqrt{-\frac{\partial}{\partial y}\left(\langle \overline{u'v'} \rangle\right) \frac{2(1-\phi)}{C_D a}} = \frac{1}{U_\infty} \sqrt{\frac{u_*^2}{b} \frac{2(1-\phi)}{C_D a}} \tag{2.37}$$

Using $C_D = 1$, (Eq. 2.37) closely predicts the interior velocity of the low flow-blockage canopy (shown as dashed line in Fig. 2-12a). If measurements of u_* are not available, previous researchers have predicted the strength of the turbulent stress based on canopy morphology and the free stream velocity profile [10, 9].

For the high flow-blockage canopy of $C_D ab = 2$, the uniform interior velocity is set by a balance between the pressure gradient and canopy drag, derived from (Eq. 2.26),

$$\langle \overline{u} \rangle = \sqrt{-\frac{2}{\rho} \frac{\partial p}{\partial x} \frac{(1-\phi)}{C_D a}} \tag{2.38}$$

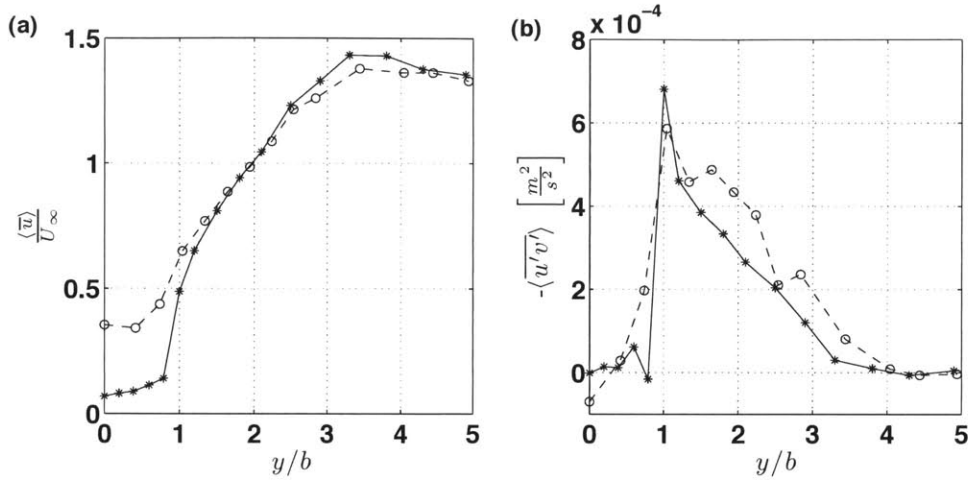

Figure 2-13: The cross-stream profiles of (a) streamwise velocity and (b) Reynolds stress profiles in the fully-developed region of the flow for $C_D ab = 0.53$ ($\circ$, dashed line) and 2.0 ($*$, solid line). The profiles were measured at streamwise distances of $x = 360$ cm and $x = 262$ cm, respectively. The canopy centerline is at $y/b = 0$, and the canopy edge is at $y/b = 1$. The error in the velocity data is $\pm$ 0.0025 m/s within the canopy, and is negligible in the free stream ($y/b > 1$). The error in the Reynolds stress is $4 \cdot 10^{-5}$ m^2/s^2 within the canopy, and is negligible in the free stream.

The background pressure gradient can be estimated from the momentum balance in the free stream, i.e. the balance between bed friction and the pressure gradient shown in (Eq. 2.29). Then, (Eq. 2.38) can be written

$$\frac{\langle\overline{u}\rangle}{U_\infty} = \sqrt{\frac{C_f}{h}\frac{(1-\phi)}{C_D a}} \tag{2.39}$$

The interior flow velocity was predicted from (Eq. 2.39) using the known coefficient of friction for the PVC baseboards, $C_f = .006$ and C_D was set equal to unity. The prediction, shown with the dashed line in Fig. 2-12b, is in agreement with the observed velocity, confirming the force balance suggested in (Eq. 2.26). The near reversal in the streamwise velocity at $x = 100$ cm for $C_D ab = 2.0$ is likely associated with the high velocity/low pressure region at the leading corners, which was discussed previously in §2.4.1.

Figure 2-13 shows the lateral profiles of the mean streamwise velocity and Reynolds

stress in the fully-developed region of the two canopies described in figures 2-11 and 2-12. Note that Fig. 2-13 shows the stress profile over only half the canopy. The outer-layer, which is the portion of the shear layer in the free stream is similar in scale for both canopies because it is set by h/C_f [113]. The inner shear layer scale, or penetration scale, is $\delta_i/b = 0.5/(C_D ab)$ [113]. When $C_D ab = 2.0$, $\delta_i/b \approx 0.25$ and turbulent stress does not penetrate to the canopy interior. The experimental results show that the Reynolds stress is essentially zero, within uncertainty, over the span from the centerline, $y/b = 0$, to near the edge, $y/b \approx 0.8$, so that the gradient equals zero at the centerline. For these conditions, the mean streamwise velocity at the centerline is driven by the pressure gradient (Eq. 2.26), as shown in Fig. 2-12b. For $C_D ab = 0.53$, $\delta_i/b \approx 1$, and the stress profile is approximately linear from one canopy edge to the other, passing through zero near the canopy centerline, consistent with the change in velocity gradient at the centerline. Based on the measured stress profile, $\partial\langle\overline{u'v'}\rangle/\partial y = .0024$ m/s^2 at the centerline, which is comparable to the estimator used previously, $\langle\overline{u'v'}\rangle_{y=b}/b = .0040$ m/s^2. For this canopy ($C_D ab = 0.53$), the streamwise velocity increases after the flow adjustment region (Fig. 2-12a) because turbulent stress can penetrate to the canopy interior, and the streamwise velocity at the centerline is set by the balance of turbulent stress and drag (Eq. 2.27).

2.4.3 Vortex organization and enhancement

Studies of canopies with a single flow-parallel edge have shown that the Kelvin-Helmholtz vortices induce a pressure response beyond the scale of the vortex [30, 113]. The center of each vortex is a point of low pressure which induces a wave response in the array beyond the penetration length, δ_i. In this study, the canopy has two streamwise interfaces separated by the full canopy width, $B = 2b$ (Fig. 2-1). The time-records of the surface displacement at the canopy edges suggest that the vortices interact across the canopy width. Specifically, the vortices organize such that there is a phase shift of π radians between the vortex streets that form on either side of the canopy (Fig. 2-14). The resulting cross-canopy pressure gradient induces a trans-

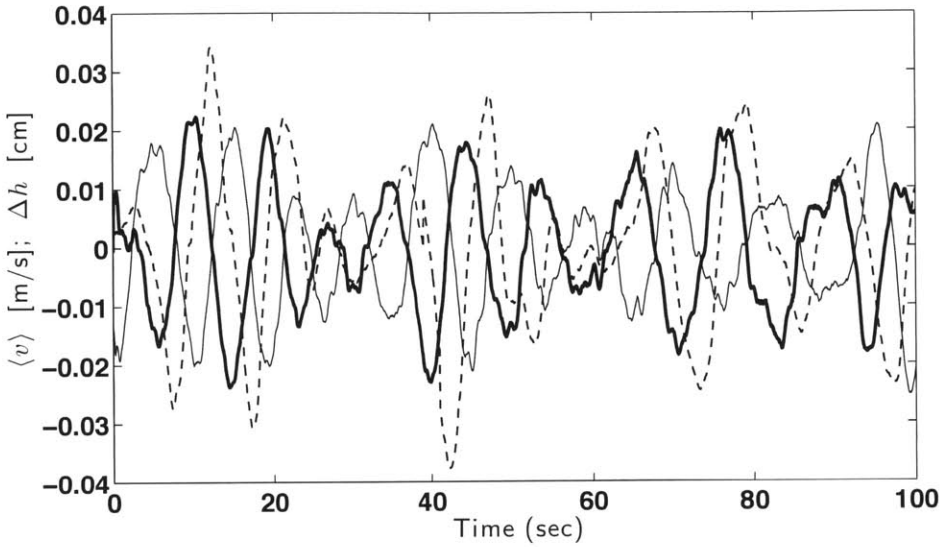

Figure 2-14: A time record of the surface displacement, Δh, just outside of the canopy edges (x = 160 cm, y = 13 cm, thin solid line; y = -13 cm, heavy solid line) as well as the response of the instantaneous in-canopy lateral velocity, $\langle v \rangle$ (dashed line), in the fully-developed region of the canopy of $C_D ab = 0.53$. The surface displacements show a phase shift of π radians while the velocity lags the low-pressure events by $\pi/2$ radians.

verse velocity (v) within the canopy that lags the pressure forcing by $\pi/2$ radians (Fig. 2-14).

The vortex pattern evolves from the leading edge as shown diagrammatically in Fig. 2-4. Figure 2-15 provides evidence that traveling vortices appear at x = 50 cm, which is near the end of the adjustment region, $x = L$. Upstream of $x = L$, the flow is diverting laterally and the shear layer has not yet formed. Once formed, the vortices quickly organize, such that by x = 100 cm, there is a phase shift of π radians between the vortex streets on either side of the canopy, which is evident in the cross-canopy lag of 1/2 of the vortex period (Fig. 2-15).

The communication of vortices across the canopy not only results in self-organization, but also in a significant enhancement of the strength of the vortices. The strength of the vortices can be described by the magnitude of the peak Reynolds stress. This magnitude was compared for conditions in which the vortices were able to communicate across the canopy, and conditions in which this communication was blocked

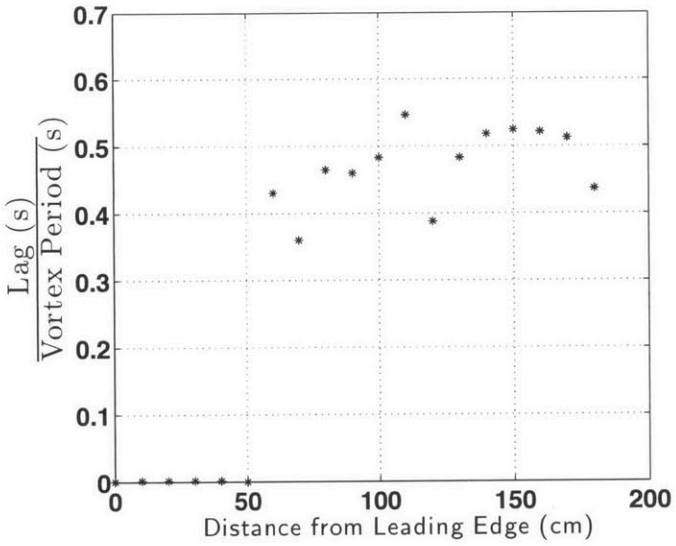

Figure 2-15: The shift between the surface displacement at the two canopy edges for $C_D ab = 3.0$, in seconds, normalized by the measured instability period. The normalized phase shift converges to a value 0.5 downstream of the leading edge, indicating that the two canopy edges are perfectly out of phase. Near the leading edge, vortices have not yet formed and the turbulence is of a random nature and therefore the two signals are uncorrelated.

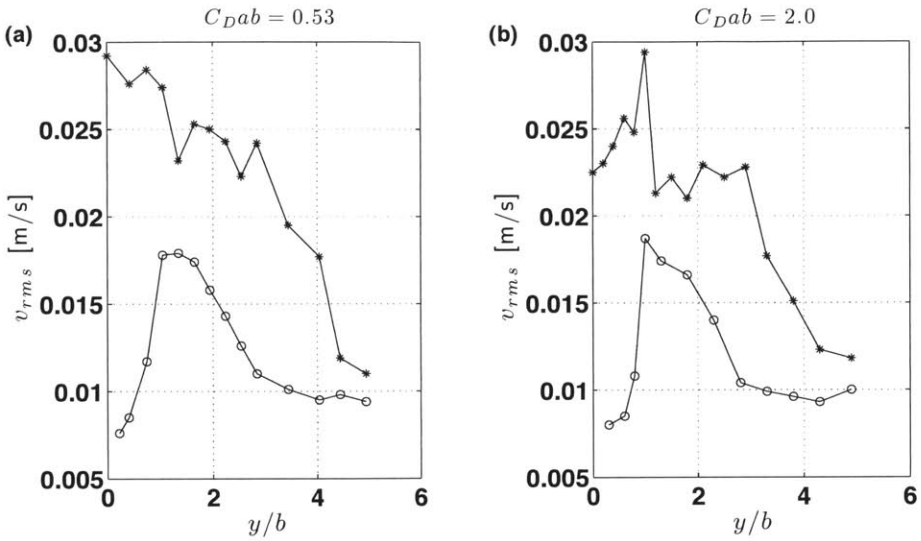

Figure 2-16: The lateral, root-mean-square velocity, v_{rms} shown for both canopy densities with ($\circ$) and without ($*$) a splitter plate at the canopy centerline. The values of v_{rms} are greatly reduced in the presence of the splitter plate and approach zero at the canopy centerline, $y/b = 0$. The error in the velocity data is $\pm$ 0.0025 m/s within the canopy ($y/b \leq 1$), and is negligible in the free stream ($y/b > 1$).

by a splitter plate placed at the canopy centerline. For both the low and high flow-blockage canopies, there is a significant enhancement in stress at the interface when vortices can communicate across the canopy (no splitter plate). For $C_D ab = 0.53$, the vortices penetrate the full half-width into the canopy, $\delta_i/b \approx 1$, and the Reynolds stress increases by nearly a factor of 5 between cases with and without the splitter plate. For $C_D ab = 2$, the vortices penetrate a very small distance into the canopy, $\delta_i/b \approx 0.25$, and yet the Reynolds stress at the edge increases by a factor of 7.

The cross-canopy organization of vortices greatly enhanced the lateral transport of fluid across the canopies. This was most evident in the root mean square of the lateral velocity, v_{rms}, in the canopy interior (Fig. 2-16). Within the low flow-blockage canopy, $C_D ab = 0.53$, v_{rms} approaches 3 cm/s. Using half the period of a passing vortex as the representative time-scale, the excursion amplitude is approximately 17 cm, a distance greater than the half-width of the canopy of 10 cm. Within the high flow-blockage canopy, $C_D ab = 2.0$, v_{rms} approaches 2.5 cm/s and results in an excursion amplitude of 14 cm, which is also comparable to the canopy half-width, $b =$

10 cm. That is, despite a much smaller penetration length in the high flow-blockage canopy, $\delta_i \approx 2.5$ cm, the cross-canopy velocity response to vortex passage has nearly the same amplitude as that observed in the low flow-blockage canopy. These results indicate that fluid parcels in the center of both the low and high flow-blockage canopies containing spores, nutrients, pollution or small creatures can be drawn into the free stream and vice versa, over half the period of a single passing vortex.

In a one-sided canopy, or a canopy with a splitter plate at the centerline (Fig. 2-16), v_{rms} is reduced over the entire canopy width and necessarily approaches zero at the centerline. This reveals that two-sided canopies not only produce much stronger vortices, but that their retention time can be influenced more strongly by the lateral response to passing vortices. Indeed, in the two-edge canopies, v_{rms} is nearly the same magnitude as $\langle\overline{u}\rangle$ in the low flow-blockage canopy, while v_{rms} is larger than $\langle\overline{u}\rangle$ in the high flow-blockage canopy (figures 2-13 and 2-16). This result suggests that lateral motions, rather than streamwise advection, can control the canopy residence time. This is especially true when the aspect ratio of the canopy is greater than one, which is typical in channel vegetation, e.g. [91] report typical length-to-width aspect ratios of 2.5. The reduced retention time can have important implications for plant fecundity, structural stability and habitat viability within canopies, as well as the transport and fate of pollutants and contaminants in both aquatic and terrestrial canopies.

As the canopy half-width, b, increases, there will be a width above which the vortices at the two flow-parallel edges no longer interact in a sympathetic manner. We anticipate that this transition occurs when the pressure perturbation at the canopy edges cannot translate across the canopy within half the time period of a passing vortex. Using the shallow water wave speed, $\sqrt{gh}$, to describe the translation speed of pressure perturbations, this threshold will occur at the point when $2b/\sqrt{gh} \gg 0.5T$, where T is the vortex period. In the cases shown in Fig. 2-16, $T = 10$ s and $2b/\sqrt{gh} = 0.2$ s, so it follows that vortices could communicate across the patch width. The vortex period was measured using the zero-crossings in the surface displacement record. The vortex period is largely set by the outer scale of the shear layer, δ_o, and thus by the

water depth and friction coefficient (see White and Nepf 2003). For the same flow depth and bed conditions, and the maximum achievable flow speed of near 0.5 m/s, we would need a canopy of width 10-20 m in order to test the predicted disconnection of edge-vortices. Unfortunately, this was not possibly within the flume available.

2.5 Conclusions

In this study, we present a set of experiments on unidirectional flow through rectangular porous obstructions. Upstream of the canopy, the flow adjusts over a length scale proportional to the canopy width. The length scale of the interior adjustment region depends on the canopy flow-blockage, described by $C_D ab$. For high flow-blockage canopies ($C_D ab \geq 2$), the adjustment length is set by the half-width, b. For low flow-blockage canopies ($C_D ab < 2$), the adjustment length is set by the canopy drag length scale, $(C_D a)^{-1}$.

Downstream of the adjustment region, shear layers form along the flow-parallel edges. Shear layer vortices form and grow to a finite size within this layer. The penetration of shear-layer vortices into the canopy scales with the drag length scale, i.e. $\delta_i = 0.5(C_D a)^{-1}$. The ratio of the vortex penetration length to the canopy half-width ($\delta_i / b = 0.5(C_D ab)^{-1}$) determines the dominant force driving the flow in the canopy interior. If $\delta_i < b$ ($C_D ab > 2$), the interior flow is governed by a balance between the pressure gradient and canopy drag. If $\delta_i \gtrsim b$ ($C_D ab < 2$), the interior flow is governed by a balance between the turbulent stress gradient and canopy drag. Thus, the flow-blockage parameter $C_D ab$, the ratio of the canopy width to the canopy drag length scale, controls both the behavior of the flow adjustment regions as well as the behavior in the canopy interior region.

When a porous obstruction has two interfaces parallel to the mean flow direction, the strength of the vortices that form on the flow-parallel edges is greatly increased relative to vortices that form at a single interface. With two interfaces, the vortices communicate across the canopy width and organize such that there is a phase shift of π radians with respect to each other. This organization enhances the vortex strength,

measured by the Reynolds stress or v_{rms}, relative to identical canopies with a single flow parallel edge. The stronger vortices and the sympathetic response from both interfaces results in much higher turbulence within the canopy and, potentially, a significantly reduced residence time.

Chapter 3

Forces on flexible blades in a vortex street

3.1 Introduction and Motivation

Flexible structures in flow are pervasive throughout nature and the built environment. Manifestations of this system are found in the modeling of flow through pipes and in the design of aquatic and aerial vehicles [76]. In biology, simplified models of this system are applied to study the adaptation of plants and animals to flow; plants adapt their rigidity and buoyancy to modulate both light exposure and fluid drag force [67]; animals undulate their bodies to generate thrust and interact with vortices shed by upstream neighbors [108, 86]. Recent studies have also looked to flexible structures in flow as potential energy sources [5, 69].

The fluid forces on a slender body can be modified by its flexural rigidity. For bodies oriented perpendicular to steady flow, flexural rigidity determines the degree of mean reconfiguration, or streamlining: the process by which drag forces are attenuated via changes in the structure's frontal area [4, 39]. Flexural rigidity can also induce surprising dynamic behaviors including vortex-induced-vibrations [114], regular and chaotic flapping in uniform flows [20] and the production of enhanced thrust forces [82, 70, 2]. Furthermore, by allowing structures to rapidly deform, low values of flexural rigidity can also introduce large inertial forces to a system [23].

In aquatic environments, plants move in response to fluid forcing, which can change the relative fluid velocity at the plant surface, change the frontal area of the plant normal to the flow and create inertial forces as the plant accelerates. A key parameter in controlling how the plant moves relative to the surrounding fluid is the ratio of the fluid forcing to the plant's structural properties. This ratio largely determines the dynamic response of the plant, which can modify the drag forces as well as inertial forces on the structure. Specifically, this ratio can indicate when reductions in drag force due to plant streamlining are outweighed by the presence of inertial forces due to high plant accelerations

In this chapter, we develop a generalized model system which examines the response of thin flags (a model for aquatic plants) in a model turbulent flow field. By systematically varying the ratio of fluid forcing to the flexural rigidity of the flags, we can experimentally find a relationship for the total force on the flags as a function of a single parameter. This ratio of fluid to structural forces can indicate when changes in frontal area and relative velocity alter the drag force, and when inertial forces become a significant component of the total force on the system. We then construct a simplified theoretical model of this system to investigate the fundamental dynamic phenomena underlying the experimental data. In §3.2, we derive the governing equation for the flag in our model system. We describe the experimental methods used in this study in §3.3.1 and in §3.3.3, we discuss the theoretical model we use to inform our experimental results. The results of both the experiments and the theoretical model are presented in §3.4. In §3.5, we compare the experimental and theoretical results and discuss the implications of this study. The experimental results from this chapter, along with the results from Chapter 4, will be submitted to the journal *Limnology & Oceanography* for publication.

3.2 Theory

We model the flag as a slender, inextensible beam of constant thickness h, width b, length l, elastic modulus E and density ρ. We define a curvilinear coordinate system

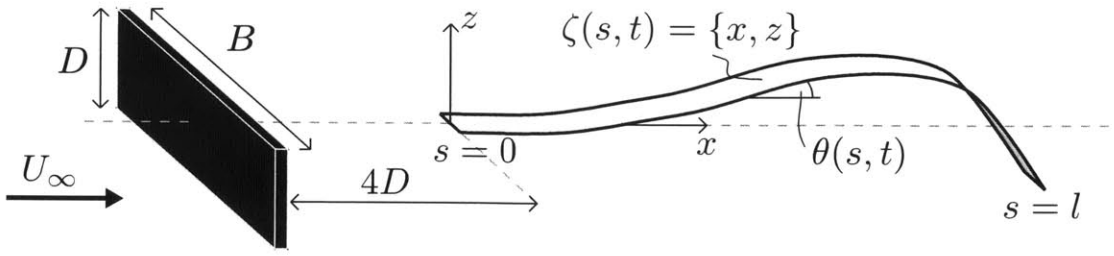

Figure 3-1: A flexible flag of length l in a vortex street created by a bar of height D. The bar spans the flume, which has width B. The flag has width $b \ll B$. Flag position is described by $\zeta = \{x, z\}$. The fluid velocity upstream of the bar is U_∞.

in which s is the distance along the flag, θ is the angle formed between the flag and the x-axis and $\zeta = \{x, z\}$ is the flag position vector (Fig. 3-1). To derive the governing equations for the beam dynamics, we first construct a two-dimensional force balance for a unit length of the flag (Fig. 3-2). The horizontal and vertical force balances on this length of flag are:

$$-T\cos\theta + (T + T_s ds)\cos(\theta + \theta_s ds) + S\sin\theta - (S + S_s ds)\sin(\theta + \theta_s ds) + F_{iner.,x} = 0 \tag{3.1}$$

$$-T\sin\theta - S\cos\theta + (T + T_s ds)\sin(\theta + \theta_s ds) + (S + S_s ds)\cos(\theta + \theta_s ds) + F_{iner.,z} = 0 \tag{3.2}$$

in which T is the internal tension in the flag, S is the shear force within the flag, θ is the angle formed between the flag and the x-axis, ds is the section length of the flag, and $F_{iner.,x}$ and $F_{iner.,z}$ are the inertial reaction forces in the horizontal and vertical directions, respectively. By expanding the trigonometric terms in a Taylor series, we simplify the above equations to the following:

$$-T\cos\theta + (T + T_s ds)(\cos\theta - \sin\theta\theta_s ds) + S\sin\theta - (S + S_s ds)(\sin\theta + \cos\theta\theta_s ds) + F_{iner.,x} = 0 \tag{3.3}$$

$$-T\sin\theta - S\cos\theta + (T+T_s ds)(\sin\theta + \cos\theta\theta_s ds) + (S+S_s ds)(\cos\theta - \sin\theta\theta_s ds) + F_{iner.,z} = 0 \tag{3.4}$$

After expanding the terms in the above equations, we neglect small terms of order $(ds)^2$. Multiplying through by $1/(ds)$ and collecting terms within the partial derivatives gives

$$\frac{\partial}{\partial s}\left[T\cos\theta\right] - \frac{\partial}{\partial s}\left[S\sin\theta\right] + \frac{F_{iner.,x}}{ds} = 0 \tag{3.5}$$

$$\frac{\partial}{\partial s}\left[T\sin\theta\right] + \frac{\partial}{\partial s}\left[S\cos\theta\right] + \frac{F_{iner.,z}}{ds} = 0 \tag{3.6}$$

The shear force, S, can be related to the beam curvature through $S = -EI\theta_{ss}$, in which EI is the flexural rigidity of the beam. Utilizing this relationship and by replacing $F_{iner.,x}$ and $F_{iner.,z}$ with the beam inertia, we find the following two-dimensional equations of motion:

$$\frac{\partial}{\partial s}\left[T\cos\theta\right] + \frac{\partial}{\partial s}\left[EI\theta_{ss}\sin\theta\right] = \rho_s bh\frac{\partial^2 x}{\partial t^2} \tag{3.7}$$

$$\frac{\partial}{\partial s}\left[T\sin\theta\right] - \frac{\partial}{\partial s}\left[EI\theta_{ss}\cos\theta\right] = \rho_s bh\frac{\partial^2 z}{\partial t^2} \tag{3.8}$$

The unit normal and unit tangent vectors for the flag surface are $\boldsymbol{n} = \{-\sin\theta, \cos\theta\}$ and $\boldsymbol{t} = \{\cos\theta, \sin\theta\}$. With these vectors, Eqs. 3.7 and 3.8 can be written as a single system of equations.

$$\frac{\partial}{\partial s}\left[T\boldsymbol{t}\right] - \frac{\partial}{\partial s}\left[EI\theta_{ss}\boldsymbol{n}\right] = \rho_s bh\frac{\partial^2 \zeta}{\partial t^2} \tag{3.9}$$

In a moving fluid, the fluid will exert forces on the beam. By taking these additional forces into account, the non-dimensional, dynamic beam-bending equation for large amplitude motion with arbitrary fluid forcing is [71, 70]:

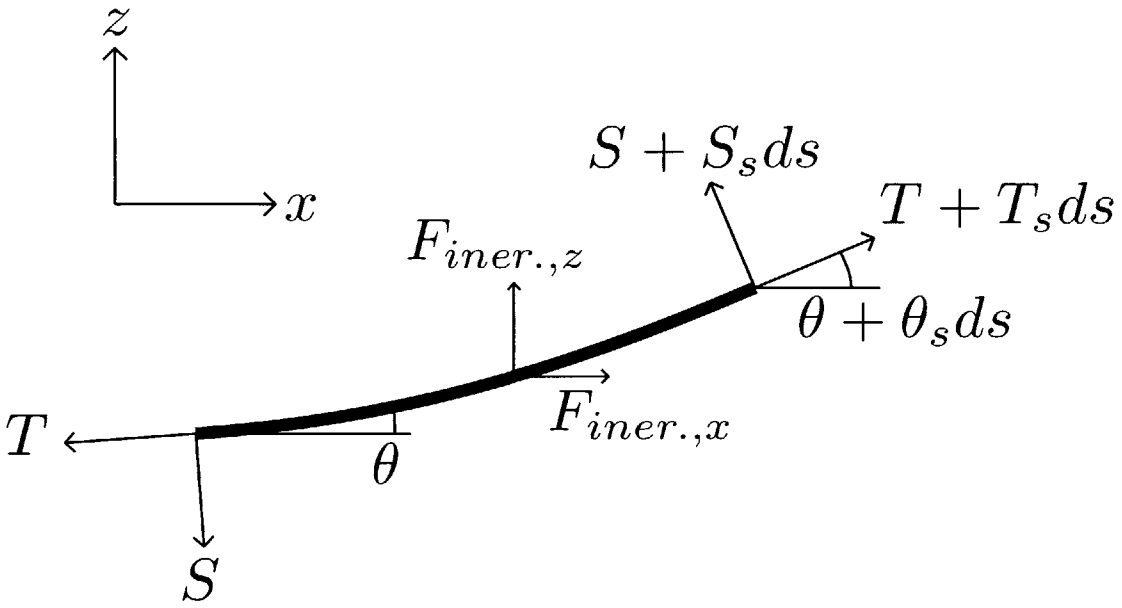

Figure 3-2: A schematic of the force balance on a unit section of the flexible flag, in which S is the shear force the flag section, T is the flag tension, θ is the local angle formed between the flag section and the x-axis, ds is the section length, $F_{iner.,x}$ and $F_{iner.,z}$ are the reactive inertial forces on the flag section and the subscript s indicates a partial derivative with respect to arc length.

$$\mu \frac{\partial^2}{\partial \tau^2} \hat{\zeta} = -\eta \frac{\partial}{\partial \hat{s}} \left[\theta_{\hat{s}\hat{s}} \boldsymbol{n} \right] + \frac{\partial}{\partial \hat{s}} \left[T \boldsymbol{t} \right] + F \tag{3.10}$$

in which we have used the flag length, l, as the characteristic length scale and the advection timescale, l/U_∞, where U_∞ is the upstream fluid velocity, as the characteristic timescale, i.e. $\hat{s} = s/l$, $\hat{\zeta} = \zeta/l$ and $\tau = tU_\infty/l$. For small amplitude motion, flag deflections can be approximated as one-dimensional, and the system can be simplified to a one-dimensional (z direction) equatio. For more general large amplitude motions, the full two-dimensional equations of motion must be retained. The dimensionless flag tension T and fluid forcing F represent their dimensional forms scaled by $\rho_f U_\infty^2 bl$ and $\rho_f U_\infty^2 b$, respectively, where ρ_f is the fluid density and U_∞ is the upstream fluid velocity. The local unit normal and tangential vectors are denoted $\boldsymbol{n}$ and $\boldsymbol{t}$, respectively, and the subscript $\hat{s}$ indicates $\partial/\partial\hat{s}$. This form of the equation reveals two governing parameters:

$$\mu = \rho h / \rho_f l \tag{3.11}$$

$$\eta = EI / \rho_f b U_\infty^2 l^3 \tag{3.12}$$

Physically, μ represents a ratio of solid to fluid inertia; and η represents a ratio of elastic to fluid forces [71]. The flag's boundary conditions are $\hat{\zeta}(0,\tau) = 0$, $\theta(0,\tau) = 0$, $\theta_{\hat{s}}(1,\tau) = 0$, $\theta_{\hat{s}\hat{s}}(1,\tau) = 0$ and $T(1,\tau) = 0$.

3.3 Methods

3.3.1 Experimental Methods

We conducted experiments in a water channel of 38-cm width and 22-cm depth. A regular Kármán vortex street was created at mid-depth using a 1-cm thick bar of height D = 2.5 or 5.0 cm that spanned the width of the channel. We chose to use a regular Kármán vortex street instead of simply open channel flow so that we could have a predictable, periodic, coherent form of turbulence in our system. Whereas the turbulence in open channel flow is broadly distributed over a range of frequencies, the structures in the Kármán vortex street are closely centered around a specific frequency, which is a function of the mean flow speed and vortex street height (discussed below). The sharp corners of the bar encourage the formation of stronger vortices than those produced by a cylinder[12, 63]. We cut five slender, rectangular model blades of width b = 3.0 cm and length l = 30.0 cm from polyethylene sheeting (low-density, LDPE, and ultra-high molecular weight, UHMWPE) of thicknesses, h = 50 μm, 100 μm, 150 μm and 250 μm (LDPE), and h = 500 μm (UHMWPE). A sixth flag with thickness h = 1000 μm was cut from Aluminum 6061. The two vortex street sizes allow us to examine the role that the ratio of flag length to vortex size, l/D, (where the vortex size is known to scale with vortex street height) plays in setting the flag response.

The flexural rigidity, EI, was measured for each flag with a cantilevered bending

test. In these tests, for each flag thickness, we cut several small lengths of the flags (between 3 cm and 8 cm) and placed the flag in a horizontal clamp, in air. The flag sections deflect slightly under their own weight and the deflection at the free end of the flag section is measured. The flag flexural rigidity can then be calculated from Euler-Bernoulli beam theory with the following relationship:

$$EI = \frac{q_b l_{sec}^4}{8\delta_{max}} \tag{3.13}$$

where $q_b = \rho_s bhg$ is the weight per unit length of the flag section, l_{sec} is the length of the flag section and δ_{max} is the measured deflection at the free end. This procedure was repeated several times for each flag thickness and the results were averaged to find EI for each flag thickness and the uncertainty in the measured EI for each thickness.

In the flume, flags were attached to a slender clamp, which held the flags horizontally at the centerline of the vortex street and a distance $\Delta x = 4D$ downstream of the bar (Fig. 3-1). Below the channel false bottom, the clamp was attached to a load cell (Futek LSB210) which recorded the streamwise forces on the clamp plus the flag at 2 kHz for 300 seconds. The load cell was connected to a computer through a National Instruments NI-USB 9237 bridge completion module. The strain data was collected and recorded with NI Labview. The clamp force was measured separately and subtracted from the total force to give the force on the flag alone. The load cell strain measurements were calibrated with a series of known weights over the range 0 to 0.006 N, and responded linearly over this range with an error of approximately 9%.

To capture the response of the flags over the course of the experiments, we recorded the instantaneous flag postures with a CCD camera (DALSA Falcon 1.4M100) at 40 frames per second for 30 s (Fig. 3-3). For these recordings, the flags were illuminated with two 60W incandescent light fixtures mounted below the glass flume bottom. A black canvas shroud was hung on the back side of the flume to provide a dark, contrasting background to the color of the polyethylene flags.

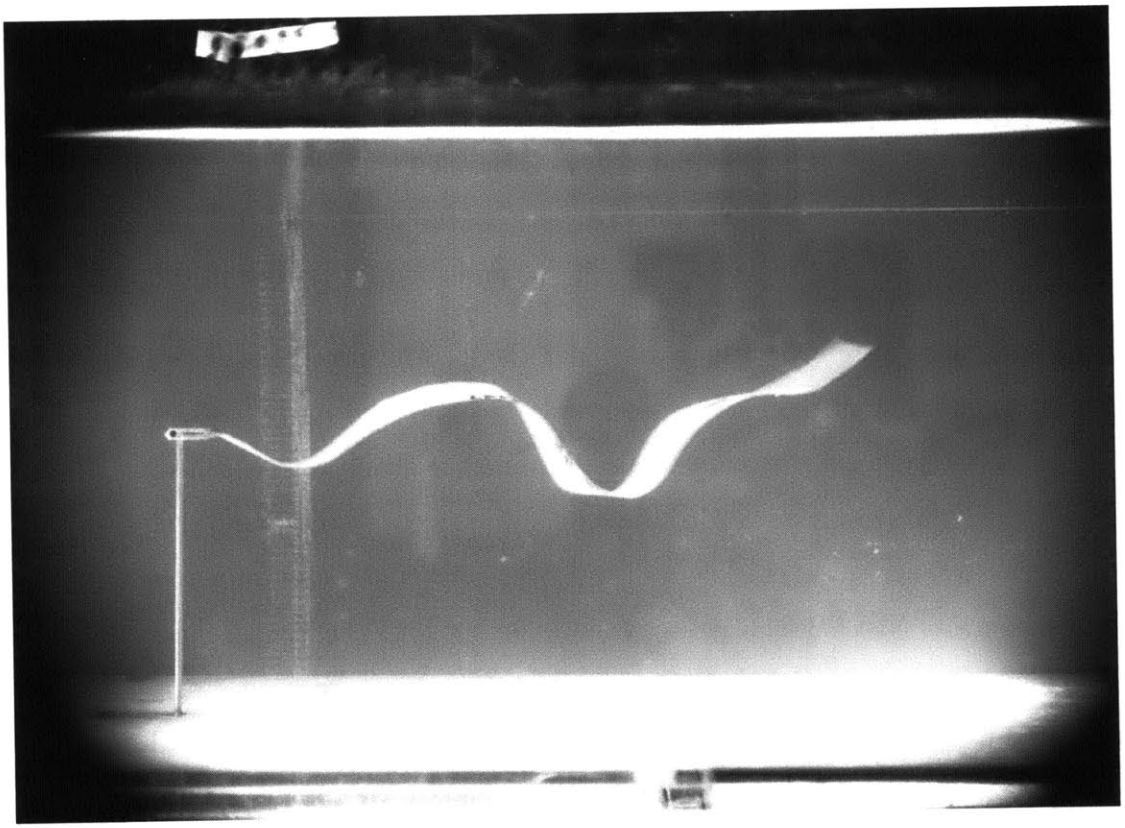

Figure 3-3: A photograph of the $\eta = 4.4E-6$ model blade in flow.

3.3.2 Experimental Flowfield

We characterized the flow using point measurements and planar particle image velocimetry (PIV). The upstream velocity was $U_\infty = 0.20$ m/s for all cases, and was both steady and spatially uniform away from the channel perimeter (i.e. $u(x, y, z, t) = U_\infty$). For the PIV measurements, the flume water (total volume of 2.2 m^3) was seeded with 25 g of Pliolite particles. The flow was illuminated from downstream with a laser light sheet of a power between 2.6 - 2.9 W(Fig. 3-9). The light sheet was placed at the centerline of the flume in the $x - z$ plane. No flags were in place during the PIV measurements. A CCD Camera (DALSA 1.4M100HG) recorded a 40 cm by 30 cm window with a resolution of 1400 x 1024 pixels, giving a pixel density of 3.5 pixel/mm. Images were were captured at 50 Hz, with a shutter speed of 15000 μs. We used an open source software package (PIVLab v. 1.32) which calculates velocities down to a resolution of 8 x 8 pixel grids (2.3 mm x 2.3 mm). We measured the vortex street wavelength, λ, using the PIV images. For $D = 2.5$ cm, $\lambda = 6D \pm 0.5D$, and for $D = 5.0$ cm, $\lambda = 4D \pm 0.5D$.

We measured the velocity deficit at the wake centerline using a Nortek Vectrino, sampling at 5 cm intervals at 25 hz (Fig. 3-4). To characterize vortex strength, we used w_{rms}, the root-mean-square of the velocity in the z direction. Peak vortex strength occurred at $\Delta x \approx 3D$ downstream of the bar, or $\Delta x \approx D$ upstream of the flag's leading edge. Over the flag length, the longitudinal profiles of normalized mean velocity, $\overline{u}/U_\infty$, and vortex strength, w_{rms}/U_∞, measured for both $D = 2.5$ cm and $D = 5.0$ cm were in close agreement (Fig. 3-4). At the flag leading edge, both flags experience the same mean velocity, $\overline{u}(x = 0)/U_\infty = 0.42$, and vortex strength, $w_{rms}(x = 0)/U_\infty = 0.51$. By design, the difference between the two cases is only the vortex street frequency ($f(D = 2.5$ cm$) = 1.2$ hz; $f(D = 5.0$ cm$) = 0.8$ hz) and the size of the vortices, which scale with D. The Strouhal number increased from 0.15 (for $D = 2.5$ cm) to 0.20 (for $D = 5.0$ cm) due to the increased flow blockage.

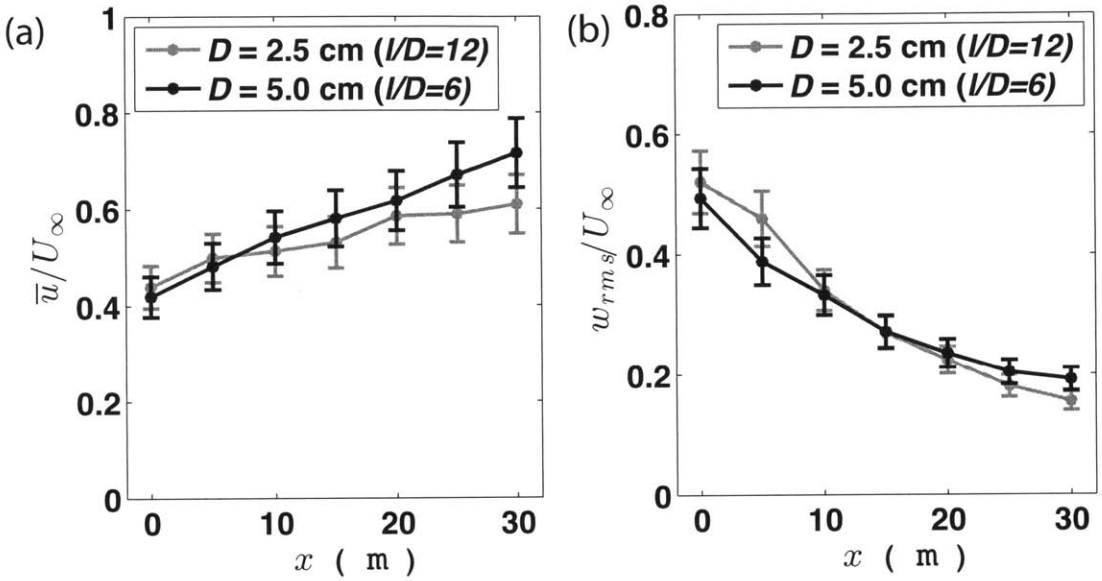

Figure 3-4: (a) The time-averaged streamwise velocity, $\overline{u}$, and (b) rms vertical velocity, w_{rms}, both normalized by U_∞, measured at the flow centerline over the length of the flag's neutral position ($x = 0$ to 30 cm). The bar which produces the vortex street is located a distance $\Delta x = 4D$ upstream of $x = 0$.

Table 3.1: The experimental flow parameters for both vortex streets. The vortex street wavelength and Strouhal number change due to the change in flow blockage, which increases from 12.5% to 25% from $D = 2.5$ cm to $D = 5.0$ cm.

U (m/s)	D (cm)	λ (cm)	f (hz)	St
0.2	2.5	15	1.2	0.15
0.2	5.0	20	0.8	0.20

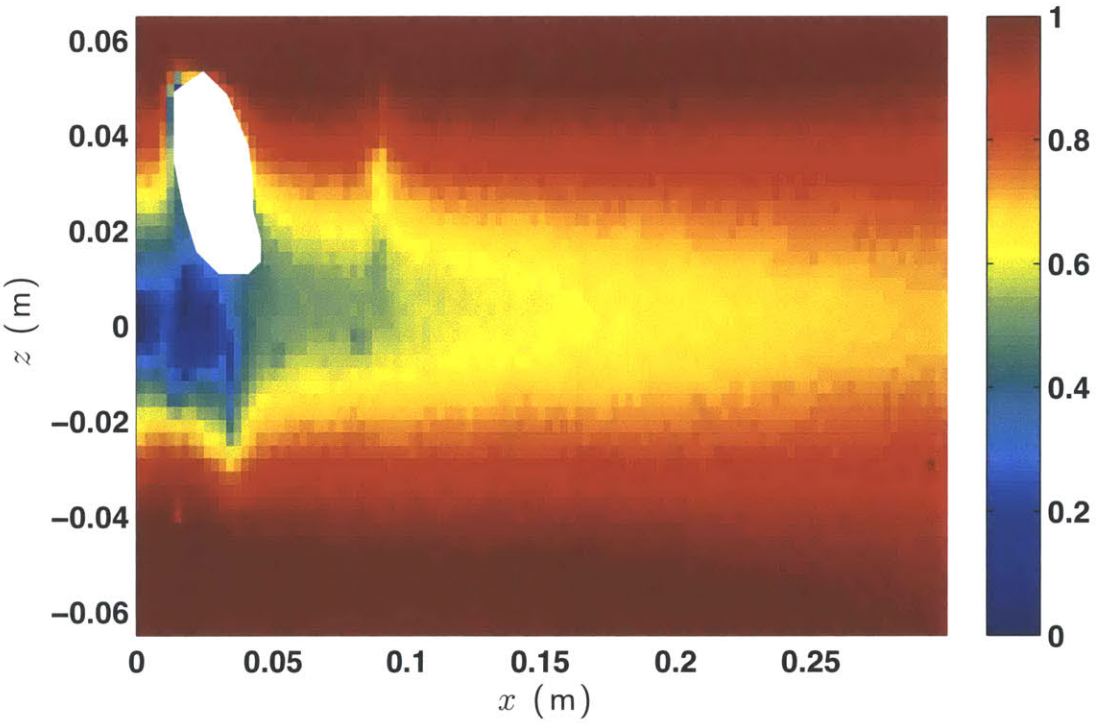

Figure 3-5: The time-averaged streamwise flowfield, normalized by U_∞, calculated from the PIV images for $D = 2.5$ cm. Flow statistics in the white region were unavailable due to errors in the PIV processing.

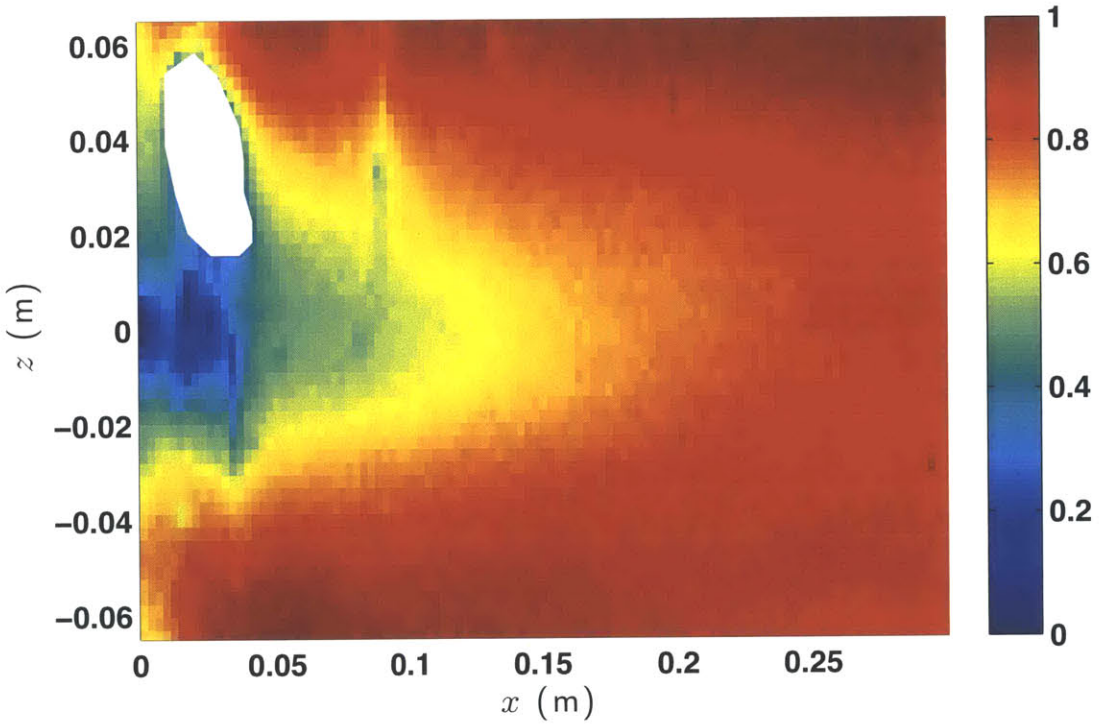

Figure 3-6: The time-averaged streamwise flowfield, normalized by U_∞, calculated from the PIV images for $D = 5.0$ cm. Flow statistics in the white region were unavailable due to errors in the PIV processing.

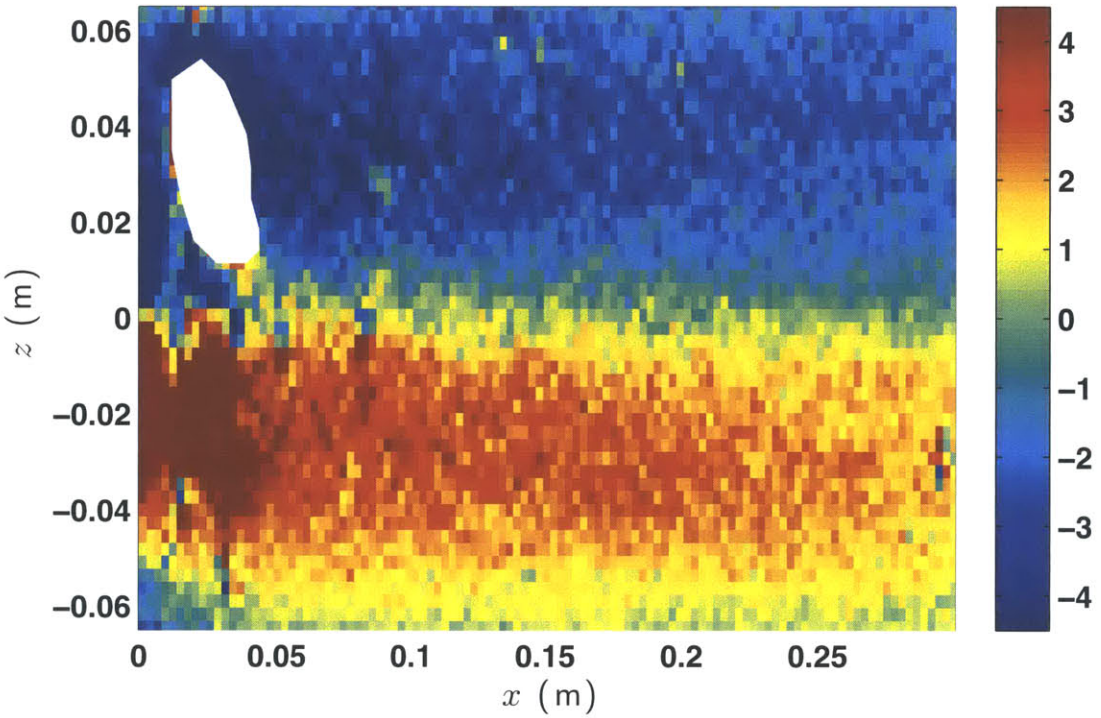

Figure 3-7: The time-averaged vorticity field, normalized by l/U_∞, calculated from the PIV images for $D = 2.5$ cm. Flow statistics in the white region were unavailable due to errors in the PIV processing.

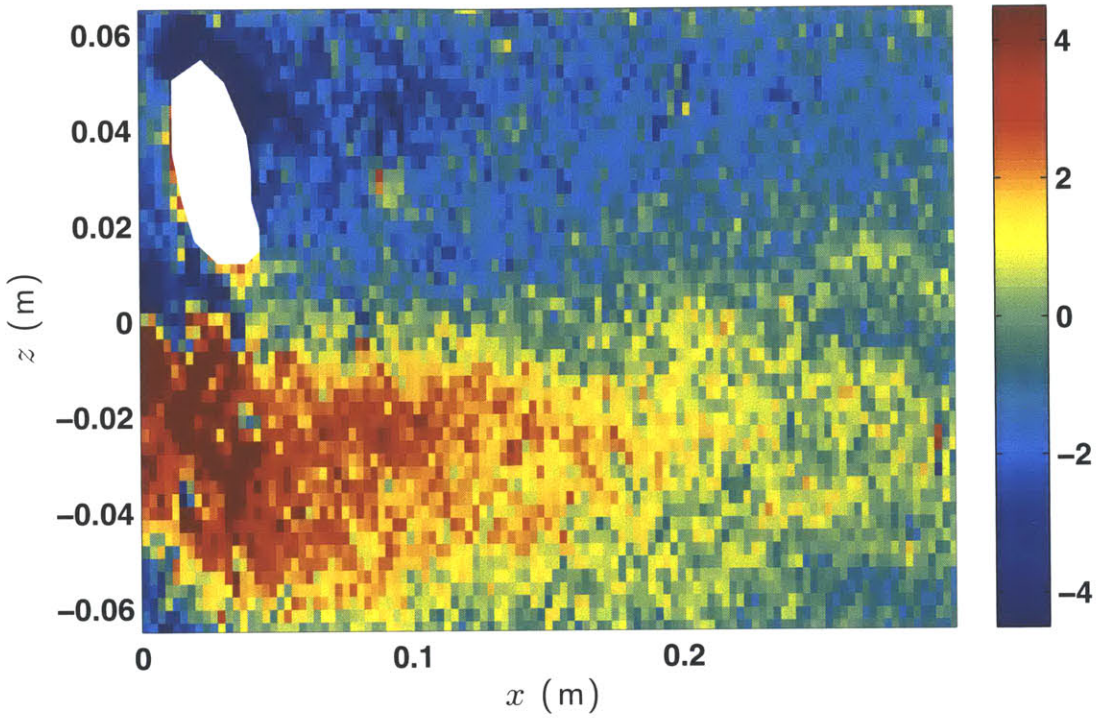

Figure 3-8: The time-averaged vorticity field, normalized by l/U_∞, calculated from the PIV images for $D = 5.0$ cm. Flow statistics in the white region were unavailable due to errors in the PIV processing.

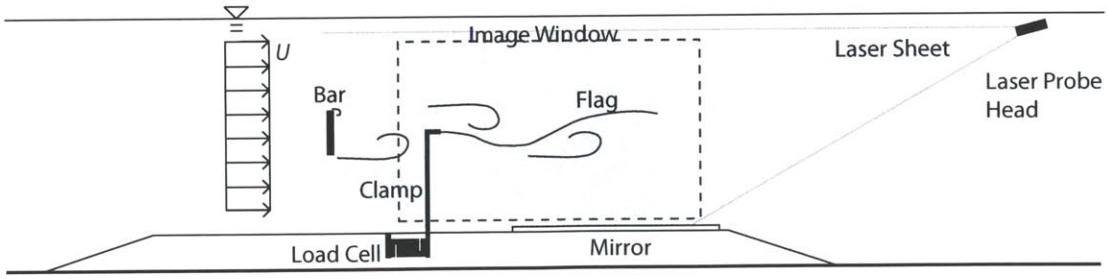

Figure 3-9: The experimental setup for the PIV measurements of the flow field. The laser probe head is submerged downstream of the flag's position in the vortex street, illuminating the vortex street. The flag was not in place during the PIV measurements.

3.3.3 Numerical Model

To gain physical insight into our experimental system, we develop a theoretical model of the model blade motion in a vortex street. We model the velocity at the flag surface using the complex Kármán vortex street velocity potential [90, 2]. The theoretical vortex street model (Eq. 3.14), described in Saffman [90], provides a tractable model which captures the essential characteristics of the vortex street, while eliminating the stochastic component of the flow that is present experimentally. This model, however, was not chosen to completely reproduce the experimental flowfield, notably lacking dissipation of the vortex street. Assuming a vortex circulation strength of $\Gamma = -2.5U_\infty D$ [68] and using the measured wavelengths of $\lambda = 4D$ and $6D$ (for $D = 5.0$ cm or 2.5 cm, respectively), the dimensionless complex conjugate velocity at the flag surface is described by:

$$\left.\frac{\partial\phi}{\partial Z}\right|_{Z=\hat{\zeta}_c} = 1 + \frac{2.5Di}{2\lambda}\cot\left(\frac{\pi}{4}\hat{\zeta}_c(l/D) - \frac{\pi i}{8}\right) - \frac{2.5Di}{2\lambda}\cot\left(\frac{\pi}{4}\hat{\zeta}_c(l/D) + \frac{\pi}{2} + \frac{\pi i}{8}\right) \tag{3.14}$$

where $\hat{\zeta}_c = \hat{x} + i\hat{z}$, is the flag position vector in complex notation. The velocity vector at the flag surface is then:

$$\hat{V} = \{\Re(\partial\phi/\partial Z), -\Im(\partial\phi/\partial Z)\} \tag{3.15}$$

From [2], the vortex advection speed is set at

$$U_c/U_\infty = 1 - (5D/4\lambda)\tanh(\pi D/\lambda). \tag{3.16}$$

To account for the singularity in the vortex cores, where $\cot(0) = \infty$, we set the maximum magnitude of the local velocity vectors to be equal to U_∞.

In the model, the fluid forcing terms are a combination of resistive and reactive forces. The resistive forces are simply the fluid drag forces in the normal and tangential directions, both of which can be expressed by quadratic drag laws. The reactive force is the inertial force caused by the acceleration of a volume of fluid adjacent at

the flag. For a slender body of rectangular cross section, this fluid volume per unit flag length is $\pi b^2/4$ [11].

The resistive forces in the normal and tangential directions, modeled with a quadratic dependence on the relative velocity at the blade surface can be written as

$$\hat{F}_d = \tfrac{1}{2}C_D\left(\hat{V} - \frac{\partial\hat{\zeta}}{\partial\tau}\right)\left|\left(\hat{V} - \frac{\partial\hat{\zeta}}{\partial\tau}\right)\boldsymbol{n}\right| + \tfrac{1}{2}C_f\left(\hat{V} - \frac{\partial\hat{\zeta}}{\partial\tau}\right)\left|\left(\hat{V} - \frac{\partial\hat{\zeta}}{\partial\tau}\right)\boldsymbol{t}\right| \qquad (3.17)$$

where C_D and C_f are the normal and tangential drag coefficients, set at $C_D = 1.9$ [109] and $C_f = 0.02$ (close to the theoretical value of [93], however, we note that the results in this range of C_f are not at all sensitive to the precise value of C_f chosen. The results are sensitive to the choice of C_D, however. This choice of coefficient is discussed in §3.4.3). The reactive force in this system is commonly referred to as the fluid added mass, and is a function of the relative fluid acceleration at the flag surface:

$$\hat{F}_{a.m} = \frac{\pi}{4}\frac{b}{l}\frac{\partial\hat{V}}{\partial\tau} - \frac{\pi}{4}\frac{b}{l}\frac{\partial^2\hat{\zeta}}{\partial\tau^2} \qquad (3.18)$$

The total dimensionless fluid force acting on the flags, F, is the sum of the pressure and viscous drag acting on the flag surface as well as the effects of the fluid added mass.

This fluid-structure problem has three parameters of interest. Along with μ and η, the dimensionless velocity potential (Eq. 3.14) reveals the parameter l/D, the ratio of flag length to vortex size. With U_∞, l and b held constant, varying flag thickness, and thus flexural rigidity, produced values of η that spanned six decades: $\eta \approx$ 4E-6 to $\eta \approx$ 5.6E0. The six flags produced values of μ, ranging from $\mu =$ 1.7E-4 to $\mu =$ 9E-3. When $\mu \ll 1$, however, the solid inertia can safely be neglected when compared with fluid inertia. The two vortex street sizes produced values of l/D of 12 and 6. Field observations of live kelp indicate that blades have values of η between $1E-5$ and $1E-6$ (discussed in detail in Chapter 5).

Table 3.2: The experimental flag parameters for the six different flags. The upstream velocity, U_∞, flag width, b, and flag length, l were held constant for all of the flags.

Material	h (μm)	EI/b (Pa m^3)	μ	η
LDPE	50	$4.8E-6 \pm 1.8E-6$	1.7E-4	4.4E-6
LDPE	100	$2.5E-5 \pm 0.6E-5$	3.3E-4	2.3E-5
LDPE	150	$4.1E-5 \pm 1.1E-5$	5.0E-4	3.8E-5
LDPE	250	$5.6E-4 \pm 1.0E-4$	8.5E-4	5.2E-4
UHMWPE	500	$8.3E-3 \pm 1.5E-3$	3.4E-3	7.7E-3
AL 6061	1000	$6.0E0 \pm 1.2E0$	9.1E-3	5.6E0

We solved the nonlinear set of Eqs. 3.10 & 3.14-3.17 numerically utilizing a Chebyshev spectral method and advanced the system through time semi-implicitly using Broyden's method. This solution method is discussed in detail in Appendix B. We make the assumption that in the limit of a slender body with negligible solid inertia, this system can be approximated with one-way coupling between the prescribed fluid flow (Eq. 3.14) and the resulting flag dynamics. We simulated values of η between 1E-5 and 1E2 for both values of l/D. For all of the theoretical cases, μ was set at 1E-4. We initiated each simulation with the flag at rest in an un-deflected position. The velocity potential (Eq. 3.14) and the vortex celerity were smoothly ramped up to their long-time values using the function $[1-\exp(-\tau)]$. Each simulation was run until $\tau = 60$.

3.4 Results

3.4.1 Flow Field Comparison

The vortex street model accurately reproduces the experimental vortex street height, wavelength and frequency, but there are notable differences between the theoretical vortex street model and the experimental flow field. Statistics from the experimental and theoretical vortex street flow fields are presented alongside each other in Fig. 3-10. The instantaneous snapshot of the vorticity field in Fig. 3-10a and b shows how the experimental vortex street creates large interacting structures which extend over

the full water depth, while in the Saffman model [90], the vortices remain discrete, isolated and coherent. When the experimental vorticity field is averaged over more than 30 vortex street cycles (Fig. 3-10c), much of the randomness is averaged out and the characteristic bands of positive and negative vorticity are seen in the bottom and top halves of the vortex street respectively. The time-averaged vorticity shows that the experimental vortex street is much more diffuse than the theoretical model. In the model, the vorticity is confined to narrow bands centered about $h = \pm D$ (Fig. 3-10d). Further, the experimental vortex street dissipates downstream of the bar (Fig. 3-4b), whereas the theoretical vortex street remains constant in strength. There is similar disparity in the time-averaged component of the streamwise velocity, u. The experimental velocity at the vortex street centerline increases with distance downstream of the bar, approaching U_∞, as the vortex street loses its strength (Fig. 3-4a). The velocity at the center of the theoretical vortex street centerline remains at a constant value (Figs. 3-10 & 3-11). The model also produces a step-change in velocity at the vortex street height $h = \pm D$, while there is a much more diffuse vertical velocity gradient in the experimental velocity field.

3.4.2 Experimental Results

Amplitude

Using the image sequence of the flag response captured during the experiments (Fig. 3-12), we extracted the instantaneous flag postures from the series of images. As η decreases, the oscillation amplitude over a vortex cycle increases. For the most flexible blades, i.e. $\eta < 1E-4$, we observed instances where the model blades oscillate asymmetrically over a single vortex street period, either in the upper half or the lower half of the vortex street, while for the more rigid blades, the oscillations were primarily symmetric about the vortex street centerline. The asymmetric oscillations are generally only observed as instances over 1 or 2 vortex periods, before the blade reverts to oscillations that are approximately symmetric about the vortex street centerline. Using the sequence of experimental flag postures and the theoretical

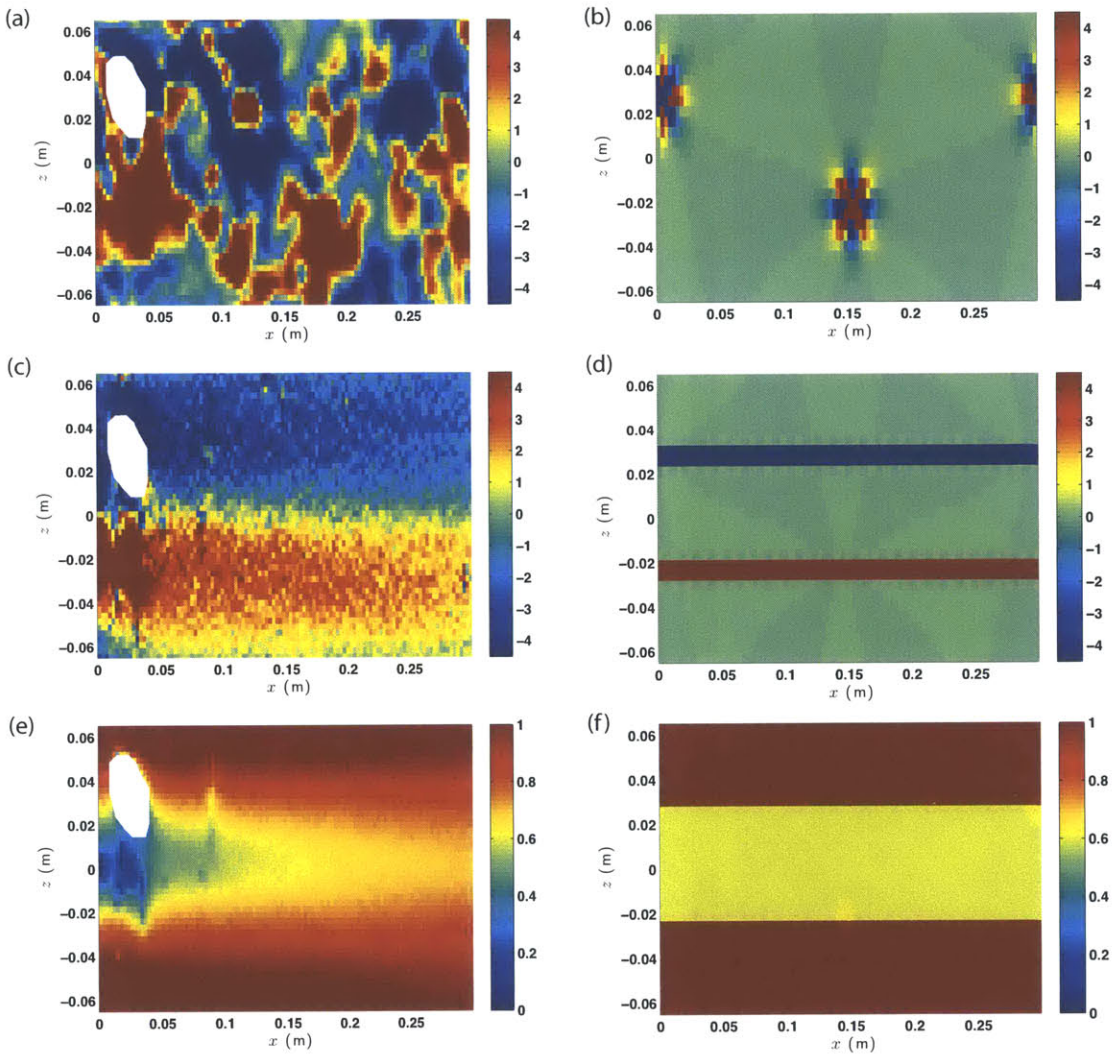

Figure 3-10: A side by side comparison of the experimental and theoretical flow fields for $D = 2.5$ cm. (a) An instantaneous snapshot of the experimental vorticity field from PIV data, alongside (b) an instantaneous snapshot of the dimensionless vorticity field from Eq. 3.14, normalized by l/U_∞, with red representing positive vorticity and blue representing negative vorticity. (c) The dimensionless, time-averaged experimental vorticity over 30 vortex street periods and (d) the dimensionless, time-averaged theoretical vorticity, normalized by l/U_∞, with red representing positive vorticity and blue representing negative vorticity. (e) The time-averaged experimental streamwise velocity alongside (f) the time-averaged streamwise velocity component of Eq. 3.14, both normalized by U_∞. Flow statistics in the white region of (a),(c) and (e) were unavailable due to errors in the PIV processing.

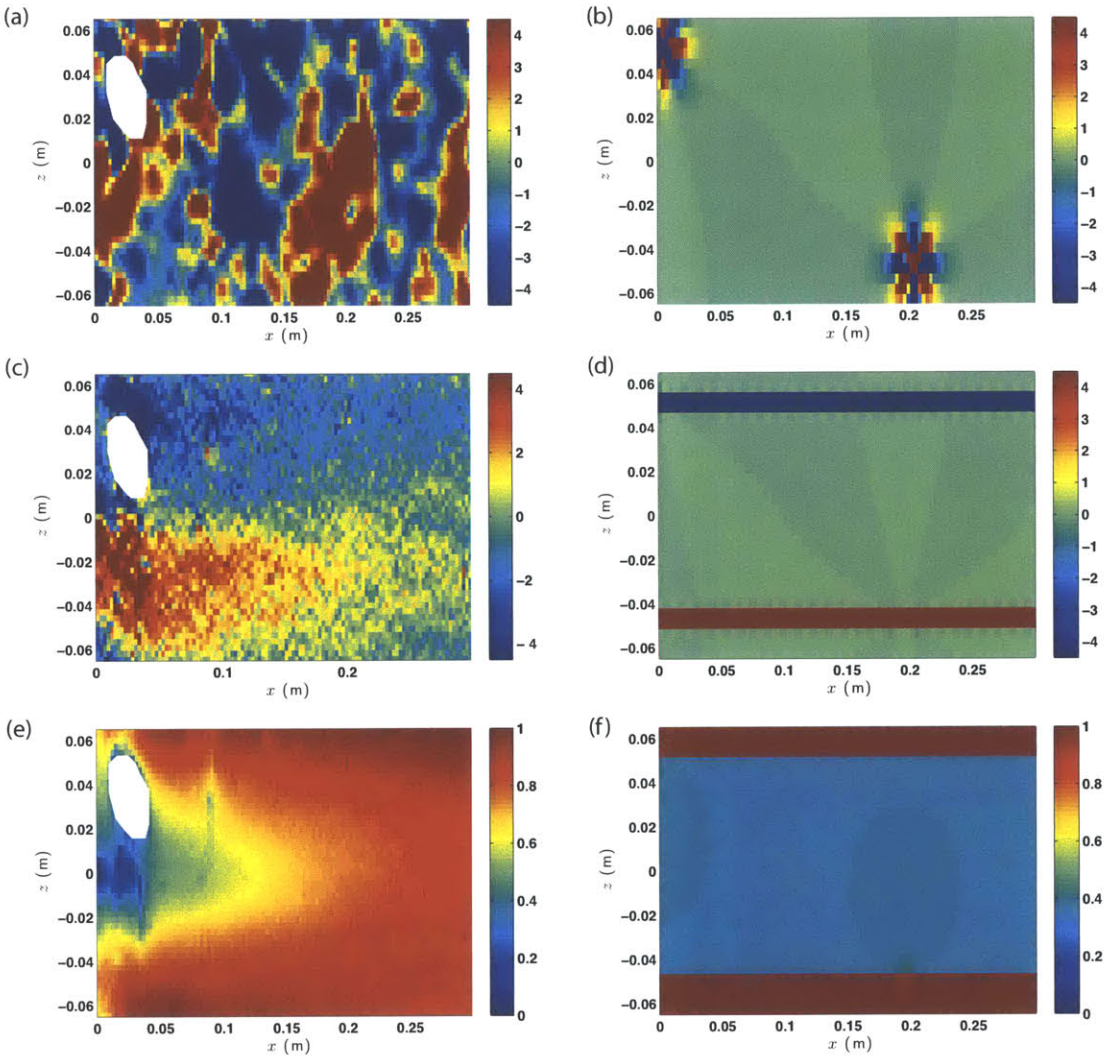

Figure 3-11: A side by side comparison of the experimental and theoretical flow fields for $D = 5.0$ cm. (a) An instantaneous snapshot of the experimental dimensionless vorticity field from PIV data, alongside (b) an instantaneous snapshot of the dimensionless vorticity field from Eq. 3.14, normalized by l/U_∞, with red representing positive vorticity and blue representing negative vorticity. (c) The dimensionless, time-averaged experimental vorticity over 30 vortex street periods and (d) the dimensionless, time-averaged theoretical vorticity, in units of s^{-1}, with red representing positive vorticity and blue representing negative vorticity. (e) The time-averaged experimental streamwise velocity alongside (f) the time-averaged streamwise velocity component of Eq. 3.14, both normalized by U_∞. Flow statistics in the white region of (a),(c) and (e) were unavailable due to errors in the PIV processing.

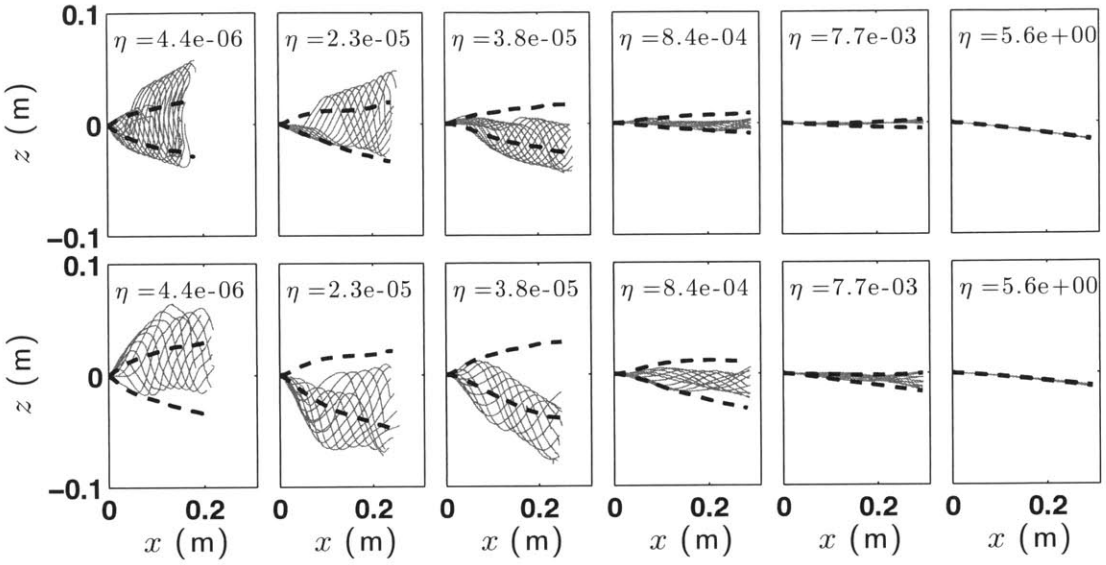

Figure 3-12: Selected instantaneous postures observed in the (top row) $D = 2.5$ cm and (bottom row) $D = 5.0$ cm vortex streets overlaid for one vortex period. Below η_c, the dimensionless value of the bifurcation, the postures were selected to demonstrate the asymmetric oscillation regime. The rms envelope of flag postures about the flag's mean posture, based on the full 30 s record, is shown by the bold dashed lines. Note that the vertical axis is exaggerated.

flag motion produced by our numerical model, we characterized the flag oscillation amplitude using the rms value of the vertical distance from the flag tip to the vortex street centerline (Fig. 3-13). Without any fitted parameters, the modeled flag oscillation amplitude agrees well with the experimental data over the full range of η. The oscillation amplitude is largest for the smallest values of η and the amplitude decreases as η increases. Below $\eta \approx 1E-4$, the oscillation amplitude no longer changes with η and remains constant near the height of the vortex street. This behavior is evident in both the experiments and in the numerical model. In the numerical model, this transition point happens at the critical value of dimensionless flexural rigidity, $\eta_c = 8.85E-5$for $l/D = 6$ and at $\eta_c = 1.40E-4$ for $l/D = 12$. When normalized by the vortex street height, the flag's amplitude response is the same for both vortex street heights.

Tab 3.3: The experimental mean force, inertia and amplitude data for both vortex street sizes. These data are plotted in Fig. 3-13 and Fig. 3-14a & b. The uncertainty in both the mean force data and the amplitude data is 10%. The estimated uncertainty in the inertia measurements is 0.08 m^2/s, owing to the error inherent in the flag posture tracking.

		$D = 2.5$ cm $(l/D = 12)$				$D = 5.0$ cm $(l/D = 6)$				
		F_D (mN)	$x_{tt,rms}$ (m^2/s)	$\Delta z_{rms}/D$	$F_{D,peaks}$ (mN)	η	F_D (mN)	$x_{tt,rms}$ (m^2/s)	$\Delta z_{rms}/D$	$F_{D,peaks}$ (mN)
4.4	-6	4.3	5.6E-1	1.0E0	7.3	4.2E-6	4.8	7.2E-1	6.6E-1	8.8
2.3	-5	3.0	5.8E-1	1.1E0	6.1	2.2E-5	3.6	4.0E-1	7.0E-1	7.3
3.6	-5	2.3	5.0E-1	8.4E-1	5.4	3.5E-5	2.7	3.8E-1	6.8E-1	6.6
5.2	-4	2.4	3.5E-2	3.7E-1	5.2	5.0E-4	2.1	1.4E-1	4.3E-1	6.2
7.4	-3	1.6	1.7E-1	1.5E-1	4.4	7.5E-3	2.0	1.0E-1	1.6E-1	6.3
5.2	0	0.3	4.6E-2	1.2E-2	3.5	5.2E0	1.0	2.7E-2	1.0E-2	6.2

Because solid inertia is negligible compared to fluid inertia in this system ($\mu \ll 1$), we can derive a scaling relationship between Δz_{rms} and η by balancing the fluid torque ($\rho_f b l^2 U_\infty^2$) and the elastic bending moment ($EI\theta_s$). The vortex circulation strength is given by $\Gamma = -2.5 U_\infty D$ [68], and the resulting vertical velocity component of the vortex street has been shown to be directly proportional to U_∞ [2]. It is this vertical velocity component of the vortex street which is responsible for deflecting the flag vertically. The scale of the vertical force on the flag is then $\rho_f U_\infty^2 bl$, which exerts a torque that scales with $\rho_f b l^2 U_\infty^2$. If curvature is confined to a fraction of the flag length, we scale θ_s using a bending length-scale, $l_o < l$, giving $\theta \sim \Delta z_{rms}/l_o$ and such that $\theta_s \sim \Delta z_{rms}/l_o^2$. We consider whether the steady bending length-scale defined in [4], $l_o = (EI/\rho_f b U_\infty^2)^{1/3}$, can be applied to this unsteady system. This formulation yields $\Delta z_{rms} \sim l\eta^{-1/3}$, or $\Delta z_{rms}/D \sim (l/D)\eta^{-1/3}$, which is plotted with the experimental data in Fig. 3-13. For $\eta > 1$, the elastic bending moment is sustained over the entire flag length, i.e. $l_o = l$, and $\Delta z_{rms}/D \sim (l/D)\eta^{-1}$. These scaling relationships are consistent with the observed trends in Δz_{rms} versus η (Fig. 3-13) which suggests that unsteady responses in the low solid inertia regime are governed by the same bending length-scale as steady responses.

Drag Force Measurements

The drag force also has a strong dependence on η and a clear transition in behavior near η_c. Broadly, drag force increases as η decreases (Fig. 3-14a). Above η_c (denoted by the vertical dashed lines in Fig. 3-14), the measured forces decrease gradually as η is increased, following the same trend as oscillation amplitude (Fig. 3-13). These results suggest that above η_c, drag is primarily affected by flag frontal area, which is proportional to oscillation amplitude. Below η_c, the drag force increases more rapidly as η is decreased. This occurs despite the fact that the amplitude of oscillation remains constant below η_c, indicating that in this range drag is no longer correlated to oscillation amplitude. To explain this behavior, we look to the inertial forces on the flags. Notably, the time-averaged drag force measurements across the full range of η are independent of l/D. This is due to the similarity of the mean velocity profiles in

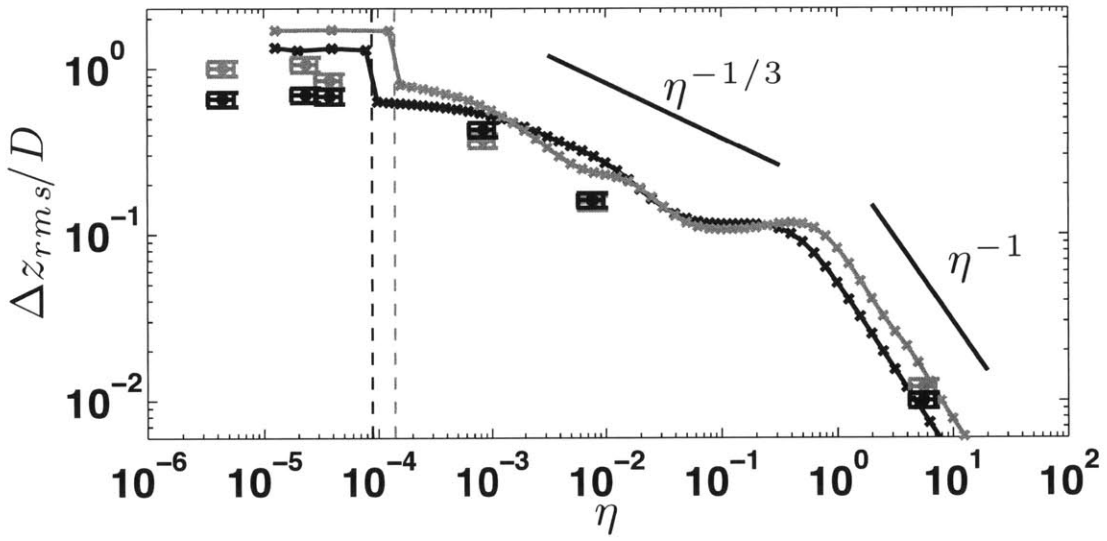

Figure 3-13: The experimental (solid circles) and numerical (solid line with crosses) flapping amplitude at $s = 1$ normalized by D, plotted against η. The data for $D = 2.5$ cm ($l/D = 12$) is plotted with the gray symbols and lines, and the data for $D = 5.0$ cm ($l/D = 6$) is plotted with the black symbols and lines. A sharp change in amplitude is clearly evident in the numerical results at η_c (vertical dashed lines). The experimental and numerical results show good agreement across the full range of η. The scalings predicted from the balance of fluid torque and the elastic bending moment are shown with the solid lines. Below η_c, Δz_{rms} saturates near the vortex street height. Above, η_c, the data agree with the proposed scaling laws.

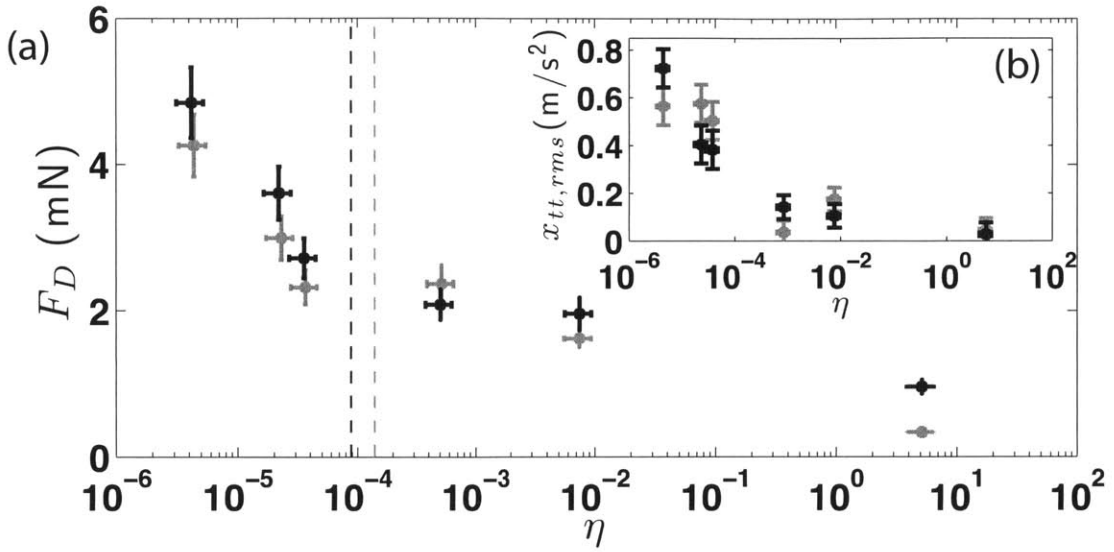

Figure 3-14: (a) Measured drag force versus η for both vortex streets. The slope of F_D versus η shows a clear transition near $\eta = 1E-4$, which is close to the calculated values of η_c (vertical dashed lines). (b) The rms stream-wise acceleration measured at $s = 1$. The data for $D = 2.5$ cm ($l/D = 12$) is plotted with the gray symbols and lines, and the data for $D = 5.0$ cm ($l/D = 6$) is plotted with the black symbols and lines.

the vortex street wakes, when scaled by D. As the flag oscillation amplitude in both vortex streets is the same when normalized by D (Fig. 3-13), the flags encounter the same mean velocity profile, despite having different absolute oscillation amplitudes.

In response to the vortex street fluid forcing, the flag tip ($s = 1$) cyclically translates upstream and downstream at the vortex street frequency. The downstream portion of the flag tip cycle, however, is constrained by the flag length and the flag's inextensibility. As the flag reaches it's full length, rather than continue downstream in the direction of the mean flow, streamwise motion at the flag tip is rapidly arrested, creating a high negative acceleration and a high instantaneous tensile force in the flag. Although there are large accelerations in the upstream portion of the flag motion, the upstream motion is not constrained by the flag's inextensibility and therefore does not produce a corresponding response in the flag's internal tension. We characterize these inertial spikes with the rms of streamwise acceleration at the flag tip (Fig. 3-14b). These inertial spikes lead to an increase in the time-averaged

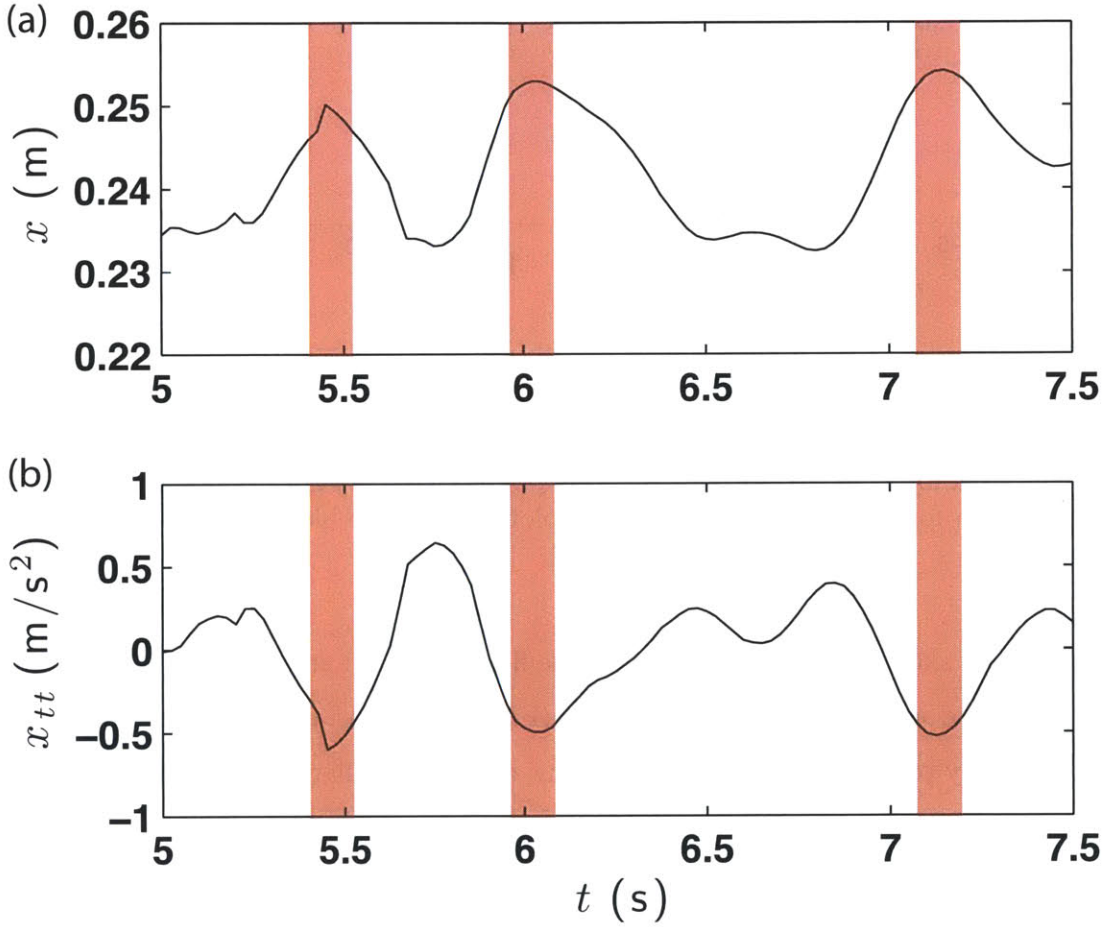

Figure 3-15: (a) A sample time record of the streamwise flag tip position and (b) streamwise flag tip acceleration for $\eta = 2.3E-5$ and $D = 2.5$ cm. Three examples of downstream motions which are rapidly arrested, producing large negative accelerations, and which translate into a tensile forces along the flag length are highlighted with the red bars. The spikes occur at the vortex street period, except for occasional periods of posture reorganization due to the flow randomness.

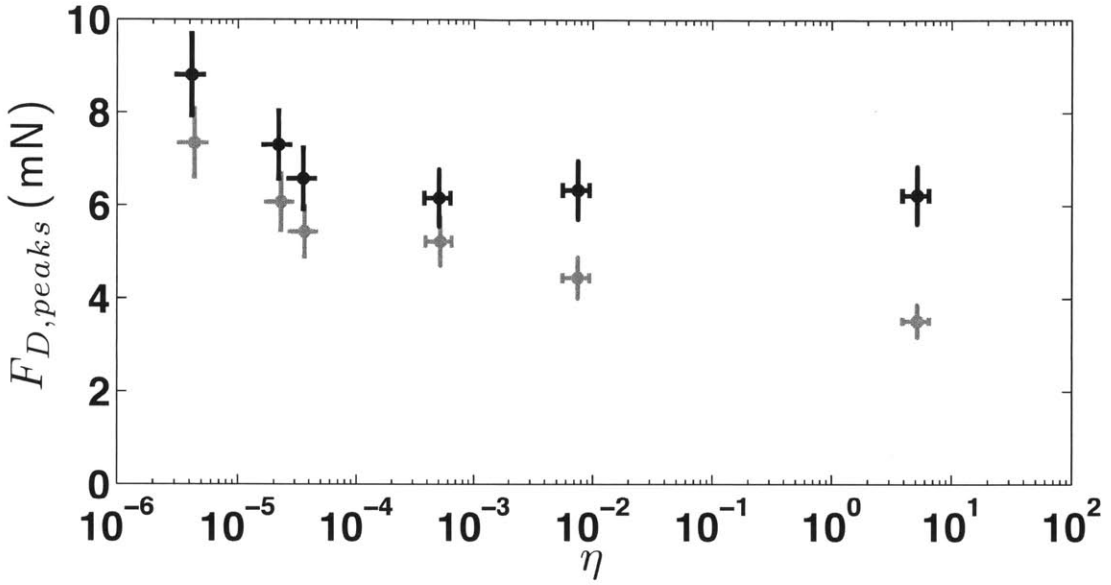

Figure 3-16: The average peak force on the flag over several vortex street cycles as a function of η. The peak force follows the same trend as the mean drag force, however the peak forces for $D = 5.0$ cm are uniformly larger than the peak forces for $D = 2.5$ cm. The data for $D = 2.5$ cm ($l/D = 12$) is plotted with the gray symbols and lines, and the data for $D = 5.0$ cm ($l/D = 6$) is plotted with the black symbols and lines.

force on the flag (Fig. 3-14a). In Fig. 3-15, we have plotted the streamwise position of the blade tip ($s = 1$) and have highlighted the resulting spikes in acceleration. Aside from occasional aperiodic behavior due to randomness in the flow field, these acceleration spikes occur regularly at the vortex street frequency.

The instantaneous force on the blades is also an important force statistic to consider. Kelp blades in the coastal ocean not only have to survive high time-averaged forces, but also instantaneous forces due to high accelerations that could be much larger than the mean force. These instantaneous forces can cause high mechanical stresses and strains within the kelp blade that can lead to either blade breakage or dislodgment of the entire kelp frond. In Fig. 3-16, we plot the average peak force on the model blades over several vortex street cycles. The peak forces are significantly higher than the time-averaged drag forces, however, the peak forces follow the same broad trend as the mean drag forces. The peak forces for the larger vortex street are uniformly higher than the peak forces for the smaller vortex street, indicating that

the larger vortices create higher instantaneous forces.

3.4.3 Numerical Results

In our simple numerical model, we have removed the stochastic component of the experimental vortex street and looked at the behavior of the flags in an idealized system. In our model, we identified two stable response states for flags in a vortex street. For large values of η, the flag oscillates symmetrically about the vortex street centerline (Fig. 3-17a). In this state, the flag motion closely resembles the first modes of vibration of a flexible beam, and the oscillation amplitude increases as η is decreased. Below a critical value of η, however, the system bifurcates, adopting an asymmetric oscillatory state in which the flag is trapped in either the upper or lower half of the vortex street and can deflect beyond $z/D = 1$ (Fig. 3-17b). In this asymmetric state, the streamwise accelerations become much more evident. This numerical prediction of a stable asymmetric state supports our observations of occasional periods of asymmetric oscillation for the most flexible blades. Although we do not observe continuous asymmetric oscillations in the experiments, in Fig. 3-12 we identified vortex street periods over which the flag remained trapped in half of the vortex street. Further experiments and simulations will be necessary to conclusively establish whether or not this asymmetric oscillation state can stably exist in experimental flows.

The theoretical bifurcation value of η closely coincides with the experimentally observed transition value η_c. We identified the bifurcation as the value of η at which the response state of the flag switches from the symmetric state to the asymmetric state (Fig. 3-17a). For the range of parameters tested, we find that η_c is weakly controlled by the ratio of flag length to vortex size, i.e. η_c increases with l/D. For $l/D = 6$, the bifurcation occurs at $\eta_c = 8.85E-5$. For $l/D = 12$, the bifurcation occurs at $\eta_c = 1.40E-4$. We believe that the transition to the asymmetric state is linked to the point at which flag deflections are comparable to the scale of the wake, i.e. $z(s = 1) \geq D$, which can occur at higher rigidities for smaller vortices. Because the potential flow model includes no random perturbations (Figs. 3-10 & 3-11), once the flag is trapped in the asymmetric state, it remains trapped for all time in the

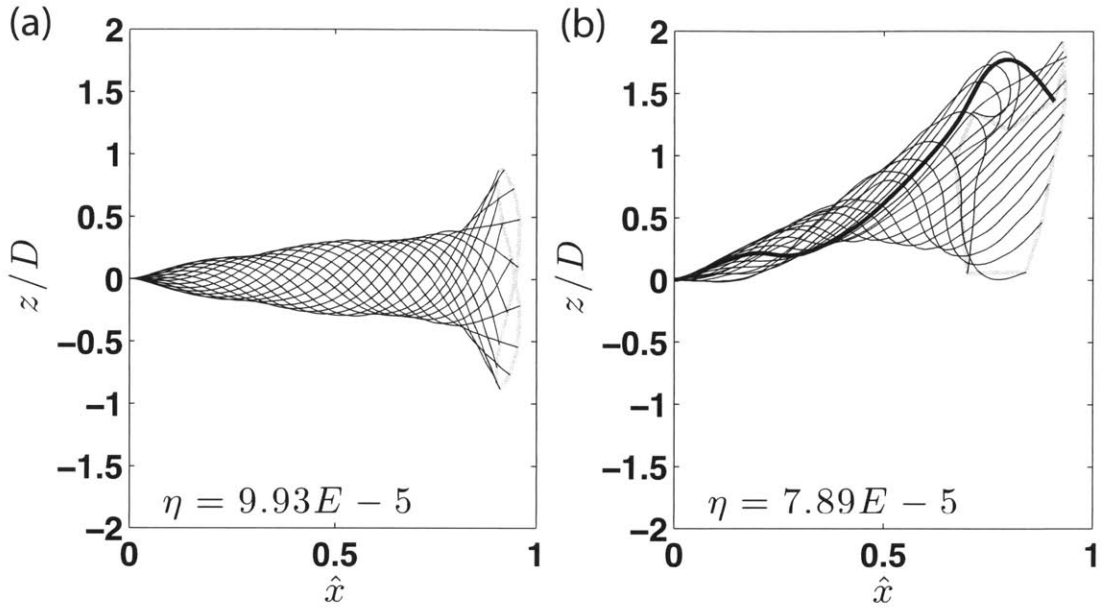

Figure 3-17: Numerical simulations depicting the symmetric and asymmetric oscillation states. (a) Above η_c, the flag oscillates in a symmetric state about the vortex street centerline. (b) Below η_c, the flag oscillates in an asymmetric state trapped in either the upper or lower half of the vortex street. It has an equal probability of becoming trapped in either half of the vortex street. For $l/D = 6$, $\eta_c = 8.85E - 5$, and we plot the postures at (a) $\eta = 9.93E - 5$ and (b) $\eta = 7.89E - 5$. In each plot, we show the trace of the motion at $s = 1$ with the light gray line. The point in the asymmetric cycle with the highest value of stream-wise acceleration is highlighted with the bold flag posture.

model.

We plot the numerical drag predictions in Fig. 3-18. The numerical drag predictions are found by calculating the internal tension in the blade at the clamped end, which is the sum of the total forces on the full blade length. The numerical predictions are larger than the experimental measurements by approximately one order of magnitude. We note that the drag and added mass coefficients are not fitted parameters, which may explain the discrepancy between the measured and modeled values. Tuning the added mass and drag coefficients may help bring the numerical predictions closer to the experimental data. We plot the predicted values of the force for $C_D = 1.0$ and $C_D = 10.0$ to demonstrate the sensitivity of the total force on the blade to the drag coefficient (Fig. 3-18). In reality, the drag and added mass coef-

ficients are a function of blade acceleration [58], and potentially, blade curvature as well, and for unsteady drag the coefficients can be much larger than $C_D = 1.9$ before the pressure fully recovers in the wake. As an exercise, we calculate the oscillation amplitude from the numerical model with three different values of C_D (Fig. 3-19). Notably, the oscillation amplitude remains largely unchanged over the full range of η for values of $C_D = 1.0$ through $C_D = 10.0$. For the largest values of η, the predicted amplitude is higher for $C_D = 10.0$, however. Also, using a value of $C_D = 10.0$ prevents the appearance of the bifurcation over the range of η that we tested.

The reason that the oscillation amplitude results are largely insensitive to the choice of C_D is that the blade has low value of solid inertia relative to the fluid inertia, exemplified by the low value of μ. The lack of solid inertia allows the blade to respond passively to the fluid motion, with the force balance largely between the fluid forces and the blade elasticity. For much of the range of η that we are interested in, the fluid forces tend to dominate the system, and the blade responds passively to the flow. The blade responds in the same manner whether $C_D = 1.0$ or $C_D = 10.0$ because the change in drag coefficient does not change the amplitude of the fluid forcing. For the largest values of eta, increasing the value of C_D to 10.0 has the most apparent effect. The choice of C_D also affects the appearance of the bifurcation (Fig. 3-19). The parameters and the fundamental physical mechanisms that control this phenomenon still remain poorly understood, and are largely beyond the scope of this dissertation.

3.5 Discussion & Conclusion

Our results reveal how flag flexural rigidity, flag length and fluid forcing combine to control flag motion and the resulting forces in a vortex street. Our experiments show that below a critical value of flexural rigidity, flexible flags can experience inertial forces that increase the total force on the system, greatly outweighing any potential benefits from drag reduction. Through a simple model, we have shown that an idealized version of our system contains a previously unreported bifurcation, below

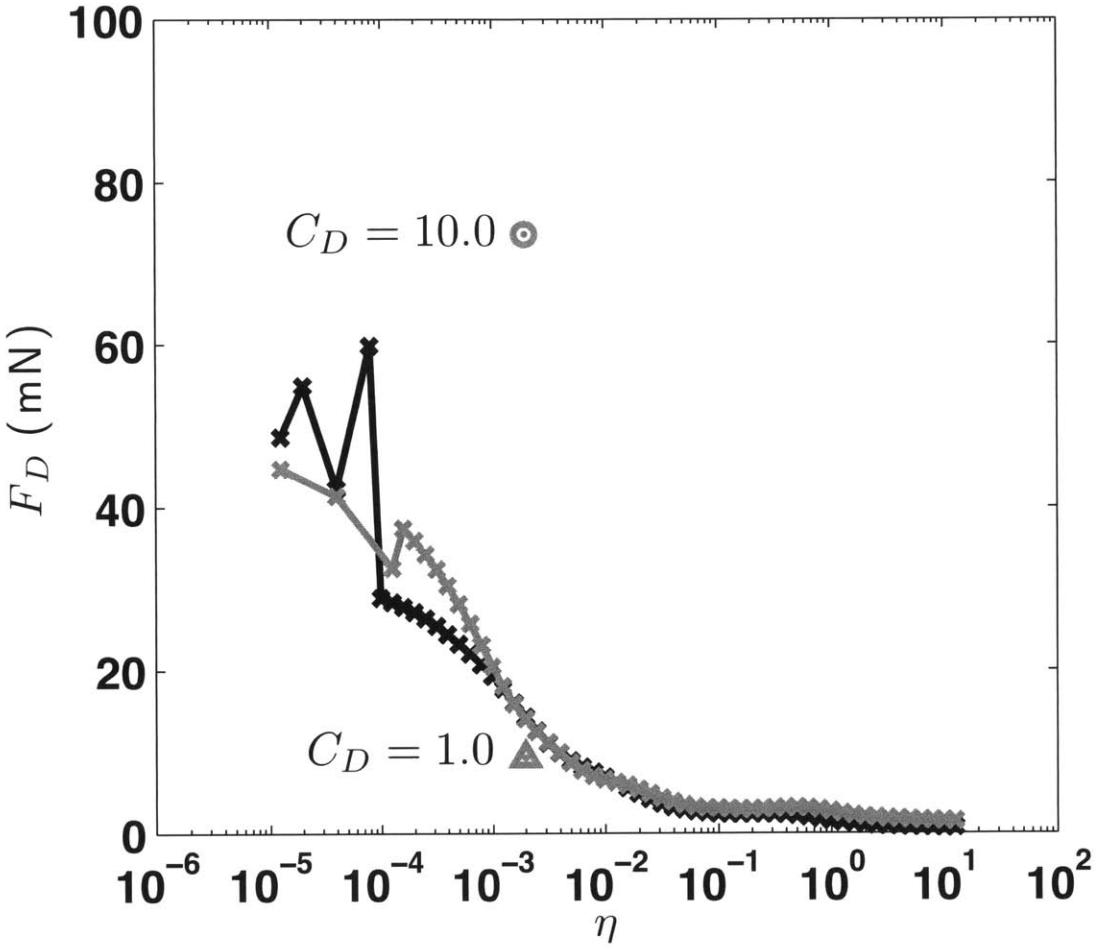

Figure 3-18: The numerical drag force predictions from the numerical model. The numerical drag predictions exceed the experimental predictions by approximately one order of magnitude. The data for $D = 2.5$ cm ($l/D = 12$) is plotted with the gray symbols and lines, and the data for $D = 5.0$ cm ($l/D = 6$) is plotted with the black symbols and lines. The numerically predicted drag for $C_D = 1.0$ and $D = 2.5$ cm is plotted with the gray triangle. The numerically predicted drag for $C_D = 10.0$ and $D = 5.0$ cm is plotted with the gray circle.

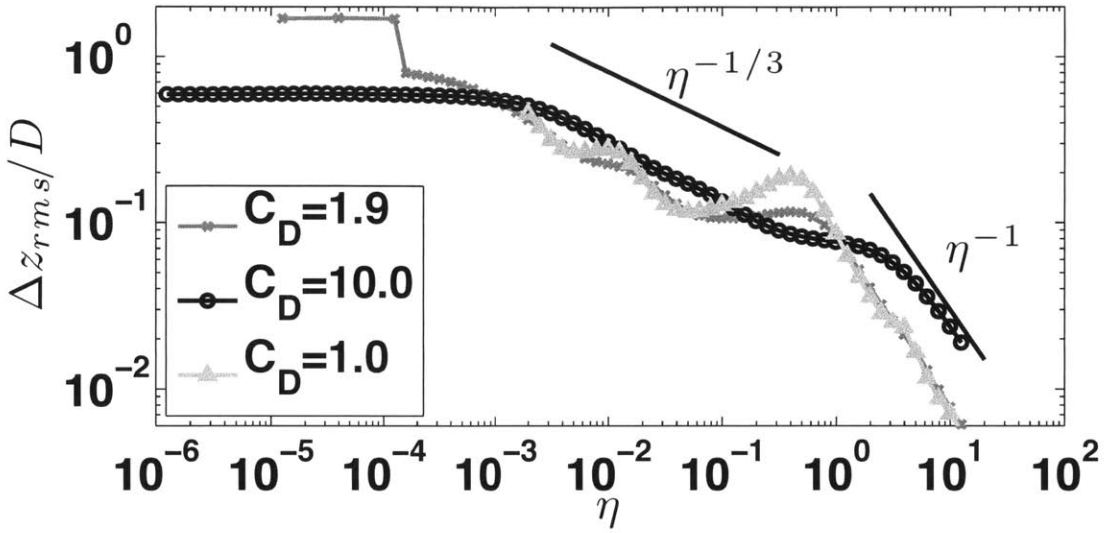

Figure 3-19: The numerical oscillation amplitude predictions from the numerical model for $l/D = 12$ and three different values of the drag coefficient, C_D.

which flags can oscillate asymmetrically, with high accelerations at the flag tip, which greatly enhance the drag force. Above the bifurcation, the flags oscillate symmetrically and drag is closely linked to the oscillation amplitude. The position of the bifurcation depends weakly on the ratio of flag length to vortex street size. These modeling results support the transition in behavior seen in our experimental data.

Chapter 4

Scalar Transfer at the Surface of a Model Blade

4.1 Introduction

Kelp not only has to withstand large drag forces in the coastal ocean environment, it must also simultaneously carry out essential biological functions such as growth and reproduction. To carry out these biological functions, kelp must acquire light energy for photosynthesis and exchange essential nutrients and gases with the surrounding water via the kelp blades. Unlike terrestrial vegetation, kelp and other aquatic vegetation lack the ability to gather nutrients from their roots, and therefore they conduct all nutrient and gas exchange at the blade surface. Due to the hydrodynamic no-slip condition at the surface of kelp blades, there is a thin fluid layer (the diffusive sublayer) adjacent to the kelp blade over which molecular diffusion controls scalar transport. This diffusive sublayer exists within the laminar sublayer, the diffusive sublayer thickness is set by the relative fluid velocity at the blade surface. Transport across this layer is much slower than transport through the bulk ocean water, and therefore this fluid layer often impedes the transport of gases and nutrients to and from the blade surface. Importantly, the concentration of essential nutrients in coastal ocean waters also varies both spatially and temporally, creating spatial regions and seasons of the year in which kelp lives in nutrient-limiting conditions. In these condi-

tions, the physical processes which control the transport of nutrients at the interface between the surrounding water and kelp blades are important to understand.

Kelp has the ability to respond to its local environment in ways that may affect nutrient and gas exchange. It has been widely reported that the morphology of kelp blades changes in response to local hydrodynamic conditions [57]. Changes in morphology, and specifically, changes in flexural rigidity, will change how the blade responds to fluid forces in turbulent flow. The relative fluid velocity at the blade surface is a function of both the fluid velocity and the blade motion. Therefore, passive blade motion can alter the relative fluid velocity at the blade surface which is a critical parameter in setting the rate of scalar flux at the blade surface.

In this chapter, we experimentally and theoretically test whether changes in flexural rigidity, which alters the blade motion (Chapter 3), can alter the rate of mass transfer for a model kelp blade in a vortex street. Furthermore, we investigate if flux models based on a relative surface velocity scale can accurately predict mass transfer at the interface of a passively moving model kelp blade. This information can be used not only to better understand nutrient and gas transfer in kelp, but can also be applied more generally to scalar transfer at dynamic fluid-solid boundaries. Specifically, over rigid boundaries, scalar flux and momentum flux (drag) are described in analogous ways. We ask whether the similarity in momentum and scalar fluxes extends to flexible boundaries.

In §4.2, we describe several recent studies which measured nutrient flux to kelp blades, both in situ and ex situ, and both with live kelp blades and with models. In §4.3, we describe our experimental methods used to measure the scalar flux at the surface of a model kelp blade in a vortex street. In §4.5 we describe the theoretical model we have built to model the scalar flux. This section utilizes velocity scales extracted from the fluid-structure model described in §3.3.3. In §4.6, we present and compare the experimental and theoretical results. Finally, in §4.7, we discuss the validity of the theoretical model, the applicability of this model to other systems, and the implications of changes in flexural rigidity for nutrient transfer to kelp and the implications for differences in nutrient transfer along the length of kelp blades. The

results of this chapter, along with the experimental results from Chapter 3, will be submitted to the journal *Limnology & Oceanography* for publication.

4.2 History of Nutrient Flux Measurements

Many researchers have studied nutrient flux to kelp blades using a variety of experimental methods, oftentimes using live kelp blades. Gerard [36] measured uptake rates of NO_3^- into live kelp blades in situ by enclosing blades in a kelp forest with impermeable bags and measuring the decrease in nutrient concentration in the bag over a period of several hours. Other studies have placed live kelp blades in laboratory flumes and measured rates of NO_3^- and NH_4^+ uptake to blades by monitoring the decrease in nutrient concentration in the flume [33, 49]. Koehl and Alberte [56] placed live blades in a flume to measure carbon uptake rates, which help determine rates of photosynthesis in flow. Hepburn and colleagues measured kelp growth rates and tissue nitrogen concentrations in situ to determine the effects of waves on nutrient uptake [45]. Hurd and Pilditch attempted to measure the thickness of the diffusive boundary layer directly using O_2 probes at different locations on the surface of a kelp blade. One study created copper model blades and measured heat flux while mechanically oscillating the blades at different frequencies [24].

These methods can provide a great deal of insight into the hydrodynamics that control nutrient transfer, but they also contain many intrinsic drawbacks. The use of live kelp blades introduces many biological factors into the nutrient uptake measurements that are difficult to both measure and to model. First, kelp blades have the ability to store nutrients for short periods of time until they are needed during times of low nutrient acquisition. Therefore, studies with live kelp blades must be able to account for the historical nutrient acquisition of the selected blades, as blades may have accumulated different amounts of nutrients in the recent past. Second, both temperature and light directly affect the rate of nutrient utilization by kelp blades through inter-related processes such as photosynthesis [112, 34, 56, 55]. Finally, the physiology of kelp blades is often adapted hyper-locally to position in the water col-

umn or position in the kelp forest. Kelp blades from near the water surface have been shown to have higher rates of nutrient uptake than their counterparts from deeper in the water column, even when both were incubated simultaneously with the same conditions [36]. The method of creating copper models of kelp blades has eliminated several of the confounding factors that have been difficult to model, however, important physical characteristics of kelp are lost with perfectly rigid models. Kelp blades are highly flexible and respond passively to the surrounding fluid forces. This passive response by kelp alters the relative velocity at the blade surface which is a key variable in all nutrient uptake models.

Here we present a novel experimental method for measuring scalar flux at the surface of a model kelp blade. In this method, we create model blades from a widely-available polymer. This simple model allows us to eliminate biological factors such as the nutrient history of the blade, the effects of sunlight and other physiological effects that affect nutrient transfer. Furthermore, by retaining control over the structural properties of the model blades, we can vary the flexural rigidity of our model blades in a controlled manner, allowing us to measure differences in uptake rates that account for the passive motion of the blades.

4.3 Methods

4.3.1 Application of the Passive Sampler Technology

We have developed and tested an experimental method which we use to measure scalar transfer at the surface of the passively deforming, flexible flag. This method draws on the technology of passive polyethylene samplers, which has been established in an environmental sensing context over the past decade [13, 73, 1, 64]. When deployed, passive polyethylene samplers accumulate organic compounds from the surrounding fluid, ultimately reaching an equilibrium concentration that is proportional to the ambient environmental concentration of the compound. These passive samplers present a cheap, low-maintenance approach to in-situ measurements of organic compounds in

various water bodies and sediments. Furthermore, for many compounds, the equilibrium concentration within polyethylene can be between 10^4 and 10^5 times the ambient environmental concentration, thus greatly increasing the sensitivity of the sampling method over a direct measurement of environmental concentration.

The accumulation of mass of an organic compound over time within the polyethylene can provide important information on not only the environmental concentration, but also on the hydrodynamical conditions controlling transport of the compound of interest. In a moving fluid, the no-slip boundary condition at a fluid-solid interface produces a sharp velocity gradient at this interface. In a small layer near the interface, called the diffusive sublayer, turbulent motions are damped out and scalars are transported to the solid surface through molecular diffusion. Away from the fluid-solid interface, the transport of scalars is controlled by the eddy diffusivity of the fluid, which is much larger than the molecular diffusivity of the species. By measuring concentrations within the polyethylene over time, one can determine information about this dynamical layer and also about the hydrodynamical conditions in the bulk of the fluid.

4.3.2 Laboratory Methods: Full Strips

For these experiments, we use a 24 m long, 38 cm wide recirculating flume, with a water depth of 20 cm and a mean flow speed of 20 cm/s. The flume was filled three days prior to the experiments to allow the water temperature to reach the room temperature of 23.5 °C. We inject 70 μL of dibromochloromethane ($CHBr_2Cl$) in the flowing water and allow it to fully mix over the entire flume volume of approximately 2.2 m^3 (Appendix C). Dibromochloromethane is a trihalomethane (THM) that occurs naturally in the ocean and occurs in drinking water as a treatment byproduct. When fully mixed, the concentration of $CHBr_2Cl$ in the flume was 80 ppb. The top of the flume was sealed with aluminum foil to prevent losses of the volatile compound from the water (Figs. 4-1 & 4-2).

In the flume we create a vortex street of height $D = 2.5$ cm (Fig. 3-1). We cut LDPE sheets into 3 cm by 30 cm strips: the same size and shape used in the

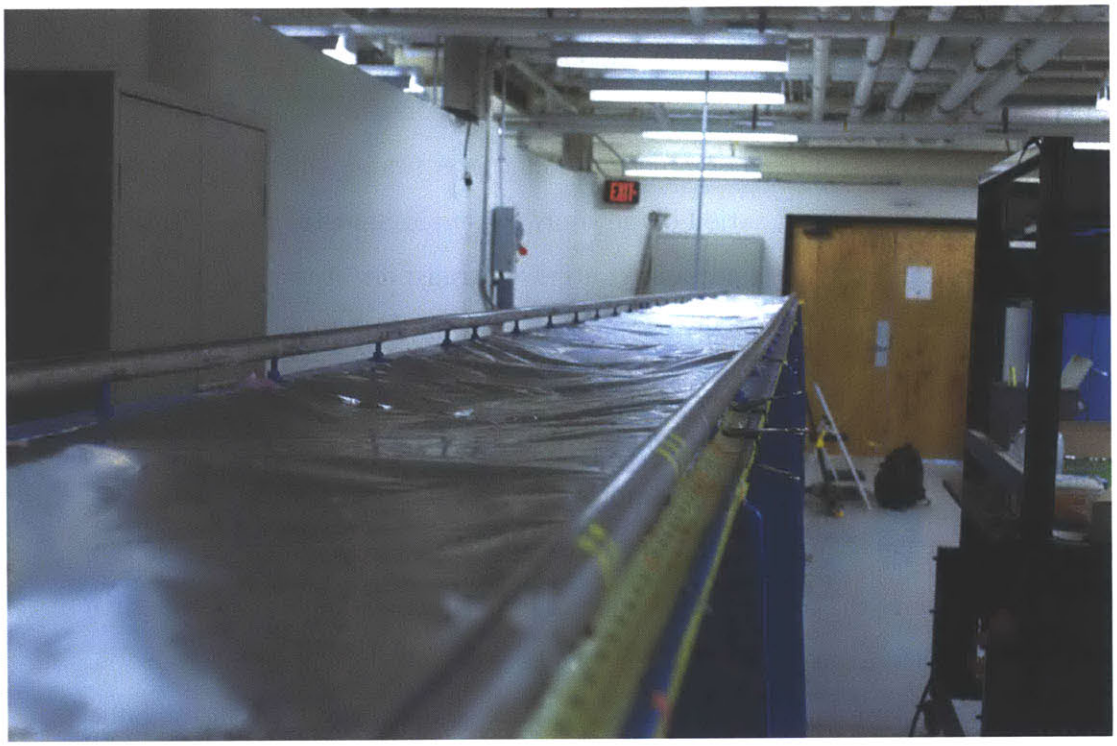

Figure 4-1: Photograph of the flume covered in aluminum foil to prevent losses of $CHBr_2Cl$ from the flume water.

Table 4.1: The experimental exposure time intervals for the LDPE strips in a vortex street, in the flume containing 80 ppb $CHBr_2Cl$.

50 μm LDPE times (s)	250 μm LDPE times (s)
15	60
30	120
60	180
120	300
180	600
300	900
600	1200

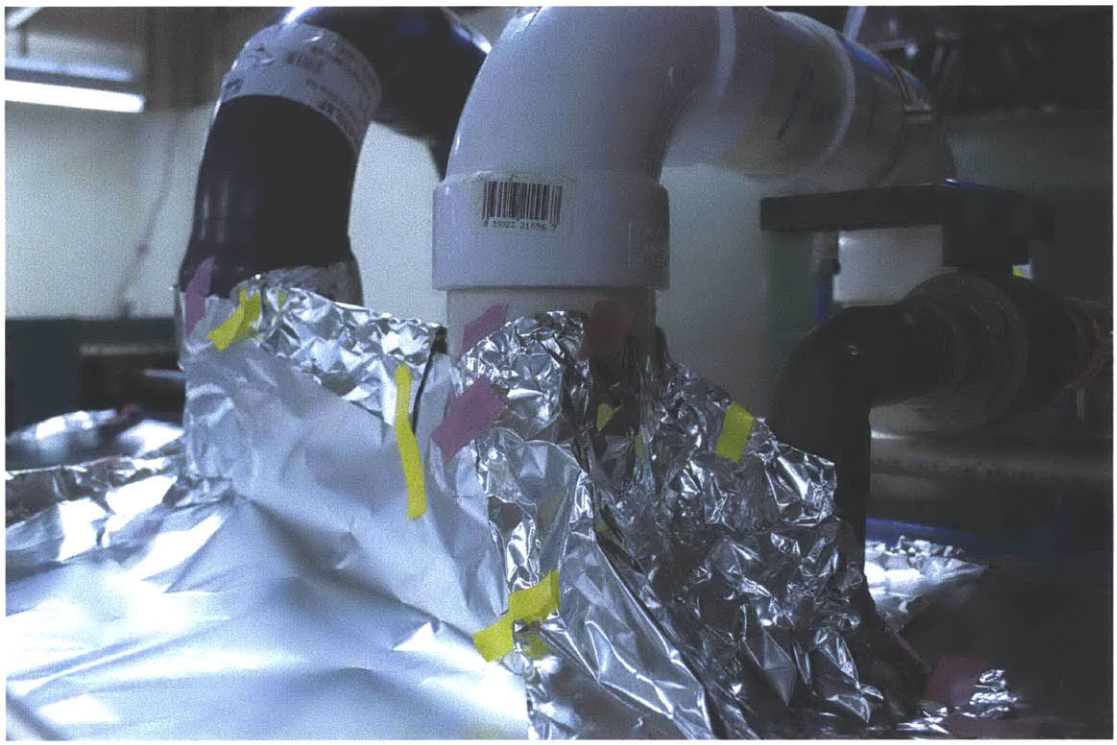

Figure 4-2: Photograph of the aluminum foil around the PVC recirculation fixtures to prevent losses of $CHBr_2Cl$ from the flume water.

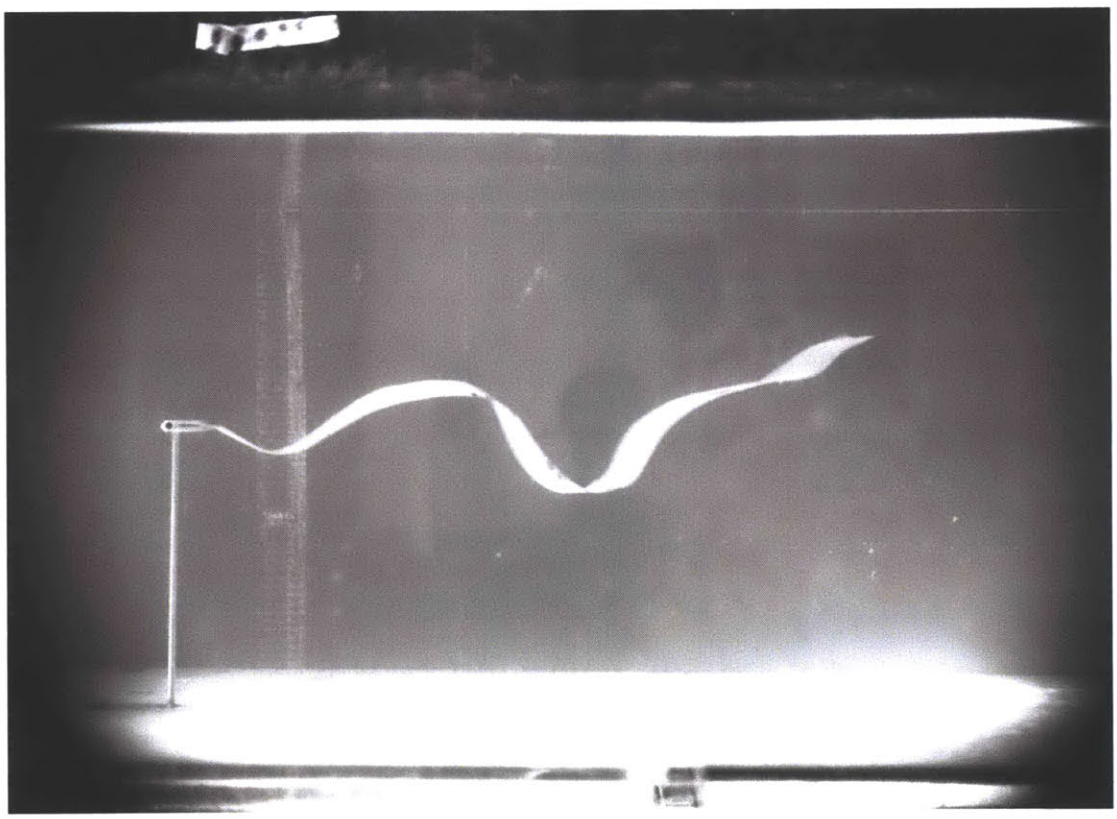

Figure 4-3: Photograph of an LDPE strip ($h = 50$ μm) mounted in the vortex street in the flume.

experiments in §3. We use two thicknesses of LDPE: 50 μm and 250 μm. These two thicknesses were specifically selected from either side of the bifurcation predicted in §3.4.3 because of their different oscillation amplitudes (Fig. 3-13), and thus different relative velocities, in the vortex street (Fig. 3-13). We placed the LDPE strips in the stainless steel clamp, then inserted the clamp and strip into the flow a distance $4D$ = 10 cm downstream of the bar (Fig. 4-3). The LDPE strip accumulated $CHBr_2Cl$ from the surrounding water for a set amount of time (Table 4.1), then was quickly removed from the flume. Using the model described in §4.5, we selected a series of exposure times such that the total mass in the blade at the longest exposure time will be far from the saturation portion of the mass equilibration curve, and will be close to 20% of the equilibrium value. The blade was then removed from the clamp, wiped clean with a Kimwipe to remove any residual flume water from the surface, then inserted into clean 40 mL amber vials (Qorpak) which were filled with clean water (18 MΩ at 25 °C) and then sealed. In the sealed vials, the $CHBr_2Cl$ re-partitioned between the LDPE and water phases, ultimately reaching equilibrium. The vials were left for at least seven days on a shaker table to allow for equilibrium to be reached (this was experimentally confirmed by comparing the measured concentrations in vials that were left for seven days and twenty-one days, respectively, from which we found no differences). This procedure was repeated for increasing time intervals of exposure in the flume with a new LDPE strip used for each new exposure time (Table 4.1). At each experimental time interval, a water sample was taken to account for any changes in the flume water concentration.

The partition coefficient between water and the LDPE strips for $CHBr_2Cl$ was measured with a preliminary set of equilibration experiments to be $K_{PEW} = 100 \pm 15$ for $h = 50$ mum and $K_{PEW} = 300 \pm 30$ for $h = 250$ μm, where K_{PEW} is defined

$$C_{PE,\infty} = K_{PEW} C_{W,\infty} \tag{4.1}$$

in which $C_{PE,\infty}$ and $C_{W,\infty}$ are the LDPE and water concentrations at equilibrium, respectively. In these preliminary experiments, we placed clean model blades in 40

mL amber vials that contained a known mass of of $CHBr_2Cl$ in the water phase. Upon reaching equilibrium, we re-measured the concentration of $CHBr_2Cl$ in the water phase and calculated the amount of mass in the polyethylene phase. Because the total mass of $CHBr_2Cl$ remains constant throughout the partitioning experiment, the partition coefficient was determined from the following equation:

$$K_{PEW} = \frac{C_{W,i}V_W - C_{W,meas.}V_W}{C_{W,meas.}V_{PE}} \tag{4.2}$$

in which $C_{W,i}$ is the known, initial concentration in the vial water phase, $C_{W,meas.}$ is the measured final concentration in the vial water, V_W is the volume of water in the vial and V_{PE} is the volume of the polyethylene blade in the vial.

After the experimental samples were removed from the shaker table, we calculated the mass of $CHBr_2Cl$ in the LDPE indirectly, through measuring the $CHBr_2CL$ concentration in the water (see Appendix E). Because the total mass of $CHBr_2CL$ remains constant in the sample vial both before and after equilibration between the water and LDPE phases, the initial mass in the LDPE (i.e. the mass accumulated during the experiment) is the sum of the final mass in the LDPE and the final mass in the water:

$$M_{PE}(t) = K_{PEW}C_{W,vial}V_{PE} + C_{W,vial}V_W \tag{4.3}$$

where we have used Eq. 4.1 to define $C_{PE,vial} = K_{PEW}C_{W,vial}$.

During each experiment, the $CHBr_2CL$ concentration in the flume water sample was analyzed as well. The mass in the polyethylene for each time interval was then normalized by the theoretical equilibrium mass in the polyethylene, calculated using the instantaneous flume water concentration:

$$\frac{M_{PE}(t)}{M_{PE,\infty}(t)} = \frac{M_{PE}(t)}{C_{W,\infty}(t)K_{PEW}V_{PE}} \tag{4.4}$$

where $C_{W,\infty}(t)K_{PEW}V_{PE}$ is the theoretical equilibrium mass in the polyethylene, and $C_{W,\infty}(t)$ is the measured flume water concentration at each experimental time point. This normalization allows us to account for any losses of $CHBr_2CL$ from the flume

water to the atmosphere. The measured concentration in the flume water, $C_{W,\infty}(t)$, was found to decrease negligibly over the course of the series of experiments, and on a timescale much longer than the experimental time points (Table 4.1). Specifically, the concentration in the flume decreased by 2% over a period of 4 hours, while the longest experimental time point was 20 minutes.

4.3.3 Laboratory Methods: Strip Sections

The relative velocity at the strip surface is a function of position along the length of the strip. This relative velocity is a function of the amplitude of oscillation, which varies as a function of length (Figs. 3-12 & 3-17), and a function of the phase between the blade oscillation and the periodic vortex street flow. At the clamped end, the oscillation amplitude is zero, and the relative velocity is entirely due to the vortex street velocity. Away from the clamped end, the model blade can respond to the flow, however it may not be in phase with the vortex street, creating a relative velocity at the blade surface. The fact that there can be differences in relative fluid velocity along the blade length indicates that different sections of the strip may accumulate mass at different rates. Using the same experimental apparatus and experimental parameters, we measure the differences in mass accumulation between the clamped end of the strip and the free end of the strip.

In these experiments, LDPE strips are placed in the flume for the same durations shown in Table 4.1. After the set time interval, the strips are removed from the flume. The strips are wiped clean with a Kimwipe to remove any residual flume water from the surface, then placed flat on a sheet of aluminum foil. Sections 2.5 cm in length are cut from both the clamped end and the free end of the strip (Fig. 4-4). These two sections are placed in separate vials which are filled with clean water and sealed with negligible head space. The vials are then placed on a shaker table to accelerate the equilibration process. The mass within the LDPE sections is then determined following the same procedure described above.

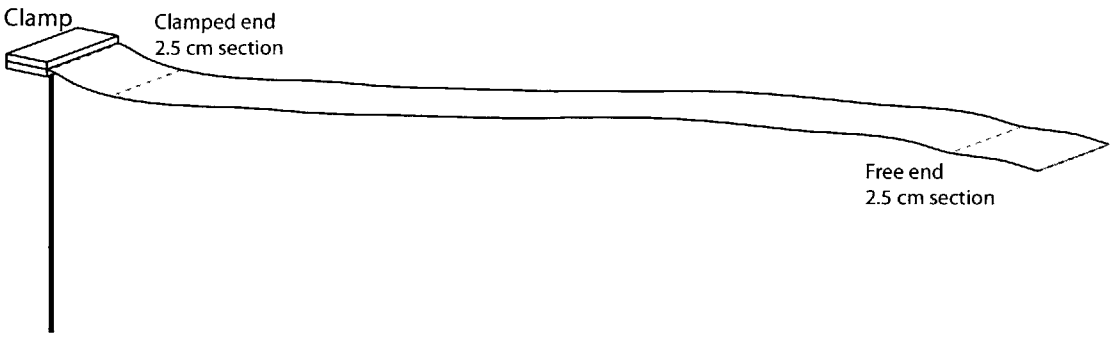

Figure 4-4: The schematic of a sample blade mounted in the clamp. The 2.5 cm sections at the clamped and free ends are outlined with the dashed lines.

4.4 Flux Models

In this section, we introduce three different models that can be used to predict mass transfer at a fluid-solid interface. We will refer to these models throughout this chapter as the steady diffusive boundary layer model, the surface renewal model, and the Ledwell model (or the relative normal velocity model). The steady diffusive boundary layer model is a common model that is applied to a range of systems, ranging from plants in flow [97], flat plates [93] and to the bed of the ocean [42]. For the application of a kelp blade in flow, we make the assumption that roughness near the kelp leading edge will trip the boundary layer from laminar to turbulent and base the discussion of the model on this assumption of a turbulent boundary layer. Within the turbulent boundary layer at a fluid-solid interface there is a thin layer of fluid with thickness δ_ν, called the laminar sublayer, over which the diffusion of fluid momentum is controlled by the kinematic viscosity of the fluid. Within this laminar sublayer, there is a diffusive sub-layer, δ_b. Transport across the diffusive sublayer is controlled by molecular diffusion which is a much slower process than turbulent diffusion in the bulk of the flow, and therefore this thin layer is the limiting step in mass transfer to the solid interface. In a steady, uniform flow, the thicknesses of the laminar sublayer [93] and the diffusive sublayer [14] can be modeled using the shear velocity of the flow, u_*.

$$\delta_\nu = \frac{5\nu}{u_*} \tag{4.5}$$

$$\delta_b = \delta_\nu Sc^{-1/3} \tag{4.6}$$

The shear velocity is formally defined using the shear stress at the solid interface: $u_* = (\tau_w/\rho)^{1/2}$, but can also be described empirically using the mean flow velocity as $u_* = [1/20 \text{ to } 1/5]U_\infty$ [93]. The relationship between the diffusive sublayer thickness and the laminar sublayer thickness as a function of the Schmidt number, $Sc = \nu/D_W$, Eq. 4.6, in which ν is the kinematic viscosity of the fluid and D_W is the molecular diffusivity of the species in water, comes from the behavior of the turbulent eddy diffusivity near a solid interface. Close to a fluid-solid interface, the eddy diffusivity scales cubicly with distance from the interface, $E_t(z) \sim z^3$. The height at which $E_t(z) \approx \nu$ is the top of the viscous sublayer and the height at which $E_t(z) \approx D_W$ is the top of the diffusive sublayer. Because of the eddy viscosity's cubic dependence on distance from the boundary , the ratio between the diffusive and viscous sublayer thicknesses can be described through the Schmidt number, as in Eq. 4.6 [14, 48]. As the mean flow speed or the shear velocity increases, both the laminar sublayer and the diffusive sublayer are compressed, resulting in a smaller layer of resistance to molecular transport and thus higher rates of flux. The primary assumption of this model is that this diffusive sublayer is steady in thickness and can be modeled with simple system parameters. The transfer velocity for mass transfer across a steady diffusive sublayer can be written as

$$K_{D.B.L.} = \frac{D_W}{\delta_b}. \tag{4.7}$$

For steady, uniform flows, the diffusive sublayer thickness can be modeled explicitly. In unsteady flows, such as a vortex street, however, it can difficult to model the diffusive sublayer thickness and, in these cases, other models such as the surface renewal model or the Ledwell model (the relative normal velocity model) may be better suited to model the mass transfer.

There is a class of models termed surface renewal models which account for the ability of turbulent motions in a fluid to periodically renew the diffusive sublayer adjacent to a fluid-solid interface, and therefore to enhance interfacial transport over transport through a steady diffusive sublayer. This model assumes that turbulent eddies in the flow bring fresh fluid towards the surface, stripping the diffusive sublayer at a specific frequency. When the diffusive sublayer is completely renewed (i.e. turbulent motions bring fresh mass directly to the fluid-solid interface) in a periodic manner, the scalar transfer velocity at the interface can be written

$$K_{S.R.} = 2\sqrt{\frac{D_W}{\pi T_R}} \tag{4.8}$$

where T_R is the surface renewal period, D_W is the molecular diffusion coefficient of the species in water and $K_{S.R.}$ is the surface renewal transfer velocity [46, 21]. In between renewal events, the diffusive boundary layer re-grows at the rate set by the molecular diffusion coefficient. If $T_R/T_D < 0.5$, where T_D is the time scale for the establishment of the diffusive sublayer ($T_D = \delta_b^2/D_W$), then mass transfer can be well approximated by Eq. 4.8. When the renewal period is long, i.e. $T_R/T_D > 6$, then the turbulent motions that renew the boundary layer have negligible effect on mass transfer and flux can be modeled using the steady diffusive sublayer model above (Eq. 4.7). For intermediate ratios of T_R/T_D, the transfer velocity can be modeled as in [98].

Finally, mass transfer at a fluid-solid interface can also be modeled using the relative normal velocity component at the fluid-solid interface (i.e. Ledwell 1984) [62]. The normal component of velocity approaching the interface transports mass from the bulk of the fluid towards the interface. At a fluid-solid interface, there is a no-slip velocity condition, which means that the tangential and normal components at the interface equal zero. Near an interface, however, the normal velocity can be approximated by applying conservation of fluid mass at the interface and taking the Taylor expansion of the normal velocity (Eq. 4.9),

$$w'(z) = -\left(\nabla \cdot v'\right)_{z=0} z - \left(\partial \nabla \cdot v'/\partial z\right)_{z=0} z^2 + ... \tag{4.9}$$

in which $\nabla \cdot v'$ is the two-dimensional velocity divergence in plane parallel to the interface, and $z = 0$ is the interface location. Higher order terms in the expansion have been neglected. At a solid interface, the first term in Eq. 4.9 is zero, and the normal velocity approaching the interface scales with z^2. The eddy diffusivity in the fluid, D_t, can be modeled as a product of the velocity scale, $w'(z) \sim \left(\partial \nabla \cdot v'/\partial z\right)_{z=0} z^2$, and a mixing length, taken to be the distance from the interface, z, giving $D_t \sim \left(\partial \nabla \cdot v'/\partial z\right)_{z=0} z^3$. Ledwell [62] used this result to derive the transfer velocity at a solid-liquid interface in the following form:

$$K = \frac{3\sqrt{3}}{2\pi} \left(\frac{\partial}{\partial z}\left(\nabla \cdot v'\right)\right)_{z=0}^{1/3} D_W^{2/3}. \tag{4.10}$$

We refer the interested reader to the full derivation in [62], which takes into account only the normal velocity profile near the fluid-solid interface. This mass transfer model was developed for a stationary boundary, but using the relative velocity instead of the absolute velocity, this model can be adapted for use at a moving boundary. We make the assumption that the same eddy diffusivity dependence applies to a moving boundary as to a solid boundary. Ultimately, as this model depends only on the relative normal velocity approaching the interface, it can be constructed independently of the mean fluid velocity, U_∞, the renewal frequency and the diffusive sublayer thickness.

4.5 Model

We model the transfer of mass from the flume water to the LDPE strip by solving the one-dimensional (vertical, z dimension) diffusion equation inside the polyethylene (Eq. 4.11). We neglect lateral diffusion within the PE based on the fact that the lateral (x) diffusion timescale is long compared with the vertical (z) diffusion timescale, i.e. $h^2/D_{PE} \ll l^2/D_{PE}$. This simplification by dimensional reduction in heat and mass transfer systems when there is a clear separation of length scales is commonly termed

the "fin approximation" [22]. We first divide the length of the strip into 100 sections and solve the diffusion equation independently for each section, allowing for different transfer velocities along the strip length. For each section, we assume the following boundary conditions: no net flux at the strip centerline due to symmetry (Eq. 4.12) and a prescribed transfer velocity, $K(s)$, at the strip surface (Eq. 4.13).

$$\frac{\partial C_{PE}}{\partial t} = D_{PE}\frac{\partial^2 C_{PE}}{\partial z^2} \tag{4.11}$$

$$\left.\frac{\partial C_{PE}}{\partial z}\right|_{z=0} = 0 \tag{4.12}$$

$$D_{PE}\left.\frac{\partial C_{PE}}{\partial z}\right|_{z=h/2} = J(s) = \Delta C K(s) \tag{4.13}$$

In Eqs. 4.11 - 4.13, $J(s)$, is the mass flux per unit area unique to section s of strip, $(h/2)$ is the half-thickness of the LDPE strip, z is the coordinate in the surface normal direction, D_{PE} is the molecular diffusion coefficient of $CHBr_2CL$ within the LDPE, C_{PE} is the concentration of $CHBr_2CL$ within the LDPE, ΔC is the concentration difference between the surface of the strip and the bulk of the fluid, i.e. $\Delta C = C_{W,\infty} - C_{W,z=h/2}$, $K(s)$ is the transfer velocity for section s of the strip and t is the time coordinate. At the strip-water interface, the following condition is true by definition of the partition coefficient:

$$C_{PE}|_{z=h/2^-} = K_{PEW}\, C_W|_{z=h/2^+}. \tag{4.14}$$

We do not model $C_W(z > h/2)$, however. We non-dimensionalize the governing equations in the following manner: $\hat{z} = z/(h/2)$, $\tau = tD_{PE}/(h/2)^2$ and $\hat{C}_{PE} = C_{PE}/(K_{PEW}C_{W,\infty})$. This results in the dimensionless form of the governing equation and boundary conditions:

$$\frac{\partial \hat{C}_{PE}}{\partial \tau} = \frac{\partial^2 \hat{C}_{PE}}{\partial \hat{z}^2} \tag{4.15}$$

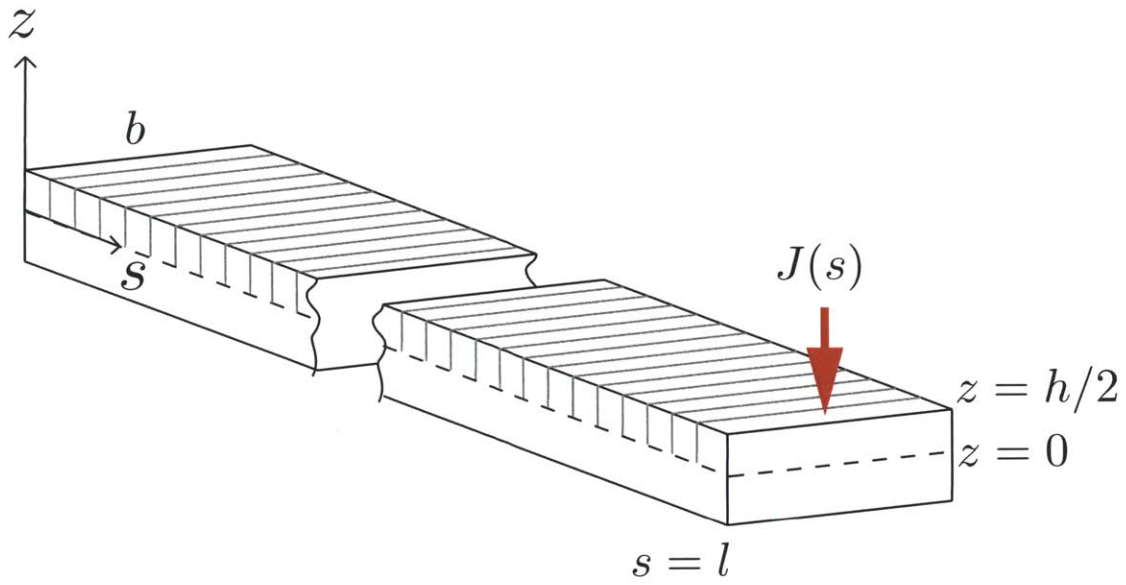

Figure 4-5: A schematic of how the blade is broken up into sections along its length, s. In each section, the 1-D (vertical, z) diffusion equation is solved with a unique prescribed flux, $J(s)$. The equation is solved between the blade centerline, $z = 0$, and the blade surface, $z = h/2$.

$$\left.\frac{\partial \hat{C}_{PE}}{\partial \hat{z}}\right|_{\hat{z}=0} = 0 \tag{4.16}$$

$$\left.\frac{\partial \hat{C}_{PE}}{\partial \hat{z}}\right|_{\hat{z}=1} = \frac{(h/2)}{D_{PE} K_{PEW} C_{W,\infty}} \Delta C K(s) \tag{4.17}$$

We solve the above equations (Egs. 4.15-4.17) using an implicit finite difference (FD) method. This script is included in Appendix F.

4.5.1 Transfer Velocity

To model the transfer velocity at the interface, $K(s)$, we must select a model that captures the physics of the transport in our experimental system. As was seen in §3.4, there is a strong component of the flow normal to the surface of the strip which drives the large-amplitude, vertical oscillations of the strip. This normal component of the flow also transports dissolved species in the flow to the blade interface. The oscillatory flow of the vortex street coupled with the dynamic response of the blade

suggests that the viscous sublayer at the strip surface is periodically disturbed and, therefore, a steady diffusive sublayer model, in which mass flux at the interface is set by the rate of molecular diffusion across a thin layer of steady thickness, would not be appropriate to apply to this system. More appropriate to this system is a model that accounts for the ability of normal component of the fluid velocity to transport mass from the bulk fluid to the blade surface.

We model the mass transfer to the model blades using the Ledwell [62] model for the relative normal velocity at the fluid-solid interface (Eq. 4.10). In these experiments, rather than reconstructing the surface-normal velocity through the use of continuity (Eq. 4.9), we extract the scale of the interface-normal velocity, $w_{rel,rms}$, directly from the fluid-structure model described in §3.3.3. Using these velocities, we can adapt the Ledwell model derived in [62] (Eq. 4.10), which uses the normal velocity near the interface, and apply it to our experimental system (Eq. 4.18).

$$K = \frac{3\sqrt{3}}{2\pi}\left(\frac{w_{rel,rms}(s)}{b^2}\right)^{1/3} D_W^{2/3} \tag{4.18}$$

In Eq. 4.18, we make the physically motivated assumption that the characteristic lengthscale of the velocity divergence is the blade width, b. It has been demonstrated that the blade width, b, is the lengthscale for flow divergence upstream of a flow-normal flat plate moving relative to the fluid [58]. We extract the interface-normal velocities over the full length of the strip over several vortex street cycles (> 10) from our model, take the rms of the time series and repeat this for both strip thicknesses. This gives us a unique transfer velocity for each of the 100 sections over the length of the strip for both strip thicknesses. These values are used in the diffusion model (Eq. 4.17) to calculate the accumulated mass within each section along the strip length, we sum the total mass in the strip, normalize this value by the theoretical mass in the strip at equilibrium and compare the model with our experimental data. We repeated this procedure to predict transfer velocities and to create mass accumulation curves for the 2.5 cm cut sections at the clamped and free ends of the blades. The model-predicted transfer velocities for the full blades as well as for the cut sections

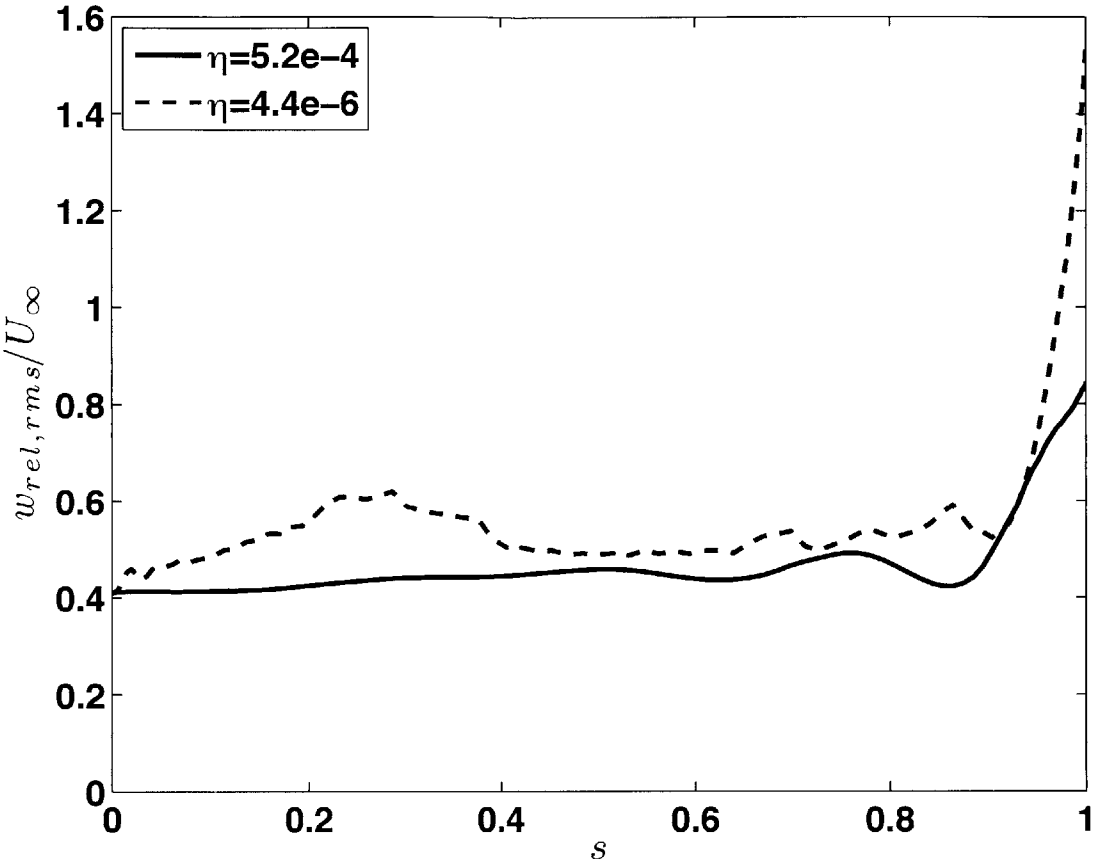

Figure 4-6: The profiles of the rms of the relative velocity normal to the surface of the LDPE strips, for both thicknesses.

from the ends of the blades are presented in Table 4.2. In §4.7 we compare this model prediction and the experimental results with the steady diffusive boundary layer model and the surface renewal model.

4.5.2 Diffusion Coefficient

The diffusion coefficient of $CHBr_2CL$ in the LDPE was calculated from a regression of available experimental diffusion coefficients of polyaromatic hydrocarbons (PAHs) [64]. The regression is a function of the molar volumes of the compounds, and is based on data from experimentally derived diffusion coefficients. This information provides the current best estimate of the diffusion coefficient of $CHBr_2CL$ in the LDPE as there are currently no known measurements of this value. The regression calculated

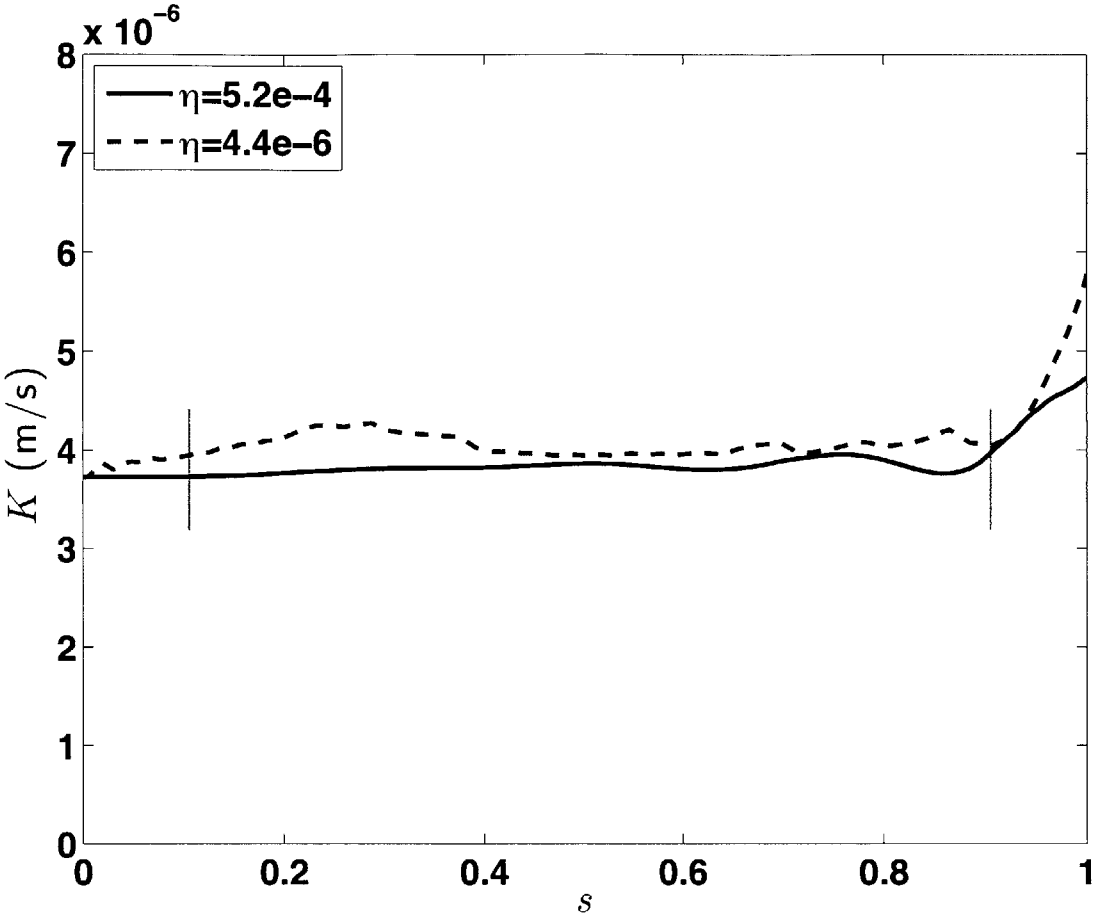

Figure 4-7: The profiles of the model-predicted transfer velocity as a function of strip length for both LDPE strips. The average transfer velocity for $\eta = 5.2E-4$ is $K = 3.87E-6$ m/s and for $\eta = 4.4E-6$, $K = 4.10E-6$ m/s. The location of the cuts are denoted with the thin gray vertical lines. Between $s = 0$ and the first gray line is the clamped-end section. Between the second gray line and $s = 1$ is the free-end section.

Table 4.2: The model-predicted transfer velocities for the full blades as well as for the 2.5 cm cut sections at the clamped and free ends of the blades. The transfer velocities are presented in units of m/s.

	$h = 50$ μm	$h = 250$ μm
Full Blade Average	$4.10E-6$	$3.87E-6$
Clamped End 2.5 cm section	$3.86E-6$	$3.73E-6$
Free End 2.5 cm section	$4.89E-6$	$4.49E-6$

from the data of PAHs provided in [64], with the 95% C.I., is

$$\log D_{PE} = \{-0.0159 \pm 0.0036\}V_m + \{-9.9655 \pm 0.6909\} \tag{4.19}$$

The molar volume of $CHBr_2CL$ is 85.01 cm^3/mol, and the molecular diffusion coefficient in LDPE with the 95% C.I. is

$$\log D_{PE} = -11.3\ \{-10.3, -12.3\}\ m^2/s. \tag{4.20}$$

4.6 Results

4.6.1 Full Blade Results

At each experimental time point, we calculate the mass of $CHBr_2CL$ in the blade using Eq. 4.4. We then find the experimental transfer velocity that best fits the full experimental data set (Table 4.3) using the least squares method, i.e. the transfer velocity that minimizes the sum of squares error with the measured mass accumulation data time series is the best-fit experimental transfer velocity. This process was repeated for the bounds of the 95% C.I. on the diffusion coefficient within the LDPE, providing a different experimental transfer velocity for each modeled diffusion coefficient. The experimental data and the calculated experimental transfer velocity are shown in Tables 4.3 & 4.4 and Fig. 4-8.

The experimental transfer velocity for $h = 50\ \mu m$ was higher than for $h = 250\ \mu m$ (Table 4.4). Recall that $h = 50\ \mu m$ corresponds to $\eta = 4.4E-6$, and $h = 250\ \mu m$ corresponds to $\eta = 5.2E-4$, and therefore the more flexible blade, which responds to the vortex street flow with larger amplitude oscillations (Fig. 3-13), has a higher measured transfer velocity (Figs. 4-6 & 4-7). This result, that the transfer velocity was higher for the more flexible blade was true for the entire 95% C.I (Table 4.4).

For each blade thickness, we calculate the theoretical transfer velocity that is predicted using the Ledwell model (Eq. 4.18) for comparison with the experimental data sets. We input this theoretical transfer velocity into the finite difference (FD) model

Table 4.3: The experimental mass accumulation data for the full blade experiments. The uncertainty for the measurements is $\approx 30\%$ of the value of $M_{PE}/M_{PE,sat.}$, and is calculated based on the variability in the replicate measurements of concentration both in the vial water and in the flume water (See Appendix D). The value of $M_{PE}/M_{PE,sat.}$ for $h = 50$ μm and $t = 600$ s is not included due to an experimental error. The measured concentrations in the vial water and flume are tabulated in Appendix D.

50 μm LDPE		250 μm LDPE	
times (s)	$M_{PE}/M_{PE,sat.}$	times (s)	$M_{PE}/M_{PE,sat.}$
15	0.030	60	0.023
30	0.029	120	0.047
60	0.041	180	0.044
120	0.109	300	0.053
180	0.127	600	0.088
300	0.154	900	0.121
600	Error	1200	0.163

Table 4.4: The calculated best-fit experimental transfer velocities that minimize the sum of squares error of the experimental time series. The transfer velocities were also calculated for the bounds of the 95% C.I. on the LDPE diffusion coefficient.

D (m^2/s)	K (m/s) for $h = 50$ μm	K (m/s) for $h = 250$ μm	$K_{h=50\mu m}/K_{h=250\mu m}$
$D = 10^{-10.3}$	$5.0E-6$	$1.9E-6$	2.6
$D = 10^{-11.3}$	$5.1E-6$	$2.2E-6$	2.3
$D = 10^{-12.3}$	$6.2E-6$	$4.6E-6$	1.4

(Appendix F) and use the FD model to produce the theoretical mass accumulation curve for each blade. We repeat this procedure using the 95% C.I. on the diffusion coefficient within the LDPE, as different values of D_{PE} cause mass to accumulate at different rates within the strip, despite having the same theoretical transfer velocity. This procedure produces a 95% C.I. for the theoretical mass accumulation curve.

Importantly, our model captures the main result that the more flexible blade, ($h = 50$ μm, $\eta = 4.4E-6$), accumulates mass more rapidly than the more rigid blade, ($h = 250$ μm, $\eta = 5.2E-4$) (Fig. 4-7). Furthermore, the model predictions and the experimental data show good agreement for both blade thicknesses. The results are presented in Figs. 4-9 & 4-10. We note that the theoretical model includes no fitted parameters. For $h = 50$ μm, within uncertainty, the model agrees with half of the experimental time points. For $h = 250$ μm, within uncertainty, the model agrees with the full experimental data set. Specifically, for $h = 250$ μm, $D_{PE} = 1E-12.3$ m^2/s, the lower bound of the 95 % C.I., produces the most consistent agreement between the model and the experimental data. For $h = 50$ μm, the 95% C.I. of the theoretical prediction is more narrow, with effectively no difference in the prediction between $D_{PE} = 1E-10.3$ and $D_{PE} = 1E-11.3$ m^2/s. For $h = 50$ μm, the lower bound of the theoretical mass accumulation curve, with $D_{PE} = 1E-12.3$ m^2/s, only captures two of the six experimental data points in the set.

4.6.2 Blade Section Results

The experimental data series are presented in Tables 4.5 & 4.6 and Figs. 4-11 & 4-12. We then used the finite difference model to find the transfer velocities that fit the data series in a manner than minimized the sum of squares error between the model and the measurements. These calculated best-fit transfer velocities are presented in Table 4.6. The experimental data are far below the predictions of the model which suggests either that the model fails to capture the flux to these sections of the strip or a flaw in the experimental method.

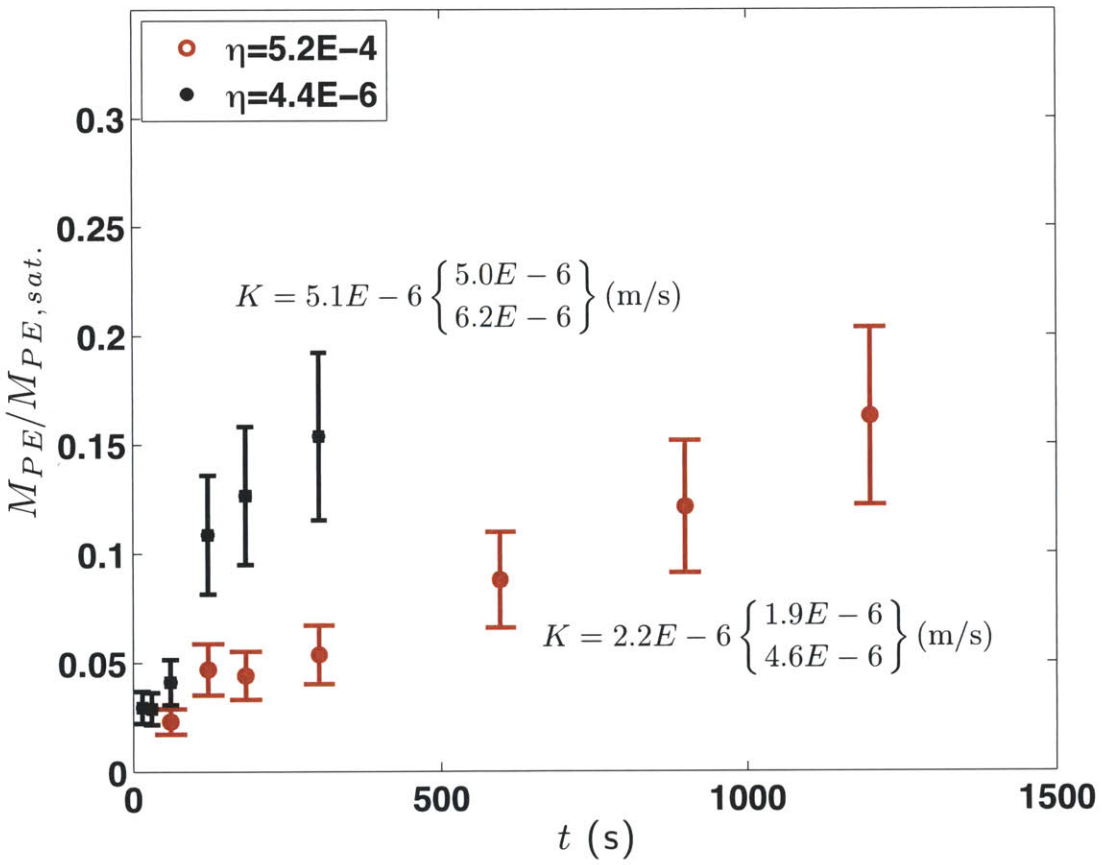

Figure 4-8: The relative mass accumulation within the LDPE blades versus time for both blade thicknesses: h=50 μm ($\eta = 4.4E-6$) and h=250 μm ($\eta = 5.2E-4$).

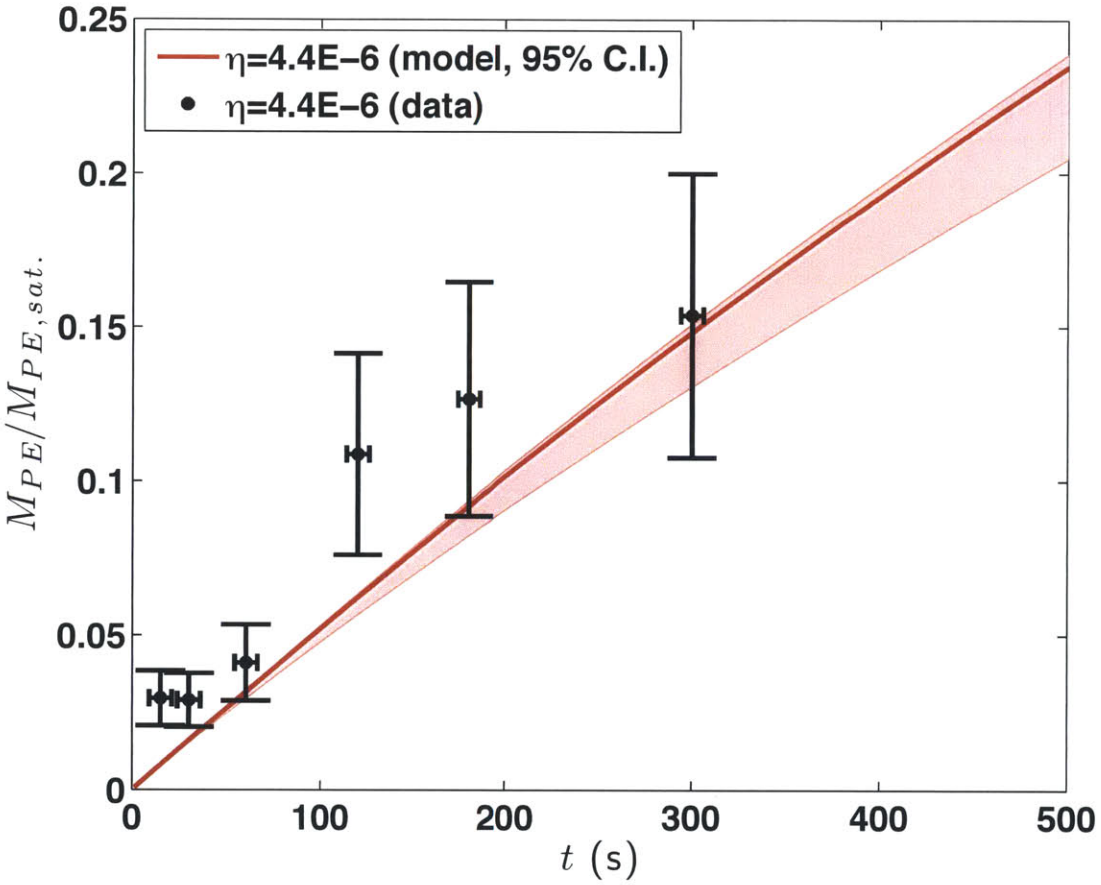

Figure 4-9: The relative mass accumulation within the LDPE blades versus time for h=50 μm ($\eta = 4.4E-6$) plotted with the diffusion model prediction (red solid line) using the Ledwell model (Eq. 4.18) for the transfer velocity and 95% C.I. (red shaded area) based on uncertainty in the diffusion coefficient within the LDPE.

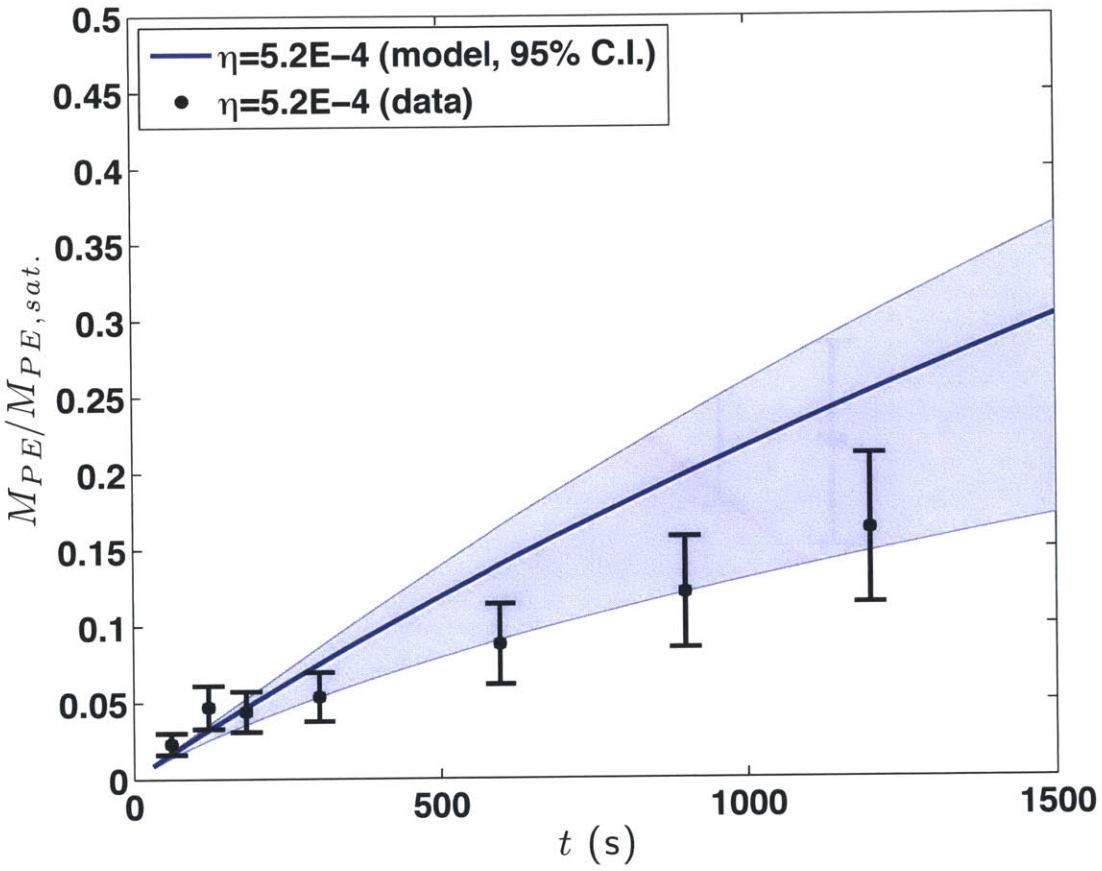

Figure 4-10: The relative mass accumulation within the LDPE blades versus time for h=250 μm ($\eta = 5.2E-4$) plotted with the diffusion model prediction (blue solid line) using the Ledwell model (Eq. 4.18) for the transfer velocity and 95% C.I. (blue shaded area) based on uncertainty in the diffusion coefficient within the LDPE.

Table 4.5: The experimental data from the cut sections experiments. The value of $M_{PE}/M_{PE,sat.}$ for both the clamped and free ends is included in the table. The uncertainty for the measurements is $\approx$ 30% of the value of $M_{PE}/M_{PE,sat.}$, and is calculated based on the variability in the replicate measurements of concentration both in the vial water and in the flume water (See Appendix D). The measured concentrations in the vial water and flume are tabulated in Appendix D.

50 μm LDPE			250 μm LDPE		
times (s)	Clamped	Free	times (s)	Clamped	Free
15	0.010	0.007	60	0.010	0.010
30	0.014	0.014	120	0.012	0.012
60	0.020	0.018	180	0.018	0.018
120	0.029	0.024	300	0.026	0.025
180	0.031	0.035	600	0.035	0.048
300	0.043	0.049	900	0.046	0.059
600	0.065	0.067	1200	0.069	0.081

Table 4.6: The best-fit values of the transfer velocities for the cut sections at the clamped and free ends of the blades. To reflect the uncertainty in the LDPE diffusion coefficient, D_{PE}, three fits were done, using the predicted D_{PE} and the bounds of the 95% C.I.

	h = 50 μm		h = 250 μm	
D	K_{clamp}	K_{free}	K_{clamp}	K_{free}
$D = 10^{-10.3}$	$1.0E-6$	$1.0E-6$	$0.8E-6$	$0.9E-6$
$D = 10^{-11.3}$	$1.0E-6$	$1.0E-6$	$0.8E-6$	$1.0E-6$
$D = 10^{-12.3}$	$1.0E-6$	$1.1E-6$	$1.0E-6$	$1.2E-6$

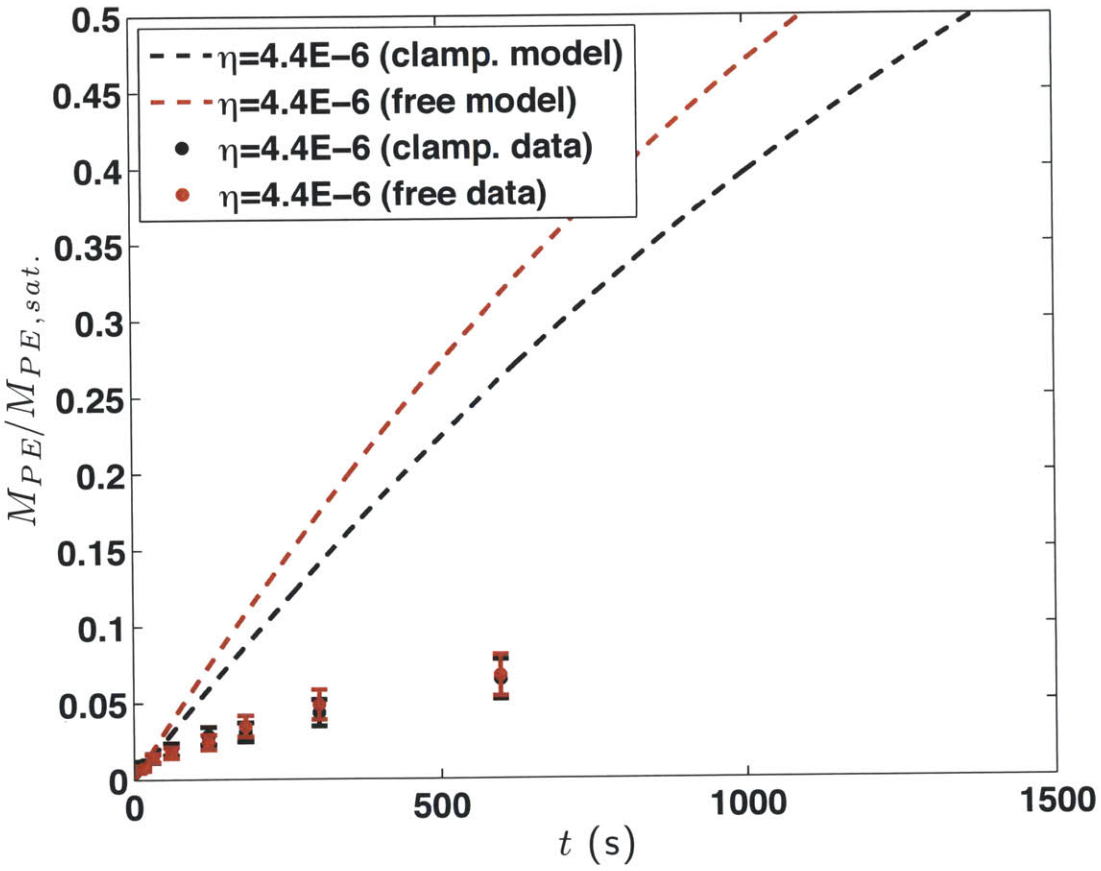

Figure 4-11: The measured mass accumulation within the LDPE blade sections versus time for h=50 μm ($\eta = 5.2E-4$) plotted with the diffusion model prediction (dashed lines) using the Ledwell model (Eq. 4.18) for the transfer velocity. The clamped end is plotted in black. The free end is plotted in red.

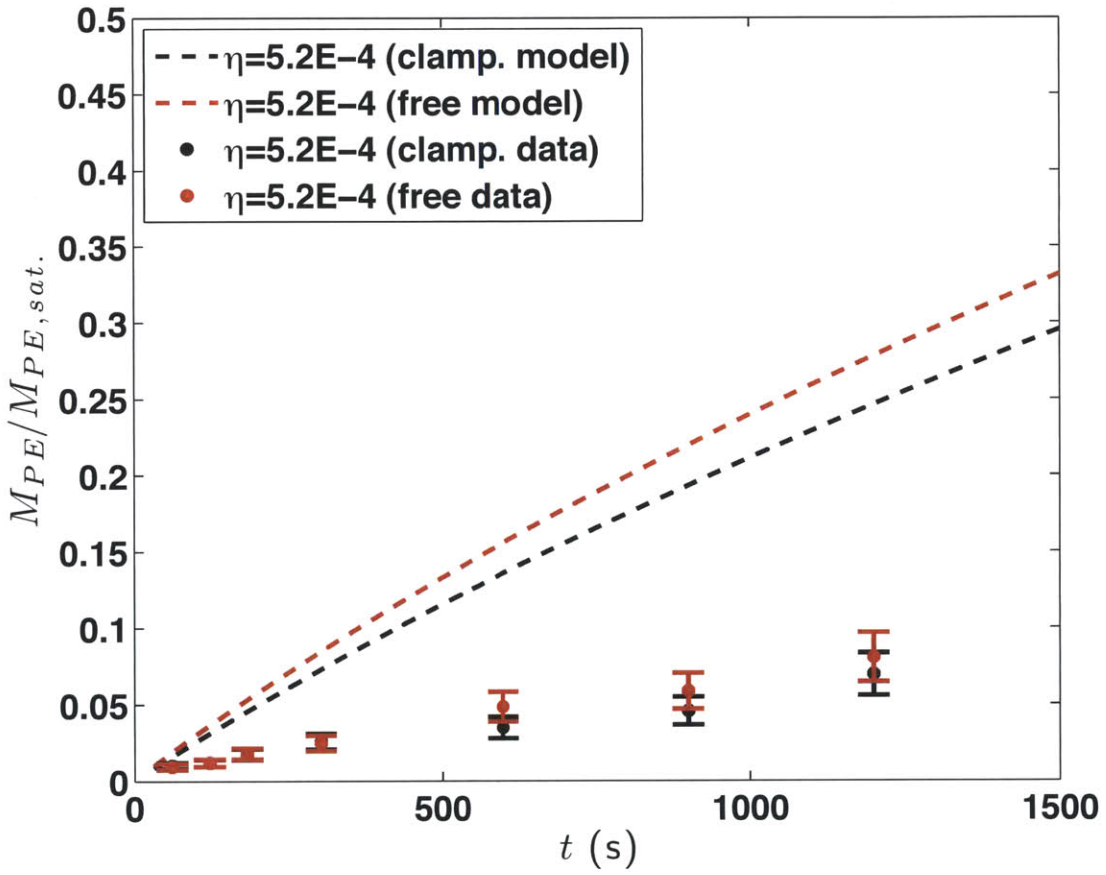

Figure 4-12: The measured mass accumulation within the LDPE blade sections versus time for h=250 μm ($\eta = 5.2E-4$) plotted with the diffusion model prediction (dashed lines) using the Ledwell model (Eq. 4.18) for the transfer velocity. The clamped end is plotted in black. The free end is plotted in red.

4.7 Discussion

The transfer velocity model derived by Ledwell [62] and modified to be applied to this system predicts the mass flux to the blade within uncertainty for the full blade experiments. The measurements from the cut blade sections, however, neither agree with the model, nor are they consistent with the experimental full blade results. Specifically, the measurements of flux to the cut sections are far below predictions of the model, and are far below what is anticipated based on the full blade experiments. Together, these two sets of results provide us important information about how mass transfer occurs at the surface of a flexible, passively responding blade in flow. Specifically, it is intriguing that in identical flow fields, the more flexible blade accumulated mass more rapidly. Moreover, these results also provide us important insight into the capabilities and limits of the design of our experimental method.

4.7.1 Flux is set by relative fluid motion

The primary conclusion we can draw from this set of experiments is that flux at the surface of a flexible blade moving in flow is set by the relative fluid motion at the blade surface. We measured the mass transfer to two different model blades, which differed only in their relative motion in the flow, and found that the blade with higher relative motion gained mass more rapidly. Using our model for the motion of a thin flexible body in a vortex street (Chap. 3) in concert with a model for the transfer velocity at fluid-solid interface (§4.5.1), we estimated the relative blade-normal velocities along the full length of the blades. The estimated relative velocity was used to predict the transfer velocity. The model indicates that more flexible blades have higher relative velocities along their length (Fig. 4-6), which corresponds with a higher average transfer velocity at the blade surface (Fig. 4-7). This is indeed the result that we find experimentally: the fitted transfer velocity of the more flexible blade is greater than the fitted transfer velocity of the more rigid blade. In fact, we find that the flux enhancement to the more flexible blade is slightly higher than that predicted by our model. Specifically, the model predicts that $K_{h=50\mu m}/K_{h=250\mu m} = 1.06$, while we find

Table 4.7: The back-calculated effective velocity scales based on the measured experimental transfer velocities from Table 4.4 and using Eq. 4.18.

D (m^2/s)	$w_{eff.}$ (m/s) for $h = 50$ μm	$w_{eff.}$ (m/s) for $h = 250$ μm
$D = 10^{-10.3}$	0.20	0.01
$D = 10^{-11.3}$	0.21	0.02
$D = 10^{-12.3}$	0.38	0.15

$K_{h=50\mu m}/K_{h=250\mu m} = 2.6$ (using $D_{PE} = 10^{-10.3}$ m^2/s), $K_{h=50\mu m}/K_{h=250\mu m} = 2.3$ (using $D_{PE} = 10^{-11.3}$ m^2/s) and $K_{h=50\mu m}/K_{h=250\mu m} = 1.4$ (using $D_{PE} = 10^{-12.3}$ m^2/s). This confirms that the combination of our dynamic blade model with the mass transfer model of [62] captures the essential features of our model system, despite under-predicting the actual enhancement in transfer velocity. A possible explanation for the under-prediction of the transfer velocity ratio could be our choice of parameterization of the relative velocity at the blade surface. The relative velocity at the blade surface varies in time, and therefore we used the rms of the relative velocity record as the velocity scale in the flux model. It is possible, however, that the root mean square of the velocity does not fully capture the effects of the unsteady velocity on mass transfer. Infrequent, high-velocity events may impact flux in ways not captured by the rms of the velocity record. It is possible, as well, that our transfer velocity model, which we calculated using the modeled velocities rather than measured velocities, fails to fully capture the relative velocity at the surface of the experimental blades. Ultimately, though, the experimental results indicate that the relative velocity at the blade surface is a key variable in setting the rate of mass transfer at the blade surface. Both in these experiments and for kelp in the ocean, the relative velocity at the blade surface can be a function of the blade flexural rigidity.

We can use the experimentally measured transfer velocity to back-calculate an effective relative velocity scale for each model blade and each modeled diffusion coefficient using Eq. 4.18. These effective velocity scales are displayed in Table 4.7. The model predicted rms relative velocities (Fig. 4-6) are between $0.4U_\infty$ and $1.5U_\infty$, while the calculated effective velocities (Table 4.7) are between 0.01 m/s and 0.38 m/s, or

$0.05U_\infty$ and $1.9U_\infty$. The difference between the effective velocities for the two blade thicknesses is larger than predicted by the model. However, as we noted above, it is possible that the root mean square of the velocity record does not adequately capture the effect that the varying velocity at the blade surface has on mass transfer, and that the calculated velocity scales in Table 4.7 are better representations of the flow.

Our experiments allow us to ultimately conclude that flux to a passively deforming blade is a function of the blade flexural rigidity. This result is novel in that current models for flux at a fluid-solid interface have not taken into consideration the role of the structure's flexural rigidity. Below, we discuss the application of the three flux models (introduced in §4.4) to our kelp blade system.

In the coastal ocean, kelp blades flap and flutter in the flow [56, 48], resulting in a normal velocity at the blade surface. Therefore, successful modeling of nutrient flux at the blade surface requires information about the relative normal velocity at the blade surface, which is a function of both the blade motion and the fluid motion. We acknowledge that constructing a numerical model to extract relative velocity information at the blade surface is often prohibitively time-consuming and computationally expensive. In §4.7.3, we develop a simple model that can be used to predict nutrient flux in the field based basic knowledge of the blade and the fluid motion.

Thin film model

We can use the steady diffusive boundary layer model (§4.4) to calculate a transfer velocity for our experimental system. For a mean flow speed $U_\infty = 0.20$ m/s, $u_* =$ 0.01 to 0.04 m/s, and the laminar sublayer thickness, using Eq. 4.5, is $\delta_\nu = 1.25E-4$ to $5E-4$ m. We assume that the leading edge of the blade trips the boundary layer into a turbulent boundary layer state. Using the Schmidt number relationship between the diffusive sublayer thickness and the laminar sublayer thickness (Eq. 4.6), the diffusive sublayer is between $1.25E-5$ and $5E-5$ m thick. This thickness produces a transfer velocity of between $K_{D.B.L} = 2E-5$ and $8E-5$ m/s. These values are much larger than the measured transfer velocity for the $h = 50$ μm and $h = 250$ μm blades of between $2E-6$ and $6E-6$ m/s. (Table 4.4). Moreover, the steady diffusive

Table 4.8: The calculated values of the diffusive boundary layer thickness, using the measured transfer velocities reported in Table 4.4 and Eq. 4.7.

D (m^2/s)	$\delta_{b,eff.}$ (m) for $h = 50$ μm	$\delta_{b,eff.}$ (m) for $h = 250$ μm
$D = 10^{-10.3}$	$2.00E-4$	$5.26E-4$
$D = 10^{-11.3}$	$1.96E-4$	$2.55E-4$
$D = 10^{-12.3}$	$1.61E-4$	$2.17E-4$

boundary layer model cannot differentiate between the two values of flexural rigidity, and thus cannot predict the observed differences in flux.

Furthermore, in many systems, including the vortex street flow in our system, the flow is unsteady, making accurate modeling of the diffusive sublayer thickness very difficult. Indeed, in rapidly changing systems, where the timescale of the flow unsteadiness is short compared with the timescale for establishment of the diffusive sublayer, accurate modeling is often not possible, and use of the steady diffusive sublayer model in a predictive manner is crude simplification, at best. Direct measurements of unsteady diffusive sublayers are often possible at stable interfaces, such as the ocean floor [42], however, these measurements are limited by the spatial and temporal resolution of the sensor. Furthermore, for dynamic interfaces undergoing rapid large-amplitude motion and high curvatures, measuring the diffusive sublayer thickness is currently not possible. In our system, the unsteadiness of the flow violates the primary assumptions of the steady diffusive sublayer model and the flow unsteadiness is likely the main cause of disagreement between the model predictions and the experimental measurements. It is also possible that the boundary layer at the blade interface is not fully turbulent, however, we cannot assume a laminar sublayer model without treating the blade like a rigid flat plate, an assumption which violates the fundamental nature of our experiment.

We can, however, use the experimentally calculated transfer velocities (Table 4.4) to calculate an effective diffusive boundary layer thickness using Eq. 4.7. Although the system is unsteady, this exercise allows us to calculate an average, effective diffusive boundary layer thickness over the course of the experiment. These values are

reported in Table 4.8. We find values of the effective diffusive sublayer thickness between 1.6E-4 and 5.3E-4 m, which are physically reasonable values for this system. Other authors have calculated the effective diffusive sublayer thickness on flexible kelp blades in flow using flux measurements and found thicknesses between 1.5E-4 and 2.0E-4 m for free stream velocities near 0.20 m/s [97, 49]. Gundersen directly measured the diffusive boundary layer thickness at the bed of the ocean and found a mean thickness of 5.9E-4 m [42].

Surface renewal model

In turbulent systems with a single dominant frequency, the classic surface renewal model developed by Higbie [46] and Danckwerts [21] is often successfully applied [96, 97, 48]. This model has also been extended to accept a distribution of renewal times, rather than just a single period [31]. In our system, the single dominant frequency is the vortex street frequency, which is related to the mean flow speed and vortex street height through the Strouhal number (§3.3.1). The coherent fluid structures of the vortex street impinge on the blade surface and induce a dynamic blade response at the same frequency as the vortex street. For the $D = 2.5$ cm vortex street, $f = 1.2$ Hz, or $T_R = 0.83$ s. For these parameters, the classic surface renewal model predicts a transfer velocity of $K_{S.R.} = 3.92E - 5$ m/s. This transfer velocity is an order of magnitude larger than the measured transfer velocity and therefore grossly fails to capture the actual rate of mass transfer at the surface of the flexible blade. Through this comparison, it becomes clear that the actual mechanism of mass transfer to the interface can not be a complete renewal of the diffusive sub-layer every T_R seconds, but is likely a slower process of diffusive sublayer compression (i.e. thinning the boundary layer though not fully replenishing it) and the delivery of fresh mass to the surface at a rate set by the local normal velocity. In addition, the surface renewal model cannot differentiate between different blade flexural rigidities. The two blades in our experiments oscillate at exactly the same frequency, which is set by the vortex street. However, differences in rigidity produced differences in blade motion that translated into differences in flux. These differences cannot be predicted

Table 4.9: The calculated values of the surface renewal timescale, using the measured transfer velocities reported in Table 4.4 and Eq. 4.8.

D (m^2/s)	$T_{R,eff.}$ (s) for $h = 50$ μm	$T_{R,eff.}$ (s) for $h = 250$ μm
$D = 10^{-10.3}$	51	353
$D = 10^{-11.3}$	49	263
$D = 10^{-12.3}$	31	60

by the surface renewal model.

Similar to the exercise in §4.7.1, we can use the experimentally measured transfer velocity to calculate an effective surface renewal timescale from Eq. 4.8. These calculated, effective renewal timescales are displayed in Table 4.9. The vortex street frequency sets both the frequency of the fluid oscillation and the blade oscillation and is narrowly centered around $f = 1.2$ Hz or T=0.83 s. The calculated effective renewal time scales are between one and two orders of magnitude larger than the vortex street period. As there is no physical basis for renewal timescales between 30 s and 350 s in our experimental flow, this calculation further reinforces the fact that the classic surface renewal model cannot be successfully applied to this system.

4.7.2 Similarity Between Mass and Momentum Flux

Drawing on our results from this chapter as well as our results from Chapter 3, we can examine the relationship between the measured values of momentum flux (drag force) and the measured values of mass flux to the model blades as a function of the blade flexural rigidity. In §3.4.2, we reported the measurements of the drag force on the $h = 50$ μm and $h = 250$ μm model blades. The ratio of the drag force, or momentum flux, for these blades was $F_{D,h=50\mu m}/F_{D,h=250\mu m} = 1.8$. The ratio of the mass transfer velocities to these blades, as reported above in §4.7.1, was between $K_{h=50\mu m}/K_{h=250\mu m} = 2.6$ (using $D_{PE} = 10^{-10.3}$ m^2/s) and $K_{h=50\mu m}/K_{h=250\mu m} = 1.4$ (using $D_{PE} = 10^{-12.3}$ m^2/s), with a value of $K_{h=50\mu m}/K_{h=250\mu m} = 2.3$ (using the mean regression value of $D_{PE} = 10^{-11.3}$ m^2/s). Within the uncertainty of the calculated ratio of mass transfer velocities, the ratios of mass flux and momentum flux for the

two model blades are in agreement.

For a flat plate oriented parallel to the mean flow direction, we expect that the mass flux and momentum flux to the plate should scale similarly. This concept is called the Reynold's Analogy for heat and momentum flux [85, 22, 110]. The Reynold's Analogy is specifically valid in cases where there is no form (pressure) drag, and momentum flux is entirely due to friction. In our experiments, not only is form drag present due to the large-amplitude oscillations which present a frontal area normal to the flow, but inertial forces also contribute to the total measured force on the model blades. The Reynolds Analogy has not been extended to cases where there is form drag or inertial forces, and there is currently no theoretical support for the similarity between scalar and momentum flux extending to this regime, either. Our results, however, certainly provoke the possibility that there exists a similarity between scalar and momentum flux for a flexible body moving in flow.

As we have shown above, the relative velocity at the model blade surface changes with blade flexural rigidity. This change in the relative fluid velocity is responsible both for the change in the drag force and the change in the mass flux to the blade surface. If, in future research, it can be shown that the change in relative velocity at the blade surface affects mass flux and the fluid force in the same manner, then it may be possible to experimentally demonstrate an analogy between momentum and mass flux for flexible bodies in flow.

4.7.3 Predicting Transfer Velocities in the Field

We have demonstrated that we can successfully predict the scalar flux using the modeled surface normal relative velocity at the oscillating blade. We have further shown that two simple models, the steady diffusive sublayer model and the surface renewal model cannot account for the changes in flux caused by changes in flexural rigidity. Accurately modeling the fluid-structure dynamics for dynamic flexible blades and other structures in flow is often analytically intractable, however, and in many instances, a simple flux model based on empirical relationships and flow observations is desirable. In this section we develop a simple model that can be applied to blades

in the field.

We can approximate the blade normal velocity using the blade oscillation amplitude and the oscillation frequency. By fitting the scaling prediction derived in §3.4.2 to the observed oscillation amplitude (Fig. 3-13) we derived an empirical expression for amplitude at the blade tip.

$$\Delta z_{rms} = \frac{l\eta^{-1/3}}{258} \tag{4.21}$$

Combining the above equation with the frequency of oscillation gives an approximate average blade normal velocity: $w_{blade} = (4l/2)\eta^{-1/3}f/258$. The relative normal velocity at the blade surface is a combination of the blade normal velocity and the normal component of the fluid velocity. These two factors do not sum linearly, however, because of the potential for a phase difference between the blade and fluid motion. We have shown that as the blade amplitude increases and the normal component of the flow remains constant, the relative normal velocity at the blade surface increases (Figs. 3-13 & 4-6). Therefore, to simply model the relative normal velocity at the blade surface, we sum the blade normal velocity and the normal component of the flow in quadrature:

$$w_{rel,rms} = \sqrt{w_{blade}^2 + w_{flow}^2} \tag{4.22}$$

where w_{blade} and w_{flow} can come either from observations or empirical models. For our system, using the empirical expression for blade amplitude given above, and using the obesrved normal component of the vortex street ($\approx 0.4U_\infty$; see Fig. 4-6), we can write the model for $w_{rel,rms}$ in the following form:

$$w_{rel,rms} = \sqrt{\left(\frac{2l/\eta^{-1/3}f}{258}\right)^2 + (0.4U_\infty)^2} \tag{4.23}$$

This approximation for $w_{rel,rms}$ is only an approximation as we are unable to model the complex relationship between blade and fluid motion.

We can then use this velocity to form a transfer velocity at the blade surface using

Eq. 4.18. This simple formulation gives transfer velocities of $K_{h=50\mu m} = 4.9E-6$ m/s and $K_{h=250\mu m} = 3.8E-6$ and a transfer velocity ratio of $K_{h=50\mu m}/K_{h=250\mu m} = 1.3$. In §4.7.1 we showed that using the modeled relative velocity at the blade surface produced $K_{h=50\mu m}/K_{h=250\mu m} = 1.06$, while the experiments showed that $K_{h=50\mu m}/K_{h=250\mu m} = 2.3$ (using $D_{PE} = 10^{-11.3}$ m^2/s) and that $K_{h=50\mu m}/K_{h=250\mu m} = 1.4$ (using $D_{PE} = 10^{-12.3}$ m^2/s). Therefore, the simple model presented above gives a flux prediction that is close to both the prediction using the fully-modeled relative normal velocity at the blade surface and to the experimental results.

4.7.4 Cut blade sections discussion

The transfer velocities measured at the cut sections from the clamped and free ends of the blades do not agree with the predictions from the model (Tables 4.5 & 4.6 and Figs. 4-11 & 4-12). These results, however, are also inconsistent with the measured values of flux for the full blade experiments (Tables 4.3 & 4.4 and Figs. 4-9 & 4-10). The cut section portion of the experiments was designed to compare the transfer velocities from the portions of the blade with the most disparate relative normal velocities (Fig. 4-6). Specifically, we expect the transfer velocity at the free end of the blade to be higher than the average transfer velocity of the full blade, and we expect the transfer velocity at the clamped end of the blade to be less than the average transfer velocity of the full blade (Fig. 4-7). What we find is that the measured transfer velocities at both the clamped and free ends are much lower than the average transfer velocities for the full blades. This repeated trend in the results suggests that there is a flaw in the experimental method, rather than a random human or instrument error.

The only difference in the experimental method between the full blade experiments and the cut sections experiments that could result in this consistent bias is the time spent measuring and cutting the blades once they are removed from the flume (§4.3.2 & §4.3.3). The full blades are removed from the flume, rapidly dried and placed directly in the clean vials which are then filled with clean water. The entire process for the full blades lasts less than 20 s. The cut sections are removed from the flume, rapidly dried, then placed on a sheet of aluminum foil where the 2.5 cm sections at

either end are carefully measured and cut. After they are cut they are placed in the clean vials which are then filled with water. The extra steps of measuring and cutting the 2.5 cm sections adds between one and two minutes to the process during which the blades are exposed to the air. A possible explanation for the discrepancy in the experimental data is that mass of $CHBr_2CL$ is lost to the atmosphere in the lab. The loss of mass from the blade sections during the processing of the sections would cause the measured transfer velocity to be artificially low and could explain the inconsistency in the results.

4.7.5 Mass Loss from Blades

We modeled the loss of mass from the model blades to the atmosphere using an extension of the finite difference model described in §4.5. In this extended version of the model, we first model the accumulation of $CHBr_2CL$ into the blade, as described previously. We then model the loss of $CHBr_2CL$ to the surrounding air to account for the time between removal of the blades from the flume, and sealing the blades in the 40 mL amber vials. To model the loss to the atmosphere, we solve the 1-D, vertical diffusion equation inside the LDPE blade, with a no-flux boundary condition at the blade centerline ($z = 0$), and a diffusive boundary layer (air-side boundary layer) flux condition at the blade surface ($z = h/2$). The governing equation and these boundary conditions are written as follows:

$$\frac{\partial C_{PE}}{\partial t} = D_{PE}\frac{\partial^2 C_{PE}}{\partial z^2} \tag{4.24}$$

$$\left.\frac{\partial C_{PE}}{\partial z}\right|_{z=0} = 0 \tag{4.25}$$

$$D_{PE}\left.\frac{\partial C_{PE}}{\partial z}\right|_{z=h/2} = D_A\frac{C_{PE}}{K_H K_{PEW}\delta_A}. \tag{4.26}$$

In Eq. 4.26, the product of the Henry's Law constant, K_H, and the PE-water partitioning coefficient, K_{PEW}, is the PE-air partitioning coefficient. We select an air-side

diffusive boundary layer thickness of $\delta_A = 50E - 6$ m. This choice of the air-side boundary layer thickness is arbitrary and the results are completely insignificant to air-side diffusive boundary layer thicknesses of any size less than a few millimeters in thickness (which is unreasonably large). Loss to the atmosphere is not significantly affected by the size of this layer thickness, however, because mass transfer is limited by diffusion through the PE, rather than transport across the air-side diffusive boundary layer. This fact is exemplified by the system's Biot number [22], which is larger than 1E4 for this case, indicating that resistance in the polyethylene dominates the system. We non-dimensionalize Eqs. 4.24-4.26 with the same scales used previously, giving

$$\frac{\partial \hat{C}_{PE}}{\partial \tau} = \frac{\partial^2 \hat{C}_{PE}}{\partial \hat{z}^2} \tag{4.27}$$

$$\left.\frac{\partial \hat{C}_{PE}}{\partial \hat{z}}\right|_{\hat{z}=0} = 0 \tag{4.28}$$

$$\left.\frac{\partial \hat{C}_{PE}}{\partial \hat{z}}\right|_{\hat{z}=1} = \frac{hD_A \hat{C}_{PE,\hat{z}=1}}{2D_{PE}K_H K_{PEW}\delta_A}. \tag{4.29}$$

For each experimental time point listed in Table 4.1, we model loss to the atmosphere for durations of 10, 20, 60 and 120 s. We also model loss to the atmosphere for $D_{PE} = 1E - 11.3$ m^2/s as well as for the bounds of the 95% C.I. on D_{PE}. These results are reported in Tables 4.10 - 4.15. Across the three diffusion coefficients and the two blade thicknesses that we modeled mass loss from, the blades with the shortest time (e.g. 15 or 60 s) in the flume lose the most relative mass, while the blades with the longest time in the flume (e.g. 600 or 1200 s) lose the least relative mass. As expected, the model blades lose more mass the longer they are exposed to the laboratory air. Using the model predictions with $D_{PE} = 1E - 11.3$ m^2/s as an example (Tables 4.12 & 4.13), the model predicts that the $h = 50$ μm blade that spends 15 s in the flume loses 60% of the mass of $CHBr_2CL$ after 10 s in the air, while the same blade that spends 600 s in the flume loses about 30% of the mass of

Table 4.10: The model predictions of the fractional mass of $CHBr_2CL$ remaining in the $h = 50E - 6$ m PE model blade after exposure to the laboratory air for times of 10, 20, 60 and 120 s, using $D_{PE} = 1E - 10.3$ m^2/s.

	Atmosphere Exposure Times (s)			
Exp. times (s)	10	20	60	120
15	0.10	0.01	0	0
30	0.11	0.02	0	0
60	0.11	0.02	0	0
120	0.11	0.02	0	0
180	0.11	0.02	0	0
300	0.12	0.02	0	0
600	0.12	0.02	0	0

$CHBr_2CL$ after 10 s in the air. The thicker blade, $h = 250$ μm, loses 40% of its mass at the $t = 60$ s time point after 10 s in the air, while only losing 10% of its mass at the $t = 1200$ s time point after 10 s in the air.

For the cut blade experiments, the blades can be exposed to the laboratory air for up to 120 s, and can lose a significant amount of mass of $CHBr_2CL$. This loss to the ambient can partially explain the large discrepancy between the cut blade experiments and the full blade experiments. Again using $D_{PE} = 1E - 11.3$ m^2/s as an example, between the experimental time points of $t = 15$ s and $t = 600$ s, the $h = 50$ μm blade loses between 96% and 93% of the mass of $CHBr_2CL$, respectively, when exposed to the laboratory air for 120 s. The $h = 250$ μm blade loses 73% and 32% of the mass of $CHBr_2CL$, respectively, when exposed to the laboratory air for the same durations. The experimental measurements show that the cut blade sections have only 28% to 44% of the mass that the full blades do at the same experimental time points. The only difference between the cut blade experiments and the full blade experiments is the duration of exposure to the laboratory air. Although we cannot pinpoint the exact time of exposure of the blades to the ambient air, the model predictions of mass loss to the ambient over a range of exposure times are consistent with the observations of mass loss to the cut blade sections.

Notably, this portion of the experiments, and the subsequent modeling of mass

Table 4.11: The model predictions of the fractional mass of $CHBr_2CL$ remaining in the $h = 250E-6$ m PE model blade after exposure to the laboratory air for times of 10, 20, 60 and 120 s, using $D_{PE} = 1E-10.3$ m^2/s.

	Atmosphere Exposure Times (s)			
Exp. times (s)	10	20	60	120
60	0.61	0.51	0.34	0.21
120	0.69	0.60	0.41	0.25
180	0.72	0.64	0.44	0.27
300	0.75	0.67	0.47	0.29
600	0.77	0.69	0.48	0.30
900	0.78	0.70	0.49	0.30
1200	0.78	0.70	0.49	0.31

Table 4.12: The model predictions of the fractional mass of $CHBr_2CL$ remaining in the $h = 50E-6$ m PE model blade after exposure to the laboratory air for times of 10, 20, 60 and 120 s, using $D_{PE} = 1E-11.3$ m^2/s.

	Atmosphere Exposure Times (s)			
Exp. times (s)	10	20	60	120
15	0.41	0.31	0.14	0.04
30	0.51	0.40	0.18	0.05
60	0.59	0.46	0.21	0.06
120	0.63	0.50	0.23	0.07
180	0.65	0.52	0.23	0.07
300	0.66	0.53	0.24	0.07
600	0.67	0.54	0.24	0.07

Table 4.13: The model predictions of the fractional mass of $CHBr_2CL$ remaining in the $h = 250E-6$ m PE model blade after exposure to the laboratory air for times of 10, 20, 60 and 120 s, using $D_{PE} = 1E-11.3$ m^2/s.

	Atmosphere Exposure Times (s)			
Exp. times (s)	10	20	60	120
60	0.60	0.50	0.35	0.27
120	0.69	0.61	0.45	0.36
180	0.74	0.66	0.52	0.42
300	0.79	0.72	0.59	0.49
600	0.85	0.80	0.68	0.60
900	0.87	0.83	0.73	0.65
1200	0.89	0.85	0.76	0.68

Table 4.14: The model predictions of the fractional mass of $CHBr_2CL$ remaining in the $h = 50E - 6$ m PE model blade after exposure to the laboratory air for times of 10, 20, 60 and 120 s, using $D_{PE} = 1E - 12.3$ m^2/s.

	Atmosphere Exposure Times (s)			
Exp. times (s)	10	20	60	120
15	0.40	0.31	0.19	0.14
30	0.50	0.41	0.27	0.20
60	0.61	0.51	0.36	0.27
120	0.70	0.61	0.46	0.36
180	0.74	0.67	0.52	0.42
300	0.79	0.73	0.59	0.49
600	0.84	0.80	0.67	0.57

Table 4.15: The model predictions of the fractional mass of $CHBr_2CL$ remaining in the $h = 250E - 6$ m PE model blade after exposure to the laboratory air for times of 10, 20, 60 and 120 s, using $D_{PE} = 1E - 12.3$ m^2/s.

	Atmosphere Exposure Times (s)			
Exp. times (s)	10	20	60	120
60	0.55	0.46	0.32	0.25
120	0.65	0.57	0.43	0.34
180	0.71	0.64	0.50	0.40
300	0.77	0.70	0.58	0.49
600	0.83	0.78	0.68	0.59
900	0.86	0.82	0.73	0.65
1200	0.88	0.84	0.76	0.69

loss to the ambient, revealed an important flaw in the experimental design: the time between removal of the blades from the flume and insertion into the vials must be minimized. The laboratory atmosphere acts as a perfect sink and it is possible for a portion of the accumulated mass in the polyethylene to be lost, artificially reducing the measured transfer velocity. A possible technique to address this flaw in the experiments is to have two people conduct each experiment. Processing time could be saved with one person holding the blade in place with tweezers while the second person makes the cuts, eliminating the difficulty of one person holding a flexible blade in place along a meter stick while making precise cuts along its length. Cutting the blades into precise sections will increase the processing time, regardless, and more sophisticated modeling of the mass lost to the atmosphere may be necessary.

Ultimately, modeling the mass loss from the blades during the processing of the model blades can provide important insight into the experimental method and can also influence how the experimental data is fitted to calculate the experimental transfer velocities. From Tables 4.10 - 4.15, it's clear that the $h = 50$ μm blade loses more relative mass than the $h = 250$ μm blade over the same time period. Also, regardless of blade thickness, more relative mass is lost for the shorter time durations. Controlled experiments investigating the phenomenon of mass loss to the atmosphere during processing are needed to confirm this model. With model confirmation, mass loss adjustment factors could be applied to each experimental time point before fitting a transfer velocity to the data. We note however that the elevated loss of mass from the $h = 50$ μm blade over the loss of mass from the $h = 250$ μm blade does not affect our overall conclusion that the more flexible blade accumulates more mass than the more rigid blade. In fact, the mass loss modeling results suggest that the ratio of transfer velocities between the $h = 50$ μm and $h = 250$ μm blades could be higher than calculated above.

4.7.6 Experimental method discussion

In this chapter we have developed an experimental method that extends the technology of passive polymer samplers and which can be used to measure rates of flux

between the sampler and the surrounding medium. The method can be used to derive information about the physical interactions between the sampler and the surrounding fluid. Specifically, from measuring the rate of flux, and knowing a priori the target compound's concentration in the fluid and its diffusion coefficient in the sampler and in the fluid, we can gather information about the fluid velocity at the fluid-solid interface and the boundary layer dynamics.

When used in this manner, this passive sampling method can be used as an analog for nutrient and gas transfer in aquatic vegetation. Previous methods have modeled scalar transfer between aquatic vegetation and flow using rigid structures such as copper [24] and gypsum [65], and have therefore been unable to test the effects of the plant's flexural rigidity on flux (copper and gypsum in flow are effectively in the limit of a perfectly rigid body, $\eta \gg 1$). Many of the most abundant types of aquatic vegetation are highly flexible, however, particularly seagrasses and macroalgae, and the plants' flexural rigidity can modify the fluid motion near the vegetation surface, affecting rates of flux. In these experiments, we carefully measure and control the flexural rigidity of the sampler, treating this structural property as an independent variable and measure the resulting transfer velocity. Indeed, in the set of experiments presented in this chapter, we have not only demonstrated the efficacy of this experimental method, we also show that the flexural rigidity of the structure can change the rate of flux from the surrounding fluid.

Importantly, by demonstrating the capabilities of this experimental method, we have opened the door to several new areas of investigation, with application not only to aquatic vegetation but to our understanding of the fundamentals of scalar transfer in different flow regimes. By directly extending the methods discussed in this chapter, one can investigate the role of flexural rigidity on scalar transfer in unidirectional flow, grid-generated turbulence and waves, and on scalar transfer to mechanically actuated model blades. Extensions of this work can help us understand the meaning behind the specific geometries and structural properties of different species of aquatic vegetation, and how these morphological parameters relate to the local flow environment.

Chapter 5

Kelp Blade Morphologies: Implications for Drag Force and Nutrient Flux

Using the experimental and theoretical results of the previous two chapters, in this chapter we ask how documented changes in blade morphology that impact blade stiffness may affect drag and nutrient flux to real kelp blades. In §5.1, we discuss the typical morphology of many kelp blades and discuss some of the mechanisms by which morphology can change. We also highlight specific measurements of *Macrocystis* blade morphology. In §5.2, we examine how changes in blade morphology can affect blade drag force and nutrient flux at the blade surface. In §5.3, we discuss an interesting set of observations of kelp blade morphology from within a single kelp forest. Finally, in §5.4, we take relative velocity estimates from the literature and construct a mass transfer velocity for kelp which we compare with other published values. Portions of §5.1 and §5.2 are included with the experimental results of Chapters 3 & 4 in the paper to be submitted to *Limnology & Oceanography.*

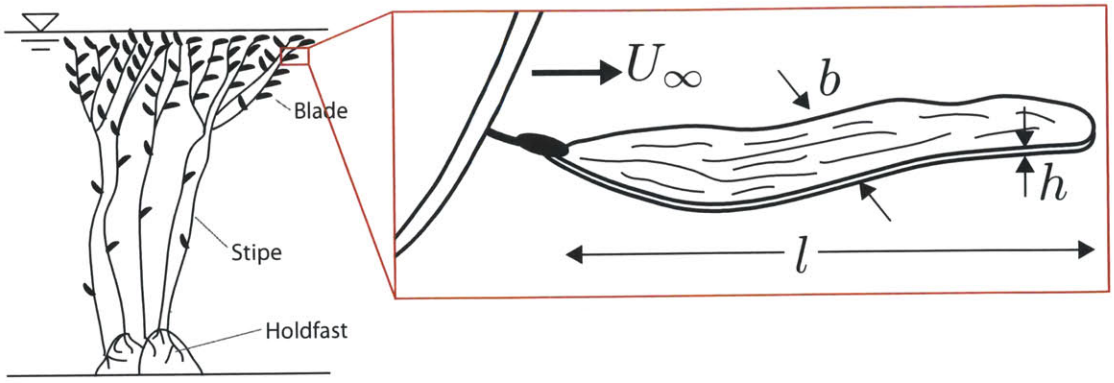

Figure 5-1: A schematic of a typical *Macrocystis* frond, which is composed of holdfasts (akin to roots on terrestrial plants, but are purely structural), the stipe, and branching off of the stipe are the blades. The closeup of the blade shows the separation of geometric length scales, with $h \ll b \ll l$.

5.1 Blade Morphology and Plasticity

Kelp blades are elongated, flexible bodies, that deform and oscillate in response to the flow. Often, this elongation results in a clear separation of length scales between the thickness, width and blade length (Fig. 5-1). Blades of *Macrocystis pyrifera* are an ideal example of this elongated morphology: typically the blade thickness, h, is less than 1 mm, the blade width, b, is approximately 9-10 cm, and the blade length, l, is near 50 cm. Species of *Nereocystis* and *Laminaria* are very similar in morphology, although the overall blade length is longer than for *Macrocystis*.

Just as other species adapt to environmental stimuli, kelp, and specifically the morphology of kelp blades, can adapt to its environment. The first mechanism by which kelp blade morphology can adapt to its environment is the process of evolution by natural selection. In this process, specific morphological traits that confer some advantage to the kelp are selected for and passed on to future generations, gradually causing a change in the blade morphology that is better suited to the coastal ocean environment. The time-scale of morphological change by evolution is generally long, between millenia and eons. Moreover, the process of evolution does not give rise to the rapid morphological changes that can appear in kelp on the order of a single growing season.

The mechanism by which kelp can rapidly adapt its morphology to the local environment is phenotypic plasticity. Phenotypic plasticity is the process through which the manifested traits of an organism adapt to changes in environmental stimuli, such as changes in light or nutrient availability, changes in mechanical stresses, changes in climate and so forth. Phenotypic plasticity in kelp blades means that the length, width and thickness of the blades, as well as the overall characteristics of the shape (e.g. rectangular, tapered, undulatory, etc.) can change over the timescale of the kelp life cycle in response to its environment [26, 57].

For kelp, one of the most important environmental stimuli is fluid drag, and the resulting mechanical stresses and strains it causes in kelp blades. In the coastal ocean, kelp blades can be exposed to strong currents and waves which can break kelp blades or dislodge entire fronds from the substrate. For this reason, documented observations of kelp blade morphology are traditionally grouped into two categories: "exposed" and "sheltered," which describe the blades' general exposure to rapid flow and the concomitant high drag forces from waves and currents, and to slow flow and reduced drag forces, respectively [57].

Early observations of morphological differences in kelp blades come from [35], who observed stark differences in blade thickness between flow-exposed and flow-sheltered sites in *Laminaria longicruris*. The thickness of the flow-exposed blades was more than three times larger than the thickness of the flow-sheltered blades. The same trend of thicker blades at exposed sites has further been documented in the following macroalgae genera: *Agarum* [27], *Durvillaea* [18], *Ecklonia* [111], *Eisenia* [87], *Gigartina* [51], *Laminaria* [27, 101, 95, 77], *Macrocystis* [49] and *Pachydictyon* [44]. Moreover, the same behavior has been observed in seagrass blades of various species [78].

Changes in blade thickness can have significant effects on the mechanical properties of the blade. The blade stiffness in tension is directly proportional to the blade elastic modulus and blade cross-sectional area: Ebh. Increasing the stiffness in tension reduces blade extension under a tensile load, such as a drag force, potentially preventing excessive strains and breakage. Increases in blade thickness, however, have

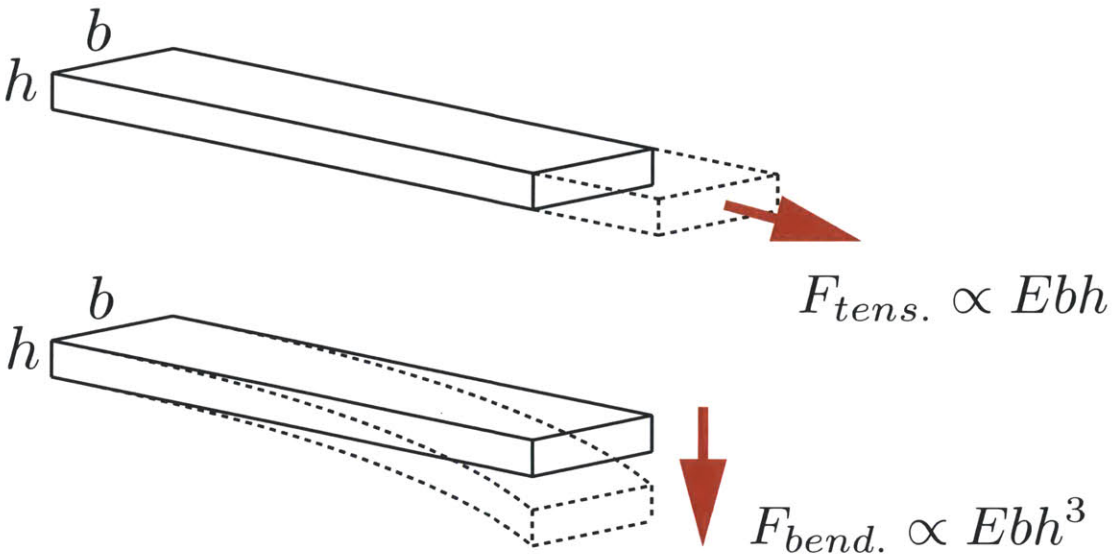

Figure 5-2: A simple schematic of the effects blade morphology has on a blade's resistance to tensile and bending forces. The Young's, or elastic, modulus, E, is a property of a material describing its stiffness.

a more pronounced effect on the blade bending rigidity. For a blade with a nominally rectangular cross section, the bending rigidity is the product of the elastic modulus of the material and the second moment of area. The second moment of area, or bending moment of inertia, is a function of the blade width times the cube of the blade thickness. This gives a bending rigidity, $B = EI = Ebh^3/12$. By comparing the effects of thickness on stiffness in tension and stiffness under bending, we see that changes in thickness have a more pronounced effect on the structure's resistance to bending (Fig. 5-2).

An interesting case study on phenotypic plasticity in kelp blades comes from *Macrocystis*, commonly known as Giant Kelp. The blades of *Macrocystis* not only have an increased thickness at exposed sites, but they also exhibit longitudinal corrugations (Fig. 5-4). At flow sheltered sites, studies have found that these corrugations are either entirely absent [50] or greatly reduced in amplitude [49]. These corrugations are very regular in amplitude and wavelength, and generally extend almost the full blade length (Fig. 5-3).

Longitudinal corrugations in blades are an efficient way to increase blade bending

rigidity. The bending rigidity for a corrugated sheet, which can effectively model a *Macrocystis* blade, was calculated by Lau [61] as

$$EI = E\frac{a^2hb}{2}\left(1 + \frac{\pi^2 a^2}{8(\lambda/2)^2}\right) \tag{5.1}$$

in which a is the corrugation amplitude and λ is the corrugation wavelength (Fig. 5-5). This equation reveals that for a thin blade, in which thickness is small compared with corrugation amplitude ($h \ll a$), the bending rigidity scales with the amplitude squared, times the thickness. *Macrocystis* blades generally satisfy this requirement that the blade thickness is small compared to the corrugation amplitude. Importantly, corrugations present a method of increasing bending rigidity by simply changing shape, rather than adding material in order to increase blade thickness. This change of blade shape has important effects for scalar transfer at the blade surface. All of the nutrient transfer happens at the blade surface, and by increasing bending rigidity with corrugations, blades maintain a high surface area to volume ratio. Increasing bending rigidity through increasing thickness decreases the surface area to volume ratio, increasing the nutrient requirements for the plant, while decreasing nutrient acquisition surface area. Furthermore, there is an energy cost for adding more blade material to increase blade thickness, whereas forming corrugations is simply a reorganization of existing blade material.

Hurd and Pilditch [50] provided a complete set of morphological observations (Table 5.1) that we can use to calculate the dimensionless blade flexural rigidity, η (Eq. 3.12), of real *Macrocystis* blades. Recall that η is a ratio of structural to fluid forces, and for kelp is thus a function of both morphological parameters as well as parameters of the fluid environment. At flow-sheltered sites, Hurd and Pilditch report that the characteristic velocity is less than 6 cm/s [59, 50]. At flow-exposed sites, Hurd and Pilditch do not provide a velocity value. We note that at flow-exposed sites, the combination of wave orbital velocities and tidal currents makes it difficult to determine whether the mean, rms or the maximum velocity during storms is relevant to the kelp. For the purposes of this case study, we select a flow-exposed velocity

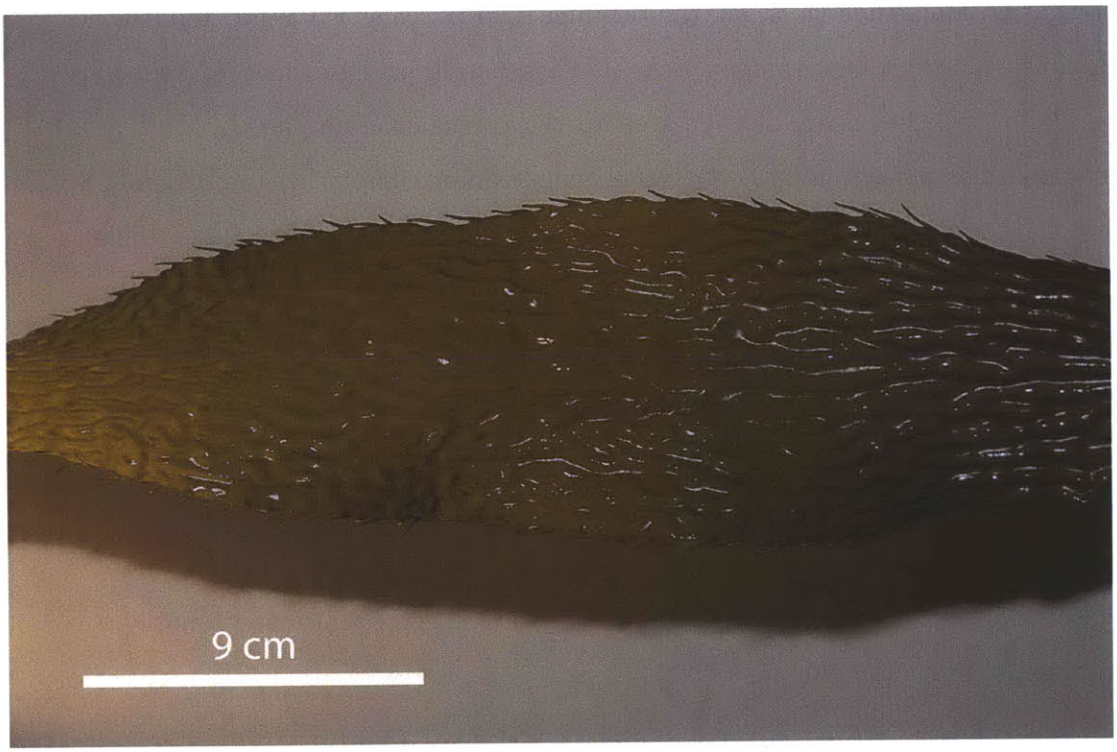

Figure 5-3: A photo of a *Macrocystis* blade, showing the longitudinal corrugations running the full length of the blade.

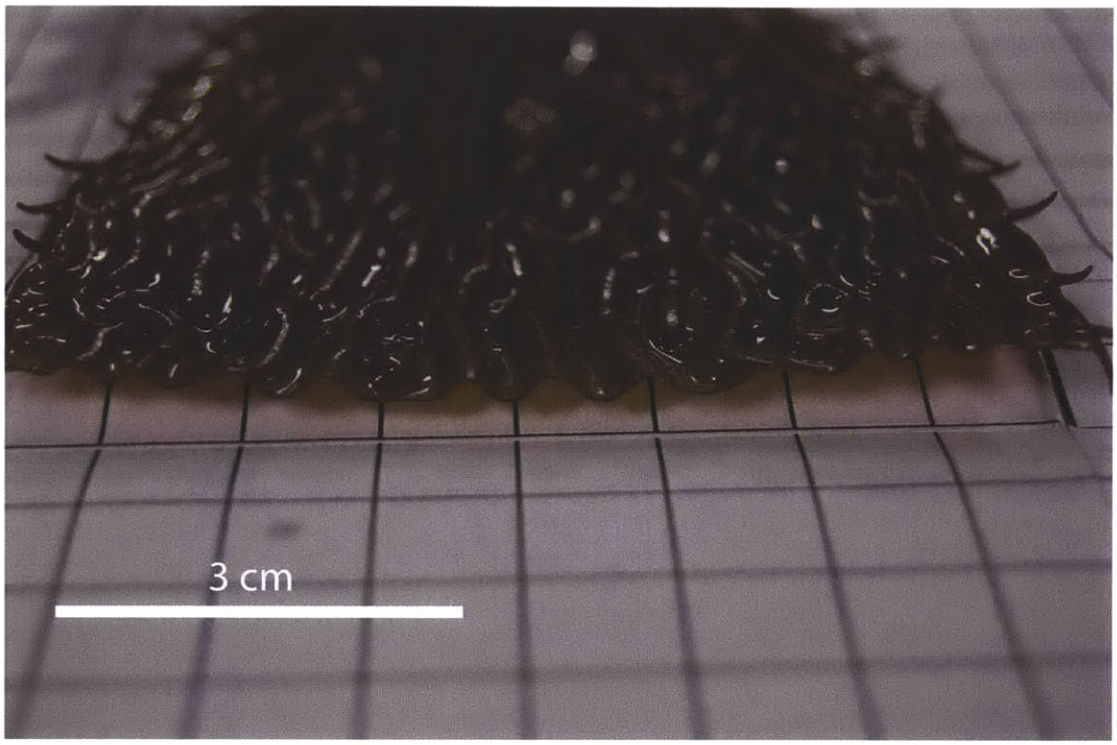

Figure 5-4: A cut section of a *Macrocystis* blade, showing the corrugation structure. The cut-away shows the regularity of the corrugation wavelength and amplitude.

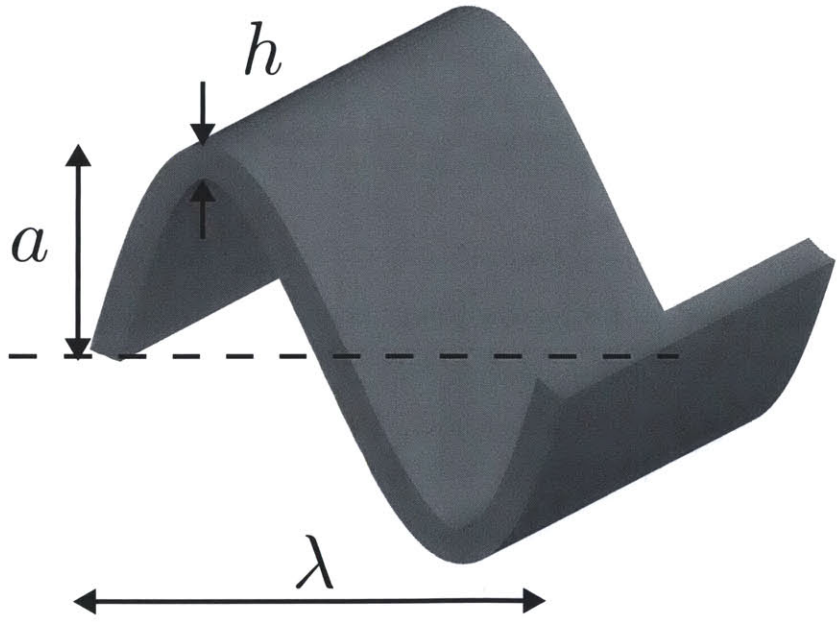

Figure 5-5: A drawing of a single corrugation and its length scales. The corrugation has amplitude a and wavelength λ. The blade thickness, h, remains constant over the corrugations.

Table 5.1: A summary of *Macrocystis* blade morphology observations from Hurd and Pilditch [50] documenting the measurements of blades from flow-exposed and flow-sheltered sites. The blades at the flow-sheltered sites had no corrugations. The elastic modulus of algal material was reported by Hal [43].

	Exposed Morphology	Sheltered Morphology
blade thickness, h (mm)	0.470	0.425
elastic modulus, E (Pa)	5E6	5E6
blade length, l (m)	0.62	0.52
corrugation amplitude, a (mm)	1.37	-
corrugation wavelength, λ (mm)	3.08	-
bending rigidity, EI, formula	$E\frac{a^2hb}{2}\left(1+\frac{\pi^2a^2}{8(\lambda/2)^2}\right)$	$Ebh^3/12$
bending rigidity/width, EI/b (Pa m^3)	4.4E-3	3.2E-5

value of 0.50 m/s, but with an uncertainty of +0.45 m/s to account for possible high velocity events [27]. For the flow-sheltered site, we use a velocity of 0.05 m/s with negligible uncertainty, consistent with the observations from [50]. The fluid density is set at $\rho_f = 1030$ kg/m^3.

In Table 5.2, we calculate the values of η for the exposed morphology at the exposed flow velocity, as well as for the sheltered morphology at the sheltered flow velocity. For the sheltered morphology, the flexural rigidity, $EI = Ebh^3/12$, while for the exposed morphology, we calculate EI using Eq. 5.1. For comparison purposes, we also calculate the value of η for the sheltered morphology at the exposed flow velocity. This calculation allows us to understand how a blade with the sheltered morphology would respond in the flow-exposed velocities. We also calculate the values of η at the flow-exposed velocity of 0.95 m/s to account for possibility of high velocity events at these sites. In the next section we consider what these values of η indicate about drag and nutrient flux.

Table 5.2: Calculations of the dimensionless blade flexural rigidity, η, based on the observations of [50] summarized in Table 5.1. The exposed morphology value of η is calculated using Eq. 5.1.

	Exposed Morphology	Sheltered Morphology
Exposed $U_\infty = 0.50$ m/s	7.1E-5	8.8E-7
$U_\infty = 0.95$ m/s	2.0E-5	2.5E-7
Sheltered $U_\infty = 0.05$ m/s	-	8.8E-5

5.2 Benefits for Kelp from Morphological Plasticity

5.2.1 Drag Force Benefits

As we have demonstrated in Chap. 3, the drag force on a model kelp blade is a strong function of the blade flexural rigidity. Specifically, for blades in a vortex street (an ideal form of turbulence), as blade flexural rigidity decreases, the blade responds to turbulence in the flow with oscillations of increasing amplitude (Fig. 3-13). Below a critical value of the blade flexural rigidity, inertial forces on the blade become an important component of the total force on the blade, and the resulting total force increases more sharply with decreasing η (Fig. 3-14). The experimental results show that the critical value of η below which inertial forces become important is near $\eta = 1E-4$ (Fig. 3-14). If a sheltered morphology blade is transplanted into an exposed flow site, we have calculated that $\eta = 8.8E-7$, which is far below the critical value of η. Therefore, the sheltered morphology would result in high forces at the exposed flow velocities. The exposed morphology results in a significantly higher value of η at the flow-exposed velocities ($\eta = 7.1E-5$), which we have calculated to be approximately two orders of magnitude larger than the sheltered morphology at the exposed flow velocity, an adaptation that should reduce the total force on the blade (Table 5.2 and Fig. 5-6). Interestingly, the values of η for both the exposed and sheltered morphologies, at their respective flow velocities are nearly identical in magnitude, suggesting that there may be an optimal ratio of blade stiffness to

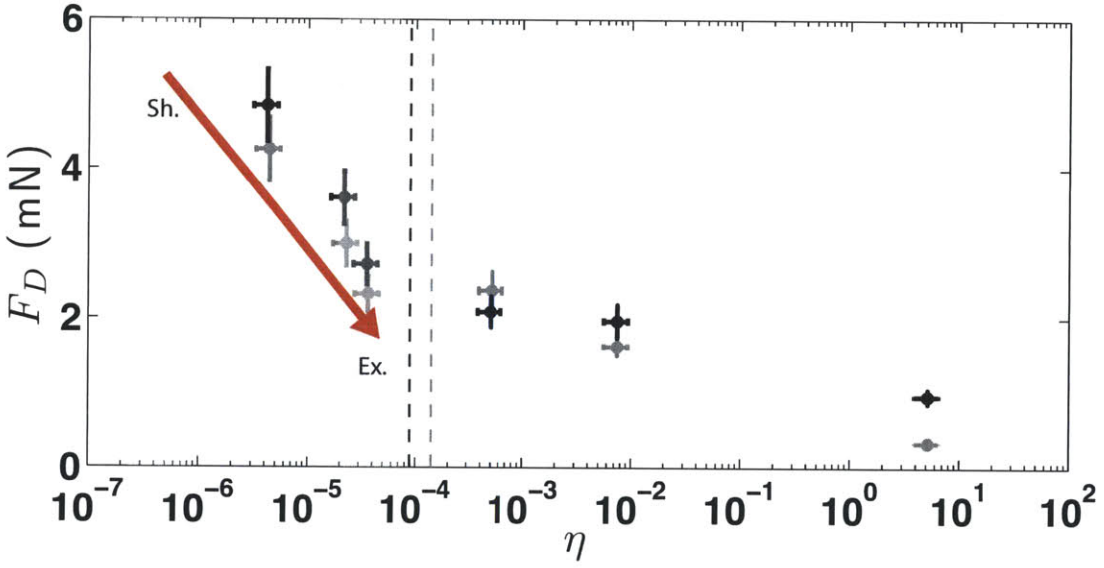

Figure 5-6: The measured drag force in the vortex street (from Fig. 3-14), plotted on an expanded axis to show the potential reduction in drag caused by the shift from the sheltered morphology to the exposed morphology. The drag data for $D = 2.5$ cm ($l/D = 12$) is plotted with the gray symbols and lines, and the data for $D = 5.0$ cm ($l/D = 6$) is plotted with the black symbols and lines. The vertical lines indicate the calculated values of η_c (§3.4.3). The red arrow points from the value of η of the sheltered morphology at the exposed flow speed (Sh.) to the value of η for the exposed morphology at the exposed flow speed (Ex.) (η values from Table 5.2 indicated with the vertical gray bars). As we can see from our experiments in Chap. 3, the increase in blade flexural rigidity at the flow-exposed site prevents an increase in the drag force due to enhanced flapping and inertial forces in response to turbulence.

fluid forcing, towards which the kelp morphology adjusts. While lower values of η may indicate that blades have insufficient rigidity to survive the mechanical stresses caused by high flow velocities, higher values of η could indicate unnecessary and biologically-expensive structural strengthening.

With the presence of unsteady currents and waves, there is a wide spectrum of turbulent fluctuations in the coastal ocean. In a vortex street, which is a periodic form of turbulence narrowly centered around a single frequency and wavelength, blade flexural rigidity strongly controls the forces, both pressure drag and inertial forces, on the blade. We do not, however, believe that the introduction of inertial forces to the system is unique to the vortex street system. Our experiments in the vortex street indicate that the blade responds to each passing vortex. Therefore, we anticipate that even in the presence of a single passing vortex, blades with low values of flexural rigidity would be subjected to inertial forces. Plew and coauthors found that seagrass blades responded most strongly to turbulent fluctuations that were near in scale to the blade length, supporting this idea that our experimental conclusions could be seen in the field [79]. By extension, it's possible that this same behavior could be observed for blades subjected to wave orbital velocities. This idea needs further experimentation before we can conclusively state how kelp blades respond to the wide range of flow conditions in the coastal ocean.

5.2.2 Flapping Flag Instability

A second morphological consideration for kelp blades is the flapping flag instability. The flapping flag instability is a phenomenon that happens to blades in uniform flow, i.e. a steady, mean current lacking large scale turbulent structures. This phenomenon is distinct from the phenomenon of forced oscillations in a vortex street. Specifically, the flapping flag instability describes the point at which a streamlined flag (or blade) in uniform flow becomes unstable and begins to undergo large, self-excited oscillations [107, 115, 94, 6, 20, 71, 3]. The transition from the streamlined state to the oscillatory state results in a step change in the total force on the flag of more than one order of magnitude [103, 72]. Blades that are streamlined with the flow experience primarily

frictional drag. Blades undergoing oscillations in uniform flow experience significantly higher drag due to pressure and inertial forces.

The dynamics of this system and the location of the transition between the two states have been extensively studied. We briefly summarize the methods and results of these studies here. A flexible flag in uniform flow can be defined using Eq. 3.10, reprinted here:

$$\mu \frac{\partial^2}{\partial \tau^2} \hat{\zeta} = -\eta \frac{\partial}{\partial \hat{s}} \left[\theta_{\hat{s}\hat{s}} \boldsymbol{n} \right] + \frac{\partial}{\partial \hat{s}} \left[T \boldsymbol{t} \right] + F \tag{5.2}$$

Different studies have described the fluid forcing, F, in different forms, ranging from a pseudo-steady pressure and frictional drag formulation [107], to an incompressible, irrotational potential flow formulation which is the sum of a non-circulatory flow and circulatory flow due to vortex shedding from the flag trailing edge [6], to a vortex sheet formulation [71, 3], to a fully-coupled solution of the flag dynamics with the Navier-Stokes equation [20]. Despite the differing fluid formulations, the results of each of these studies reveal the same physical phenomenon: below a specific threshold, the stable, streamlined state of a flexible flag in uniform flow becomes unstable to flapping, and large-amplitude oscillatory motions are initiated.

The location of the stability boundary, as a function of the two main system parameters, μ and η, can be found with two methods. In the first method, a linear stability analysis, the flag dynamics are linearized around the stable, streamlined state and therefore assumed to be of small amplitude [20, 94, 6]. The flag posture is then written in the form of a traveling wave perturbation, e.g.

$$\hat{\zeta}(s, \tau) = A e^{i(ks - \omega\tau)} \tag{5.3}$$

where A is an arbitrary amplitude function, k is the wavenumber and ω is the frequency of the traveling wave. Substituting Eq. 5.3 into Eq. 5.2 yields a dispersion relationship between the wavenumber and frequency. The streamlined state becomes unstable when, for the lowest dimensionless wavenumber of the system, $k = 2\pi$, and for a given value of μ, the traveling wave perturbation grows exponentially in time,

i.e. the imaginary component of ω in Eq. 5.3 is positive. The critical value of η that produces instability can be solved for a range of values of μ, producing the instability boundary in $\mu - \eta$ space [94]. This is the method used to produce the dashed boundary, SVZ (2005), in Fig. 5-7. Alternatively, the instability boundary can be found by direct simulation of the governing equation coupled with the fluid forcing model. In this method, the flags are numerically perturbed with small amplitude oscillations and the resulting dynamics are observed for a range of values of μ and η. The critical parameter values at the transition between the streamlined state and the oscillation state are recorded as the stability boundary, e.g. the solid line, AS (2008) in Fig. 5-7.

The critical value of dimensionless rigidity, η, (above which the streamlined state is stable, and below which the oscillatory state is stable) increases with μ for both sets of results that we plot in Fig. 5-7. This means that as flags become "heavier" relative to the surrounding fluid, i.e. increasing μ, or as flags become more flexible, i.e. decreasing η, they become more unstable to flapping. In Fig. 5-7, we plot the sheltered and exposed morphology parameters on the stability boundary curve. As shown in Table 5.2, the values of η in both the flow-exposed and flow-sheltered sites are similar. For comparison, we have also plotted the morphological parameters of the flow-sheltered blade geometry at the flow-exposed fluid velocity. This comparison shows that at flow-exposed fluid velocities, the sheltered morphology would be unstable to flapping, resulting in significantly higher forces on the blade. The flow-exposed and flow-shelterd morphologies (gray triangle and black circle, respectively) cluster near the instability boundary, again suggesting a possible optimal ratio of structural properties to fluid forcing in both flow environments.

Interestingly, in our experiments, our model blades have values of η between 4.46E-6 and 5.6E0, and cross the theoretical instability threshold shown in Fig. 5-7. In our limited (unpublished) trials with our model blades in open channel flow, we did not observe the flapping flag instability. It is not clear however, if this is due to the fact that the actual instability boundary is different from the theoretical boundary, and that, in fact, all of our model blades exist in the stable regime. It is clear that in the vortex street flow, though, the assumptions that were used to construct the instability

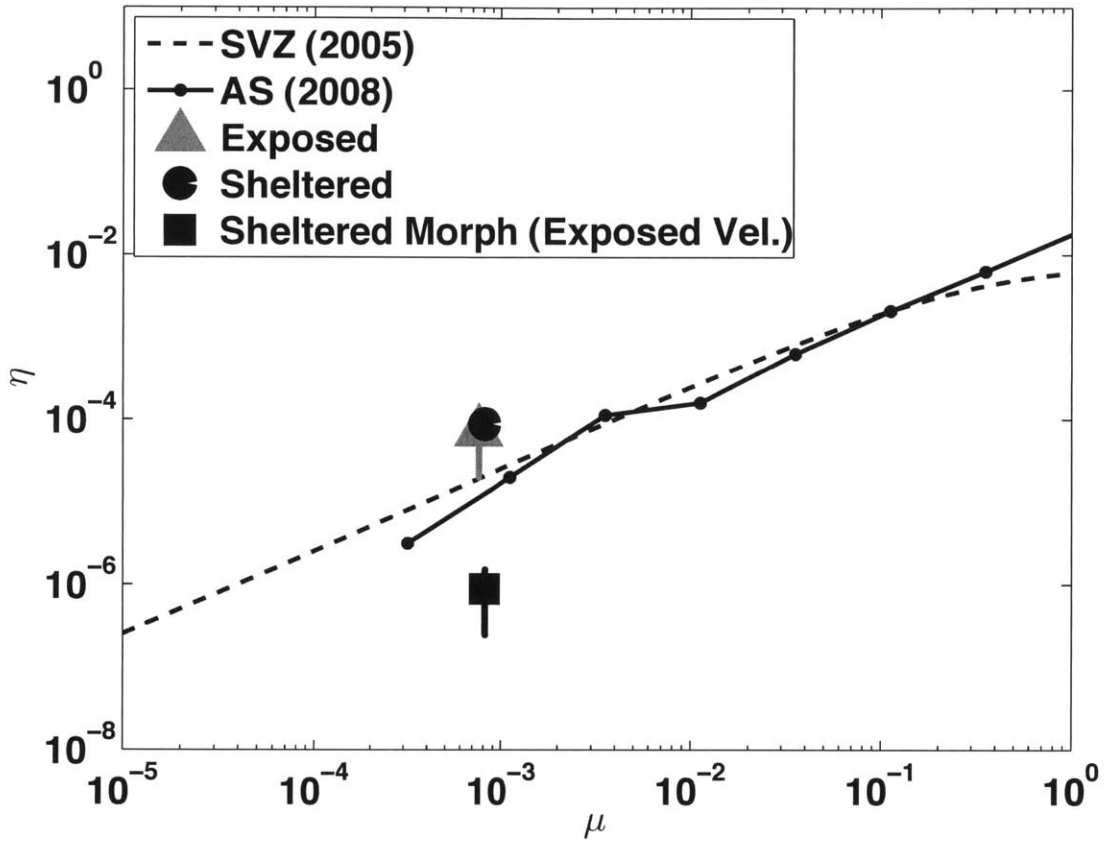

Figure 5-7: The flapping flag instability boundary in $\mu - \eta$ space. The dashed line, SVZ (2005), is a reduced order model prediction from [94] and the solid line, AS (2008), is a fully-nonlinear prediction calculated in [3]. The two lines show good agreement over much of the range of μ. We plot both predictions as experimentally observed threshold values are not available for this μ range. Above the stability boundary lines, the streamlined state (low drag) is stable. Below the boundary, the flapping state (higher drag) is the stable state. We plot the values of μ and η based on the experimental observations in [50] (Table 5.2) for the exposed and sheltered morphologies at the exposed and sheltered flow conditions, respectively. These points fall at the same location on the stability diagram, within uncertainty, suggesting a stiffening of the blade that is proportional to the fluid forcing. For comparison, we also plot the calculated value of η for the sheltered morphology at the exposed flow speed. The error bars for the flow-exposed velocity account for the possibility of velocities up to 0.95 m/s (Table 5.2).

boundary are violated (namely, uniform flow), and that the model blades move under the prescribed forcing rather than a self-excited instability.

Together, our understanding of the blade response to turbulence (Chap. 3) and of the drag forces resulting from the flapping flag instability indicate that morphological changes in kelp are strongly related to hydrodynamic environmental stimuli. We next consider how morphological changes relate to kelp's physiological requirement for nutrients.

5.2.3 Nutrient Acquisition

Changes in kelp blade flexural rigidity have the ability to not only modulate fluid drag forces, but also to affect the rate of nutrient uptake at the blade surface. By modifying the passive response of the blade, flexural rigidity controls the relative fluid motion at the blade surface, which is the key parameter in setting the rate of flux at the blade surface (Chap. 4). From the observations of actual kelp blades, we see that kelp blades become more rigid in the more flow-exposed environment. This morphological adaptation effectively reduces the nutrient acquisition rate at a specified velocity, by limiting the blade's dynamic response to the turbulence, and reducing the relative fluid velocity at the blade surface as shown in Fig. 4-6.

It may seem counterintuitive that kelp would adapt in a manner that reduces its ability to acquire nutrients from the flow. Based on previous experimental studies, however, we find that in flow-exposed environments, kelp can already acquire nutrients at a rate that exceeds its nutrient requirements. Indeed, various studies on uptake rates of different essential nutrients have found that uptake rates saturate at velocities between 2 - 6 cm/s [36, 33, 56, 49]. This means that at high fluid velocities, nutrients are delivered to the blade surface faster than the nutrients can be utilized and/or stored by the kelp. This saturation of the uptake rate is not controlled by hydrodynamics, but rather represents the transition of the uptake rate from hydrodynamic controls to physiological controls. The specific rates at which kelp utilizes nutrients are a function of temperature, salinity, light availability, season and nutrient concentration and these physiologically controlled rates are largely still active

areas of study. Understanding this, it is evident that kelp can undergo morphological changes that decrease the rate of nutrient flux to the blade surface without suffering any negative consequences. Altogether, these results indicate that in flow-exposed environments, nutrient requirements are already satisfied, and hydrodynamic forces are likely the most important environmental stimulus affecting kelp blade morphology.

5.3 Kelp Blade Differences Across a Kelp Forest

Stewart and colleagues [100] reported a set of intriguing observations of differences in kelp blade and kelp frond morphology between the canopy edge and the canopy center in a single kelp forest. Using our combined understand of the spatial patterns of currents through and around a kelp forest (Chapter 2) and our understanding of nutrient uptake rates as they relate to fluid velocity (Chapter 4), in this section we discuss the observations of Stewart et al. in the context of this thesis.

Stewart and colleagues specifically found differences in blade and frond morphology, and blade and frond growth rates between the canopy edge and the canopy interior regions. Current meters placed at the canopy edge and the canopy interior regions documented a 25% reduction in the mean flow speed from the canopy edge to the canopy interior. As we found in Chapter 2, the reduced interior flow in a canopy is governed by the canopy drag force. The main difference between the canopy edge and the canopy interior regions are the difference in current speed and the difference in light levels, which are higher at the canopy edge due to less shading from neighboring blades. The blades and fronds, however, responded to these differences in easily measurable ways. First, the blades at the canopy edges were both larger in terms of overall surface area than their counterparts in the canopy interior, and the blades at the edge also had a higher elongation rate. The fronds at the canopy edges exhibited higher elongation rates and a higher density of blades per frond length than the fronds at the canopy interior regions.

These morphological differences and the differences in growth rates are explained by the ability of the blades at both the canopy edge and interior regions to acquire

nutrients from the surrounding flow. Nutrient uptake rates are regulated in part by light levels which control the rate of photosynthesis in the kelp blades, but nutrient uptake rates are also limited by hydrodynamic constraints. The higher flow velocities at the canopy edge result in a higher potential nutrient uptake rate at the canopy edge.

Unfortunately, Stewart and colleagues did not report measurements of blade thickness at the two different canopy positions. As we discussed above, differences in exposure to flow at separate sites can induce morphological changes in blades, particularly in the blades' flexural rigidity. While it has not yet been documented, it is possible that blades at different positions within a single canopy could exhibit phenotypic plasticity in response to the spatial differences in flow between the canopy edge and interior regions. Interestingly, even if blades across a canopy do not exhibit differences in thickness and flexural rigidity, the spatial differences in current speed will produce variations in the dimensionless rigidity parameter η, which can have interesting implications for drag force and nutrient uptake.

5.4 Relative Velocity Measurements and Modeling

As we demonstrated in Chapter 4, the relative fluid velocity at the blade surface is an important variable that sets the rate of mass transfer between a fluid and a kelp blade. Direct measurements of the relative fluid velocity at a kelp blade surface currently do not exist, however, this information would be very valuable to better understand the process of nutrient transfer at the surface of a kelp blade. In our modeling, we extracted relative velocities at the blade surface from a numerical model of the blade motion in flow. Stevens, Hurd and Smith [99] extracted the relative velocities between a kelp frond and combined wave and current flow from a dynamic model of the frond motion. These authors chose a current speed of 0.05 m/s and a wave height of 0.25 m, a wavelength of 51 m and a period of 7 s. Their results revealed an average relative fluid velocity of near 0.05 m/s.

The authors did not include the motion of the kelp blades relative to the kelp

frond in their model; they treated the entire kelp frond as a single body. We can, however, use their model as a first approximation to the relative velocities found at the surface of kelp blades in the field. This value of relative velocity can then be used to construct an approximate transfer velocity at the blade surface, via the transfer velocity model introduced in §4.5.1. We note that Stevens, Hurd and Smith report the total relative velocity, rather than just the normal component of the fluid velocity, and thus this estimate represents an upper bound on the transfer velocity. Using Eq. 4.18, and a blade width of $b = 0.09$ m (typical of *Macrocystis pyrifera* blades), the transfer velocity at the surface of a kelp blade in those wave and current conditions would be $K = 1.5E-6$ m/s. We know of no published values of transfer velocities for mass transfer to a kelp blade in both waves and currents, however, this value of K can be used as a comparison with other experiments. Hurd et al. [49] calculated the effective diffusion boundary layer thickness from a series of uptake experiments in unidirectional currents. At a mean current speed of 0.05 m/s, the back-calculated, effective diffusion boundary layer thickness was 0.2 mm. Using this back-calculated thickness, we estimate a nitrate transfer velocity of $K = 8E-6$ m/s (using $D_{NO_3^-} = 16.1E-10$ m^2/s [97]). We anticipate that the presence of waves should enhance the transfer velocity over that of transfer in currents alone, however, the process is certainly nonlinear and measurements of relative velocities and of mass transfer in combined wave and current regimes are needed to answer this question.

Chapter 6

Conclusions

Using a kelp forest as a model physical system, this thesis has investigated hydrodynamic and transport phenomena at multiple scales, ranging from the scale of a kelp canopy to the scale of a kelp blade. In this chapter, we review the key findings of this thesis and discuss some of the related research questions provoked through these studies.

In Chap. 2, we studied the flow adjustment and interior flow regions of a rectangular porous obstruction (a simplified model of a kelp canopy). We defined a dimensionless parameter, the canopy flow-blockage, which classifies canopies as either low or high flow-blockage based on the canopy width and frontal area per unit volume. The flow adjustment length for high flow-blockage canopies is set by the canopy width, while for low flow-blockage canopies, the adjustment length is set by the canopy drag lengthscale. In §2.2.2, we demonstrate how the flow at the canopy interior can either be set by a balance between canopy drag and the background pressure gradient, or between canopy drag and the lateral penetration of the KH vortices at the canopy edges. The magnitude of the canopy flow-blockage parameter predicts which of these balances governs the interior flow.

Moreover, in §2.4.3, we identify the phenomenon of cross-canopy vortex synchronization and enhancement. A canopy with two edges parallel to the flow, vortex streets will communicate across the canopy width, enhancing vortex strength and enhancing lateral transport across the canopy. In this section, we predict that lateral

vortex communication is limited by the relative timescales of the shallow water wave speed and the vortex period. Our experimental setup did not allow testing of this limit, and to our knowledge there are no other studies that probe this limit. Detailed field studies of flow through kelp forests would help to confirm if these phenomena and lengthscales exist and are relevant in natural canopies.

We then transitioned our studies from the canopy scale and focused on phenomena at the meter and sub-meter scales of the kelp blade. In Chap. 3, through theory and experiments we studied the forces and motion of a flag (a model for a kelp blade) in an ideal form of turbulence: the Kármán vortex street. We found that the flag motion and the resulting forces are a strong function of the flag flexural rigidity. Both drag force and oscillation amplitude increase as flexural rigidity decreases. Below a critical threshold, inertial forces on the flag become significant, affecting the total measured force. Numerical simulations, absent the randomness found in the experimental flow, showed a bifurcation in the response states of the flag. Below the critical threshold, the flag adopted an asymmetric oscillation state. Further stochastic modeling of this system may help reveal the mechanisms which prevent the bifurcation from being consistently observed experimentally. Further, in our model of the system, we assumed steady values of the drag and added mass coefficients. For a bluff body in unsteady flow, the drag coefficient is initially large while the wake develops, then the drag coefficient decreases, approaching its steady value. Experiments directly studying the variation of these coefficients in highly oscillatory systems would be a valuable contribution for studying these types of systems. Changes in these coefficients can affect the amplitude of motion, the values of the relative velocity at the blade surface and the position of the oscillation bifurcation. With robust estimates of C_D, C_f and the added mass coefficient as a function of acceleration and blade curvature, we could more accurately numerically model this system.

While the experimental study and the simulations revealed the behavior of a blade in our model system, there are remaining questions about blade behavior in less ideal systems. In the coastal ocean, turbulence exists at many length-scales and frequencies, as well as both currents and waves, which can all influence the dynamics

of the blades. In these settings, however, we fully expect the same physics to apply, specifically that fluid drag and inertial forces will be a function of blade flexural rigidity. Another important difference between our lab-scale study and actual kelp forests is the proximity between neighboring blades. In kelp forests, blades grow in close proximity to one another, and the blade-blade interactions may affect blade motion and drag force in ways not currently understood.

In Chap. 4, we studied how the passive response of model blades, a function of the blade flexural rigidity, can affect scalar flux at the blade surface. We developed an experimental method, based on the technology of passive polyethylene samplers, that we use to mimic nutrient flux at the surface of a kelp blade. Our results revealed that blade flexural rigidity does indeed affect scalar flux: more flexible blades move more in response to the flow, creating higher relative velocities at the surface which increases flux. These results agree with the theory developed for renewal at a solid-liquid boundary. Moreover, the validation of the experimental method opens the door to explore new phenomena at the interface between flexible solids and flow, including the effects of waves, grid-generated turbulence and other flow phenomena.

We note that for scalar transfer at a solid boundary in unsteady flow, there exists a no-slip boundary condition which can produce a diffusive sublayer. While comparison between experimental flux data and flux models can provide some information on this unsteady diffusive sublayer, direct visualization of this layer either through flow visualization or scalar measurement can further confirm models. Development of a method that can directly measure this layer at an unsteady boundary, either through acoustic, optical or direct measurement of scalars, would be an invaluable asset for studying the physics of flux at a dynamic fluid-solid interface.

Finally, in Chap. 5, we relate published morphological observations of kelp blades to our laboratory studies on blade drag force and flux. Changes in blade morphology between flow-sheltered sites and flow-exposed sites effectively reduce the drag force on blades at flow-exposed sites. These same morphological changes have the potential to reduce nutrient flux, though. Through a review of previous nutrient flux studies, however, we find that kelp nutrient requirements are nearly always satisfied at flow-

exposed sites, and therefore fluid drag is likely the overriding environmental stimulus in these environments.

A species of *Macrocystis* exhibits corrugations as a technique for increasing blade flexural rigidity. While these corrugations significantly affect flexural rigidity and thus drag forces, they will likely have a secondary effect on the blade surface roughness and the resulting friction drag. The effect that surface corrugations and other surface geometries have on the drag force, both in kelp and in engineered structures, is a phenomenon that is currently poorly understood.

Moreover, morphological measurements of kelp blades are often not accompanied by detailed information about the flow environment, e.g. the mean, rms and maximum fluid velocities. Rather than simply grouping kelp blades into two groups based on qualitative descriptions of the flow environment, a detailed set of morphological data coupled with information about the local flow environment would be a great asset to understanding the role that phenotypic plasticity plays in the survival of kelp. Furthermore, by combining our understanding of the flow through kelp canopies from Chap. 2, we note that there can be significant differences in flow environment for kelp blades within the same canopy, and that these cross-canopy differences could themselves produce significant morphological differences among blades. A thorough survey of kelp blades across a single kelp canopy, coupled with the local flow information could also provide information as to how kelp adapts at the intra-canopy scale.

Appendix A

Patch Experiments Data

In this appendix we tabulate the data from Chapter 2.

Table A.1: Table of both the raw and scaled velocity statistics for the $C_D ab = 0.21$ patch. The dimensionless streamwise position x/scaling, is the dimensional position normalized by either the upstream or within-canopy adjustment scaling, as defined in §2.2. U adj. is the measured velocity that has been adjusted to account for the canopy solid volume fraction. The canopy leading edge is at $x = 0$ and the canopy centerline is at $y = 0$. These measurements are all made at the canopy centerline unless otherwise noted.

x (cm)	x/b	$x(C_D a)$	x/scaling	U (m/s)	U adj. (m/s)	U_{rms} (m/s)	V_{rms} (m/s)	W_{rms} (m/s)	$\langle uv \rangle_{y=0}$ (cm^2/s^2)
-103.0	-25.8		-25.75	1.01E-01	1.01E-01	2.17E-02	1.58E-02	5.50E-03	7.47E-02
-93.0	-23.3		-23.25	1.01E-01	1.01E-01	2.16E-02	1.52E-02	5.60E-03	1.04E-01
-83.0	-20.8		-20.75	1.02E-01	1.02E-01	2.09E-02	1.45E-02	5.70E-03	-3.30E-03
-73.0	-18.3		-18.25	1.01E-01	1.01E-01	2.00E-02	1.58E-02	5.80E-03	7.24E-02
-63.0	-15.8		-15.75	1.02E-01	1.02E-01	2.10E-02	1.51E-02	5.80E-03	-7.75E-02
-53.0	-13.3		-13.25	1.03E-01	1.03E-01	2.02E-02	1.46E-02	5.60E-03	4.71E-02
-43.0	-10.8		-10.75	1.03E-01	1.03E-01	1.92E-02	1.42E-02	5.50E-03	6.41E-02
-33.0	-8.3		-8.25	1.00E-01	1.00E-01	2.06E-02	1.38E-02	5.70E-03	5.55E-02
-23.0	-5.8		-5.75	9.95E-02	9.95E-02	2.00E-02	1.32E-02	5.70E-03	8.34E-02
-18.0	-4.5		-4.50	1.01E-01	1.01E-01	1.71E-02	1.37E-02	5.60E-03	2.56E-02
-13.0	-3.3		-3.25	1.01E-01	1.01E-01	1.67E-02	1.26E-02	5.50E-03	6.79E-02
-8.0	-2.0		-2.00	9.76E-02	9.76E-02	1.62E-02	1.31E-02	5.50E-03	1.48E-02

Continued on next page

Table A.1 – continued from previous page

x (cm)	x/b	$x(C_D a)$	x/scaling	U (m/s)	U adj. (m/s)	U_{rms} (m/s)	V_{rms} (m/s)	W_{rms} (m/s)	$\langle uv \rangle_{y=0}$ (cm^2/s^2)
-3.0	-0.8		-0.75	9.54E-02	9.54E-02	1.55E-02	1.09E-02	4.90E-03	1.15E-02
4.5	1.1	0.12	0.12	7.49E-02	7.30E-02	2.85E-02	3.86E-02	8.70E-03	4.10E-01
10.5	2.6	0.28	0.28	7.69E-02	7.49E-02	3.09E-02	3.41E-02	8.20E-03	-4.34E-01
17.5	4.4	0.46	0.46	6.41E-02	6.24E-02	2.99E-02	3.22E-02	7.80E-03	-1.27E-01
24.0	6.0	0.64	0.63	5.76E-02	5.61E-02	2.66E-02	2.69E-02	7.50E-03	-5.26E-01
31.0	7.8	0.82	0.82	5.27E-02	5.13E-02	2.50E-02	2.65E-02	7.10E-03	-2.76E-02
37.3	9.3	0.99	0.98	4.38E-02	4.27E-02	2.26E-02	2.39E-02	6.90E-03	-4.15E-01
44.0	11.0	1.17	1.16	3.15E-02	3.07E-02	2.01E-02	2.12E-02	6.60E-03	-8.35E-02
50.8	12.7	1.35	1.34	2.68E-02	2.61E-02	1.76E-02	2.22E-02	6.20E-03	5.00E-04
57.5	14.4	1.52	1.52	2.96E-02	2.88E-02	1.67E-02	2.01E-02	5.50E-03	-7.00E-02
64.0	16.0	1.70	1.69	2.63E-02	2.56E-02	1.62E-02	1.87E-02	5.20E-03	-1.65E-01
70.3	17.6	1.86	1.85	2.19E-02	2.13E-02	1.66E-02	1.81E-02	5.10E-03	-7.90E-02
76.8	19.2	2.04	2.02	1.85E-02	1.80E-02	1.53E-02	1.61E-02	5.10E-03	-1.24E-01
83.5	20.9	2.21	2.20	1.81E-02	1.76E-02	1.58E-02	1.97E-02	5.70E-03	6.78E-02
90.0	22.5	2.39	2.37	1.64E-02	1.60E-02	1.76E-02	1.91E-02	5.70E-03	9.30E-03
96.7	24.2	2.56	2.55	1.88E-02	1.83E-02	1.86E-02	2.12E-02	6.20E-03	-4.02E-01
107.0	26.8	2.84	2.82	2.08E-02	2.03E-02	1.72E-02	1.58E-02	6.20E-03	1.67E-01

Continued on next page

Table A.1 – continued from previous page

x (cm)	x/b	$x(C_Da)$	x/scaling	U (m/s)	U adj. (m/s)	U_{rms} (m/s)	V_{rms} (m/s)	W_{rms} (m/s)	$\langle u'v' \rangle_{y=0}$ (cm^2/s^2)
120.8	30.2	3.20	3.18	2.14E-02	2.08E-02	1.74E-02	1.73E-02	6.30E-03	3.63E-01
132.5	33.1	3.51	3.49	2.78E-02	2.71E-02	2.01E-02	2.07E-02	6.80E-03	5.68E-01
145.5	36.4	3.86	3.83	2.94E-02	2.86E-02	2.13E-02	1.94E-02	6.90E-03	1.12E-01
158.6	39.7	4.20	4.18	3.62E-02	3.53E-02	2.20E-02	2.30E-02	7.30E-03	-3.13E-02
170.1	42.5	4.51	4.48	3.62E-02	3.53E-02	2.20E-02	2.28E-02	7.20E-03	-1.32E-02
184.2	46.1	4.88	4.85	3.63E-02	3.54E-02	2.47E-02	2.36E-02	7.60E-03	6.64E-01
197.6	49.4	5.24	5.21	3.73E-02	3.63E-02	2.28E-02	2.35E-02	7.30E-03	-1.71E-01

Table A.2: Table of both the raw and scaled velocity statistics for the $C_Dab = 0.53$ patch. The dimensionless streamwise position x/scaling, is the dimensional position normalized by either the upstream or within-canopy adjustment scaling, as defined in §2.2. U adj. is the measured velocity that has been adjusted to account for the canopy solid volume fraction. The canopy leading edge is at $x = 0$ and the canopy centerline is at $y = 0$. These measurements are all made at the canopy centerline unless otherwise noted.

x (cm)	x/b	$x(C_Da)$	x/scaling	U (m/s)	U adj. (m/s)	U_{rms} (m/s)	V_{rms} (m/s)	W_{rms} (m/s)	$\langle u'v' \rangle_{y=0}$ (cm^2/s^2)
-103.0	-10.3		-10.30	9.48E-02	9.48E-02	1.15E-02	1.21E-02	4.10E-03	1.77E-02
-83.0	-8.3		-8.30	9.58E-02	9.58E-02	1.13E-02	1.10E-02	4.00E-03	2.27E-02
-63.0	-6.3		-6.30	9.47E-02	9.47E-02	1.13E-02	1.19E-02	4.20E-03	5.17E-02
-43.0	-4.3		-4.30	9.44E-02	9.44E-02	1.13E-02	1.12E-02	4.20E-03	9.08E-02
-23.0	-2.3		-2.30	9.24E-02	9.24E-02	1.10E-02	1.09E-02	4.10E-03	6.49E-02
-13.0	-1.3		-1.30	9.07E-02	9.07E-02	1.07E-02	1.02E-02	4.00E-03	2.13E-02
-3.0	-0.3		-0.30	8.39E-02	8.39E-02	1.03E-02	1.11E-02	4.80E-03	1.27E-02
16.5	1.7	0.44	0.42	6.28E-02	6.12E-02	2.34E-02	2.36E-02	7.50E-03	4.60E-01
36.7	3.7	0.97	0.94	4.69E-02	4.57E-02	1.84E-02	1.73E-02	6.50E-03	2.10E-01
56.1	5.6	1.49	1.44	3.61E-02	3.52E-02	1.65E-02	1.47E-02	5.70E-03	2.94E-01
76.2	7.6	2.02	1.95	2.86E-02	2.79E-02	1.32E-02	1.21E-02	4.90E-03	1.19E-01
96.0	9.6	2.54	2.46	2.31E-02	2.25E-02	1.18E-02	1.18E-02	4.00E-03	1.11E-01

Continued on next page

Table A.2 – continued from previous page

x (cm)	x/b	$x(C_D a)$	x/scaling	U (m/s)	U adj. (m/s)	U_{rms} (m/s)	V_{rms} (m/s)	W_{rms} (m/s)	$\langle uv \rangle_{y=0}$ (cm^2/s^2)
115.7	11.6	3.07	2.96	1.53E-02	1.49E-02	1.00E-02	1.10E-02	3.20E-03	-2.58E-02
137.3	13.7	3.64	3.52	1.06E-02	1.03E-02	9.70E-03	1.36E-02	3.20E-03	2.97E-02
157.0	15.7	4.16	4.02	9.20E-03	8.96E-03	1.10E-02	1.72E-02	4.00E-03	-3.51E-02
177.5	17.8	4.70	4.55	9.20E-03	8.96E-03	1.31E-02	1.97E-02	4.90E-03	1.84E-01
197.9	19.8	5.24	5.07	1.19E-02	1.16E-02	1.48E-02	2.25E-02	5.40E-03	1.49E-01
217.7	21.8	5.77	5.58	1.47E-02	1.43E-02	1.65E-02	2.13E-02	5.50E-03	3.21E-02
237.5	23.8	6.29	6.08	1.93E-02	1.88E-02	1.81E-02	2.48E-02	6.30E-03	2.99E-01
258.1	25.8	6.84	6.61	2.11E-02	2.06E-02	1.81E-02	2.30E-02	5.90E-03	3.15E-01
277.9	27.8	7.36	7.12	2.46E-02	2.40E-02	1.76E-02	2.59E-02	6.20E-03	1.75E-01
297.7	29.8	7.89	7.63	2.54E-02	2.47E-02	1.81E-02	2.46E-02	6.10E-03	5.61E-01
316.6	31.7	8.39	8.11	2.63E-02	2.56E-02	1.93E-02	2.60E-02	6.50E-03	-5.61E-02
336.9	33.7	8.93	8.63	3.27E-02	3.18E-02	2.02E-02	2.94E-02	6.60E-03	2.86E-01
356.6	35.7	9.45	9.13	3.05E-02	2.97E-02	1.96E-02	2.91E-02	6.40E-03	1.09E-01
377.3	37.7	10.00	9.66	3.11E-02	3.03E-02	2.06E-02	2.90E-02	6.70E-03	4.33E-01
397.3	39.7	10.53	10.18	3.02E-02	2.94E-02	2.00E-02	2.90E-02	6.60E-03	9.64E-02

Table A.3: Table of both the raw and scaled velocity statistics for the $C_D ab = 0.58$ patch. The dimensionless streamwise position x/scaling, is the dimensional position normalized by either the upstream or within-canopy adjustment scaling, as defined in §2.2. U adj. is the measured velocity that has been adjusted to account for the canopy solid volume fraction. The canopy leading edge is at $x = 0$ and the canopy centerline is at $y = 0$. These measurements are all made at the canopy centerline unless otherwise noted.

x (cm)	x/b	$x(C_D a)$	x/scaling	U (m/s)	U adj. (m/s)	U_{rms} (m/s)	V_{rms} (m/s)	W_{rms} (m/s)	$\langle uv \rangle_{y=0}$ (cm^2/s^2)
-101.0	-16.8		-16.83	1.03E-01	1.03E-01	2.34E-02	1.80E-02	6.70E-03	4.83E-02
-91.0	-15.2		-15.17	1.05E-01	1.05E-01	2.39E-02	1.69E-02	6.50E-03	-2.51E-02
-81.0	-13.5		-13.50	1.05E-01	1.05E-01	2.31E-02	1.58E-02	6.70E-03	1.86E-02
-71.0	-11.8		-11.83	1.06E-01	1.06E-01	2.22E-02	1.58E-02	6.60E-03	-1.28E-01
-61.0	-10.2		-10.17	1.06E-01	1.06E-01	2.22E-02	1.54E-02	6.60E-03	6.47E-02
-51.0	-8.5		-8.50	1.05E-01	1.05E-01	2.18E-02	1.45E-02	6.40E-03	-6.78E-02
-41.0	-6.8		-6.83	1.05E-01	1.05E-01	2.07E-02	1.35E-02	6.40E-03	-4.13E-02
-31.0	-5.2		-5.17	1.05E-01	1.05E-01	1.98E-02	1.27E-02	6.30E-03	-4.13E-02
-21.0	-3.5		-3.50	1.06E-01	1.06E-01	1.88E-02	1.27E-02	6.00E-03	3.40E-03
-11.0	-1.8		-1.83	1.01E-01	1.01E-01	1.83E-02	1.18E-02	5.90E-03	8.13E-02
-3.5	-0.6		-0.58	8.66E-02	8.66E-02	1.41E-02	9.20E-03	5.20E-03	-8.70E-03
8.7	1.5	0.42	0.40	7.76E-02	7.40E-02	3.60E-02	3.56E-02	8.00E-03	-2.65E-01

Continued on next page

Table A.3 – continued from previous page

x (cm)	x/b	$x(C_Da)$	x/scaling	U (m/s)	U adj. (m/s)	U_{rms} (m/s)	V_{rms} (m/s)	W_{rms} (m/s)	$\langle uv \rangle_{y=0}$ (cm^2/s^2)
18.6	3.1	0.89	0.86	6.09E-02	5.81E-02	2.95E-02	2.92E-02	8.00E-03	-2.47E-01
28.5	4.8	1.37	1.31	4.50E-02	4.29E-02	2.29E-02	2.41E-02	6.80E-03	-8.95E-02
38.2	6.4	1.83	1.76	3.32E-02	3.17E-02	1.82E-02	1.91E-02	6.00E-03	-8.39E-02
48.0	8.0	2.30	2.21	2.56E-02	2.44E-02	1.48E-02	1.49E-02	5.00E-03	-1.02E-01
58.2	9.7	2.79	2.68	1.76E-02	1.68E-02	1.15E-02	1.14E-02	3.70E-03	3.62E-02
68.3	11.4	3.28	3.15	9.90E-03	9.44E-03	1.03E-02	1.09E-02	3.30E-03	4.74E-02
78.3	13.1	3.76	3.61	5.30E-03	5.06E-03	1.12E-02	1.68E-02	4.00E-03	2.28E-02
88.5	14.8	4.25	4.08	4.60E-03	4.39E-03	1.47E-02	1.89E-02	4.80E-03	2.88E-01
98.0	16.3	4.70	4.52	6.20E-03	5.91E-03	1.72E-02	2.14E-02	5.40E-03	-6.43E-02
108.0	18.0	5.18	4.98	9.60E-03	9.16E-03	1.77E-02	2.02E-02	5.70E-03	3.45E-01
119.0	19.8	5.71	5.49	1.48E-02	1.41E-02	2.14E-02	2.61E-02	6.40E-03	2.27E-01
129.0	21.5	6.19	5.95	1.78E-02	1.70E-02	2.33E-02	2.63E-02	6.80E-03	-2.23E-01
138.7	23.1	6.66	6.40	2.49E-02	2.38E-02	2.46E-02	2.65E-02	7.10E-03	-3.17E-01
149.0	24.8	7.15	6.87	2.24E-02	2.14E-02	2.45E-02	2.35E-02	6.70E-03	2.05E-01
159.0	26.5	7.63	7.33	2.44E-02	2.33E-02	2.45E-02	2.62E-02	6.70E-03	-1.68E-01
168.7	28.1	8.10	7.78	3.30E-02	3.15E-02	2.68E-02	2.64E-02	7.10E-03	-3.03E-01

Table A.4: Table of both the raw and scaled velocity statistics for the $C_Dab = 0.96$ patch. The dimensionless streamwise position x/scaling, is the dimensional position normalized by either the upstream or within-canopy adjustment scaling, as defined in §2.2. U adj. is the measured velocity that has been adjusted to account for the canopy solid volume fraction. The canopy leading edge is at $x = 0$ and the canopy centerline is at $y = 0$. These measurements are all made at the canopy centerline unless otherwise noted.

x (cm)	x/b	$x(C_Da)$	x/scaling	U (m/s)	U adj. (m/s)	U_{rms} (m/s)	V_{rms} (m/s)	W_{rms} (m/s)	$\langle u'v' \rangle_{y=0}$ (cm^2/s^2)
-153.5	-15.4		-15.35	1.05E-01	1.05E-01	1.03E-02	9.80E-03	4.10E-03	2.35E-02
-143.5	-14.4		-14.35	1.06E-01	1.06E-01	1.08E-02	1.02E-02	4.30E-03	4.36E-02
-133.5	-13.4		-13.35	1.05E-01	1.05E-01	1.03E-02	9.70E-03	4.30E-03	7.18E-02
-123.5	-12.4		-12.35	1.06E-01	1.06E-01	1.02E-02	9.80E-03	4.20E-03	2.90E-03
-113.5	-11.4		-11.35	1.05E-01	1.05E-01	1.01E-02	9.00E-03	4.10E-03	2.15E-02
-103.5	-10.4		-10.35	1.11E-01	1.11E-01	1.43E-02	1.42E-02	5.30E-03	-4.00E-03
-93.5	-9.4		-9.35	1.09E-01	1.09E-01	1.40E-02	1.32E-02	5.10E-03	-2.26E-02
-83.5	-8.4		-8.35	1.11E-01	1.11E-01	1.30E-02	1.26E-02	4.70E-03	2.06E-02
-73.5	-7.4		-7.35	1.10E-01	1.10E-01	1.37E-02	1.27E-02	4.80E-03	6.95E-02
-63.5	-6.4		-6.35	1.09E-01	1.09E-01	1.22E-02	1.21E-02	4.40E-03	-1.31E-02
-53.5	-5.4		-5.35	1.05E-01	1.05E-01	1.34E-02	1.46E-02	4.40E-03	-3.26E-02
-43.5	-4.4		-4.35	1.03E-01	1.03E-01	1.27E-02	1.39E-02	4.70E-03	-2.00E-03

Continued on next page

Table A.4 – continued from previous page

x (cm)	x/b	$x(C_D a)$	x/scaling	U (m/s)	U adj. (m/s)	U_{rms} (m/s)	V_{rms} (m/s)	W_{rms} (m/s)	$\langle u'v' \rangle_{y=0}$ (cm^2/s^2)
-33.5	-3.4		-3.35	1.02E-01	1.02E-01	1.21E-02	1.36E-02	4.80E-03	4.41E-02
-23.5	-2.4		-2.35	1.01E-01	1.01E-01	1.17E-02	1.28E-02	4.70E-03	3.69E-02
-13.5	-1.4		-1.35	9.70E-02	9.70E-02	1.21E-02	1.25E-02	4.60E-03	5.83E-02
-3.0	-0.3		-0.30	8.57E-02	8.57E-02	9.70E-03	8.30E-03	3.70E-03	5.26E-02
9.0	0.9	0.43	0.39	8.04E-02	7.67E-02	3.28E-02	3.35E-02	8.00E-03	-2.63E-01
19.5	2.0	0.94	0.84	6.62E-02	6.32E-02	2.87E-02	2.79E-02	7.80E-03	-2.57E-01
29.0	2.9	1.39	1.25	5.55E-02	5.29E-02	2.51E-02	2.42E-02	7.40E-03	-5.07E-01
38.5	3.9	1.85	1.67	4.46E-02	4.25E-02	2.07E-02	2.06E-02	7.00E-03	-2.67E-01
49.0	4.9	2.35	2.12	3.28E-02	3.13E-02	1.72E-02	1.59E-02	6.00E-03	-2.92E-01
59.0	5.9	2.83	2.55	3.12E-02	2.98E-02	1.42E-02	1.40E-02	5.20E-03	-3.85E-02
68.7	6.9	3.30	2.97	2.34E-02	2.23E-02	1.25E-02	1.37E-02	4.60E-03	-4.86E-02
79.0	7.9	3.79	3.42	1.72E-02	1.64E-02	1.07E-02	1.22E-02	3.60E-03	4.42E-02
89.0	8.9	4.27	3.85	1.37E-02	1.31E-02	9.30E-03	1.06E-02	3.10E-03	-4.11E-02
99.0	9.9	4.75	4.28	9.80E-03	9.35E-03	7.90E-03	1.18E-02	2.60E-03	-2.25E-02
109.0	10.9	5.23	4.72	6.30E-03	6.01E-03	8.60E-03	1.45E-02	2.90E-03	9.34E-02
119.0	11.9	5.71	5.15	4.10E-03	3.91E-03	8.40E-03	1.43E-02	3.00E-03	-3.75E-02
129.5	13.0	6.22	5.60	3.30E-03	3.15E-03	1.06E-02	1.82E-02	3.90E-03	-5.26E-02

Continued on next page

Table A.4 – continued from previous page

x (cm)	x/b	$x(C_Da)$	x/scaling	U (m/s)	U adj. (m/s)	U_{rms} (m/s)	V_{rms} (m/s)	W_{rms} (m/s)	$\langle u'v' \rangle_{y=0}$ (cm^2/s^2)
139.5	14.0	6.70	6.04	2.90E-03	2.77E-03	1.18E-02	1.76E-02	3.80E-03	9.76E-02
149.5	15.0	7.18	6.47	3.50E-03	3.34E-03	1.30E-02	2.07E-02	4.80E-03	6.51E-02
159.5	16.0	7.66	6.90	6.60E-03	6.30E-03	1.50E-02	2.24E-02	5.10E-03	2.40E-03
169.5	17.0	8.14	7.33	7.80E-03	7.44E-03	1.79E-02	2.35E-02	5.40E-03	-2.14E-01
179.0	17.9	8.59	7.75	1.07E-02	1.02E-02	1.75E-02	2.25E-02	5.30E-03	1.16E-01
189.5	19.0	9.10	8.20	1.31E-02	1.25E-02	1.81E-02	2.36E-02	5.60E-03	5.37E-01
199.0	19.9	9.55	8.61	1.44E-02	1.37E-02	1.90E-02	2.45E-02	5.70E-03	1.67E-01
209.0	20.9	10.03	9.04	1.52E-02	1.45E-02	1.81E-02	2.44E-02	5.70E-03	3.22E-01
219.0	21.9	10.51	9.48	1.97E-02	1.88E-02	1.97E-02	2.76E-02	6.10E-03	-3.28E-01
228.5	22.9	10.97	9.89	2.22E-02	2.12E-02	2.02E-02	2.61E-02	6.00E-03	-3.00E-04
239.0	23.9	11.47	10.34	2.87E-02	2.74E-02	2.13E-02	2.56E-02	6.20E-03	1.75E-02

Table A.5: Table of both the raw and scaled velocity statistics for the $C_D ab = 1.20$ patch. The dimensionless streamwise position x/scaling, is the dimensional position normalized by either the upstream or within-canopy adjustment scaling, as defined in §2.2. U adj. is the measured velocity that has been adjusted to account for the canopy solid volume fraction. The canopy leading edge is at $x = 0$ and the canopy centerline is at $y = 0$. These measurements are all made at the canopy centerline unless otherwise noted.

x (cm)	x/b	$x(C_D a)$	x/scaling	U (m/s)	U adj. (m/s)	U_{rms} (m/s)	V_{rms} (m/s)	W_{rms} (m/s)	$\langle uv \rangle_{y=0}$ (cm^2/s^2)
-103.0	-17.2		-17.17	9.42E-02	9.42E-02	1.87E-02	1.19E-02	5.50E-03	1.62E-02
-93.0	-15.5		-15.50	9.35E-02	9.35E-02	1.99E-02	1.23E-02	5.60E-03	-9.80E-03
-83.0	-13.8		-13.83	9.06E-02	9.06E-02	2.03E-02	1.27E-02	5.80E-03	1.00E-03
-73.0	-12.2		-12.17	9.25E-02	9.25E-02	1.93E-02	1.29E-02	5.70E-03	-1.32E-02
-63.0	-10.5		-10.50	9.00E-02	9.00E-02	1.85E-02	1.31E-02	5.70E-03	-2.54E-02
-53.0	-8.8		-8.83	8.85E-02	8.85E-02	1.93E-02	1.33E-02	5.70E-03	4.02E-02
-43.0	-7.2		-7.17	8.78E-02	8.78E-02	1.93E-02	1.30E-02	5.50E-03	2.80E-02
-33.0	-5.5		-5.50	8.74E-02	8.74E-02	1.92E-02	1.25E-02	5.90E-03	-3.64E-02
-23.0	-3.8		-3.83	8.82E-02	8.82E-02	1.84E-02	1.31E-02	5.80E-03	1.42E-02
-13.0	-2.2		-2.17	7.63E-02	7.63E-02	2.23E-02	1.70E-02	6.90E-03	1.97E-02
-3.0	-0.5		-0.50	5.45E-02	5.45E-02	2.27E-02	1.74E-02	7.40E-03	-1.07E-01
0.0	0.0	0.00	0.00	6.02E-02	5.42E-02	2.17E-02	1.73E-02	8.10E-03	9.34E-02

Continued on next page

Table A.5 – continued from previous page

x (cm)	x/b	$x(C_Da)$	x/scaling	U (m/s)	U adj. (m/s)	U_{rms} (m/s)	V_{rms} (m/s)	W_{rms} (m/s)	$\langle uvt \rangle_{y=0}$ (cm^2/s^2)
10.0	1.7	1.00	0.86	5.70E-03	5.13E-03	2.40E-02	2.51E-02	7.90E-03	1.80E-01
15.0	2.5	1.50	1.29	4.71E-02	4.24E-02	2.51E-02	2.40E-02	8.10E-03	-2.45E-01
20.0	3.3	2.00	1.71	1.99E-02	1.79E-02	1.71E-02	1.69E-02	5.50E-03	-9.86E-02
25.0	4.2	2.50	2.14	1.73E-02	1.56E-02	1.38E-02	1.18E-02	4.20E-03	-1.93E-02
30.0	5.0	3.00	2.57	9.20E-03	8.28E-03	1.16E-02	1.07E-02	3.40E-03	-1.02E-02
35.0	5.8	3.50	3.00	4.90E-03	4.41E-03	1.18E-02	1.15E-02	3.70E-03	4.30E-03
40.0	6.7	4.00	3.43	4.50E-03	4.05E-03	1.19E-02	1.34E-02	3.70E-03	-2.36E-02
45.0	7.5	4.50	3.86	4.80E-03	4.32E-03	1.65E-02	1.56E-02	5.30E-03	3.82E-02
50.0	8.3	5.00	4.29	1.60E-03	1.44E-03	1.37E-02	1.24E-02	4.30E-03	8.33E-02
55.0	9.2	5.50	4.72	-3.00E-04	-2.70E-04	1.37E-02	1.41E-02	4.40E-03	-1.70E-02
60.0	10.0	6.00	5.14	-2.40E-03	-2.16E-03	1.30E-02	1.33E-02	4.20E-03	1.98E-02
65.0	10.8	6.50	5.57	1.50E-03	1.35E-03	1.78E-02	1.52E-02	5.80E-03	-3.10E-02
70.0	11.7	7.00	6.00	-3.40E-03	-3.06E-03	1.61E-02	1.55E-02	5.20E-03	-4.49E-02
75.0	12.5	7.50	6.43	-2.50E-03	-2.25E-03	1.33E-02	1.64E-02	4.40E-03	2.49E-02
80.0	13.3	8.00	6.86	-1.20E-03	-1.08E-03	1.60E-02	1.68E-02	5.10E-03	3.35E-02
85.0	14.2	8.50	7.29	-1.70E-03	-1.53E-03	1.37E-02	1.75E-02	4.50E-03	1.94E-02
90.0	15.0	9.00	7.72	-4.00E-04	-3.60E-04	1.46E-02	1.71E-02	4.70E-03	1.11E-01

Continued on next page

Table A.5 – continued from previous page

x (cm)	x/b	$x(C_Da)$	x/scaling	U (m/s)	U adj. (m/s)	U_{rms} (m/s)	V_{rms} (m/s)	W_{rms} (m/s)	$\langle u'v' \rangle_{y=0}$ (cm^2/s^2)
95.0	15.8	9.50	8.15	8.00E-04	7.20E-04	1.67E-02	2.02E-02	5.50E-03	-1.69E-01
100.0	16.7	10.00	8.57	5.00E-03	4.50E-03	1.86E-02	1.99E-02	5.90E-03	6.93E-02
105.0	17.5	10.50	9.00	4.20E-03	3.78E-03	1.76E-02	2.02E-02	6.00E-03	2.34E-01
110.0	18.3	11.00	9.43	7.50E-03	6.75E-03	1.71E-02	1.65E-02	5.50E-03	-5.48E-02
115.0	19.2	11.50	9.86	1.14E-02	1.03E-02	1.85E-02	1.76E-02	5.80E-03	-1.00E-02
120.0	20.0	12.00	10.29	1.00E-02	9.00E-03	1.65E-02	1.99E-02	5.40E-03	-1.93E-01

Table A.6: Table of both the raw and scaled velocity statistics for the $C_Dab = 1.25$ patch. The dimensionless streamwise position x/scaling, is the dimensional position normalized by either the upstream or within-canopy adjustment scaling, as defined in §2.2. U adj. is the measured velocity that has been adjusted to account for the canopy solid volume fraction. The canopy leading edge is at $x = 0$ and the canopy centerline is at $y = 0$. These measurements are all made at the canopy centerline unless otherwise noted.

x (cm)	x/b	$x(C_Da)$	x/scaling	U (m/s)	U adj. (m/s)	U_{rms} (m/s)	V_{rms} (m/s)	W_{rms} (m/s)	$\langle uv \rangle_{y=0}$ (cm^2/s^2)
-103.0	-7.9		-7.92	9.92E-02	9.92E-02	2.47E-02	1.73E-02	6.70E-03	-1.35E-02
-93.0	-7.2		-7.15	1.00E-01	1.00E-01	2.23E-02	1.58E-02	6.40E-03	3.63E-02
-83.0	-6.4		-6.38	9.88E-02	9.88E-02	2.19E-02	1.57E-02	6.50E-03	8.91E-02
-73.0	-5.6		-5.62	9.81E-02	9.81E-02	2.15E-02	1.48E-02	6.40E-03	-1.14E-01
-63.0	-4.8		-4.85	9.92E-02	9.92E-02	1.96E-02	1.40E-02	6.20E-03	5.29E-02
-53.0	-4.1		-4.08	9.79E-02	9.79E-02	1.97E-02	1.38E-02	6.30E-03	5.96E-02
-43.0	-3.3		-3.31	9.85E-02	9.85E-02	1.88E-02	1.25E-02	6.00E-03	2.81E-02
-33.0	-2.5		-2.54	9.72E-02	9.72E-02	1.80E-02	1.20E-02	5.90E-03	-2.70E-03
-23.0	-1.8		-1.77	9.60E-02	9.60E-02	1.80E-02	1.21E-02	6.00E-03	6.42E-02
-13.0	-1.0		-1.00	9.02E-02	9.02E-02	1.79E-02	1.14E-02	5.80E-03	2.31E-02
-3.0	-0.2		-0.23	7.72E-02	7.72E-02	1.49E-02	9.80E-03	5.70E-03	6.30E-02
8.2	0.6	0.39	0.33	7.67E-02	7.32E-02	3.67E-02	3.27E-02	8.60E-03	-3.08E-01

Continued on next page

Table A.6 – continued from previous page

x (cm)	x/b	$x(C_Da)$	x/scaling	U (m/s)	U adj. (m/s)	U_{rms} (m/s)	V_{rms} (m/s)	W_{rms} (m/s)	$\langle u'v' \rangle_{y=0}$ (cm^2/s^2)
18.5	1.4	0.89	0.75	5.75E-02	5.49E-02	3.51E-02	3.01E-02	8.00E-03	4.83E-01
28.5	2.2	1.37	1.16	4.89E-02	4.67E-02	2.73E-02	2.42E-02	7.30E-03	2.96E-01
38.5	3.0	1.85	1.57	4.20E-02	4.01E-02	2.28E-02	2.09E-02	6.80E-03	4.22E-01
48.5	3.7	2.33	1.98	3.27E-02	3.12E-02	2.00E-02	1.85E-02	6.30E-03	3.78E-01
58.5	4.5	2.81	2.38	2.72E-02	2.59E-02	1.71E-02	1.46E-02	5.30E-03	9.12E-02
68.5	5.3	3.29	2.79	2.50E-02	2.39E-02	1.49E-02	1.32E-02	4.90E-03	-1.12E-01
78.5	6.0	3.77	3.20	2.08E-02	1.98E-02	1.38E-02	1.20E-02	4.60E-03	-4.50E-02
88.5	6.8	4.25	3.60	1.57E-02	1.50E-02	1.31E-02	1.11E-02	4.50E-03	1.70E-03
98.5	7.6	4.73	4.01	1.20E-02	1.14E-02	1.31E-02	1.21E-02	4.80E-03	8.92E-02
108.5	8.3	5.21	4.42	1.07E-02	1.02E-02	1.19E-02	1.06E-02	4.30E-03	4.46E-02
118.5	9.1	5.69	4.83	8.50E-03	8.11E-03	1.15E-02	1.12E-02	4.20E-03	2.52E-02
128.5	9.9	6.17	5.23	7.50E-03	7.16E-03	1.26E-02	1.28E-02	4.60E-03	8.77E-02
138.5	10.7	6.65	5.64	5.70E-03	5.44E-03	1.34E-02	1.37E-02	4.80E-03	1.20E-01
148.5	11.4	7.13	6.05	4.50E-03	4.29E-03	1.16E-02	1.30E-02	4.30E-03	7.63E-02
158.5	12.2	7.61	6.45	2.80E-03	2.67E-03	9.80E-03	1.45E-02	3.60E-03	6.65E-02
168.5	13.0	8.09	6.86	4.00E-03	3.82E-03	1.44E-02	1.78E-02	5.00E-03	1.50E-02
178.5	13.7	8.57	7.27	6.10E-03	5.82E-03	1.64E-02	2.21E-02	5.70E-03	2.26E-01

Table A.7: Table of both the raw and scaled velocity statistics for the $C_D ab = 2.0$ patch. The dimensionless streamwise position x/scaling, is the dimensional position normalized by either the upstream or within-canopy adjustment scaling, as defined in §2.2. U adj. is the measured velocity that has been adjusted to account for the canopy solid volume fraction. The canopy leading edge is at $x = 0$ and the canopy centerline is at $y = 0$. These measurements are all made at the canopy centerline unless otherwise noted.

x (cm)	x/b	$x(C_D a)$	x/scaling	U (m/s)	U adj. (m/s)	U_{rms} (m/s)	V_{rms} (m/s)	W_{rms} (m/s)	$\langle uv \rangle_{y=0}$ (cm^2/s^2)
-94.0	-9.4		-9.40	9.23E-02	9.23E-02	2.61E-02	2.09E-02	6.40E-03	1.35E-01
-84.0	-8.4		-8.40	9.23E-02	9.23E-02	2.49E-02	2.18E-02	6.30E-03	1.57E-01
-74.0	-7.4		-7.40	9.22E-02	9.22E-02	2.37E-02	2.12E-02	6.30E-03	1.97E-01
-64.0	-6.4		-6.40	9.17E-02	9.17E-02	2.46E-02	2.18E-02	6.40E-03	5.90E-02
-54.0	-5.4		-5.40	9.05E-02	9.05E-02	2.49E-02	2.35E-02	6.40E-03	-2.02E-01
-44.0	-4.4		-4.40	9.08E-02	9.08E-02	2.44E-02	2.14E-02	6.30E-03	6.19E-02
-34.0	-3.4		-3.40	8.85E-02	8.85E-02	2.20E-02	2.13E-02	6.20E-03	1.36E-01
-24.0	-2.4		-2.40	8.67E-02	8.67E-02	2.35E-02	2.21E-02	6.20E-03	4.02E-01
-14.0	-1.4		-1.40	8.41E-02	8.41E-02	2.30E-02	2.10E-02	6.10E-03	7.00E-04
-4.0	-0.4		-0.40	6.64E-02	6.64E-02	2.13E-02	2.04E-02	6.90E-03	1.39E-02
15.7	1.6	1.57	1.11	3.92E-02	3.53E-02	2.23E-02	2.38E-02	6.70E-03	-1.45E-01
22.4	2.2	2.24	1.58	2.99E-02	2.69E-02	1.55E-02	1.98E-02	5.10E-03	3.04E-02

Continued on next page

Table A.7 – continued from previous page

x (cm)	x/b	$x(C_D a)$	x/scaling	U (m/s)	U adj. (m/s)	U_{rms} (m/s)	V_{rms} (m/s)	W_{rms} (m/s)	$\langle u'v' \rangle_{y=0}$ (cm^2/s^2)
29.1	2.9	2.91	2.06	1.72E-02	1.55E-02	1.21E-02	1.80E-02	4.00E-03	5.25E-02
36.0	3.6	3.60	2.55	1.53E-02	1.38E-02	1.01E-02	1.54E-02	3.20E-03	-1.21E-02
42.2	4.2	4.22	2.98	1.09E-02	9.81E-03	8.70E-03	1.67E-02	2.60E-03	1.51E-02
48.9	4.9	4.89	3.46	9.00E-03	8.10E-03	7.60E-03	1.89E-02	2.20E-03	-1.95E-02
55.4	5.5	5.54	3.92	7.10E-03	6.39E-03	9.20E-03	2.02E-02	2.70E-03	2.22E-02
62.7	6.3	6.27	4.43	2.60E-03	2.34E-03	8.70E-03	1.80E-02	2.70E-03	-9.32E-02
72.3	7.2	7.23	5.11	2.30E-03	2.07E-03	9.30E-03	1.82E-02	3.00E-03	7.83E-02
81.9	8.2	8.19	5.79	1.50E-03	1.35E-03	1.19E-02	1.67E-02	3.50E-03	-5.13E-02
91.3	9.1	9.13	6.46	-7.00E-04	-6.30E-04	9.80E-03	1.74E-02	3.00E-03	6.81E-02
100.0	10.0	10.00	7.07	6.00E-04	5.40E-04	9.50E-03	1.63E-02	3.00E-03	1.77E-02
111.5	11.2	11.15	7.88	-2.10E-03	-1.89E-03	1.14E-02	1.76E-02	3.40E-03	1.65E-01
121.4	12.1	12.14	8.58	-5.00E-04	-4.50E-04	1.06E-02	1.75E-02	3.30E-03	4.62E-02
129.5	13.0	12.95	9.16	-6.00E-04	-5.40E-04	1.11E-02	1.92E-02	3.60E-03	2.53E-01
139.7	14.0	13.97	9.88	2.00E-04	1.80E-04	1.19E-02	2.16E-02	3.90E-03	1.20E-01
149.0	14.9	14.90	10.54	-6.00E-04	-5.40E-04	1.22E-02	1.72E-02	3.60E-03	1.42E-02
159.4	15.9	15.94	11.27	1.40E-03	1.26E-03	1.27E-02	2.05E-02	3.80E-03	1.70E-01
169.1	16.9	16.91	11.96	1.70E-03	1.53E-03	1.28E-02	2.10E-02	4.00E-03	-2.10E-03

Continued on next page

Table A.7 – continued from previous page

x (cm)	x/b	$x(C_Da)$	x/scaling	U (m/s)	U adj. (m/s)	U_{rms} (m/s)	V_{rms} (m/s)	W_{rms} (m/s)	$\langle u'v' \rangle_{y=0}$ (cm^2/s^2)
181.4	18.1	18.14	12.83	3.40E-03	3.06E-03	1.25E-02	2.34E-02	3.80E-03	-6.81E-02
191.1	19.1	19.11	13.51	3.20E-03	2.88E-03	1.37E-02	2.07E-02	4.00E-03	1.10E-01
200.9	20.1	20.09	14.21	4.60E-03	4.14E-03	1.50E-02	2.46E-02	4.40E-03	-5.96E-02
209.0	20.9	20.90	14.78	6.50E-03	5.85E-03	1.63E-02	2.26E-02	4.50E-03	1.65E-01
220.7	22.1	22.07	15.61	5.40E-03	4.86E-03	1.79E-02	2.58E-02	5.00E-03	1.60E-01
230.3	23.0	23.03	16.28	7.00E-03	6.30E-03	1.77E-02	2.50E-02	4.70E-03	5.81E-02
240.9	24.1	24.09	17.03	7.20E-03	6.48E-03	1.73E-02	2.33E-02	4.90E-03	1.78E-02
250.8	25.1	25.08	17.73	9.20E-03	8.28E-03	1.82E-02	2.26E-02	5.10E-03	2.07E-01
260.3	26.0	26.03	18.41	6.40E-03	5.76E-03	1.74E-02	2.53E-02	4.60E-03	2.74E-02
270.2	27.0	27.02	19.11	6.70E-03	6.03E-03	1.77E-02	2.45E-02	5.00E-03	-2.46E-01

Table A.8: Table of both the raw and scaled velocity statistics for the $C_Dab = 3.0$ patch. The dimensionless streamwise position x/scaling, is the dimensional position normalized by either the upstream or within-canopy adjustment scaling, as defined in §2.2. U adj. is the measured velocity that has been adjusted to account for the canopy solid volume fraction. The canopy leading edge is at $x = 0$ and the canopy centerline is at $y = 0$. These measurements are all made at the canopy centerline unless otherwise noted.

x (cm)	x/b	$x(C_Da)$	x/scaling	U (m/s)	U adj. (m/s)	U_{rms} (m/s)	V_{rms} (m/s)	W_{rms} (m/s)	$\langle uv \rangle_{y=0}$ (cm^2/s^2)
-103.0	-6.9		-6.9	9.07E-02	9.07E-02	1.63E-02	1.26E-02	4.90E-03	4.47E-02
-93.0	-6.2		-6.2	9.01E-02	9.01E-02	1.72E-02	1.24E-02	5.20E-03	-3.80E-03
-83.0	-5.5		-5.5	8.91E-02	8.91E-02	1.67E-02	1.32E-02	5.40E-03	1.00E-02
-73.0	-4.9		-4.9	8.75E-02	8.75E-02	1.72E-02	1.35E-02	5.40E-03	4.08E-02
-63.0	-4.2		-4.2	8.91E-02	8.91E-02	1.75E-02	1.37E-02	5.40E-03	7.59E-02
-53.0	-3.5		-3.5	8.80E-02	8.80E-02	1.74E-02	1.40E-02	5.50E-03	-3.17E-02
-43.0	-2.9		-2.9	8.75E-02	8.75E-02	1.79E-02	1.32E-02	5.00E-03	4.01E-02
-33.0	-2.2		-2.2	8.56E-02	8.56E-02	1.76E-02	1.36E-02	5.40E-03	5.56E-02
-23.0	-1.5		-1.5	8.23E-02	8.23E-02	1.75E-02	1.30E-02	5.20E-03	4.23E-02
-13.0	-0.9		-0.9	7.29E-02	7.29E-02	1.78E-02	1.28E-02	5.10E-03	1.08E-01
-3.0	-0.2		-0.2	5.38E-02	5.38E-02	1.71E-02	1.13E-02	7.20E-03	7.85E-02
5.4	0.4	0.5	0.3	7.54E-02	6.79E-02	3.11E-02	3.23E-02	9.90E-03	-5.94E-02

Continued on next page

Table A.8 – continued from previous page

x (cm)	x/b	$x(C_Da)$	x/scaling	U (m/s)	U adj. (m/s)	U_{rms} (m/s)	V_{rms} (m/s)	W_{rms} (m/s)	$\langle uvt \rangle_{y=0}$ (cm^2/s^2)
8.0	0.5	0.8	0.4	7.08E-02	6.37E-02	3.80E-02	3.85E-02	9.60E-03	-8.80E-02
10.1	0.7	1.0	0.6	6.83E-02	6.15E-02	2.96E-02	3.11E-02	8.10E-03	-6.49E-02
13.0	0.9	1.3	0.7	3.59E-02	3.23E-02	2.69E-02	2.63E-02	7.20E-03	-7.08E-01
15.0	1.0	1.5	0.8	4.58E-02	4.12E-02	2.55E-02	2.23E-02	7.30E-03	-5.47E-01
18.3	1.2	1.8	1.0	4.12E-02	3.71E-02	2.26E-02	2.18E-02	6.70E-03	9.07E-02
21.0	1.4	2.1	1.2	3.09E-02	2.78E-02	1.99E-02	1.90E-02	6.40E-03	-5.04E-01
23.4	1.6	2.3	1.3	1.99E-02	1.79E-02	1.79E-02	1.72E-02	5.50E-03	-2.51E-01
26.0	1.7	2.6	1.4	2.83E-02	2.55E-02	1.73E-02	1.55E-02	5.80E-03	-1.57E-01
28.3	1.9	2.8	1.6	2.90E-02	2.61E-02	1.60E-02	1.36E-02	5.30E-03	1.94E-02
30.9	2.1	3.1	1.7	2.48E-02	2.23E-02	1.46E-02	1.34E-02	4.90E-03	-9.72E-02
33.0	2.2	3.3	1.8	2.15E-02	1.94E-02	1.32E-02	1.29E-02	4.50E-03	-1.89E-02
36.0	2.4	3.6	2.0	1.55E-02	1.40E-02	1.17E-02	1.17E-02	3.80E-03	-1.05E-01
40.1	2.7	4.0	2.2	1.34E-02	1.21E-02	1.09E-02	1.09E-02	3.30E-03	-4.44E-02
41.8	2.8	4.2	2.3	1.29E-02	1.16E-02	1.02E-02	1.00E-02	3.30E-03	7.80E-03
45.0	3.0	4.5	2.5	1.04E-02	9.36E-03	1.13E-02	9.90E-03	3.40E-03	-2.80E-02
47.0	3.1	4.7	2.6	1.23E-02	1.11E-02	1.03E-02	9.50E-03	3.20E-03	-1.93E-02
50.1	3.3	5.0	2.8	1.18E-02	1.06E-02	1.04E-02	1.09E-02	3.00E-03	-1.30E-03

Continued on next page

Table A.8 – continued from previous page

x (cm)	x/b	$x(C_Da)$	x/scaling	U (m/s)	U adj. (m/s)	U_{rms} (m/s)	V_{rms} (m/s)	W_{rms} (m/s)	$\langle u'v' \rangle_{y=0}$ (cm^2/s^2)
54.0	3.6	5.4	3.0	1.02E-02	9.18E-03	1.00E-02	1.14E-02	3.00E-03	-1.74E-02
57.1	3.8	5.7	3.2	8.50E-03	7.65E-03	9.40E-03	1.14E-02	2.80E-03	-4.82E-02
60.5	4.0	6.1	3.4	9.30E-03	8.37E-03	1.01E-02	1.39E-02	3.10E-03	5.98E-02
63.0	4.2	6.3	3.5	7.40E-03	6.66E-03	1.02E-02	1.29E-02	3.10E-03	-2.27E-02
65.6	4.4	6.6	3.6	7.30E-03	6.57E-03	1.02E-02	1.59E-02	3.20E-03	3.71E-02
67.7	4.5	6.8	3.8	6.50E-03	5.85E-03	1.20E-02	1.45E-02	3.50E-03	4.55E-02
70.0	4.7	7.0	3.9	6.90E-03	6.21E-03	5.30E-03	7.20E-03	1.60E-03	1.05E-02
72.4	4.8	7.2	4.0	5.70E-03	5.13E-03	5.10E-03	5.80E-03	1.60E-03	-1.02E-02
74.9	5.0	7.5	4.2	7.20E-03	6.48E-03	4.50E-03	7.40E-03	1.30E-03	2.00E-04
76.9	5.1	7.7	4.3	7.30E-03	6.57E-03	4.80E-03	7.00E-03	1.40E-03	8.20E-03
79.7	5.3	8.0	4.4	6.50E-03	5.85E-03	5.70E-03	8.80E-03	1.70E-03	2.31E-02
83.1	5.5	8.3	4.6	4.50E-03	4.05E-03	9.60E-03	8.80E-03	2.90E-03	1.10E-02
86.7	5.8	8.7	4.8	4.00E-03	3.60E-03	1.06E-02	7.90E-03	3.50E-03	3.62E-02
88.9	5.9	8.9	4.9	4.10E-03	3.69E-03	8.80E-03	8.90E-03	2.70E-03	1.84E-02
91.7	6.1	9.2	5.1	4.00E-03	3.60E-03	7.10E-03	7.80E-03	2.10E-03	-7.30E-03
95.0	6.3	9.5	5.3	4.90E-03	4.41E-03	9.30E-03	9.20E-03	2.70E-03	1.39E-02
98.2	6.5	9.8	5.4	2.60E-03	2.34E-03	7.20E-03	7.10E-03	2.40E-03	-2.15E-02

Continued on next page

Table A.8 – continued from previous page

x (cm)	x/b	$x(C_Da)$	x/scaling	U (m/s)	U adj. (m/s)	U_{rms} (m/s)	V_{rms} (m/s)	W_{rms} (m/s)	$\langle uv \rangle_{y=0}$ (cm^2/s^2)
101.1	6.7	10.1	5.6	1.90E-03	1.71E-03	7.60E-03	7.80E-03	2.50E-03	9.10E-03
103.5	6.9	10.4	5.7	1.70E-03	1.53E-03	9.20E-03	8.40E-03	2.90E-03	4.29E-02
106.2	7.1	10.6	5.9	1.50E-03	1.35E-03	7.50E-03	7.90E-03	2.60E-03	5.30E-02
108.1	7.2	10.8	6.0	1.70E-03	1.53E-03	8.60E-03	8.40E-03	3.00E-03	1.39E-02
111.0	7.4	11.1	6.2	5.00E-04	4.50E-04	1.34E-02	9.80E-03	4.00E-03	-2.51E-02
114.1	7.6	11.4	6.3	4.00E-04	3.60E-04	9.40E-03	9.30E-03	3.10E-03	-2.07E-02
117.0	7.8	11.7	6.5	1.90E-03	1.71E-03	1.11E-02	1.47E-02	3.40E-03	-3.60E-03
119.7	8.0	12.0	6.6	1.20E-03	1.08E-03	1.06E-02	9.90E-03	3.40E-03	2.90E-02
122.1	8.1	12.2	6.8	2.70E-03	2.43E-03	1.40E-02	1.05E-02	3.70E-03	-1.24E-02
124.3	8.3	12.4	6.9	-1.00E-04	-9.00E-05	1.14E-02	1.08E-02	3.30E-03	5.30E-03
126.2	8.4	12.6	7.0	4.00E-04	3.60E-04	9.10E-03	1.06E-02	3.00E-03	3.48E-02
132.1	8.8	13.2	7.3	7.00E-04	6.30E-04	8.30E-03	9.80E-03	2.70E-03	7.80E-03
134.5	9.0	13.5	7.5	0.00E+00	0.00E+00	1.13E-02	1.29E-02	3.70E-03	6.69E-02
136.5	9.1	13.7	7.6	8.00E-04	7.20E-04	1.38E-02	1.85E-02	4.10E-03	1.72E-02
139.4	9.3	13.9	7.7	4.60E-03	4.14E-03	2.09E-02	1.44E-02	5.70E-03	2.74E-01
142.6	9.5	14.3	7.9	3.50E-03	3.15E-03	1.67E-02	1.43E-02	5.00E-03	9.07E-02
145.4	9.7	14.5	8.1	-3.00E-04	-2.70E-04	1.21E-02	1.36E-02	3.90E-03	1.05E-01

Continued on next page

Table A.8 – continued from previous page

x (cm)	x/b	$x(C_D a)$	x/scaling	U (m/s)	U adj. (m/s)	U_{rms} (m/s)	V_{rms} (m/s)	W_{rms} (m/s)	$\langle uvt \rangle_{y=0}$ (cm^2/s^2)
148.1	9.9	14.8	8.2	7.00E-04	6.30E-04	1.41E-02	1.46E-02	4.20E-03	-2.21E-02
150.7	10.0	15.1	8.4	5.00E-04	4.50E-04	1.31E-02	1.61E-02	3.90E-03	3.76E-02
153.5	10.2	15.4	8.5	-3.00E-04	-2.70E-04	1.13E-02	1.47E-02	3.80E-03	7.50E-02
155.8	10.4	15.6	8.6	9.00E-04	8.10E-04	1.40E-02	1.45E-02	4.30E-03	-2.30E-03
159.0	10.6	15.9	8.8	2.10E-03	1.89E-03	1.46E-02	1.71E-02	4.40E-03	1.01E-01
161.0	10.7	16.1	8.9	5.10E-03	4.59E-03	4.04E-02	1.76E-02	7.50E-03	1.25E-01
163.7	10.9	16.4	9.1	-2.50E-03	-2.25E-03	3.64E-02	1.73E-02	7.50E-03	-8.40E-02
166.1	11.1	16.6	9.2	1.80E-03	1.62E-03	1.98E-02	1.68E-02	5.40E-03	1.51E-01
168.8	11.3	16.9	9.4	3.00E-03	2.70E-03	1.27E-02	1.78E-02	3.90E-03	2.12E-01
172.0	11.5	17.2	9.5	2.70E-03	2.43E-03	1.37E-02	1.97E-02	4.20E-03	2.50E-01
175.3	11.7	17.5	9.7	2.60E-03	2.34E-03	2.20E-02	1.34E-02	5.70E-03	1.68E-01
177.7	11.8	17.8	9.9	2.90E-03	2.61E-03	1.40E-02	2.07E-02	4.50E-03	4.17E-02
180.0	12.0	18.0	10.0	-9.00E-04	-8.10E-04	1.57E-02	1.97E-02	6.40E-03	2.27E-01

Table A.9: Table of both the raw and scaled velocity statistics for the $C_D ab = 4.8$ patch. The dimensionless streamwise position x/scaling, is the dimensional position normalized by either the upstream or within-canopy adjustment scaling, as defined in §2.2. U adj. is the measured velocity that has been adjusted to account for the canopy solid volume fraction. The canopy leading edge is at $x = 0$ and the canopy centerline is at $y = 0$. These measurements are all made at the canopy centerline unless otherwise noted.

x (cm)	x/b	$x(C_D a)$	x/scaling	U (m/s)	U adj. (m/s)	U_{rms} (m/s)	V_{rms} (m/s)	W_{rms} (m/s)	$\langle uv \rangle_{y=0}$ (cm^2/s^2)
-103.0	-17.2		-17.17	8.52E-02	8.52E-02	1.82E-02	1.16E-02	1.16E-02	5.38E-02
-93.0	-15.5		-15.50	8.84E-02	8.84E-02	1.96E-02	1.29E-02	1.29E-02	-1.93E-02
-83.0	-13.8		-13.83	8.87E-02	8.87E-02	1.98E-02	1.50E-02	1.50E-02	4.22E-02
-73.0	-12.2		-12.17	9.11E-02	9.11E-02	2.24E-02	1.65E-02	1.65E-02	4.27E-02
-63.0	-10.5		-10.50	9.23E-02	9.23E-02	2.27E-02	1.73E-02	1.73E-02	-9.58E-02
-53.0	-8.8		-8.83	9.32E-02	9.32E-02	2.58E-02	2.05E-02	2.05E-02	-8.65E-02
-43.0	-7.2		-7.17	9.12E-02	9.12E-02	2.57E-02	2.04E-02	2.04E-02	2.22E-02
-33.0	-5.5		-5.50	8.81E-02	8.81E-02	2.82E-02	2.11E-02	2.11E-02	1.00E-02
-23.0	-3.8		-3.83	8.37E-02	8.37E-02	2.82E-02	2.03E-02	2.03E-02	-6.60E-03
-13.0	-2.2		-2.17	7.74E-02	7.74E-02	2.47E-02	1.73E-02	1.73E-02	2.51E-02
-3.0	-0.5		-0.50	4.01E-02	4.01E-02	1.70E-02	1.26E-02	1.26E-02	-1.31E-01
3.0	0.5	1.20	0.46			2.49E-02	1.33E-02	1.33E-02	4.43E-02

Continued on next page

Table A.9 – continued from previous page

x (cm)	x/b	$x(C_Da)$	x/scaling	U (m/s)	U adj. (m/s)	U_{rms} (m/s)	V_{rms} (m/s)	W_{rms} (m/s)	$\langle uvt \rangle_{y=0}$ (cm^2/s^2)
6.3	1.1	2.52	0.97	2.67E-02	1.60E-02	2.95E-02	1.94E-02	1.94E-02	-1.13E-01
9.6	1.6	3.84	1.48	2.05E-02	1.23E-02	1.58E-02	9.20E-03	9.20E-03	4.80E-02
13.1	2.2	5.24	2.02	1.29E-02	7.74E-03	8.00E-03	6.50E-03	6.50E-03	3.71E-02
16.3	2.7	6.52	2.51	7.60E-03	4.56E-03	6.20E-03	6.00E-03	6.00E-03	8.60E-03
19.7	3.3	7.88	3.03	3.20E-03	1.92E-03	6.50E-03	5.80E-03	5.80E-03	1.14E-02
22.7	3.8	9.08	3.49	7.00E-04	4.20E-04	8.00E-03	6.40E-03	6.40E-03	-1.20E-03
26.2	4.4	10.48	4.03	-1.10E-03	-6.60E-04	7.60E-03	6.40E-03	6.40E-03	-8.40E-03
29.2	4.9	11.68	4.49	-3.70E-03	-2.22E-03	7.90E-03	7.20E-03	7.20E-03	4.60E-03
31.0	5.2	12.40	4.77	-7.20E-03	-4.32E-03	6.60E-03	6.80E-03	6.80E-03	1.11E-02
34.0	5.7	13.60	5.23	-6.50E-03	-3.90E-03	7.30E-03	6.90E-03	6.90E-03	2.33E-02
37.2	6.2	14.88	5.72	-9.20E-03	-5.52E-03	6.70E-03	7.20E-03	7.20E-03	2.27E-02
40.8	6.8	16.32	6.28	-8.80E-03	-5.28E-03	6.40E-03	6.90E-03	6.90E-03	5.50E-03
44.1	7.4	17.64	6.78	-5.30E-03	-3.18E-03	6.00E-03	6.90E-03	6.90E-03	3.41E-02
47.2	7.9	18.88	7.26	-5.20E-03	-3.12E-03	6.70E-03	6.90E-03	6.90E-03	1.50E-02
51.0	8.5	20.40	7.85	-4.10E-03	-2.46E-03	8.70E-03	8.80E-03	8.80E-03	1.87E-02
54.2	9.0	21.68	8.34	-4.10E-03	-2.46E-03	9.20E-03	9.00E-03	9.00E-03	-1.70E-02
57.5	9.6	23.00	8.85	-3.40E-03	-2.04E-03	9.30E-03	8.00E-03	8.00E-03	9.40E-03

Table A.10: Table of both the raw and scaled velocity statistics for the $C_D ab = 8.0$ patch. The dimensionless streamwise position x/scaling, is the dimensional position normalized by either the upstream or within-canopy adjustment scaling, as defined in §2.2. U adj. is the measured velocity that has been adjusted to account for the canopy solid volume fraction. The canopy leading edge is at $x = 0$ and the canopy centerline is at $y = 0$. These measurements are all made at the canopy centerline unless otherwise noted.

x (cm)	x/b	$x(C_D a)$	x/scaling	U (m/s)	U adj. (m/s)	U_{rms} (m/s)	V_{rms} (m/s)	W_{rms} (m/s)	$\langle u'v' \rangle_{y=0}$ (cm^2/s^2)
-103.0	-10.3		-10.30	9.65E-02	9.65E-02	1.22E-02	1.13E-02	4.20E-03	-1.29E-02
-93.0	-9.3		-9.30	9.41E-02	9.41E-02	1.21E-02	1.15E-02	4.10E-03	2.60E-02
-83.0	-8.3		-8.30	9.54E-02	9.54E-02	1.22E-02	1.14E-02	4.10E-03	1.35E-02
-73.0	-7.3		-7.30	9.27E-02	9.27E-02	1.24E-02	1.16E-02	4.40E-03	-3.20E-03
-63.0	-6.3		-6.30	9.34E-02	9.34E-02	1.31E-02	1.18E-02	4.40E-03	2.81E-02
-53.0	-5.3		-5.30	9.44E-02	9.44E-02	1.26E-02	1.12E-02	4.30E-03	1.64E-02
-43.0	-4.3		-4.30	8.98E-02	8.98E-02	1.25E-02	1.14E-02	4.30E-03	4.60E-03
-33.0	-3.3		-3.30	8.89E-02	8.89E-02	1.24E-02	1.18E-02	4.20E-03	3.98E-02
-23.0	-2.3		-2.30	8.37E-02	8.37E-02	1.21E-02	1.11E-02	4.20E-03	4.39E-02
-13.0	-1.3		-1.30	7.39E-02	7.39E-02	1.18E-02	1.09E-02	4.30E-03	-7.20E-03
-10.0	-1.0		-1.00	7.07E-02	7.07E-02	1.45E-02	1.06E-02	4.90E-03	1.94E-02
-7.0	-0.7		-0.70	6.23E-02	6.23E-02	1.46E-02	1.10E-02	6.20E-03	-1.93E-02

Continued on next page

Table A.10 – continued from previous page

x (cm)	x/b	$x(C_Da)$	x/scaling	U (m/s)	U adj. (m/s)	U_{rms} (m/s)	V_{rms} (m/s)	W_{rms} (m/s)	$\langle u'v' \rangle_{y=0}$ (cm^2/s^2)
4.2	0.4	1.68	0.41	6.22E-02	3.73E-02	1.83E-02	2.04E-02	8.90E-03	-2.12E-02
9.2	0.9	3.68	0.89	4.76E-02	2.86E-02	1.46E-02	1.13E-02	4.60E-03	8.40E-03
14.2	1.4	5.68	1.38	1.61E-02	9.66E-03	1.19E-02	1.25E-02	3.20E-03	9.16E-02
19.5	2.0	7.80	1.89	4.00E-03	2.40E-03	9.70E-03	1.09E-02	3.20E-03	2.66E-02
24.5	2.5	9.80	2.38	2.50E-03	1.50E-03	9.50E-03	1.18E-02	3.30E-03	-1.32E-02
29.3	2.9	11.72	2.84	-6.00E-04	-3.60E-04	9.60E-03	1.00E-02	4.20E-03	-9.10E-03
34.6	3.5	13.84	3.36	-2.30E-03	-1.38E-03	1.05E-02	1.23E-02	3.90E-03	-1.33E-02
39.2	3.9	15.68	3.80	-2.50E-03	-1.50E-03	1.06E-02	1.43E-02	3.80E-03	4.32E-02
44.4	4.4	17.76	4.31	-3.70E-03	-2.22E-03	1.13E-02	1.59E-02	3.70E-03	4.68E-02
48.8	4.9	19.52	4.73	-5.60E-03	-3.36E-03	1.18E-02	2.22E-02	3.50E-03	8.80E-02
54.0	5.4	21.60	5.24	-5.00E-03	-3.00E-03	1.16E-02	1.89E-02	3.60E-03	3.26E-02
59.3	5.9	23.72	5.75	-5.70E-03	-3.42E-03	1.33E-02	1.71E-02	4.00E-03	5.90E-03
64.7	6.5	25.88	6.28	-4.70E-03	-2.82E-03	1.43E-02	1.82E-02	4.30E-03	8.88E-02
70.0	7.0	28.00	6.79	-1.80E-03	-1.08E-03	1.18E-02	1.56E-02	3.90E-03	-6.71E-02
74.6	7.5	29.84	7.24	-2.40E-03	-1.44E-03	9.70E-03	1.13E-02	3.50E-03	-3.80E-03

Table A.11: Table of the Reynolds Stress data for the $C_D ab = 0.53$ patch.

x (cm)	$\langle u'v' \rangle_{y=0}$ (cm^2/s^2)	$\langle u'v' \rangle_{y=b/2}$ (cm^2/s^2)
-103.0	1.77E-02	2.70E-02
-83.0	2.27E-02	-1.16E-02
-63.0	5.17E-02	-3.25E-02
-43.0	9.08E-02	3.15E-02
-23.0	6.49E-02	2.55E-02
-13.0	2.13E-02	9.04E-02
-3.0	1.27E-02	2.51E-02
16.5	4.60E-01	5.70E-01
36.7	2.10E-01	3.93E-01
56.1	2.94E-01	2.97E-01
76.2	1.19E-01	2.67E-01
96.0	1.11E-01	4.02E-01
115.7	-2.58E-02	5.70E-01
137.3	2.97E-02	1.40E+00
157.0	-3.51E-02	1.82E+00
177.5	1.84E-01	2.55E+00
197.9	1.49E-01	3.18E+00
217.7	3.21E-02	3.08E+00
237.5	2.99E-01	3.81E+00
258.1	3.15E-01	3.81E+00
277.9	1.75E-01	3.71E+00
297.7	5.61E-01	4.29E+00
316.6	-5.61E-02	4.30E+00
336.9	2.86E-01	5.37E+00
356.6	1.09E-01	4.80E+00
377.3	4.33E-01	4.95E+00
397.3	9.64E-02	5.22E+00

Table A.12: Table of the lateral transect velocity data for the $C_Dab = 0.53$ patch.

y (cm)	u (m/s)	$\langle u'v' \rangle_{x=360cm}$ (cm^2/s^2)	v_{rms} (m/s)
0	0.0336	0.7034	0.0292
4.2	0.0324	-0.2895	0.0276
7.4	0.0415	-1.9713	0.0284
10.4	0.0615	-5.8653	0.0274
13.4	0.0729	-4.5874	0.0232
16.4	0.084	-4.876	0.0253
19.4	0.0934	-4.3368	0.025
22.4	0.1031	-3.7899	0.0243
25.4	0.1152	-2.1075	0.0223
28.4	0.1194	-2.3658	0.0242
34.4	0.1307	-0.8064	0.0195
40.4	0.1291	-0.0874	0.0177
44.4	0.1291	0.0633	0.0119
49.4	0.1261	0.0354	0.011

Table A.13: Table of the lateral transect velocity data with a splitter plate in place for the $C_Dab = 0.53$ patch.

y (cm)	u (m/s)	$\langle u'v' \rangle_{x=360cm}$ (cm^2/s^2)	v_{rms} (m/s)
2.2	0.0078	-0.0446	0.0076
4	0.0121	0.0554	0.0085
7.4	0.016	-0.2405	0.0117
10.4	0.032	-1.0147	0.0178
13.4	0.0647	-1.21	0.0179
16.4	0.0808	-0.8194	0.0174
19.4	0.1028	-0.5023	0.0158
22.4	0.1147	-0.407	0.0143
25.4	0.127	-0.1407	0.0126
28.4	0.1325	-0.01	0.011
34.4	0.1339	0.0275	0.0101
40.4	0.1329	0.0772	0.0095
44.4	0.1301	0.0866	0.0098
49.4	0.1286	0.0191	0.0094

Table A.14: Table of the Reynolds Stress data for the $C_D ab = 2.0$ patch.

x (cm)	$\langle u'v' \rangle_{y=0}$ (cm^2/s^2)	$\langle u'v' \rangle_{y=b/2}$ (cm^2/s^2)
-94.0	1.35E-01	2.06E-01
-84.0	1.57E-01	1.60E-01
-74.0	1.97E-01	9.87E-02
-64.0	5.90E-02	5.44E-02
-54.0	-2.02E-01	5.27E-02
-44.0	6.19E-02	9.70E-03
-34.0	1.36E-01	-3.80E-02
-24.0	4.02E-01	2.20E-02
-14.0	7.00E-04	-1.02E-02
-4.0	1.39E-02	6.30E-02
15.7	-1.45E-01	6.50E-01
22.4	3.04E-02	3.95E-01
29.1	5.25E-02	3.58E-01
36.0	-1.21E-02	1.74E-01
42.2	1.51E-02	1.48E-01
48.9	-1.95E-02	1.37E-01
55.4	2.22E-02	1.52E-01
62.7	-9.32E-02	2.73E-01
72.3	7.83E-02	3.67E-01
81.9	-5.13E-02	5.10E-01
91.3	6.81E-02	1.03E+00
100.0	1.77E-02	1.29E+00
111.5	1.65E-01	1.62E+00
121.4	4.62E-02	2.31E+00
129.5	2.53E-01	3.29E+00
139.7	1.20E-01	3.74E+00
149.0	1.42E-02	4.45E+00
159.4	1.70E-01	4.31E+00
169.1	-2.10E-03	4.77E+00
181.4	-6.81E-02	4.42E+00
191.1	1.10E-01	3.79E+00
200.9	-5.96E-02	4.90E+00
209.0	1.65E-01	5.56E+00
220.7	1.60E-01	4.31E+00
230.3	5.81E-02	4.31E+00
240.9	1.78E-02	3.63E+00
250.8	2.07E-01	4.25E+00
260.3	2.74E-02	4.01E+00
270.2	-2.46E-01	4.55E+00

Table A.15: Table of the lateral transect velocity data for the $C_Dab = 2.0$ patch.

y (cm)	u (m/s)	$\langle u'v' \rangle_{x=262cm}$ (cm^2/s^2)	v_{rms} (m/s)
0	0.0064	0.0142	0.0225
2	0.0075	-0.1393	0.023
3.9	0.0082	-0.1176	0.024
6	0.0105	-0.613	0.0256
7.9	0.013	0.1588	0.0248
10	0.045	-6.8172	0.0294
12	0.06	-4.6126	0.0213
15	0.0748	-3.8494	0.0222
18	0.0869	-3.3325	0.021
21	0.0965	-2.6546	0.0229
25	0.1136	-2.0392	0.0222
29	0.1227	-1.204	0.0228
33	0.1322	-0.3007	0.0177
38	0.1319	-0.0995	0.0151
43	0.127	0.0646	0.0123
49	0.125	-0.0447	0.0118

Table A.16: Table of the lateral transect velocity data with the splitter plate in place for the $C_Dab = 2.0$ patch.

y (cm)	u (m/s)	$\langle u'v' \rangle_{x=262cm}$ (cm^2/s^2)	v_{rms} (m/s)
3	0.0032	-0.0055	0.008
6	0.0042	0.0066	0.0085
7.9	0.0046	0.0278	0.0108
10	0.0298	-1.0028	0.0187
13	0.0669	-0.8059	0.0174
18	0.1019	-0.6526	0.0166
23	0.1231	-0.2898	0.014
28	0.1298	-0.0204	0.0104
33	0.1296	0.0245	0.0099
38	0.1301	0.0061	0.0096
43	0.1287	0.0664	0.0093
49	0.1229	0.0849	0.01

Appendix B

Numerical Solution of Dynamic Flag Equation

We solved the dynamic flag equation using a Chebyshev spectral method and by advancing the system through time implicitly using Broyden's method. We began by incorporating the boundary conditions into the governing equation, such that they are automatically satisfied at every time step. The alternative approach would require manipulation of the differentiation and quadrature matrices in an ad hoc manner that would introduce error into the system. We satisfy the free end ($s = 1$) boundary conditions integrating Eq. B.1 over length, beginning from the free end. In this method, the boundary conditions appear as constants of integration, which can be easily satisfied through replacement with their known values.

$$\mu \frac{\partial^2}{\partial \tau^2} \hat{\zeta} = -\eta \frac{\partial}{\partial \hat{s}} \left[\theta_{\hat{s}\hat{s}} \boldsymbol{n} \right] + \frac{\partial}{\partial \hat{s}} \left[T \boldsymbol{t} \right] + F \tag{B.1}$$

We first integrate Eq. B.1 from $s = 1$ to s:

$$\mu \int_1^s \frac{\partial^2}{\partial \tau^2} \hat{\zeta} \mathrm{d}s = -\eta \left[\theta_{\hat{s}\hat{s}}(s,\tau) \boldsymbol{n} - \theta_{\hat{s}\hat{s}}(1,\tau) \boldsymbol{n} \right] + \left[T(s,\tau) \boldsymbol{t} - T(1,\tau) \boldsymbol{t} \right] + \int_1^s F \mathrm{d}s \tag{B.2}$$

where $\theta_{\hat{s}\hat{s}}(1,\tau) = 0$ and $T(1,\tau) = 0$. We treat the flag tension as slaved to the

flag motion, and therefore can uncouple the tension from the governing equation. By eliminating the terms that satisfy the free end condition and by taking only the normal component of Eq. B.2, leaves

$$\mu \int_1^s \frac{\partial^2}{\partial \tau^2} \hat{\zeta} \, \mathrm{d}s \, \boldsymbol{n} = -\eta \left[\theta_{\hat{s}\hat{s}}(s,\tau) \right] + \int_1^s F \, \mathrm{d}s \, \boldsymbol{n} \tag{B.3}$$

We then integrate Eq. B.3 from $s = 1$ to satisfy the curvature condition.

$$\mu \int_1^s \int_1^s \frac{\partial^2}{\partial \tau^2} \hat{\zeta} \, \mathrm{d}s \, \boldsymbol{n} \, \mathrm{d}s = -\eta \left[\theta_{\hat{s}}(s,\tau) \right] + \int_1^s \int_1^s F \, \mathrm{d}s \, \boldsymbol{n} \, \mathrm{d}s \tag{B.4}$$

This leaves the governing equation in a form which we can solve iteratively, minimizing the residual error at each step:

$$0 = \mu \int_1^s \int_1^s \frac{\partial^2}{\partial \tau^2} \hat{\zeta}^{n+1} \, \mathrm{d}s \, \boldsymbol{n}^{n+1} \, \mathrm{d}s + \eta \left[\theta_{\hat{s}}^{n+1}(s,\tau) \right] - \int_1^s \int_1^s F^{n+1} \, \mathrm{d}s \, \boldsymbol{n}^{n+1} \, \mathrm{d}s \tag{B.5}$$

Each iteration is initialized with a guess for $\theta_{\hat{s}}^{n+1}$. We then solve for θ^{n+1}, ζ^{n+1}, $\boldsymbol{t}^{n+1}$ and $\boldsymbol{n}^{n+1}$,

$$\theta^{n+1} = \int_{-1}^s \theta_{\hat{s}}^{n+1} \, \mathrm{d}s \tag{B.6}$$

$$\zeta^{n+1} = \int_{-1}^s \hat{u} \theta^{n+1} \, \mathrm{d}s \tag{B.7}$$

$$\boldsymbol{t}^{n+1} = \begin{Bmatrix} \cos \theta^{n+1} \\ \sin \theta^{n+1} \end{Bmatrix} \tag{B.8}$$

$$\boldsymbol{n}^{n+1} = \begin{Bmatrix} -\sin \theta^{n+1} \\ \cos \theta^{n+1} \end{Bmatrix} \tag{B.9}$$

The fluid forcing term, F^{n+1}, is the sum of the fluid added mass and the fluid drag forces.

$$\hat{F}_{a.m}^{n+1} = \frac{\pi}{4}\frac{b}{l}\frac{\partial \hat{V}^{n+1}}{\partial \tau} - \frac{\pi}{4}\frac{b}{l}\frac{\partial^2 \hat{\zeta}^{n+1}}{\partial \tau^2} \tag{B.10}$$

$$\begin{aligned}\hat{F}_d^{n+1} = {} & \tfrac{1}{2}C_D\left(\hat{V}^{n+1} - \frac{\partial \hat{\zeta}^{n+1}}{\partial \tau}\right)\left|\left(\hat{V}^{n+1} - \frac{\partial \hat{\zeta}^{n+1}}{\partial \tau}\right)\boldsymbol{n}^{n+1}\right| \\ & + \tfrac{1}{2}C_f\left(\hat{V}^{n+1} - \frac{\partial \hat{\zeta}^{n+1}}{\partial \tau}\right)\left|\left(\hat{V}^{n+1} - \frac{\partial \hat{\zeta}^{n+1}}{\partial \tau}\right)\boldsymbol{t}^{n+1}\right|\end{aligned} \tag{B.11}$$

The flag velocity and acceleration terms in the above equations are discretized with second order accurate backwards differentiation schemes:

$$\frac{\partial}{\partial \tau}\hat{\zeta}^{n+1} = \frac{1}{2\Delta\tau}\left(3\zeta^{n+1} - 4\zeta^{n} + 1\zeta^{n-1}\right) \tag{B.12}$$

$$\frac{\partial^2}{\partial \tau^2}\hat{\zeta}^{n+1} = \frac{1}{\Delta\tau^2}\left(2\zeta^{n+1} - 5\zeta^{n} + 4\zeta^{n-1} - \zeta^{n-2}\right) \tag{B.13}$$

Following the integration of our governing equation (Eq. B.1), we must solve a partial integro-differential equation in which there are no spatial derivatives (Eq. B.5), only spatial integrals. We employ a specific type of spectral method to solve this equation. Spectral methods are an alternative approach to spatial differentiation and integration than the more widely used finite difference methods. The defining feature of spectral methods is that rather than using local approximations to derivatives and integrals, a sum of basis functions is used that is non-zero over the entire domain, thus being a *global* approach.

Curtis-Clenshaw quadrature is a type of numerical quadrature that employs the Chebyshev grid to evaluate an integral [16, 106]. We have constructed integration matrices which spatially integrate functions from both the clamped end, $s = -1$, and the free end, $s = 1$, of the flag, as seen in Eqs. B.5, B.6 and B.7. These matrices operate in a manner identical to differentiation matrices. Below, we show the code used to generate these matrices.

The iterative method we used to advance the solution through time, Broyden's

method, works in the following manner. The system is started from rest. The flag is initially at the undeflected posture along the $\hat{z} = 0$ line and the velocity potential and the vortex street celerity are ramped up smoothly from zero using the function $[1-\exp(-\tau)]$. At each timestep, we form an initial guess for θ^{n+1} based on a quadratic extrapolation from the three previous time points. With this initial guess, we calculate the residual of Eq. B.5 and form an initial finite difference approximation to the Jacobian of the system. The Jacobian is inverted and we then proceed with Broyden's method until the iterations arrive at a θ^{n+1} that brings the residual beneath a predefined tolerance. The unique feature of Broyden's method is that within the iterative loop, the inverse Jacobian is updated directly. This greatly improves computational efficiency as inverting the Jacobian matrix is often the most computationally intensive portion of Newton's method.

```
%% script_flag_final.m

close all
clear all
clc

%%  User Defined Parameters
% Number of points in the Chebyshev grid
N=100;


%Dan Tam's quadrature code, MintCC is integral from -1 to s
[x,sx,MintCC] = clencurt(N);

%initial condition is undeflected. K(:,1:3)=curvature at the three
% previous timesteps
% K(:,4) is curvature to be solved for
K(:,1:4)=zeros(N+1,4);

% Define parameters
T_end=60;  % dimensionless time duration of simulation
dt=1E-4;  % time resolution
T=dt:dt:T_end;
TOL=1E-7;  % convergence tolerance in iterative method
mu=1E-4;  % solid/fluid inertia parameter
AR_bl=0.1;  % Added mass parameter


eta_exps=-4.5;  % ETA = 10^eta_exps

%% Advance Solution Through Time
for jjj=1:length(eta_exps)
    eta=10^(eta_exps(jjj));
    % eta=10^(-4.0);
    lD=6;

    % Pre-allocate arrays for output
    save_int=50;
    x_save=zeros(N+1,(T_end*save_int)+1);
    z_save=zeros(N+1,(T_end*save_int)+1);
    T_save_x=zeros(N+1,(T_end*save_int)+1);
    T_save_z=zeros(N+1,(T_end*save_int)+1);
            theta=MintCC*K(:,1);
            utheta=[cos(theta) sin(theta)];
            zeta=MintCC*utheta;
            x_save(:,1)=zeta(:,1);
            z_save(:,1)=zeta(:,2);

    its_save=zeros(size(T));

    tic

    % loop to advance through time
    for jj=1:length(T)
```

```
    %initial_guess is parabolic extrapolation using previous 3 times
    IG=(3*K(:,3))-(3*K(:,2))+K(:,1);
    K3=K(:,3);
    K2=K(:,2);
    K1=K(:,1);


    %solve for new curvature (k(:,3))
    % use Lindfield and Penny's broyden matlab function modified
    % pass an initial guess (IG) into broyden_mod, along with a TOL
    % solve for K(:,4)
    [K(:,4),it,fp]=broyden_final(IG,N,TOL,K3,K2,K1,mu,...
        eta,MintCC,dt,jj,T,lD,AR_bl);

    % break code if broyden's method fails to converge
    if it==100
        elapsed_time=toc;
        return;
    end

    its_save(jj)=it;
    % save x and z positions at desired intervals
    if rem(jj,(1/(save_int*dt)))==0
        theta=MintCC*K(:,4);
        utheta=[cos(theta) sin(theta)];
        zeta=MintCC*utheta;
        zeta_3=MintCC*([cos(MintCC*K3) sin(MintCC*K3)]);
        zeta_2=MintCC*([cos(MintCC*K2) sin(MintCC*K2)]);
        zeta_1=MintCC*([cos(MintCC*K1) sin(MintCC*K1)]);
        flag_accel=(1/(dt^2))*((2*zeta) - ...
            (5*zeta_3)+(4*zeta_2) - zeta_1);
        x_save(:,round(jj/(1/(save_int*dt)))+1)=zeta(:,1);
        z_save(:,round(jj/(1/(save_int*dt)))+1)=zeta(:,2);

        % calculate flag tension
        n_hat=[-sin(theta) cos(theta)];
        T_tan=mu*(MintCC_p1(flag_accel,MintCC))+(eta.*...
            [K(:,4).*n_hat(:,1) K(:,4).*n_hat(:,2)]) - ...
            MintCC_p1(fp,MintCC);
        T_save_x(:,round(jj/(1/(save_int*dt)))+1)=T_tan(:,1);
        T_save_z(:,round(jj/(1/(save_int*dt)))+1)=T_tan(:,2);
    end

    %update old curvatures
    K(:,1)=K(:,2);
    K(:,2)=K(:,3);
    K(:,3)=K(:,4);


end
elapsed_time=toc;

% Save output and display simulation metrics
```

```
    save(['flag_output_init_eta_' num2str(log10(eta), '%-0.1f')...
        '_mu_' num2str(log10(mu)) '_lD_' num2str(lD) '_lamda6d.mat'],...
        'elapsed_time','T','x_save','z_save','T_save_x','T_save_z');
    disp(jjj);
    disp(elapsed_time/60);
end
```

```
%% broyden_final.m
function [xv,it,fp,Br]=broyden_final(IG,N,TOL,K3,K2,K1,mu,eta,...
    MintCC,dt,jj,T,lD,AR_bl)
% Broyden's method for solving a system of n non-linear equations
% in n variables.
%
% IG is initial guess for the curvature
% N is number of points in the Chebyshev grid
% TOL is user defined tolerance
% K1,K2,K3 are curvatures at previous timesteps
% mu,eta, lD, AR_bl are the physical parameters of the flag system
% MintCC is the integration matrix from -1 to s
% dt is time step interval
% jj is time index in simulation
% T is time vector


% MODIFIED from Lindfield and Penny
% BY JTR 2012/10/09 to make broyden.m use f_func to calculate residual


%% Form initial Jacobian
% define small delx for finite difference approximation for initial
% Jacobian
delx=dt/100;
delx=delx(:);
it=0; xv=IG;

% calculate initial residual
[fr,fp]=f_func_final(xv,K3,K2,K1,mu,eta,MintCC,dt,N,jj,T,lD,AR_bl);

% calculate initial Jacobian
J_0=zeros(N+1,N+1);
for j=1:(N+1)
    xv2=xv;
    xv2(j)=xv(j)+delx;
    [fr2,fp]=f_func_final(xv2,K3,K2,K1,mu,eta,MintCC,dt,N,jj,T,lD,AR_bl);
    J_0(:,j)=(fr2-fr)./delx;
end


% initial Br is inv of finite Diff Jacobian created above

Br=inv(J_0);  %create initial J_inv,

%% Iterate until converges at new curvature
oldpr=0;
pr=10; %initial values of oldpr and pr to start iterations
while norm(pr-oldpr)>TOL
  it=it+1;
  if it==100
      disp('convergence failed');
      return;
  end
```

```
  oldpr=pr;
  pr=-Br*fr;
  tau=1;
  xv1=xv+tau*pr;
  xv=xv1; %updates xv1 and xv

  %update "oldfr"
  oldfr=fr;
  %update fr with new xv
  [fr,fp]=f_func_final(xv,K3,K2,K1,mu,eta,MintCC,dt,N,jj,T,lD,AR_bl);

  %Update approximation to Jacobian using Broyden's formula
  y=fr-oldfr; oldBr=Br;
  oyp=oldBr*y-pr; pB=pr'*oldBr;
  M=oyp*pB; %%%(N+1 x 1) x (1 x N+1) = (N+1 x N+1)
  Br=oldBr-M./(pr'*oldBr*y);
end;
```

```
%% f_func_final.m
function [f_output,fp]=f_func_final(IG,K3,K2,K1,mu,eta,...
    MintCC,dt,N,jj,T,lD,AR_bl)


%% Calculate zeta, theta, n_hat and t_hat from curvatures
%calculate theta, normal and tangential vectors based on IG for K(:,4)
theta=MintCC*IG;
n_hat=[-sin(theta) cos(theta)];
t_hat=[cos(theta) sin(theta)];


% calculate position vectors using known curvatures
zeta=MintCC*([cos(MintCC*IG) sin(MintCC*IG)]);
zeta_3=MintCC*([cos(MintCC*K3) sin(MintCC*K3)]);
zeta_2=MintCC*([cos(MintCC*K2) sin(MintCC*K2)]);
zeta_1=MintCC*([cos(MintCC*K1) sin(MintCC*K1)]);


%2nd order accurate back difference for velocity term
flag_vel=(1/(2*dt)).*((3.*zeta)-(4.*zeta_3)+zeta_2);
%2nd order accurate accel term
flag_accel=(1/(dt^2))*((2*zeta) - (5*zeta_3)+(4*zeta_2) - zeta_1);



%%  Calculate Fluid Velocity
% Define ramping function
Ramp_up=(1-exp(-T(jj)));
% U_v_U=(1-.2049).*Ramp_up; %for lambda = 4D (lD = 3)
U_v_U=Ramp_up.*(0.9);  % for lambda = 6D  (lD = 6)



%define flag position in complex form at current and previous timesteps
z=zeta(:,1)+(1i.*zeta(:,2))-(U_v_U*T(jj));
z_t1=zeta(:,1)+(1i.*zeta(:,2))-(U_v_U*(T(jj)-dt));
z_t2=zeta(:,1)+(1i.*zeta(:,2))-(U_v_U*(T(jj)-(2*dt)));


% Fluid potential at current and previous timesteps
dwdz_U=Ramp_up.*( 1+(1i*5/24).*cot((pi/6)*z*lD - (1i*pi/12)) - ...
    (1i*5/24).*cot((pi/6)*z*lD + (pi/2) + (1i*pi/12)) );
dwdz_U_t1=Ramp_up.*( 1+(1i*5/24).*cot((pi/6)*z_t1*lD - (1i*pi/12)) -...
    (1i*5/24).*cot((pi/6)*z_t1*lD + (pi/2) + (1i*pi/12)) );
dwdz_U_t2=Ramp_up.*( 1+(1i*5/24).*cot((pi/6)*z_t2*lD - (1i*pi/12)) -...
    (1i*5/24).*cot((pi/6)*z_t2*lD + (pi/2) + (1i*pi/12)) );


% Define dimensionless threshold to account for singularity at vortex
% cores
% Thresh = 1 corresponds to U_inf
```

```
Thresh=Ramp_up*1;


% Apply threshold to velocities
u_U=real(dwdz_U); u_U(u_U>Thresh)=Thresh; u_U(u_U<-Thresh)=-Thresh;
v_U=-imag(dwdz_U); v_U(v_U>Thresh)=Thresh; v_U(v_U<-Thresh)=-Thresh;

u_U_t1=real(dwdz_U_t1); u_U_t1(u_U_t1>Thresh)=Thresh; ...
    u_U_t1(u_U_t1<-Thresh)=-Thresh;
v_U_t1=-imag(dwdz_U_t1); v_U_t1(v_U_t1>Thresh)=Thresh; ...
    v_U_t1(v_U_t1<-Thresh)=-Thresh;

u_U_t2=real(dwdz_U_t2); u_U_t2(u_U_t2>Thresh)=Thresh; ...
    u_U_t2(u_U_t2<-Thresh)=-Thresh;
v_U_t2=-imag(dwdz_U_t2); v_U_t2(v_U_t2>Thresh)=Thresh; ...
    v_U_t2(v_U_t2<-Thresh)=-Thresh;


fluid_vel=[u_U v_U];
f_v_t1=[u_U_t1 v_U_t1];
f_v_t2=[u_U_t2 v_U_t2];


%% Calculate fluid forcing
% Define normal and tangential drag coefficients
CD=1.9;
Cf=0.02;


%calculate fp based on IG
F_D=Ramp_up.*(0.5.*CD.*(fluid_vel-flag_vel).*abs((fluid_vel-...
    flag_vel).*n_hat) + 0.5.*Cf.*(fluid_vel-flag_vel)...
    .*abs((fluid_vel-flag_vel).*t_hat));


% fluid acceleration part of the added mass term
% the solid acceleration part of the added mass term is wrapped up in
% mu=mu_0 + pi/4 * AR_bl, times the solid acceleration
F_am_temp=(pi/4).*AR_bl.*((3.*fluid_vel)-(4.*f_v_t1)+f_v_t2)./(2*dt);

F_am_solid_accel=(pi/4).*AR_bl.*flag_accel;


% total added mass is the relative acceleration between fluid and solid
F_am=F_am_temp-F_am_solid_accel;


% total fluid forcing is sum of added mass and drag forces
fp=F_D+F_am;


% utilized MintCC_p1 function which integrates from +1 to s
AA=MintCC_p1(flag_accel,MintCC);
```

```
% define output
f_output = (mu) * (MintCC_p1(dot(n_hat,AA,2),MintCC))...
        + (eta)*IG ...
        - MintCC_p1(dot(n_hat,(MintCC_p1(fp,MintCC)),2),MintCC);
```

```
% clencurt.m
% <http://www.mathworks.com CLENCURT: Computes weights and matrices for
clenshawcurtis int.
% x (Chebyshev points)
% theta (cos(theta)=x)
% Msin,Mcc,w: weight for clenshaw curtis int in diff cases.
% MintCC: Full integration matrix
%
function [x,sx,MintCC] = clencurt(N)
theta = pi*(0:N)'/N; x = cos(theta); sx = sin(theta);
%
% % Weights for Clenn Curtis integration of f(t)/sqrt(1-t^2)
% Msin  = zeros(N+1,N+1);
% for i = 1:N+1
% Msin(i,:) = -sin(theta(i)*(0:N))./(0:N);
% end
% Msin(:,1) = -theta(:);
%
% % Weights for direct integration of the singular integral equation
% Mcc   = zeros(N+1,N+1);
% for i = 1:N+1
% Mcc(:,i) = sin((i-1)*theta).*sin(theta);
% end
%
% % Weight for standart Clenn Curtis integration
% w = zeros(1,N+1); ii = 2:N; v = ones(N-1,1);
% if mod(N,2)==0
% w(1) = 1/(N^2-1); w(N+1) = w(1);
% for k=1:N/2-1, v = v - 2*cos(2*k*theta(ii))/(4*k^2-1); end
% v = v - cos(N*theta(ii))/(N^2-1);
% else
% w(1) = 1/N^2; w(N+1) = w(1);
% for k=1:(N-1)/2, v = v - 2*cos(2*k*theta(ii))/(4*k^2-1); end
% end
% w(ii) = 2*v/N;
%
% Integration matrix Clen Curtis + boundary condition.
% MintCC = zeros(N+1,N+1);
for  i = 1 : N+1
%      Compute ith column of the integration matrix.
     Y = zeros(N+1,1); Y(i) = 1; % ith base vector
     a = ChebProj(Y);             % Cheb exp of ith base vector
     MintCC(:,i) = a(1)*(1+cos(theta)) + a(2)/4*(-1+cos(2*theta));
     for j = 3:N+1
     MintCC(:,i) = MintCC(:,i) + a(j)*((-1)^(j)/((j-1)^2-1) ...
                               + 1/2*(cos(j*theta)/j-cos((j-2)*theta)/
(j-2)));                 % ith column vector.
     end
end
```

```
%% MintCC_p1.m
function [output]=MintCC_p1(input,MintCC)

if size(input,2)==1
output=MintCC*input-(MintCC(1,:)*input);

end
if size(input,2)==2
    output(:,1)=MintCC*input(:,1)-(MintCC(1,:)*input(:,1));
    output(:,2)=MintCC*input(:,2)-(MintCC(1,:)*input(:,2));

end
```

Appendix C

Flume Mixing Test

To determine when the $CHBr_2Cl$ is fully-mixed in the flume, we conducted a preliminary experiment using Rhodamine WT as a surrogate tracer. We make the physically reasonable assumption that the mixing of Rhodamine WT and $CHBr_2CL$ are governed by the same turbulent diffusivities and dispersion processes and are independent of molecular diffusivities, allowing Rhodamine to be used a physical surrogate for $CHBr_2CL$. In this experiment, we started the flume at $U_\infty = 20$ cm/s and injected a 3 mL slug of Rhodamine WT at the pump intake. We continuously measured the concentration of Rhodamine WT using a fluorometer. The concentration measurement shows the characteristic passing peaks of the initial slug, which decay in peak concentration as the plume recirculates through the flume. To determine when the initial mass is fully-mixed over the entire flume volume, we calculate the moving-window, temporal standard deviation of the concentration, using the flume recirculation period as the window size. The flume recirculation period is simply the distance between peaks in Fig. C-1a. This temporal standard deviation vanishes when the flume is fully mixed after 2000 s (Fig. C-1b).

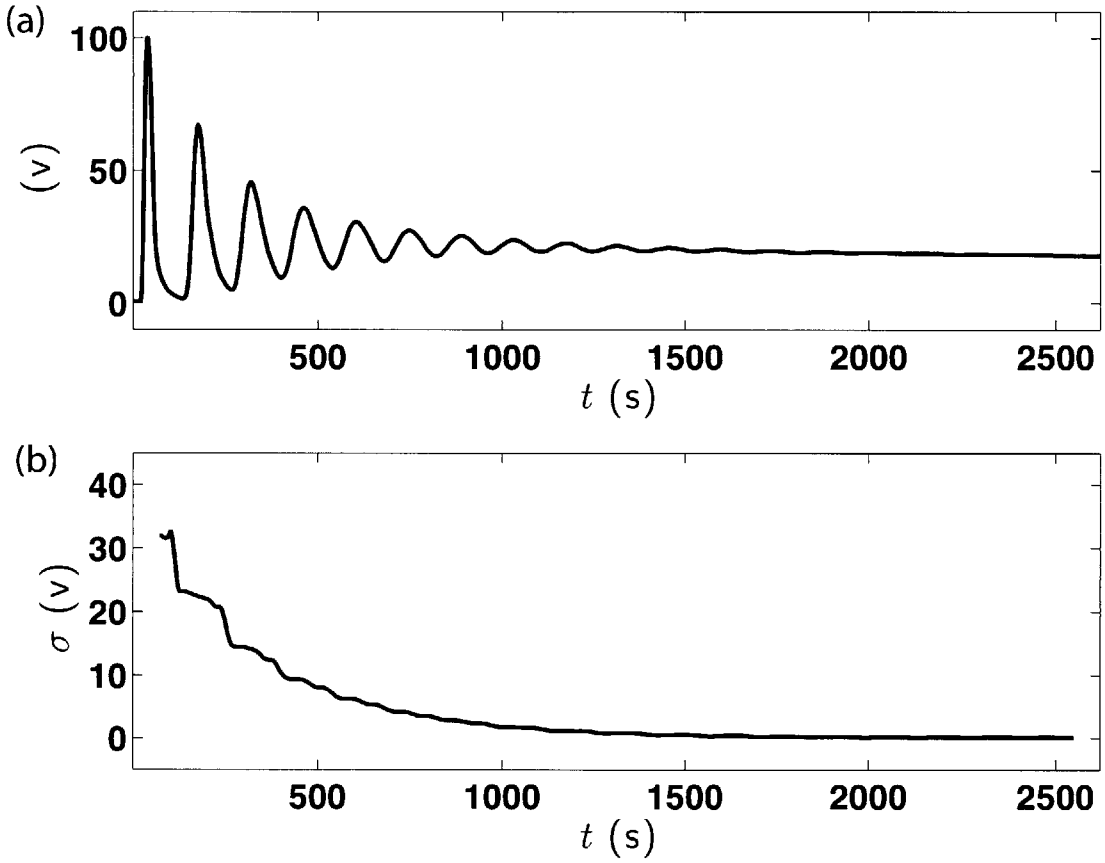

Figure C-1: (a) The measured voltage (a linear surrogate for concentration) over time for the flume mixing test using Rhodamine WT. (b) The moving-window, temporal standard deviation of the voltage, in which the moving window size is the flume recirculation period.

Appendix D

Flux Experiments Data

Table D.1: The measured concentration of $CHBr_2CL$ in the vial water and the measured concentration of $CHBr_2CL$ in the flume water for each of the experimental time points for the $h = 50$ μm blade. The normalized mass in the PE (Table 4.3) is calculated using Eqs. 4.3 & 4.4. The number of replicates for each mass measurement is denoted by n.

t (s)	$C_{W,vial}$ (ppb)	n	$C_{W,\infty}(t)$ (ppb)	n	Water mass (g)	PE mass (g)
15	0.89 ± 0.16	3	50.51 ± 6.83	4	41.6017	0.3883
30	1.38 ± 0.07	4	63.21 ± 13.74	4	41.8317	0.3883
60	1.84 ± 0.24	4	59.76 ± 13.21	4	41.6402	0.3798
120	4.98 ± 0.90	2	61.08 ± 12.31	4	41.1428	0.3772
180	5.60 ± 0.82	2	58.93 ± 8.75	4	41.5468	0.3832
300	6.85 ± 0.21	3	58.89 ± 10.53	4	41.6338	0.3962
600	-	-	-	-	-	-

Table D.2: The measured concentration of $CHBr_2CL$ in the vial water and the measured concentration of $CHBr_2CL$ in the flume water for each of the experimental time points for the $h = 250$ μm blade. The normalized mass in the PE (Table 4.3) is calculated using Eqs. 4.3 & 4.4. The number of replicates for each mass measurement is denoted by n.

t (s)	$C_{W,vial}$ (ppb)	n	$C_{W,\infty}(t)$ (ppb)	n	Water mass (g)	PE mass (g)
60	1.40 ± 0.45	4	71.02 ± 13.45	4	39.3891	2.0409
120	2.37 ± 1.04	4	59.40 ± 8.15	4	39.5145	2.0255
180	2.65 ± 0.86	3	71.18 ± 14.04	4	39.9028	2.0072
300	3.20 ± 0.73	4	70.42 ± 19.82	4	39.9552	2.0448
600	4.82 ± 0.81	3	64.67 ± 14.46	4	39.5048	2.0352
900	6.81 ± 0.41	3	66.26 ± 10.38	4	39.7494	2.0206
1200	8.59 ± 1.15	4	62.36 ± 4.47	4	39.7777	2.0123

Table D.3: The measured concentration of $CHBr_2CL$ in the vial water and the measured concentration of $CHBr_2CL$ in the flume water for each of the experimental time points for the cut sections of the $h = 50$ μm blade. The normalized mass in the PE (Table 4.3) is calculated using Eqs. 4.3 & 4.4. The number of replicates for each mass measurement is denoted by n.

	Clamped		Free				Clamped		Free	
t (s)	$C_{W,vial}$ (ppb)	n	$C_{W,vial}$ (ppb)	n	$C_{W,\infty}(t)$ (ppb)	n	Water mass (g)	PE mass (g)	Water Mass (g)	PE Mass (g)
15	0.12 ± 0.02	3	0.09 ± 0.01	3	59.16 ± 8.12	4	41.5988	0.0312	41.9689	0.0311
30	0.16 ± 0.01	3	0.16 ± 0.02	3	59.74 ± 9.62	4	41.9098	0.0302	42.1189	0.0311
60	0.22 ± 0.02	3	0.20 ± 0.01	3	56.11 ± 11.80	4	42.097	0.033	42.1068	0.0332
120	0.32 ± 0.02	3	0.26 ± 0.02	3	57.20 ± 9.46	4	41.9292	0.0308	42.2503	0.0297
180	0.31 ± 0.02	3	0.37 ± 0.05	4	54.54 ± 6.06	4	42.2405	0.0295	42.1781	0.0319
300	0.61 ± 0.02	4	0.54 ± 0.02	4	62.20 ± 10.90	4	42.278	0.032	42.2173	0.0327
600	0.69 ± 0.01	2	0.74 ± 0.05	4	54.33 ± 6.62	4	41.369	0.031	42.0471	0.0329

Table D.4: The measured concentration of $CHBr_2CL$ in the vial water and the measured concentration of $CHBr_2CL$ in the flume water for each of the experimental time points for the cut sections of the $h = 250$ μm blade. The normalized mass in the PE (Table 4.3) is calculated using Eqs. 4.3 & 4.4. The number of replicates for each mass measurement is denoted by n.

	Clamped		Free				Clamped		Free	
t (s)	$C_{W,vial}$ (ppb)	n	$C_{W,vial}$ (ppb)	n	$C_{W,\infty}(t)$ (ppb)	n	Water mass (g)	PE mass (g)	Water Mass (g)	PE Mass (g)
60	0.20 ± 0.04	4	0.18 ± 0.01	4	61.84 ± 12.94	4	41.2552	0.1848	42.0641	0.1759
120	0.28 ± 0.04	4	0.28 ± 0.03	4	71.16 ± 13.57	4	41.9568	0.1832	41.5459	0.1841
180	0.35 ± 0.02	2	0.34 ± 0.02	3	65.91 ± 9.38	4	41.4749	0.1651	41.813	0.157
300	0.61 ± 0.42	3	0.55 ± 0.04	3	74.35 ± 15.69	4	41.9401	0.1799	41.5656	0.1644
600	1.01 ± 0.52	3	1.02 ± 0.07	3	70.28 ± 12.99	4	41.7718	0.1582	41.8351	0.1649
900	1.10 ± 0.44	4	1.15 ± 0.04	3	66.16 ± 10.48	4	41.8616	0.1584	41.8668	0.1632
1200	1.12 ± 0.17	4	1.22 ± 0.21	4	52.50 ± 6.08	4	41.4587	0.1513	41.8934	0.1566

Appendix E

Measuring THM Concentration

E.1 Overview

In this appendix we describe in detail the method used to measure trihalomethane (THM) concentrations in water and in the LDPE blades. The method consists of the following steps: extracting the THMs from a water sample using purge & trap system, separating the different THMs using a gas chomatograph (GC) and measuring the THM concentration with an electron capture detector (ECD).

This method is used to directly measure the THM concentration in water, but can easily be used to also measure THM concentrations inside LDPE. This is accomplished by inserting the LDPE in a volume of clean water with no head space. The sample is then placed on a shaker table to allow the THMs to more rapidly reach equilibrium between the polyethylene and water phases. Utilizing our knowledge of the compound's partitioning coefficient between the polyethylene and water phases, we can relate the measured water concentration to the original concentration in the polyethylene.

E.2 Purge and Trap System

The THMs used in these experiments are extracted and concentrated from water samples with the use of a Tekmar LSC 2000 purge and trap system. In this system,

a 5 mL volume of the sample of interest is injected into the instrument. The sample volume is then purged with helium gas for a user-specific amount of time. We describe the choice of purge times below with the discussion of the calibration curves. The total mass of the compounds extracted from the water sample is directly dependent on the purge time. These purged gases then flow through a sorbent trap where they collect and concentrate. After the purging cycle is complete, the gas flow is turned off. The purged compounds are then removed from the trap through thermal desorption over the "desorb preheat" cycle. At the end of the cycle, the flow is re-started, and the entire volume of desorbed gases flows from the trap directly into the GC column. After the purged portion of the sample flows from the trap into the GC, the trap is baked to remove any residual sample which may interfere with subsequent samples.

E.3 Gas Chromatograph

The gas chromatograph that we use is a Perkin Elmer Autosystem XL. The column is an Agilent DB-624 column with a 1.80 μm film and 0.320 mm bore and is 60 m in length. As the purged portion of the sample flows through the GC column, each compound present interacts with the column in a unique manner, thus separating the sample components. The column length is designed to be long enough such that each compound elutes completely separately.

At the end of the column is the detector, an electron capture detector (ECD). This type of sensor is specifically used for halogenated compounds, such as $CHBr_2Cl$, and other compounds with high electronegativities. As the purged compound molecules flow through the detector, free electrons are captured by the sample molecules, changing the current between the detector cathode and anode. The voltage drop across the detector is recorded continuously at 1 Hz and the sample concentration can then be related to the integral of the instrument voltage-time curve.

E.4 Concentration Calibration

We calibrate the output from the GC-ECD system with a set of concentration standards. Standards of $CHBr_2Cl$ were prepared at the following concentrations: 80 ppb, 40 ppb, 20 ppb, 10 ppb, 4 ppb, 2 ppb, 1 ppb, 0.4 ppb, 0.2 ppb, 0.1 ppb and 0.04 ppb. These samples were injected into the Purge & Trap, GC-ECD system at a range of purge times, in order to extract differing amounts of $CHBr_2Cl$ from the sample and to create a series of calibration curves for different purge times. The calibrations are run for purge times of 4.00 min, 2.00 min, 1.50 min, 1.00 min, 0.80 min, 0.50 min, 0.30 min and 0.25 min. These calibration curves, which are presented below, provide a relationship between the time integration of the detector output (i.e. the area under the curve in voltage-time space) and the concentration of $CHBr_2Cl$ in the sample.

Table E.1: Table of $CHBr_2Cl$ curve areas from the GC-ECD, in units of mV*sec. Each prepared concentration standard was run for a range of purge times and used to produce unique calibration curves for each of these purge times. For certain concentrations, multiple runs were performed at the same purge time. In these cases, both values were used in the regression. The header row represents the purge times.

C (ppb)	0.25 min	0.30 min	0.50 min	0.80 min	1.00 min	1.50 min	2.00 min	4.00 min
80	576.083	3074.159						
40	347.610	887.554						
20	204.990	542.346	4424.950					
10	87.666	262.194	2344.130					
4	40.456	70.621	824.875	2767.371				
2	14.216		347.870	1394.985	1872.190 1906.555			
1				503.654	878.263	1523.020	2341.174	
0.4			68.462		296.438 307.581	567.170	843.836	
0.2			29.669		153.257 176.111	353.092	444.977	
0.1			19.746		87.118	166.629	221.537	396.178
0.04					60.124 60.832	89.122	91.075	177.966

Table E.2: The calibration curves at all purges times for the concentration of $CHBr_2Cl$ in the samples based on the data in Table E.1. The sample concentration, C, is in units of ppb and the curve area, A, is in units of mV*sec. When the coefficient of determination is less than 0.98, a quadratic regression is also provided.

Purge Time (min)	Linear Regression	Quadratic Regression
0.25 min	$C = 0.129217A$ $(R^2 = 0.977489)$	$C = 0.000098A^2 + 0.082282A$ $(R^2 = 0.998610)$
0.30 min	$C = 0.027832A$ $(R^2 = 0.920369)$	$C = -0.000007A^2 + 0.047529A$ $(R^2 = 0.992244)$
0.50 min	$C = 0.004359A$ $(R^2 = 0.993754)$	
0.80 min	$C = 0.001457A$ $(R^2 = 0.984371)$	
1.00 min	$C = 0.001071A$ $(R^2 = 0.995709)$	
1.50 min	$C = 0.000657A$ $(R^2 = 0.996360)$	
2.00 min	$C = 0.000433A$ $(R^2 = 0.997596)$	
4.00 min	$C = 0.000248A$ $(R^2 = 0.988807)$	

P&T Settings	Value
Standby Temp.	30° C
Preheat	NI
Purge	Variable Times*
Prepurge	NI
Sample	NI
Dry Purge	0.00 min
MCM Cooldown	No
Cap Cooldown	NI
Desorb Preheat	220° C
Desorb	2.00 min @ 225° C
Inject	NI min at NI ° C
Bake	10.00 min @ 230° C
BGB	Off
BGB Delay	0 sec
Auto Drain	On
Valve	150° C
Mount	100° C
2016 Valve	NI
2032 Valve	NI
Line	125° C
Aux HTR	NI
Line	NI
Line	NI
Cap Union	NI
Runs Per Sample	1
Bakeout	Off
MCM Heat	No

GC Settings	Value
Temp 1	40 ° C
Time 1	0.50 min
Rate	10 ° C / min
Cap 1	125 ° C
Flow 1	70 mL/min
ECD 2	200 ° C
Int 1 Atten	1
Int 2 Atten	64
Auto Zero	30 mV or lower

Appendix F

Finite Difference Flux Model

In this appendix, we present the script used to numerically solve Eqs. 4.15-4.17 using a fully-implicit finite-difference (FD) scheme. This method can either be used with a prescribed transfer velocity (as it is shown below) or with a range of transfer velocities. When a range of transfer velocities are input into the model, one can then find the transfer velocity that minimizes the sum of squares error between the model and an experimental data set.

```
close all
clear all
clc



% INPUTS
N=100;  % number of nodes over flag thickness
L=1;  % dimensionless blade thickness
dt=10^-3;   % dimensionless time step
T=10;  % dimensionless time
Ks=[100 300];  % PE / H2O partition coeff.
hs=[250E-6 50E-6];  %dimensional thickness (m)
D_PE=(10^-11.3);  % m2/s  (log10 DPE = -11.3 +- 1.0)
D_H2O = 1E-9; % m2/s
C_inf=65;  % ppb, Measured conc in Water
b=0.03;  %m, width
l=0.3;  % m, length
delta=1.9E-4;


dx=L/N; %dimensionless flag thickness coordinate
x_coord=dx:dx:L;


dl=0.01;  %dimensionless length coordinate
length_coord=dl:dl:1;


etas_of_interest=[-2.4 -4.0];
lDs=[6];


for jjj=1:length(lDs)
    lD=lDs(jjj);
    T_renew=T_renews(jjj);

    load(['Rel_Velocity_rms_tip_lD_' num2str(lD) '.mat']);
    N_Cheb=length(rms_norm_flux)-1;  %different Ns for lD=3 and lD=6;

    % get chebyshev nodes (x) from clencurt.m
    [x,~,~] = clencurt(N_Cheb);


    for jj=1:length(etas_of_interest)

        etas_ind=find(round(etas*10)==round(etas_of_interest(jj)*10));
        h=hs(jj);
        K=Ks(jj);
        for kk=1:length(length_coord) %calculate flux over flag length


            rms_norm_flux_reg_grid=interp1(((x./2)+0.5),...
```

```
    rms_norm_flux(:,etas_ind),length_coord(kk));


BJ_23=(h/(2.*D_PE.*K)).*(3*sqrt(3)/(2*pi)).*...
    ((rms_norm_flux_reg_grid.*0.2./(b^2)).^(1/3)).*...
    (D_H2O^(2/3));


%%%%%%%%%%%%%%%%%%%%
%MATRIX A  D^2/3 flux
aa_23=zeros(N,1)+(-1/dx);
bb_23=zeros(N,1)+((2/dx)+(dx/dt));
cc_23=zeros(N,1)+(-1/dx);


%modify "b" (the center diagonal) vector to account for
%boundary conditions
bb_23(1)=((1/dx)+(dx/dt));
bb_23(N)=((1/dx)+(dx/dt)+BJ_23);

abc_23=[aa_23 bb_23 cc_23];


%create SPARSE matrix, with a,b and c along diagonals 1,0,-1
%respectively
A_23=spdiags(abc_23,[1,0,-1],N,N);
%%%%%%%%%%%%%%%%%%%%


%%%%%%%%%%%%%%%%%%%%
%INITIAL CONDITION D^2/3 flux
C_23=zeros(N,1)+0;
%%%%%%%%%%%%%%%%%%%%


%%%%%%%%%%%%%
% Build RHS Vector   D^2/3 flux
BCs_23=zeros(N,1);
BCs_23(end)=BJ_23;  % right boundary constant flux b.c.
%%%%%%%%%%%%%

t=dt:dt:T;


% Advance system through time
for i=1:length(t)
    %%%%%%%%%%%%%%%%%%%%%%
    %Solve for B_23
    % D^2/3 flux
    B_23=(C_23.*dx./dt)+BCs_23;
    C_new_23=A_23\B_23;
    C_23=C_new_23;
```

```
            %mass per unit width per unit length
            Mass_dim_23(i)=sum(C_23).*dx;

            %flux at z=1
            dimless_flux_23(i)=BJ_23.*(1-C_23(end));


        end

        %dimensional flux
        flux_actual_23(kk,jj,:)=dimless_flux_23.*(D_PE.*K.*...
            C_inf./(h/2));

        % Dimensional mass per unit length inside half thickness of PE
        % at all times D^2/3
        Mass_23(kk,jj,:)=Mass_dim_23.*(C_inf.*K.*(h/2).*b);
    end


    % integrate mass over length
    % dimensional mass
    % Surface Renewal Flux
    Mass_integr_23(jj,:)=sum(Mass_23(:,jj,:).*dl,1).*0.3*2; %sum over
    % dimensionless length, multiply by dimensional length
    % also multiply by two to account for both sides accumulating mass
    % simultaneously



    % average the flux over length
    flux_avg_23(jj,:)=mean(flux_actual_23(:,jj,:),1);

    % integrated mass in the clamped-end and free-end sections
    Mass_integr_23_origin(jj,:)=sum(Mass_23(1:8,jj,:).*dl,1).*0.3*2;
    Mass_integr_23_tip(jj,:)=sum(Mass_23(93:100,jj,:).*dl,1).*0.3*2;
  end
end


% Mass_integr_23=Mass_integr_23.*1000;

Mass_integr_23_norm(1,:)=Mass_integr_23(1,:)./(Ks(1)*C_inf*hs(1)*b*l);
Mass_integr_23_norm(2,:)=Mass_integr_23(2,:)./(Ks(2)*C_inf*hs(2)*b*l);

Mass_integr_SR_norm(1,:)=Mass_integr_SR(1,:)./(Ks(1)*C_inf*hs(1)*b*l);
Mass_integr_SR_norm(2,:)=Mass_integr_SR(2,:)./(Ks(2)*C_inf*hs(2)*b*l);


% Normalize Origin and Tip sections
Mass_integr_23_origin_norm(1,:)=Mass_integr_23_origin(1,:)./(Ks(1)*...
    C_inf*hs(1)*b*l.*(2.4/30));
Mass_integr_23_origin_norm(2,:)=Mass_integr_23_origin(2,:)./(Ks(2)*...
    C_inf*hs(2)*b*l.*(2.4/30));
```

```
Mass_integr_23_tip_norm(1,:)=Mass_integr_23_tip(1,:)./(Ks(1)*C_inf*...
    hs(1)*b*l.*(2.4/30));
Mass_integr_23_tip_norm(2,:)=Mass_integr_23_tip(2,:)./(Ks(2)*C_inf*...
    hs(2)*b*l.*(2.4/30));
```

Bibliography

[1] R.G. Adams, R. Lohmann, L.A. Fernandez, J.K. MacFarlane, and P.M. Gschwend. Polyethylene devices: passive samplers for measuring dissolved hydrophobic organic compounds in aquatic environments. *Environ. Sci. Technol.*, 41:1317–1323, 2007.

[2] S. Alben. Passive and active bodies in vortex-street wakes. *J. Fluid Mech.*, 642:99–125, 2009.

[3] S. Alben and M.J. Shelley. Flapping states of a flag in an inviscid fluid: bistability and the transition to chaos. *Physical Review Letters*, 100(074301), 2008.

[4] S. Alben, M.J. Shelley, and J. Zhang. Drag reduction through self-similar bending of a flexible body. *Nature*, 420(6915):479–481, 2002.

[5] J.J. Allen and A.J. Smits. Energy harvesting eel. *Journal of Fluids and Structures*, 15:629–640, 2001.

[6] M. Argentina and L. Mahadevan. Fluid-flow-induced flutter of a flag. *Proc. Nat. Acad. Sci*, 102(6):1829–1834, February 8 2005.

[7] G.S. Beavers and D.D. Joseph. Boundary conditions at a naturally permeable wall. *J. Fluid Mech.*, 30:197–207, 1967.

[8] S.E. Belcher, J.J. Finnigan, and I.N. Harman. Flows through forest canopies in complex terrain. *Ecological Applications*, 18(6):1436–1453, 2008.

[9] S.E. Belcher, N. Jerram, and J.C.R. Hunt. Adjustment of a turbulent boundary layer to a canopy of roughness elements. *J. Fluid Mech.*, 488:369–398, 2003.

[10] T. Bentham and R. Britter. Spatially averaged flow within obstacle arrays. *Atmospheric Environment*, 37:2037–2043, 2003.

[11] R.D. Blevins. *Formulas for natural frequency and mode shape.* Krieger, 1984.

[12] R.D. Blevins. *Flow Induced Vibration.* Krieger Publishing Company, 2nd edition, 1990.

[13] K. Booij, H.M. Sleiderink, and F. Smedes. Calibrating the uptake kinetics of semipermeable membrane devices using exposure standards. *Environmental Toxicology and Chemistry*, 17(7):1236–1245, 1998.

[14] B.P. Boudreau and B.B. Jorgensen, editors. *The benthic boundary layer.* Oxford, 2001.

[15] T.J. Bouma, L.A. van Duren, S. Temmerman, T. Claverie, A. Blanco-Garcia, T. Ysebaerty, and P.M.J. Herman. Spatial flow and sedimentation patterns within patches of epibenthic structures: combining field, flume and modelling experiments. *Continental Shelf Research*, 27:1020–1045, 2007.

[16] J.P. Boyd. *Chebyshev and Fourier Spectral Methods.* Dover, second edition, 2000.

[17] G. Brown and A. Roshko. On density effects and large structure in turbulent mixing layers. *J. Fluid Mech.*, 64:775–816, 1974.

[18] A.C. Cheshire and N.D. Hallam. Morphological differences in the southern bull-kelp (durvillaea potatorum) throughout south-eastern australia. *Bot. Mar.*, 32:191–197, 1989.

[19] O. Coceal and S.E. Belcher. A canopy model of mean winds through urban areas. *Quart. J. R. Met. Soc.*, 130:1349–1372, 2004.

[20] B.S.H. Connell and D.K.P. Yue. Flapping dynamics of a flag in a uniform stream. *Journal of Fluid Mechanics*, 581:33–67, 2007.

[21] P.V. Danckwerts. Significance of liquid-film coefficients in gas absorption. *Industrial and Engineering Chemistry*, 43(6):1460–1467, 1951.

[22] W.M. Deen. *Analysis of transport phenomena.* Oxford, 1998.

[23] M. Denny, B. Gaylord, B. Helmuth, and T. Daniel. The menace of momentum: dynamic forces on flexible organisms. *Limnol. Oceanogr.*, 43(5):955–968, 1998.

[24] M.W. Denny and B. Gaylord. The mechanics of wave-swept algae. *J. Exp. Biol.*, 205:1355–1362, 2002.

[25] P. Drazin and W. Reid. *Hydrodynamic Stability.* Cambridge University Press, 1981.

[26] L.D. Druehl and L. Kemp. Morphological and growth responses of geographically isolated macrocystis integrifolia populations when grown in a common environment. *Canadian Journal of Botany*, 80:1409–1413, 1982.

[27] D.O. Duggins, J.E. Eckman, C.E. Siddon, and T. Klinger. Population, morphometric and biomechanical studies of three understory kelps along a hydrodynamic gradient. *Mar. Ecol. Prog. Ser.*, 265:57–76, 2003.

[28] I. Eames, J.C.R. Hunt, and S.E. Belcher. Inviscid mean flow through and around groups of bodies. *J. Fluid Mech.*, 515:371–389, 2004.

[29] J.J. Finnigan. Turbulence in plant canopies. *Annu. Rev. Fluid Mech.*, 32:519–571, 2000.

[30] J.J. Finnigan and R.H. Shaw. A wind-tunnel study of airflow in waving wheat: an eof analysis of the structure of the large-eddy motion. *Boundary Layer Meteorology*, 96:211–255, 2000.

[31] C.S. Garbe, U. Schimpf, and B. Jaehne. A surface renewal model to analyze infrared image sequences of the ocean surface for the study of air-sea heat and gas exchange. *J. Geophys. Res.*, 109:C08S15, 2004.

[32] B. Gaylord, J.H. Rosman, D.C. Reed, and et al. Spatial patterns of flow and their modification within and around a giant kelp forest. *Limnol. Oceanogr.*, 52(5):1838–1852, 2007.

[33] V.A. Gerard. In situ water motion and nutrient uptake by the giant kelp macrocystis pyrifera. *Marine Biology*, 69:51–54, 1982.

[34] V.A. Gerard. In situ water motion and nutrient uptake by the giant kelp macrocystis pyrifera. *Marine Biology*, 69:51–54, 1982.

[35] V.A. Gerard and K.H. Mann. Growth and production of laminaria longicruris (phaeophyta) populations exposed to different intensities of water movement. *J. Phycol.*, 15:33–41, 1979.

[36] Valrie A. Gerard. In situ rates of nitrate uptake by giant kelp, macrocystis pyrifera (l.) c. agardh: Tissue differences, environmental effects, and predictions of nitrogen-limited growth. *J. Exp. Mar. Biol. Ecol.*, 62:211–224, 1982.

[37] M. Ghisalberti and H.M. Nepf. Mixing layers and coherent structures in vegetated aquatic flows. *J. Geophys. Res.*, 107(C2):3011, 2002.

[38] M. Ghisalberti and H.M. Nepf. Shallow flows over a permeable medium: the hydrodynamics of submerged aquatic canopies. *Transport in Porous Media*, 78:309–326, 2009.

[39] F. Gosselin, E. de Langre, and B.A. Machada-Almeida. Drag reduction of flexible plates by reconfiguration. *J. Fluid Mech.*, 650:319–341, 2010.

[40] W.G. Gray and P.C.Y. Lee. On the theorems for local volume averaging of multiphase systems. *International Journal of Multiphase Flow*, 3(4):333–340, 1977.

[41] C.S.B. Grimmond and T.R. Oke. Aerodynamic properties of urban areas derived from analysis of surface form. *Jounral of Applied Metcorology*, 38(9):1262–1292, 1999.

[42] J.K. Gundersen and B.B. Jorgensen. Microstructure of diffusive boundary layers and the oxygen uptake of the sea floor. *Nature*, 345:604–607, 1990.

[43] B.B. Hale. *Macroalgal materials: foiling fracture and fatigue from fluid forces.* PhD thesis, Stanford University, 2001.

[44] R.N. Haring and R.C. Carpenter. Habitat-induced morphological variatoin influences photosynthesis and drag on the marine macroalga pachidictyon coriaceum. *Mar. Biol.*, 151:243–255, 2007.

[45] C.D. Hepburn, J.D. Holborow, S.R. Wing, R.D. Frew, and C.L. Hurd. Exposure to waves enhances the growth rate and nitrogen status of the giant kelp macrocystis pyrifera. *Marine Ecology Progress Series*, 339:99–108, 2007.

[46] R. Higbie. The rate of absorption of a pure gas into a still liquid during short periods of exposure. *Trans. Am. Inst. Chem. Eng.*, 31:365–389, 1935.

[47] C. Ho and P. Huerre. Perturbed free shear layers. *Ann. Rev. Fluid Mech.*, 16:365–424, 1984.

[48] I. Huang, J.T. Rominger, and H.M. Nepf. The motion of kelp blades and the surface renewal model. *Limnol. Oceanogr.*, 56(4):1453–1462, 2011.

[49] C.L. Hurd, P.J. Harrison, and L.D. Druehl. Effect of seawater velocity on inorganic nitrogen uptake by morphologically distinct forms of macrocystis integrifolia from wave-sheltered and exposed sites. *Marine Biology*, 126:205–214, 1996.

[50] C.L. Hurd and C.A. Pilditch. Flow-induced morphological variatoins affect diffusion boundary-layer thickness of macrocystis pyrifera (heterokontophyta, laminariales). *J. Phycol.*, 47:341–351, 2011.

[51] J.J. Jackelman and J.J. Bolton. Form variation and productivity of an intertidal foliose gigartina species (rhodophyta) in relation to wave exposure. *Hydrobiologia*, 204:57–64, 1990.

[52] G.A. Jackson. Currents in the high drag environment of a coastal kelp stand off california. *Continental Shelf Research*, 17(15):1913–1928, 1997.

[53] G.A. Jackson and C.D. Winant. Effect of a kelp forest on coastal currents. *Continental Shelf Research*, 2(1):75–80, 1983.

[54] D.L. Koch and A.J.C. Ladd. Moderate reynolds number flows through periodic and random arrays of aligned cylinders. *J. Fluid Mech.*, 349:31–66, 1997.

[55] E.W. Koch. Hydrodynamics, diffusion-boundary layers and photosynthesis of the seagrasses thalassia testudinum and cymodocea nodosa. *Marine Biology*, 118:767–776, 1994.

[56] M.A.R. Koehl and R.S. Alberte. Flow, flapping, and photosynthesis of nereocystis luetkeana: a functional comparison of undulate and flat blade morphologies. *Marine Biology*, 99:435–444, 1988.

[57] M.A.R. Koehl, W.K. Silk, H. Liang, and L. Mahadevan. How kelp produce blade shapes suited to different flow regimes: A new wrinkle. *Integrative and Comparative Biology*, 48(6):834–851, 2008.

[58] P. Koumoutsakos and D. Shiels. Simulations of the viscous flow normal to an impulsively started and uniformly accelerated flat plate. *J. Fluid Mech.*, 328:177–227, 1996.

[59] L.T. Kregting, C.L. Hurd, C.A. Pilditch, and C.L. Stevens. The relative importance of water motion on nitrogen uptake by the subtidal macroalga adamsiella chauvinii (rhodophyta) in winter and summer. *J. Phycol.*, 44:320–330, 2008.

[60] F. Krzikalla. Numerical investigation of the interaction between wind and forest and heterogeneous conditions. Master's thesis, University of Karlsruhe, May 2005.

[61] J.H. Lau. Stiffness of corrugated plate. *Journal of the Engineering Mechanics Division*, 107(1):271–275, 1981.

[62] J.J. Ledwell. The variation of the g as transfer coefficient with molecular diffusivity. In W. Brutsaert and G.H. Jirka, editors, *Gas Transfer at Water Surfaces*, pages 293–302, Dordrecht, Netherlands, 1984. Reidel.

[63] J.C. Liao, D.N. Beal, G.V. Lauder, and M.S. Triantafyllou. The kármán gait: novel body kinematics of rainbow trout swimming in a vortex street. *J. Exp. Biol.*, 206:1059–1073, 2003.

[64] R. Lohmann. Critical review of low-density polyethylene's partitioning and diffusion coefficients for trace organic contaminants and implications for its use as a passive sampler. *Environ. Sci. Technol.*, 46:606–618, 2012.

[65] R.J. Lowe, J.R Koseff, and S.G. Monismith. Oscillatory flow through submerged canopies: 1. canopy mass transfer. *J. Geophys. Res.*, 110:C10017, 2005.

[66] M. Luhar, S. Coutu, E. Infantes, S. Fox, and H. Nepf. Wave-induced velocities inside a model seagrass bed. *J. Geophys. Res.*, 115:C12005, 2010.

[67] M. Luhar and H.M. Nepf. Flow-induced reconfiguration of buoyant and flexible aquatic vegetation. *Limnology and Oceanography*, 56(6):2003–2017, 2011.

[68] A. Manela and M.S. Howe. The forced motion of a flag. *J. Fluid Mech.*, 635:439–454, 2009.

[69] S. Michelin and O. Doaré. Energy harvesting efficiency of piezoelectric flags in axial flows. *J. Fluid Mech.*, 714:489–594, 2013.

[70] S. Michelin and S.G. Llewellyn Smith. Resonance and propulsion performance of a heaving flexible wing. *Physics of Fluids*, 21(071902), 2009.

[71] S. Michelin, S.G. Llewellyn Smith, and B.J. Glover. Vortex shedding model of a flapping flag. *Journal of Fluid Mechanics*, 617:1–10, 2008.

[72] M.T. Morris-Thomas and S. Steen. Experiments on the stability and drag of a flexible sheet under in-plane tension in uniform flow. *Journal of Fluids and Structures*, 25:815–830, 2009.

[73] J.F. Mueller, K. Manomanii, M.R. Mortimer, and M.S. McLachlan. Partitioning of polycyclic aromatic hydrocarbons in the polyethylene/water system. *Fresenius J Anal Chem*, 371:816–822, 2001.

[74] H.M. Nepf, M. Ghisalberti, B.L. White, and E. Murphy. Retention time and dispersion associated with submerged aquatic canopies. *Water Resources Research*, 43:W04422, 2007.

[75] V. Nikora, I. McEwan, S. McLean, S. Coleman, D. Pokrajac, and R. Walters. Double-averaging concept for rough-bed open-channel and overland flows: theoretical background. *J. Hydr. Eng.*, 133(8):873–883, 2007.

[76] M.P. Paidoussis. *Fluid-structure interactions: slender structures and axial flow Volume 2*, volume 2. Elsevier, 2004.

[77] M. Parke. Studies on british laminariaceae. i. growth in laminaria saccharina (l.) lamour. *J. Mar. Biol. Assoc. UK*, 27:651–709, 1948.

[78] G. Peralta, F.G. Brun, J.L. Pérez-Lloréns, and T.J. Bouma. Direct effects of current velocity on the growth, morphometry and architecture of seagrasses: a case study on zostera noltii. *Mar. Ecol. Prog. Ser.*, 327:135–142, 2006.

[79] D.R. Plew, G.G. Cooper, and F.M. Callaghan. Turbulence-induced forces in a freshwater macrophyte canopy. *Water Resources Research*, 44:W02414, 2008.

[80] D. Poggi, G. Katul, and J. Albertson. A note on the contribution of dispersive fluxes to momentum transfer within canopies. *Boundary Layer Meteorology*, 11(3):615–621, 2004.

[81] D. Poggi, A. Porporato, L. Ridolfi, J.D. Albertson, and G.G. Katul. The effect of vegetation density on canopy sub-layer turbulence. *Boundary Layer Meteorology*, 111:565–587, 2004.

[82] P. Prempraneerach, F.S. Hover, and M.S. Triantafyllou. The effect of chordwise flexibility on the thrust and efficiency of a flapping foil. 2003.

[83] M.R. Raupach, J.J. Finnigan, and Y. Brunet. Coherent eddies and turbulence in vegetation canopies: the mixing layer analogy. *Boundary Layer Meteorology*, 78:351–382, 1996.

[84] M.R. Raupach and R.H. Shaw. Averaging procedures for flow within vegetation canopies. *Boundary Layer Meteorology*, 22:79–90, 1982.

[85] O. Reynolds. On the extent and action of the heating surface for steam boilers. *Proc. Manchester Lit. Phil. Soc.*, 14(7), 1874.

[86] L. Ristroph and J. Zhang. Anomalous hydrodynamic drafting of interacting flapping flags. *Physical Review Letters*, 101:194502, 2008.

[87] L.M. Roberson and J.A. Coyer. Variation in blade morphology of the kelp eisenia arborica: incipient speciation due to local water motion? *Marine Ecology Progress Series*, 282:115–128, 2004.

[88] J.T. Rominger and H.M. Nepf. Flow adjustment and interior flow associated with a rectangular porous obstruction. *J. Fluid Mech.*, 680:636–659, 2011.

[89] J.H. Rosman, J.R. Koseff, S.G. Monismith, and J. Grover. A field investigation into the effects of a kelp forest (macrocystis pyrifera) on costal hydrodynamics and transport. *J. Geophys. Res.*, 112:C02016, 2007.

[90] P.G. Saffman. *Vortex Dynamics.* Cambridge University Press, 1992.

[91] K. Sand-Jensen and M.L. Pedersen. Streamlining of plant patches in streams. *Freshwater Biology*, 53:714–726, 2008.

[92] M. Schatz, D. Barkley, and H. Swinney. Instability in a spatially periodic open flow. *Phys. Fluids*, 7(2):344–358, 1995.

[93] H. Schlichting. *Boundary Layer Theory.* McGraw-Hill, fourth edition, 1962.

[94] M. Shelley, N. Vandenberghe, and J. Zhang. Heavy flags undergo spontaneous oscillations in flowing water. *Physical Review Letters*, 94:094302, 2005.

[95] K. Sjotun and S. Frederiksen. Growth allocatoin in laminaria hyperborea (laminariales, phaeophyceae) in relation to age and wave exposure. *Mar. Ecol. Prog. Ser.*, 126:213–222, 1995.

[96] A.V. Soloviev and P. Schluessel. Parameterization of the cool skin of the ocean and of the air-ocean gas transfer on the basis of modeling surface renewal. *Journal of Physical Oceanography*, 24(6):1339–1346, 1994.

[97] C.L. Stevens and C.L. Hurd. Boundary-layers around bladed aquatic macrophytes. *Hydrobiologia*, 346:119–128, 1997.

[98] C.L. Stevens, C.L. Hurd, and P.E. Isachsen. Modelling of diffusion boundary-layers in subtidal macroalgal canopies: The response to waves and currents. *Aquat. Sci.*, 65:81–91, 2003.

[99] C.L. Stevens, C.L. Hurd, and M.J. Smith. Water motion relative to subtidal kelp fronds. *Limnol. Oceanogr.*, 46(3):668–678, 2001.

[100] H.L. Stewart, J.P. Fram, D.C. Reed, S.L. Williams, M.A. Brzezinksi, S. MacIntyre, and B. Gaylord. Differences in growth, morphology and tissue carbon and nitrogen of macrocystis pyrifera within and at the outer edge of a giant kelp forest in california, usa. *Mar. Ecol. Prog. Ser.*, 375:101–112, 2009.

[101] O. Sundene. Growth in the sea of laminaria digitata sporophytes from culture. *Nor. J. Bot*, 9:5–24, 1961.

[102] N. Tamai, T. Asaeda, and H. Ikeda. Study on generation of periodical large surface eddies in a composite channel flow. *Water Resources Research*, 22:1129–1138, 1986.

[103] S. Taneda. Waving motions of flags. *Journal of the Physical Society of Japan*, 24(2):392–401, 1968.

[104] Y. Tanino and H.M. Nepf. Laboratory investigation of mean drag in a random array of rigid, emergent cylinders. *Journal of Hydraulic Engineering*, 134(1), 2008.

[105] A.S. Thom. Momentum absorption by vegetation. *Quart. J. R. Met. Soc.*, 96:414–428, 1971.

[106] L.N. Trefethen. *Spectral methods in MATLAB.* SIAM, 2000.

[107] G. Triantafyllou and C. Chryssostomidis. Stability of a string in axial flow. *Journal of Energy Resources Technology*, 107:421–425, 1985.

[108] E.D. Tytell and G.V. Lauder. The hydrodynamics of eel swimming i. wake structure. *J. Exp. Biol.*, 207:1825–1841, 2004.

[109] S. Vogel. *Life in Moving Fluids: The Physical Biology of Flow.* Princeton University Press, second edition, 1994.

[110] J.R. Welty, C.E. Wicks, R.E. Wilson, and G.L. Rorrer. *Fundamentals of momentum, heat, and mass transfer.* Wiley, 4 edition, 2001.

[111] T. Wernberg and M.S. Thomsen. The effect of wave exposure on the morphology of ecklonia radiata. *Aquat. Bot.*, 83:61–70, 2005.

[112] W.N. Wheeler. Effect of boundary layer transport on the fixation of carbon by the giant kelp macrocystis pyrifera. *Marine Biology*, 56:103–110, 1980.

[113] B.L. White and H.M. Nepf. Shear instability and coherent structures in shallow flow adjacent to a porous layer. *J. Fluid Mech.*, 593:1–32, 2007.

[114] C.H.K. Williamson and R. Govardhan. Vortex-induced vibrations. *Annual Review of Fluid Mechanics*, 36:413–455, 204.

[115] J. Zhang, S. Childress, A. Libchaber, and M. Shelley. Flexible filaments in a flowing soap film as a model for one-dimensional flags in a two-dimensional wind. *Nature*, 408:835–839, 2000.

[116] L. Zong and H. Nepf. Flow and deposition in and around a finite patch of vegetation. *Geomorphology*, 116:363–372, 2010.